Motion of a probe nanoparticle in a quantum crystal with a narrow vacancy band

A. A. Levchenko, L. P. Mezhov-Deglin,* and A. B. Trusov

Institute for Solid-State Physics, pos. Chernogolovka, Moskovskaya obl., 142432, Russia

The temperature dependence of the diffusion coefficient $D_p(T)$ of a probe particle with a diameter d_p of several nanometers and moving in a quantum crystal with a narrow vacancy band $Q_v \ll T_{melt}$ changes substantially, as a result of interactions with thermal vacancies, with decreasing temperature in the range $T_{melt} \gtrsim T_{tr} \gtrsim Q_v$, where a transition occurs from classical thermally activated vacancy hopping to coherent motion of delocalized vacancies. Moreover, in the transitional range $T \approx T_{tr}$ the diffusion coefficient of a probe particle in a viscous vacancion gas can increase if the effective vacancion mean-free path length is small compared to the particle diameter $l_v \ll d_p$ and increases with decreasing temperature more rapidly than the concentration of thermal vacancies $x_v \sim \exp(-E_v/T)$. For $T \ll T_{tr}$, in a rarefied vacancion gas where $l_v \gg d_p$ the particle diffusion coefficient $D_p(T) \sim x_v S_{vp}$ decreases as x_v if the cross section S_{vp} for the inelastic scattering of a vacancion by a probe particle is a weak function of the temperature. The model developed in this paper can be used to describe the diffusion of positive charges in ^{4}He hcp crystals, grown at pressures above the lowest solidification pressure of helium, and negative charges in parahydrogen crystals. © *2003 American Institute of Physics.*
[DOI: 10.1063/1.1542499]

1. INTRODUCTION

According to Andreev's classification[1] quantum crystals are crystals where the probability of classical thermally activated site-to-site hopping of point defects in a crystal lattice becomes comparable to the probability of subbarrier quantum tunneling of defects at sufficiently high temperatures T_{tr} close in order of magnitude to the melting point T_{melt} of the sample (the temperature T_{tr} in ordinary "classical" crystals is exponentially low compared to T_{melt}). If the widths Q_v and Q_i, respectively, of the energy bands of point defects (vacancies) and impurity atoms or molecules in the experimental quantum crystal are much less than T_{melt}, then at high temperatures close to the melting point of the sample, $T \sim T_{melt} > T_{tr}$, the diffusion of point defects is described by the same laws as in an ordinary "classical" crystal (classical thermally activated diffusion; see, for example, Ref. 2). In the low temperature limit, $T \ll T_{tr}$, point defects are delocalized and defecton waves, or defectons (correspondingly, vacancions, impuritons) can freely propagate in the volume of a perfect quantum crystal. In a sample of finite size the effective travel distances of these quasiparticles are limited by scattering at the surface of the sample, just as the travel distances of phonons or electrons in a perfect metallic crystal at temperatures close to zero.

In the transitional range $T \sim T_{tr}$, where the predominant mechanism of diffusion of defects changes, the effective travel distances of defectons are short and comparable in order of magnitude to the crystal lattice constant of the sample l_v, $l_i \sim a \sim 0.3$ nm. Here scattering of defectons by phonons or mutual defecton-defecton (for example, impuriton-impuriton) scattering and scattering by defects of a different nature (dynamical or static shift of defecton levels in the terminology of Ref. 3) can play the main role here, which is what results in defecton localization at $T > T_{tr}$.

Detailed calculations of the behavior of the diffusion coefficient of impurities in quantum crystals with a narrow impurity band at temperatures $T \lesssim T_{tr}$ for the diffusion of ^{3}He impurity atoms in ^{4}He hcp crystals ($Q_3/T_{melt} \sim 10^{-4}$) and a comparison of the calculations and the results of direct NMR measurements of impurity diffusion with different content of ^{3}He atoms in a ^{4}He sample are presented in Refs. 1 and 3. Here we should also mention the theoretical calculations of the self-diffusion coefficient of molecules in p-H$_2$ parahydrogen crystals, taking account of the contributions of classical above-barrier and quantum subbarrier transposition of molecules and vacancies occupying neighboring sites in the crystal lattice,[4] and NMR measurements of the self-diffusion coefficient (more accurately, diffusion of o-H$_2$ impurity molecules; see Ref. 5) and the diffusion coefficient of deuterium-hydrogen HD molecules ($Q_3/T_{melt} \sim 10^{-3}$) in p-H$_2$ crystals.[6] In the experiments of Ref. 6 a transition was observed from thermally activated diffusion of localized HD molecules to coherent motion of delocalized impuritons when the sample was cooled below 10 K. The maximum travel distances of impuritons in these samples at temperatures $T \lesssim 8$ K were limited by scattering by orthohydrogen molecules and decreased with increasing content of the impurity o-H$_2$ in the sample. A transition to itinerant motion of o-H$_2$ molecules in self-diffusion experiments has not been observed, probably because the orthohydrogen molecule (which at high temperatures is a freely rotating rotator) strongly deforms the surrounding crystal matrix of a p-H$_2$ crystal, so that the corresponding width of the o-H$_2$ impuriton band is appreciably smaller than that of the band of the HD impurity molecules.

In the present paper the characteristic behavior of the diffusion coefficient $D_v(T)$ of vacancies and the diffusion coefficient $D_p(T)$ of a classical probe nanoparticle with di-

ameter d_p of the order of several nanometers ($d_p \gg a$) is discussed. The probe particle moves as a result of the interaction with thermal vacancies in a quantum crystal with a narrow vacancy band $Q_v \ll T_{melt}$. This question has not been previously investigated in detail in the literature; we have published a brief note.[7] Naturally, when discussing the temperature dependence of the diffusion coefficient $D_v(T)$ of vacancies in a crystal with a narrow band we employed the well-known computational results[1–3] obtained for the behavior of the diffusion coefficient $D_3(T)$ of impuritons in ^{4}He crystals.

2. VISCOELASTIC FLOW OF A QUANTUM CRYSTAL

Viscoelastic, i.e. vacancion, flow of a crystal around a probe particle is one of the basic mechanisms whereby of a small particle moves under the action of an external force.[2] In a coordinate system tied to the probe particle incident vacancies are absorbed and emitted at the surface of the particle, so that the probe particle can be treated as moving in a "gas" of classical vacancies or in a gas of vacancions which are inelastically scattered by the probe particle. As noted in the Introduction, taking account of the transition, as temperature decreases, of the sample from classical thermally activated diffusion vacancies to coherent motion of vacancions should have a substantial effect, first and foremost, on the temperature dependences $D_v(T)$ and $D_p(T)$. However, this question was not investigated in detail.

The vacancion mechanisms of the diffusion of charges (more accurately, charged nanoparticles) produced in solid helium by radioactivity are discussed in detail in Refs. 8 and 9. It is supposed that a negative charge is an electronic vacuum bubble with radius R_- of the order of 1 nm (this model has been confirmed experimentally[10] in a study of the absorption of infrared light by negative charges in ^{4}He and ^{3}He crystals in the hcp phase). The structure of the positive charges produced by irradiation in solid helium or hydrogen has still not been determined definitively. It can be conjectured by analogy to liquid helium that a positive charge is a snow ball with average radius R_+ of the order of nanometers and consisting of a positively charged molecular ion surrounded by a layer of helium atoms or hydrogen molecules which are confined by electrostatic attraction forces; this snow ball moves as a whole in the crystal under the action of an applied electric field. Charge motion in the presence of an interaction with localized vacancies or with vacancions propagating freely through the sample, i.e. the high- and low-temperature limits in our classification, is studied in Refs. 8 and 9. Reference 14 is likewise devoted to theoretical calculations of the mobility of positive charges in a gas of long-wavelength vacancions (low-temperature limit) in solid ^{4}He. The agreement between the proposed theoretical models and the available experimental data on charge mobility in solid helium requires a separate detailed discussion, which falls outside the scope of the present paper.

Let us consider the behavior of the diffusion coefficient $D_v(T)$ of equilibrium thermal vacancies and the diffusion coefficient $D_p(T)$ of a probe nanoparticle interacting with vacancies in a quantum crystal with a narrow vacancy band. Direct measurements of the vacancy diffusion coefficient in ^{4}He and p-H_2 crystals are difficult to perform. The coeffi-

cient $D_p(T)$ calculated from the mobility of a probe particle is determined, to a first approximation, by the sum

$$D_p(T) = D_p^{cl}(T) + D_p^{qu}, \qquad (1)$$

where D_p^{cl} corresponds to diffusion in a gas of classical vacancies and D_p^{qu} to diffusion in a vacancion gas.

We recall that the behavior of the diffusion coefficient of a probe particle in the high- and low-temperature limits has been studied theoretically in detail. The behavior of the coefficient D_p^{qu} in the transitional range $T \sim T_{tr}$, where vacancion travel distances are comparable to the crystal lattice constant a of the sample and can be much less than the diameter of the probe particle

$$l_v - a \ll d_p \qquad (2)$$

requires additional analysis. Under the conditions (2) a probe particle moves under the action of an external force in a dense gas of vacancions. In a coordinate system tied to the particle this corresponds to viscous (hydrodynamic) flow of a vacancion gas around the probe particle.

It is obvious that for $l_v \ll a$ the probability of subbarrier tunneling is much lower than the probability of classical thermally acted site-to-site hopping of localized vacancy, i.e. classical above-barrier transposition with a nearest neighbor (atom or molecule) in the crystal lattice.

In the low-temperature limit the condition

$$l_v \gg d_p \qquad (3)$$

corresponds to Knudsen flow of a rarefied vacancion gas around a particle in a perfect crystal.

The temperature dependences, expected from qualitative considerations, of the diffusion coefficient $D_v(T)$ of thermal vacancies and the diffusion coefficient $D_p(T)$ of a probe nanoparticle in a crystal with a narrow vacancion band are shown schematically in Fig. 1. For convenience a semilogarithmic scale $\log D = f(1/T)$ is used. The figure also shows the variation of the relative concentration of thermal vacancies $x_v(T) \sim \exp(-E_v/T)$, where E_v is the free energy of vacancy formation.

Three temperature ranges are distinguished in Fig. 1.

I—*High temperatures*, $T \sim T_{melt}$—the region of classical thermally activated diffusion. The vacancy diffusion coefficient $D_v^{cl} \approx (1/6)a^2/t$, where $t^{-1} \sim \exp(-E_b/T)$ is the above-barrier site-to-site hopping frequency of a vacancy in the crystal lattice and E_b is the height of the potential barrier separating a vacancy and a matrix atom (molecule) which are localized in neighboring sites of the crystal lattice. The well-known Arrhenius law describes the behavior of the diffusion coefficient $D_p = D_p^{cl}(T)$ of a probe particle:

$$D_p^{cl}(T) = D_0 \exp(-E_0^{cl}/T)$$
$$\approx A^{cl} x_v D_v^{cl} \sim \exp\{-(E_v + E_b)/T\}. \qquad (4)$$

The numerical factor A^{cl} is proportional to the ratio $(a/d_p)^3$ of the specific volumes of the vacancy and the probe particle.[8,9] For qualitative estimates it is assumed that the concentration of thermal vacancies around a probe particle is close to their equilibrium concentration x_v in the volume, i.e. the diffusion activation energy of a probe particle in region I
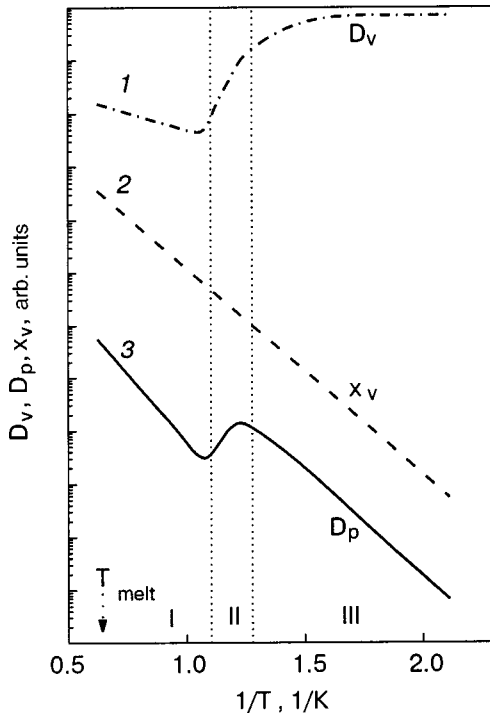
FIG. 1. Temperature dependences of the vacancy diffusion coefficient D_v, the probe-particle diffusion coefficient D_p, and the vacancy concentration x_v.

is $E_0^{cl} = E_v + E_b$. The question of the vacancy concentration around charged probe particles in quantum crystals requires a separate study.[8,9]

II—*Transitional temperature range $T \lesssim T_{tr}$, $l_v \ll d_p$.* The nanoparticle moves in a viscous gas of vacancies. The temperature dependences of the vacancion diffusion coefficient $D_v^{qu}(T)$ and the probe-particle diffusion coefficient $D_p^{qu}(T)$ in region II depend on the nature of the interaction that limits l_v.

If vacancion-phonon scattering plays the main role near T_{tr}, $l_v = l_{v\mathrm{ph}}$, then as estimated in Refs. 1 and 3 $l_{v\mathrm{ph}} \sim T^{-n}$, where $n \sim 9$, and the vacancion diffusion coefficient in the transitional range will increase with decreasing temperature as a power law

$$D_v^{qu}(T) = D_{v\mathrm{ph}}^{qu}(T) \approx V_v l_{v\mathrm{ph}} - T^{-9}, \tag{5}$$

where V_v is the vacancion velocity in the band and $V_v = aKQ_v/h$.

When vacancion-vacancion scattering predominates the temperature dependence $D_v^{qu} = D_{vv}^{qu}(T)$ is determined by the vacancy content in the volume (x_v/a^3) and by the elastic interaction energy of vacancies $U = U_0(a/r)^3 = U_0 x_v$.[1] Here $r = a/x_v^{1/3}$ is the average distance between two vacancions and U_0 is their interaction amplitude $(U_0 \gg Q_v)$. For high concentrations $x_v > (Q_v/3U_0)^{3/4}$ vacancions are localized, so that classical thermally activated site-to-site hopping of vacancies plays the main role. The vacancy diffusion mechanism changes as x_v decreases. At temperatures where r is greater than the vacancion localization radius $R = a(3U_0/Q_v)^{1/4}$ but less than the elastic interaction radius of vacancions $r_0 = a(U_0/Q_v)^{1/3}$, i.e.

$$(Q_v/3U_0)^{3/4} > x_v > Q_v/U_0, \tag{6}$$

the diffusion coefficient of a weakly localized vacancion drifting in a random potential field produced by other vacancies is proportional[1]

$$D_{vv}^{qu}(T) \sim x_v^{-4/3} - \exp(4E_v/3T), \tag{7}$$

i.e. D_{vv}^{qu} grows exponentially with decreasing temperature.

When the average intervacancion distance exceeds the elastic interaction radius of vacancions, $r > r_0$, which corresponds to $x_v < Q_v/U_0$, the vacancion-vacancion elastic scattering cross section $S_{vv} \sim r_0^2$ is independent of x_v, and the vacancion diffusion coefficient can be written as

$$D_{vv}^{qu}(T) \approx V_v l_{vv} - x_v^{-1}, \tag{8}$$

where $l_{vv} = a^3/(x_v S_{vv})$ is the effective mean-free path length.

Let us now examine the behavior of the probe particle diffusion coefficient D_p^{qu} in the transitional range. If the vacancion-phonon interaction predominates near T_{tr}, then the nanoparticle diffusion coefficient

$$D_p^{qu}(T) = A_{qu} x_v D_{v\mathrm{ph}}^{qu} \sim \exp(-E_v/T) T^{-9} \tag{9}$$

can likewise increase with decreasing temperature provided that the effective vacancion mean-free path length $l_{v\mathrm{ph}}$ and correspondingly $D_{v\mathrm{ph}}^{qu}$ (5) increase more rapidly than x_v^{-1} with decreasing temperature.

In a viscous gas of strongly interacting vacancions at temperatures such that the inequality (6) is satisfied,

$$D_p^{qu}(T) = A^{qu} x_v D_{vv}^{qu} \sim x_v^{-1/3} \sim \exp(E_v/3T), \tag{10}$$

i.e. as the sample is cooled, the exponential decrease of the coefficient $D_p(T)$ in the range I is replaced in the range II by an exponential increase. For $x_v \lesssim Q_v/U_0$ in the temperature range where $l_{vv} \sim x_v^{-1} \ll d_p$ (motion of weakly interacting vacancions in a viscous gas), the particle diffusion coefficient $D_p^{qu}(T) \sim x_v D_{vv}^{qu}$ is temperature-independent. This regime could be observed in experiments with large-diameter probe particles.

III—*Low temperatures.* $T \ll T_{tr}$, $l_v = L \gg d_p$ (L is a characteristic dimension of the sample). The vacancion travel distance is limited by scattering by the surface of a perfect crystal or by static defects in the interior volume of an imperfect sample. The vacancion diffusion coefficient is determined by the product $V_v l_v$ and is temperature-independent.

The diffusion coefficient of a probe particle is proportional to the vacancion concentration x_v and the vacancion-particle inelastic scattering cross section S_{vp}:[1,8,9,11]

$$D_p^{qu} \approx b^2 x_v (kQ_v/h)(S_{vp}/a^2). \tag{11}$$

If the cross section S_{vp} is temperature-independent, then the coefficient D_p^{qu} decreases exponentially as temperature decreases, $D_p^{qu} \sim x_v \sim \exp(-E_v/T)$. The values of the numerical factors appearing in the expressions (7)–(9) $A^{qu} \ll 1$, since the center of gravity of the probe particle is displaced by the distance $b \sim a(a/d_p)^2 \ll a$ as a result of inelastic scattering of an incident vacancion by a particle.

3. COMPARISON WITH MEASUREMENTS OF THE DIFFUSION COEFFICIENT OF CHARGES IN ^{4}He AND P-H$_2$ HCP CRYSTALS

The ratios of the energies E_v, E_b, U_0, and Q_v and the melting temperature T_{melt} substantially determine the magnitude and temperature dependence of the vacancy diffusion coefficient and the diffusion coefficient of probe particles interacting with vacancies in a quantum crystal. It is impossible to calculate the values of these energies for a specific sample from first principles. Direct measurements of the diffusion coefficient $D_v(T)$ of thermal vacancies in quantum crystals are also problematic. Consequently, the question of the width of the vacancion band and the role of various vacancy diffusion mechanisms in an experimental sample must be solved by means of intercomparisons and by comparing with published temperature dependences $x_v(T)$ and experimental data on the diffusion of various kinds probe particles (isotopic impurities, charges, foreign particles introduced into a crystal, and so on) in samples with close molar volume.

A critical review of all available experimental data on the diffusion of various kinds of defects in solid helium and hydrogen (there are more than 50 publications by different authors) is a subject for a separate study. In the present section we shall attempt to determine whether or not the model developed above can be used to explain the results of a series of measurements of charge mobility performed in our laboratory in ^{4}He and p-H$_2$ hcp crystals[11,12] which were grown from a specially purified liquid under pressures above the lowest solidification pressures for liquid helium and hydrogen. The charge mobility was measured by the time-of-flight method in a planar capacitor (diode) frozen into solid helium or hydrogen. Since hcp crystals are strongly anisotropic, the numerical values and temperature dependences of the charge mobility in samples grown under identical pressures could differ substantially (as also the thermal conductivity of helium crystals, which we investigated previously), but the overall picture was reproduced well.

It can be regarded as proven[1,8,9] that in ^{4}He hcp crystals grown at pressures above the lowest solidification pressure ($P > 25$ atm) the diffusion of positive charges, just as the diffusion of ^{3}He impurity atoms near T_{melt}, is controlled by the interaction of the charges with thermal vacancies. The temperature dependences of the coefficients $D_3(T)$ and $D_+(T)$ in samples with close molar volume $V_m \approx 20.7$ cm^3/mole (solidification pressure ~ 31 atm) is shown in Fig. 2. The curves *1* and *2* illustrate the influence of impuriton-impuriton interaction on the temperature dependence $D_3(T)$ with the impurity concentration increasing from 0.006 to 2%.[13]

The points on the curve *3* were constructed using the measurements performed in Ref. 11; the crosses describe the results of our own control measurements of $D_+(T)$ in a cell with a somewhat different construction designed for working with solid hydrogen.[12] In Ref. 11 and our present measurements the position of the minimum point and the relative height of the maximum on the curve $D_+(T)$ remained essentially unchanged as the applied electric field decreased from 10^4 to 1.5×10^3 V/cm. Therefore the maximum cannot be attributed to a change, with the temperature decreasing to 0.9
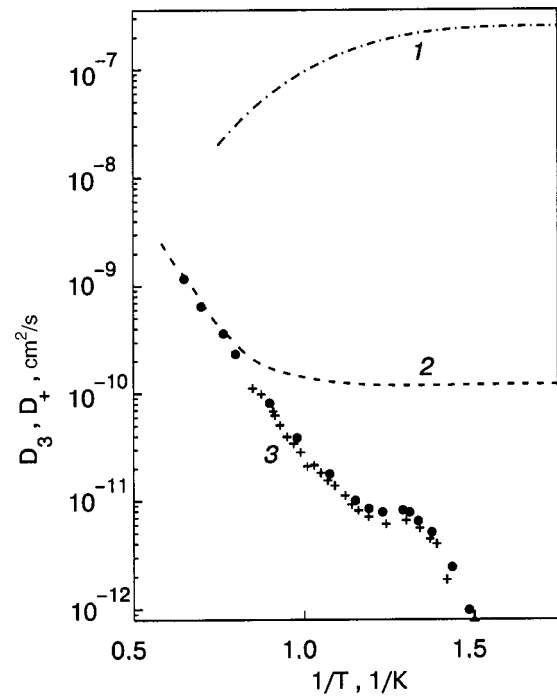

FIG. 2. Diffusion of charges and impurity atoms in ^{4}He hcp crystals with molar volume $V_m = 20.7$ cm^3/mole. The temperature dependences of the diffusion coefficient $D_3(T)$ of ^{3}He impurity atoms in ^{4}He with ^{3}He impurity content $x_3 = 0.006\%$ (*1*) and 2% (*2*)[13] and the diffusion coefficient $D_+(T)$ of positive charges: the results of this work (+); measurements performed in Ref. 11 (●).

K, of the vacancion interaction with charges drifting in a field 10^4 V/cm, as proposed in Ref. 14.

The 1.5–4-fold increase of the diffusion coefficient D_+ observed in different samples is more naturally attributed to a change in the vacancy diffusion mechanism. X-Ray data[15] show that in ^{4}He hcp samples with molar volume $V_m \approx 20.7$ cm^3/mole the concentration of thermal vacancies on the melting line ($T_{melt} \approx 1.8$ K) is $x_v(T_{melt}) = 3 \times 10^{-3}$ and decreases almost 30-fold on cooling to 0.9 K (the straight line 2 in Fig. 1 describes the temperature dependence $x_v(T)$ for such a sample). If it is assumed that below 0.9 K the vacancion-vacancion interaction predominates and the expression (10) describes the temperature dependence $D_+(T)$, which is valid when the inequalities (6) hold, then it is easily estimated that $10^{-5} < Q_v/U_0 < 10^{-4}$, i.e. in samples with molar volume $V_m \approx 20.7$ cm^3/mole the width of the vacancion energy band $Q_v \lesssim 10^{-4}$ K is 4–5 orders of magnitude greater than the values used in Refs. 1 and 14 and is close to the impuriton band width, $Q_v \lesssim Q_3$. To estimate Q_v it was assumed that the vacancion-vacancion interaction amplitude $U_0 = 1$ K, since the published values[1,16,17] are in the range $U_0 = 2 - 0.1$ K.

Numerical calculations have shown that estimates of Q_v based on the formulas presented in Ref. 3, under the assumption that near T_{tr} the dynamical (phonon) shift of the vacancy levels plays the main role, i.e. expressions of the type (5) and (9) describe the temperature dependences $D_v(T)$ and $D_+(T)$ near 0.9 K, give close values $Q_v \lesssim 10^{-4}$ K.

In support of the estimate $Q_v \lesssim Q_3$ it should be noted that according to Refs. 14 and 15 the local change $dV/V \sim 0.3 - 0.5$ (lattice compression) in the specific volume around a vacancy is greater than the local lattice expansion
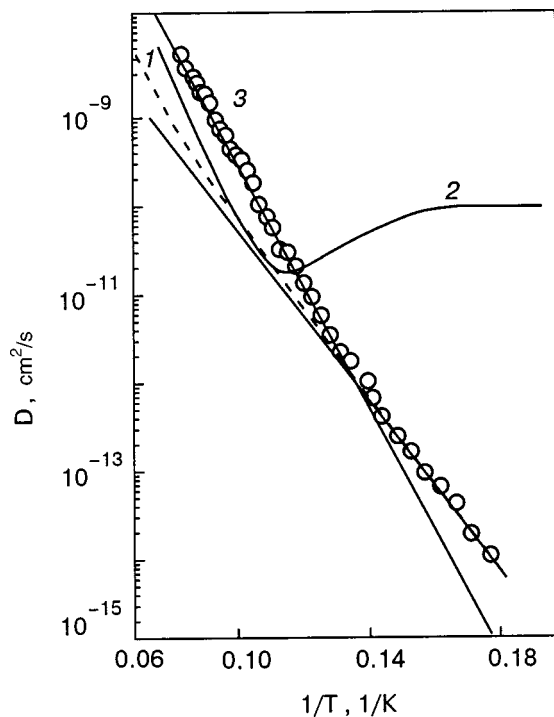
FIG. 3. Diffusion of charges and impurity molecules in p-H_2 crystals: diffusion coefficient computed for hydrogen molecules using the model of Ref. 4 (*1*); diffusion coefficient $D_{HD}(T)$ of HD impurity molecules (*2*);[6] diffusion coefficient $D_-(T)$ of negative charges (○) (*3*).[12] The two solid lines drawn through the points 3 correspond to the high- and low-temperature parts of the curve $D_-(T)$.

$dV/V \sim 0.1$–0.2 around a ^{3}He impurity atom in ^{4}He, i.e. the displacement field around a localized vacancy and the vacancion-vacancion interaction amplitude $U_0 \sim (dV/V)^2$ appreciably exceed the displacement field and the interaction energy between impurity atoms. We remind the reader especially that a vacancy, just as an impurity atom, is a defect in the crystal lattice.

The values $Q_v \ll 1$ K have also been previously published.[17] The authors[18] of the NMR studies of ^{3}He diffusion in ^{4}He concluded that the width of the vacancion energy band in ^{4}He hcp crystals does not exceed several millikelvins even in samples with the maximum molar volume (and, according to Ref. 1, it decreases rapidly with increasing solidification pressure). We also mention Ref. 19 where the interaction of first and second sound in ^{4}He crystals is investigated and, to explain the results, it is proposed that in samples grown at the lowest pressures the width of the defecton (supposedly vacancion) band can exceed 0.1 K.

In p-H_2 crystals grown from liquid under close to atmospheric pressure, it has been established[12] that the temperature dependence of the diffusion coefficient $D_-(T)$ of negative charges (points *3* in Fig. 3) is essentially identical to the temperature dependence, calculated in Ref. 4, of the self-diffusion coefficient $D_s(T)$ of molecules (curve *1*) and is close to the behavior, known from NMR measurements,[5] of the diffusion coefficient D_{HD} of an isotopic impurity in the range of thermally activated diffusion of molecules (according to Ref. 6 the minimum in curve *2* corresponds to a transition from transposition with vacancies to coherent motion of HD impuritons). The decrease in the activation energy for the diffusion $D_-(T)$ of negative charges as a sample is

cooled from 13.3 to 6 K agrees with the predicted[4] decrease of the effective diffusion activation energy E_0 of molecules as a result of a transition from thermally activated hops with $E_0^{cl} = E_b + E_v = 200$ K to subbarrier vacancy tunneling with $E_0^{qu} = E_v = 100$ K.

It is difficult to give a qualitative description of the behavior of the diffusion coefficient of vacancies and probe particles in p-H_2 in the transitional temperature range 11 K $> T > 9$ K because the hopping of vacancies and molecules into the ground state and the first excited state, which lies inside a deep potential well, must be taken into account.[4] Below 9 K the contribution of hops into the upper level can be neglected. Assuming that the relative concentration of thermal vacancies on the melting line of solid hydrogen $x_v(T_{melt}) \approx 3 \times 10^{-3}$ and decreases as $x_v(T) \sim \exp(-100/T)$ on cooling, while the vacancion-vacancion interaction amplitude U_0 is comparable to T_{melt}, i.e. $U_0 \sim 10$ K, it is easy to estimate from the inequality $x_v(9 \text{ K}) \lesssim Q_v/U_0$ that the vacancion band width in a p-H_2 crystal is close in order of magnitude to $Q_v \sim 10^{-3}$ K (we note that the width of the band of HD impurity molecules is estimated[6] to be close to 10^{-2} K).

In summary, the conjecture that in ^{4}He and p-H_2 quantum hcp crystals grown under pressures above the lowest solidification pressure of a liquid the vacancion band width $Q_v \ll T_{melt}$ makes it possible not only to explain the appearance of distinctive behavior of the diffusion coefficients of charged probe nanoparticles but also to estimate Q_v for the same samples.

*E-mail: mezhov@issp.ac.ru

[1] A. F. Andreev, Usp. Fiz. Nauk **118**, 251 (1976) [Sov. Phys. Usp. **19**, 137 (1976)].
[2] A. M. Kosevich, *The Physical Mechanics of Real Crystals*, Naukova dumka, Kiev (1981).
[3] Yu. M. Kagan and L. A. Maksimov, Zh. Éksp. Teor. Fiz. **84**, 792 (1983) [JETP **57**, 459 (1983)].
[4] C. Ebner and C. C. Sung, Phys. Rev. B **5**, 2625 (1972).
[5] F. Weinhaus and H. Meyer, Phys. Rev. B **7**, 2974 (1973).
[6] D. Zhou, M. Rall, J. P. Brison, and N. S. Sullivan, Phys. Rev. B **42**, 1929 (1990).
[7] L. P. Mezhov-Diglin, A. A. Levchenko, and A. V. Trusov, J. Low Temp. Phys. **111**, 545 (1998).
[8] V. B. Shikin, Usp. Fiz. Nauk **121**, 457 (1977) [Sov. Phys. Usp. **20**, 226 (1977)].
[9] A. J. Dahm, *Program in Low Temprature Physics*, edited by D. F. Brewer, North-Holland (1985), Vol. 9.
[10] A. I. Golov and L. P. Mezhov-Deglin, JETP Lett. **56**, 514 (1992).
[11] A. I. Golov, V. B. Efimov, and L. P. Mezhov-Deglin, Zh. Éksp. Teor. Fiz. **94**, 198 (1988) [JETP **67**, 325 (1988)].
[12] A. A. Levchenko, L. P. Mezhov-Deglin, and I. E. Shtinov, JETP Lett. **54**, 234 (1991).
[13] V. L. Mikheev, V. A. Maĭdanov, and N. P. Mikhin, Fiz. Nizk. Temp. **9**, 901 (1983) [Sov. J. Low Temp. Phys. **9**, 465 (1983)].
[14] A. F. Andreev and A. D. Savishchev, Zh. Éksp. Teor. Fiz. **96**, 1109 (1989) [JETP **69**, 630 (1989)].
[15] B. A. Fraas, P. R. Granfors, and R. O. Simmons, Phys. Rev. B **39**, 124 (1989).
[16] S. E. Kal'noĭ and M. A. Strzhemechnyĭ, Fiz. Nizk. Temp. **8**, 1025 (1982) [Sov. J. Low Temp. Phys. **8**, 515 (1982)].
[17] H. A. Goldberg and R. A. Guer, J. Low Temp. Phys. **28**, 449 (1977).
[18] I. S. Schuster, E. Polturak *et al.*, J. Low Temp. Phys. **103**, 159 (1996).
[19] J. M. Goodkind, Phys. Rev. B **89**, 095301 (2002).

Translated by M. E. Alferieff

Orientational ordering in solid hydrogens with *J*=1 in the presence of a crystal field

T. N. Antsygina, S. M. Tret'yak, and Yu. A. Freiman*

*B. Verkin Institute for Low Temperature Physics and Engineering, National Academy of Sciences
of Ukraine, pr. Lenina 47, 61102 Khar'kov, Ukraine*

R. J. Hemley

*Geophysical Laboratory and Center for High Pressure Research, Carnegie Institution of Washington,
5251 Broad Branch Road NW, Washington*

A system of quantum linear rotators with quantum rotational angular momentum $J=1$ in a
crystal field is investigated. An equation is derived for the orientational order parameter. The
critical parameters, the phase-separation curve, and the line of superheating and
supercooling points are found. It is shown that the thermodynamic behavior of a system of linear
rotators in the classical case is identical to that of the limiting quantum ($J=1$) cases
studied in this work. For positive crystal fields there is an analogy between orientational phase
transitions in a system of rotators with $J=1$ and phase transformations in a liquid–vapor
system. It is shown that states with $J>1$ radically change the character the phase transitions in
the system of rotators: instead of one critical point characteristic for a system of $J=1$,
now there is a line of critical points. © *2003 American Institute of Physics.*
[DOI: 10.1063/1.1542500]

Orientational ordering in solid hydrogens with odd values of the rotational quantum number J (orthohydrogen $o-H_2$ and paradeuterium $p-D_2$) is due primarily to the quadrupole–quadrupole interaction, since the contribution of all other components of the anisotropic potential is negligible.[1,2] In three-dimensional ($3D$) crystals with cubic symmetry the single-particle terms, with which the appearance of a crystal field H_c is associated affect phase transitions only weakly. The orientationally ordered phase appearing in these systems belongs to the space group $Pa3$. Three-dimensional solid hydrogens have been studied quite well experimentally and theoretically.[2,3]

The situation is different for adsorbed layers of solid hydrogens on substrates. In this case the interaction between the molecules in a monolayer and the substrate atoms (molecules) makes a contribution to the crystal field, and for an appropriate substrate structure this contribution can be comparable to that of the quadrupole–quadrupole interaction. Systems for which the harmonic Y_{20} determines the main contribution to H_c were studied in Refs. 4 and 5. It is known that a crystal field strongly determines the thermodynamics of a system and can radically change its critical properties.[6] The objective of the present paper is to study the influence of a crystal field on the behavior of solid hydrogens with odd J.

Since the moment of inertia I of hydrogen molecules is small and the intermolecular interaction is weak, the state of solid hydrogen at not very high pressures can be characterized by the rotational quantum number J referring to an individual molecule. We shall be interested in the behavior of a system at low temperatures $T \ll B$ ($B = \hbar^2/(2I)$ is the rotational constant). In this case, to a high degree of accuracy, it can be assumed that all molecules are in a state with $J=1$ (since the splitting from levels with $J=3$ is hundreds of

degrees) and, therefore, the kinetic energy of the molecules is a constant, equal to $2B$.

The Hamiltonian of the system in a representation where the kinetic energy operator is diagonal is

$$\mathcal{H} = 2BN + \frac{U}{2}N\sigma^2 - U(\sigma+\gamma)\sum_f \hat{p}_f, \qquad (1)$$

where $U = 4U_0/25$, $\gamma = U_1/U_0$, U_0 and U_1 are, respectively, molecular- and crystal-field constants, N is the total number of sites, the operator

$$\hat{p} = \frac{1}{2}\begin{pmatrix} -1 & 0 & 0 \\ 0 & -1 & 0 \\ 0 & 0 & 2 \end{pmatrix};$$

and $\sigma = \langle \hat{p} \rangle$ is the order parameter of the system and is normalized so that $\sigma = 1$ at $T=0$.

In the present approximation the kinetic energy of the system is constant, and consequently it can be dropped when calculating the free energy. The free energy per site is

$$\frac{\mathcal{F}}{NU/2} = \sigma^2 - 2(\sigma+\gamma) - t\ln[1 + 2\exp(-\xi)],$$

$$\xi = \frac{3}{t}(\sigma+\gamma), \qquad (2)$$

where $t = T/(U/2)$ is the dimensionless temperature. Thus, in our limiting quantum case of solid orthohydrogen B as an energy scale completely drops out of the subsequent analysis. It is well known that this also happens for classical systems, but the reason is that the potential and kinetic energies commute with one another.[7]

Minimizing the free energy (2) with respect to σ yields the following equation for the order parameter:

$$\sigma = \frac{1 - \exp(-\xi)}{1 + 2 \exp(-\xi)}. \tag{3}$$

The critical points are determined by the relations[8]

$$\frac{\partial \mathcal{F}}{\partial \sigma} = 0, \quad \frac{\partial^2 \mathcal{F}}{\partial \sigma^2} = 0, \quad \frac{\partial^3 \mathcal{F}}{\partial \sigma^3} = 0, \quad \frac{\partial^4 \mathcal{F}}{\partial \sigma^4} > 0. \tag{4}$$

In our approximation, however, the critical values t_c, γ_c, and σ_c can be obtained without solving the system (4). Indeed, making the substitutions

$$\mu = \frac{1}{3}(4\sigma - 1), \quad \tau = \frac{8t}{9} \tag{5}$$

Eq. (3) becomes the Curie–Weiss equation for the magnetization of a ferromagnet, described by the Ising Hamiltonian, in the self-consistent field approximation:

$$\mu = \tanh \frac{\mu + h}{\tau}, \tag{6}$$

where h is an effective magnetic field and is a function of temperature and the dimensionless crystal-field constant γ:

$$h = \frac{(1 + 4\gamma)}{3} - \frac{\ln 2}{2} \tau. \tag{7}$$

Using the well-known properties of Eq. (6),[9] not only can the critical values of the parameters of our system be found but an explicit equation can be obtained for the phase-separation line, i.e. the dependence of the equilibrium transition temperature τ_0 on the crystal field strength can be determined. This relation is obtained from the condition that the field h vanishes, which gives a linear dependence of τ_0 on γ:

$$\tau_0(\gamma) = \frac{2(1 + 4\gamma)}{3 \ln 2}. \tag{8}$$

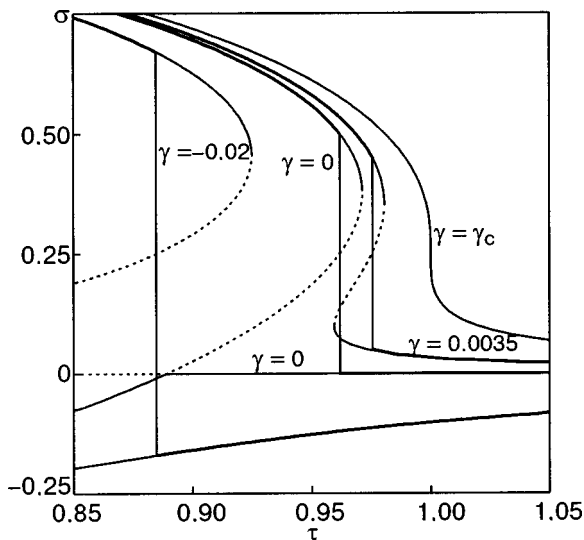Figure 1 shows the temperature dependences of the order

FIG. 1. Temperature dependences of the order parameter σ for various values of the crystal-field parameter γ. Thick solid lines—equilibrium states, thin solid lines—metastable states, dotted lines—unstable states. The vertical lines show the temperatures of equilibrium phase transitions.

parameter σ for various values of the crystal-field parameter γ. For convenience in the subsequent analysis of the behavior of the system, the temperature t in Eq. (3) is repalced by the variable $\tau = 8t/9$. According to Fig. 1, for $\gamma = 0$ a phase transition occurs from a state with a positive value of σ into a disordered state with $\sigma = 0$. For positive γ this is a transition between two states with positive order parameters, i.e. from a more ordered to a less ordered phase. We note that for $\gamma > 0$ Eq. (3) in principle also possesses solutions for negative values of σ, but these solutions correspond to maximum free energy, i.e. they are unstable. Finally, for $\gamma < 0$ an equilibrium phase transition occurs between states with positive and negative order parameters.

It follows from Eq. (6) that the critical temperature

$$\tau_{c0} = 1, \quad t_{c0} = 8/9. \tag{9}$$

Taking account of the relation (8), we obtain for the critical value of the crystal constant

$$\gamma_{c0} = \frac{3 \ln 2 - 2}{8}, \quad \alpha_{c0} = \frac{2}{5} \gamma_{c0} \approx 0.003972. \tag{10}$$

Since μ vanishes at the critical point, it follows from Eqs. (3) and (5) that

$$\sigma_{c0} = 1/4, \quad \eta_{c0} = 0.1. \tag{11}$$

The equation (6) also makes it possible to find the maximum superheating temperature τ_{max} and the minimum temperature τ_{min} to which the system can be supercooled. These points are determined from the condition that the derivative $d\sigma/d\tau$ (or, equivalently, $d\mu/d\tau$) vanishes at infinity. Differentiating both sides of Eq. (6) with respect to τ gives

$$\tau = 1 - \mu^2. \tag{12}$$

Using Eqs. (6) and (12) we arrive at the following relations for determining the temperatures τ_{max} and τ_{min} as a function of the crystal-field constant γ:

$$g_{\pm}(\tau, \gamma) = 0, \tag{13}$$

where

$$g_{\pm}(\tau, \gamma) = \frac{4}{3}(\gamma_{c0} - \gamma) - \frac{1 - \tau}{2} \ln 2$$

$$\pm \frac{\tau}{2} \ln \frac{1 - \sqrt{1 - \tau}}{1 + \sqrt{1 - \tau}} \pm \sqrt{1 - \tau}. \tag{14}$$

Figure 2 shows the functions $\gamma(\tau)$ obtained from Eqs. (14): the curves *1* ($g_- = 0$) and *2* ($g_+ = 0$) are, respectively, the geometric loci of the maximum superheating temperature and the minimum supercooling temperature. The straight line *3* determines the temperature of the equilibrium transition as a function of the parameter γ (8). For each γ in the range $0 < \gamma < \gamma_{c0}$ there exist nontrivial values of τ_{max} and τ_{min} ($\tau_{min} < \tau_0 < \tau_{max}$) which as γ increases tend toward and merge with one another and with the equilibrium transition point at the critical point (γ_{c0}, τ_{c0}). For $\gamma \geq \gamma_{c0}$ no phase transitions occur in the system.

For $\gamma = 0$, together with the nontrivial solutions of Eq. (3), there always exists a solution $\sigma = 0$, which is stable for
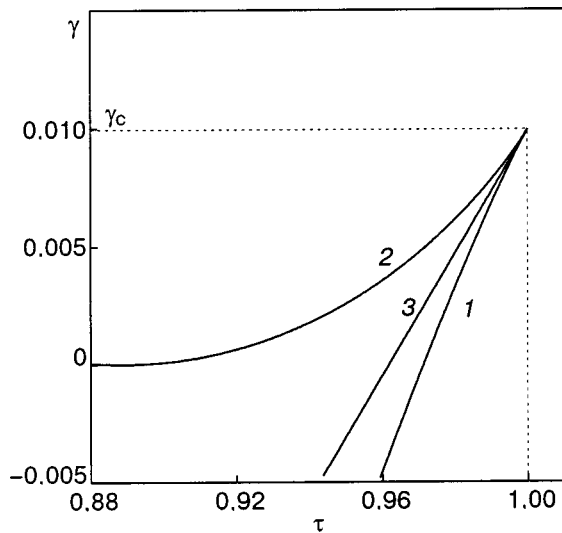
FIG. 2. Phase diagrams $\gamma(\tau)$: the curves *1* and *2* are, respectively, the geometric loci of the maximum temperature of superheating and the minimum temperature of supercooling. The straight line *3* is the line of equilibrium phase transitions.
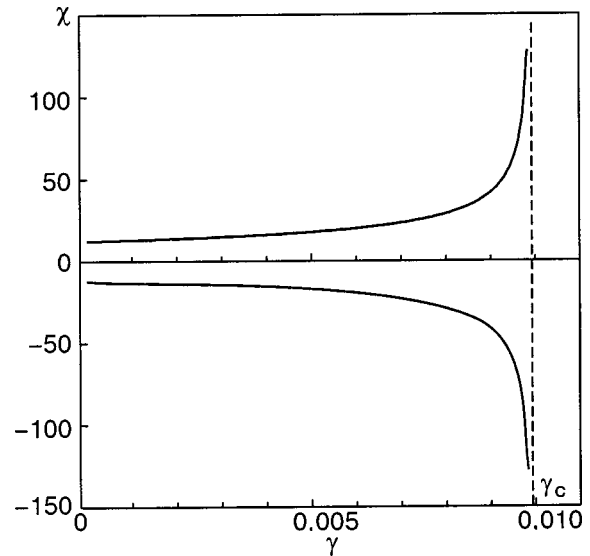

FIG. 3. Susceptibility $d\sigma/d\gamma$ along the equilibrium phase-separation curve as a function of the crystal-field parameter for two coexisting phases.

$\tau > \tau_0(0) = 2/(3 \ln 2) \approx 0.9618$ and unstable in the range $0 \leqslant \tau \leqslant 8/9$. For temperatures $8/9 \leqslant \tau \leqslant \tau_0(0)$ the trivial solution for γ corresponds to metastable states.

The situation for negative values of the crystal-field parameter is completely different. According to Fig. 2, for $\gamma < 0$ there is no line of minimum supercooling temperatures (curve *2*). Thus, in the entire temperature range where the stable phase is characterized by positive values of the order parameter σ there always exists a metastable phase corresponding to negative values of σ. This means that the system can be supercooled right down to zero temperature. According to Fig. 2, the points of maximum superheating once again lie on the line *1*. Interestingly, the phase diagram has a similar form for the opposite limiting case—a system of classical rotators.[7]

Just as for classical rotators,[7] the behavior of a system of quantum rotators with $J=1$ is entirely similar to that of a liquid–vapor system. The thermodynamic parameters τ, γ, and σ describing the state of a system of rotators correspond to the parameters temperature, pressure, and particle number density in the liquid–vapor system.

An important characteristic determining the stability of the liquid–vapor system is the compressibility. The analogous quantity for a system of rotators is the susceptibility, i.e. the derivative $d\sigma/d\gamma$ of the order parameter with respect to the crystal-field parameter. Calculating this quantity on the phase equilibrium curve we obtain

$$\frac{d\sigma}{d\gamma} = \Phi(\gamma)(\sigma_{c0} - \sigma)$$

$$\times \frac{1 - 16(\sigma_{c0} - \sigma)^2/9}{\Phi(\gamma_{c0})(\gamma - \gamma_{c0}) + 16(\sigma_{c0} - \sigma)^2/9}, \tag{15}$$

where

$$\Phi(\gamma) = \frac{4}{1 + 4\gamma}; \quad \Phi(\gamma_{c0}) = \frac{8}{3 \ln 2}.$$

According to the relation (15), the susceptibility diverges at the critical point. Using Eq. (3) it is easy to show that as the critical point is approached the susceptibility behaves as the square root of $\gamma_c - \gamma$:

$$\frac{d\sigma}{d\gamma} = \pm \frac{3}{2\sqrt{2 \ln 2}} \frac{1}{\sqrt{\gamma_c - \gamma}}. \tag{16}$$

The different signs correspond to the two values of the order parameter on the phase equilibrium curve. The susceptibility versus the crystal-field parameter is shown in Fig. 3.

As already noted, in our limiting quantum case ($J=1$) the rotational constant B has dropped out, and instead of two energy parameters U and B only the single parameter U remains in the problem. As a result, the geometric locus of critical points in the $\gamma - \tau$ plane has degenerated into a single point with the coordinates (γ_{c0}, τ_{c0}) determined by the expressions (9) and (10). The situation changes completely if levels with $J \geqslant 3$ are taken into account. Then, first, the structure of the low-lying group of levels with $J=1$ changes. Since the kinetic energy is not an additive constant in this approximation, it is natural to take the parameter B as the unit of energy. To take account of the influence of the higher-lying levels on the critical behavior of the system, we included in our analysis the next group with $J=3$ and found the eigenvalues of the Hamiltonian of the system. Then, to calculate the free energy we confined our attention to only the lowest corrected levels. The equation obtained for the order parameter in this approximation no longer reduces to the Weiss equation. The critical parameters of the system were calculated using Eqs. (4). It was found that explicit relations between them can be obtained only if additional simplifying assumptions are made. Thus, assuming the parameter U/B to be less than or of the order of 1 and using the relation between U and U_0, we obtain the following relations for the critical parameters:

$$\gamma_c = \gamma_{c0} + \frac{27}{14000} \ln^2 2 \, \frac{U_0}{B},$$

$$\sigma_c = \sigma_{c0} + \frac{3}{875} (5 \ln 2 + 3) \frac{U_0}{B}, \qquad (17)$$

$$\tau_c = \tau_{c0} + \frac{9}{1750} (\ln 2 + 5) \frac{U_0}{B}.$$

Thus, even in this very simple approximation it is evident that the phase-transition scenarios in the system depend strongly on whether the analysis is limited to states with $J=1$ or the change produced in structure of the lowest levels by levels with $J>1$ is also taken into account.

It is convenient to make the indicated comparison in the coordinates $U_0 - T$. In these coordinates, according to Eq. (9), the line of critical points is rectilinear and emanates from the origin of coordinates; the tangent of the slope angle of the line is $U_0/T = 100/9$. Phase transitions are possible in this system for crystal fields less than the critical field γ_{c0}. The lines of equilibrium phase transitions (8) are rectilinear and emanate from the origin of coordinates; the slope of the lines depends on γ; and, the condition $U_0/T > 100/9$ should hold. If the crystal field exceeds γ_{c0}, then the lines of equilibrium transitions vanish, and for any T and U_0 the system can be in only a single-phase state.

According to Eqs. (17), when the upper-lying levels are taken into account the line of critical points is a parabola. Numerical analysis shows that the lines of the equilibrium transitions for not very large U_0/B are negligibly distorted and once again can be approximated by rays emanating from the origin of coordinates. Thus, the line of critical points cuts out a region of values of T and U_0 for which phase transitions are impossible. As a result, the picture in the range $\gamma < \gamma_{c0}$ is similar to that described above, and for $\gamma > \gamma_{c0}$ only the values of T and U_0 where the line of equilibrium phase transitions lies above the critical line are admissable.

To conclude, we shall formulate the basic results. In this paper a system of quantum linear rotators, whose rotational states are limited by the value $J=1$, in a crystal field was studied. It was shown that for such a system the equation for the order parameter reduces to the Weiss equation, which is well known in the theory of magnetism. This representation made it possible to find explicitly not only the critical parameters but also the phase-separation curve without solving the equation itself for the order parameter. The lines of the points of superheating and supercooling of the system were also found. It was shown that thermodynamically the two systems of rotators—classical and limiting quantum—behave identically. For positive γ there is also a complete analogy between orientational phase transitions in a system of classical or quantum rotators with $J=1$ and phase transformations in a liquid–vapor system.

It was shown that the character of the phase transitions in a system of rotators changes radically when the changes produced in the low-lying groups of levels by states with $J>1$ are taken into account. Instead of a single critical point, characteristic for a system of $J=1$, a line of critical points appears. As a result, the analogy with ordinary systems with one critical point—liquid-vapor, magnet, and others—is lost.

*E-mail: freiman@ilt.kharkov.ua

[1] I. N. Krupskiĭ, V. A. Slyusarev, and Yu. A. Freiman, "Classical molecular crystals" in *Cryocrystals*, edited by B. I. Verkin and A. F. Prikhot'ko, Naukova dumka (1983), p. 121.

[2] *Physics of Cryocrystals*, edited by V. G. Manzhelii and Yu. A. Freiman, AIP Press, Woodbury, New York (1997).

[3] I. F. Silvera, Rev. Mod. Phys. **52**, 393 (1980).

[4] N. S. Sullivan and K. Kim, J. Low Temp. Phys. **111**, 533 (1998).

[5] N. S. Sullivan and K. Kim, J. Low Temp. Phys. **113**, 705 (1998).

[6] Yu. A. Freiman, S. M. Tretyak, and A. Jeżowski, J. Low Temp. Phys. **111**, 475 (1998).

[7] A. P. Brodyanskiĭ and Yu. A. Freĭman, Preprint No. 7022-V85, VINITI (1985); Fiz. Nizk. Temp. **12**, 107 (1986) [Sov. J. Low Temp. Phys. **12**, 63 (1986)].

[8] A. Z. Patashinskiĭ and V. P. Pokrovskiĭ, *Fluctuation Theory of Phase Transitions*, Nauka, Moscow (1982).

[9] T. Hill, *Statistical Mechanics*, McGraw-Hill, New York (1956) [Russian trans.], Inostr. Lit., Moscow (1960).

Translated by M. E. Alferieff

On the phase diagram of the development of an instability of a massive charged surface of liquid helium

V. Shikin*

Institute of Solid State Physics, Russian Academy of Sciences, p. Chernogolovka Moskovskoĭ obl., 142432 Russia

The existing interpretation of the development of an instability of a massive charged helium surface requires a definite correction that identifies this phenomenon more closely with the known spinodal and binodal decomposition processes in the theory of first-order phase transformations. The distinctive features of the development of an instability of a charged helium surface, exhibiting indications of spinodal (binodal) decomposition, are discussed and a qualitative phase diagram for such transitions is constructed in the plane surface electron density—electric field above a plane charged with $2D$ electrons. © *2003 American Institute of Physics.* [DOI: 10.1063/1.1542501]

The problem of the instability and reconstruction of a charged helium surface is well understood. The first results obtained by Frenkel' and Tonks[1–3] on the oscillations and instability of the surface of a charged metallic liquid were extended by Gor'kov and Chernikova[4,5] to a helium surface with $2D$ electrons. Subsequently, these same authors developed a theory of equipotential reconstruction of a charged surface of a liquid (see Ref. 6). The question here concerns a transition of a charged boundary of a liquid from a planar to a periodic, corrugated state. The theory predicts the type of lattice that appears, the period of the lattice, the amplitude of the corrugations, and so on. The perturbed surface of the liquid remains electrically equipotential.

In an alternative picture of the reconstruction, a charged helium surface is divided into a system of individual multielectron dimples (Shikin and Leiderer[7]). Each dimple possesses a charged nucleus surrounded by neutral liquid. The interaction between dimples can cause the dimples to assemble into clusters and, among other things, create a periodic distribution of the dimples over the surface.

Even though the idea of equipotential reconstruction has been around for a long time, the primacy of this idea still has never been questioned. The work of Mel'nikov and Meshkov[8] has encouraged this. They showed that when supercriticality (the excess electric field above the critical value) increases with the total number of electrons remaining constant, dimple reconstruction replaces equipotential reconstruction.

Experiments performed primarily using electrons on helium are in good agreement with the predicted[1–5] limits of stability of a charged liquid surface (see Ref. 9). Subsequently, the most interesting part of the dispersion law for surface oscillations, which is critically sensitive to the electron density, was studied and all expected details were confirmed.[10] Finally, it has been proved that periodic[11] and aperiodic[12] reconstruction of a liquid conducting boundary can occur.

However, this picture is not completely satisfactory. In the first place, the calculations of equipotential periodic re-

construction which are are based on perturbation theory employing the smallness of the amplitude of the surface corrugations compared with the capillary length are valid only for weak charging of a helium surface, when a so-called soft regime of reconstruction occurs (the amplitude of the perturbation is much smaller than the capillary length, in the terminology of Ref. 6). The charging of the liquid surface is the ratio ν of the average $2D$-electron density n_s to the critical density $n_s^{\max}$ [see Eq. (10)]. At the same time, periodic reconstruction along the entire accessible helium surface can be observed experimentally[11] only near the maximum values $\nu \lesssim 1$, when a strict reconstruction regime occurs (the corrugation amplitude is of the order of the capillary length). Of course, this disparity would be not fundamental if a second fact were not true. For small values $\nu \ll 1$ the observed reconstruction is aperiodic. The helium surface is not covered here by periodic corrugations covering the entire liquid surface, as follows from the predictions made in Refs. 6 and 8. Instead, the electrons collect in one or several multielectron dimples which occupy only a small part of the entire helium surface. As an illustration, the pattern of dimple reconstruction from Ref. 12 in the region $\nu \ll 1$ with ν increasing gradually is presented in Fig. 1. Obviously, the dimple scenario of reconstruction is energetically more favorable, and this circumstance needs to be understood.

In the present paper it is shown that the reconstruction process exhibits the properties of a first-order phase transition. For transformations of this type the intersection of the chemical potentials of competing phases determines the point (line) of binodal instability near which the favored phase appears as a result of a fluctuation. For helium this process is represented by the nucleation of multielectron dimples on a background of a uniform, near-critical, charged state of the liquid surface. In addition, there is a point (line) of absolute instability (spinodal), which arises in the dynamical equations governing the transition and appears without any threshold waiting. For a charged liquid the spinodal is the threshold of the dynamical Frenkel–Tonks instability. In the phase diagram the binodal, as a rule, has a large phase
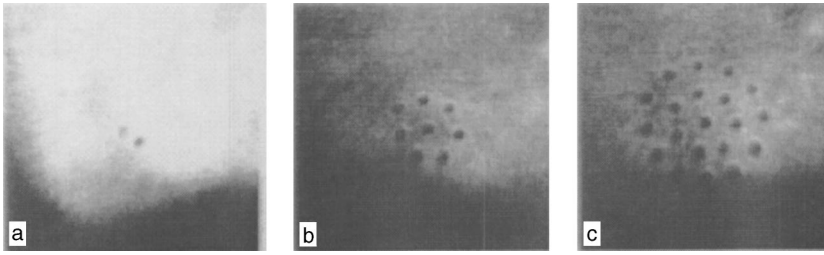
FIG. 1. System of individual multielectron dimples arising on a weakly charged helium surface with monotonic growth of the total number of electrons (from Ref. 12).

volume, though an activation time is necessary for nuclei to appear. A spinodal transition is stimulated by a sharp jump in an external parameter into the spinodal region of the diagram, after which the instability should develop, as is characteristic, exponentially in time. The question of the points of coexistence of a binodal and spinodal does not have a general solution. Sometimes such a solution exists and sometimes it does not.

If the proposed picture is correct, then all experiments on the reconstruction of a charged helium surface which have been performed thus far have been performed in the binodal region. For small fill factors the question is whether or not only individual dimples appear. As ν increases, the dimples form complexes (clusters) with internal periodicity (Figs. 1b and 1c). In the range $\nu \to 1$ the area of a cluster approaches the total area of the liquid surface. As for spinodal decomposition, it has yet to be observed.

1. Proceeding to specific results, we shall discuss the properties of a spinodal first. We shall study the system shown in Fig. 2. The electric fields E_- above and E_+ below the charged helium surface are

$$E_- = \frac{V}{h} - 4\pi\sigma\frac{d}{h}, \tag{1}$$

$$E_+ = \frac{V}{h} + 4\pi\sigma\frac{(h-d)}{h}, \tag{2}$$

where $\sigma = en_s$ and V is the potential difference between the plates of the cell.

When the external field above helium is completely screened, $E_- = 0$, and therefore

$$4\pi\sigma = \frac{V}{d}, \tag{3}$$

and the field E_+ is

$$E_+ = \frac{V}{d}. \tag{4}$$

For fixed d_0 and V, where d_0 is the thickness of the helium film in the absence of an external field, the helium surface sags under the electronic pressure $P_{el} = E_+^2/8\pi$ to the depth
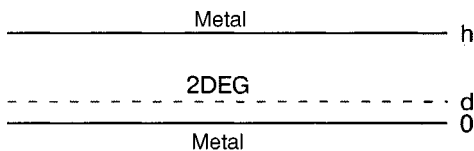

FIG. 2. Diagram of a cell with a $2D$ electronic system and geometric variables.

$$\xi_\infty = d - d_0, \tag{5}$$

which is determined by the conditions of mechanical equilibrium and conservation of the total volume of the liquid:

$$\rho g \xi_\infty + \frac{V^2}{8\pi d_0^2} = \rho g \xi_0, \tag{6}$$

$$L^2 \xi_\infty + (L_0^2 - L^2)\xi_0 = 0, \quad L_0 > L, \tag{7}$$

$$|\xi_\infty| \ll d_0.$$

Here ρ and g are the density of liquid helium and the acceleration of gravity, L is the radius of the electronic disk on the helium surface, and L_0 and ξ_0 are, respectively, the radius and deformation of the liquid surface outside the electronic disk.

Solving Eqs. (6) and (7) simultaneously gives

$$\xi_\infty = -\frac{V^2}{8\pi\rho g^* d_0^2}, \quad g^* = g\left(1 + \frac{L^2}{L_0^2 - L^2}\right). \tag{8}$$

For $\xi_\infty \ll d_0$ the deformation of the helium surface is inconsequential for the subsequent arguments.

In terms of E_- and E_+ the dynamical stability of a charged liquid is given by the condition

$$(4\pi en_s)^2 + (E_+ + E_-)^2 = 16\pi\kappa\alpha, \quad \kappa^2 = \frac{\rho g}{\alpha}, \tag{9}$$

where E_- and E_+ are given by Eqs. (1) and (2), α is the surface tension of liquid helium, and κ^{-1} is the capillary length. In this problem the potential difference V and the electron density n_s are actually independent. However, the clarity of the phase diagram in the "coordinates" (n_s, E_-) in Fig. 3 results in a somewhat artificial choice of precisely these variables as independent variables.

If $E_- = 0$ (complete screening), then

$$E_+ = \frac{V}{d} \equiv 4\pi en_s^{max},$$

and the equality (9) determines the maximum electron density n_s^{max} above helium:

$$\sigma_{max}^2 = \frac{\kappa\alpha}{2\pi} + (E_+^{max})^2 = 8\pi\kappa\alpha. \tag{10}$$

Introducing the fill factor

$$\nu = \frac{\sigma}{\sigma_{max}}, \tag{11}$$
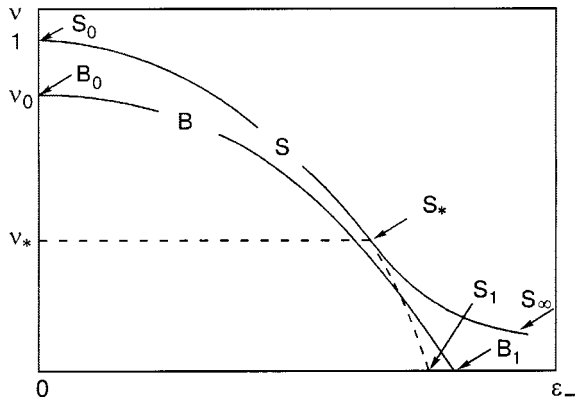
we put the relation (9) into the form

FIG. 3. Schematic phase diagram for reconstruction of a charged helium surface. The following points are marked on the spinodal (line S): S_0—asymptote (12a), S_*—the "branch" point in the definition of a spinodal [see comments to Eq. (16)], S_1—abstract point (12b) from the equipotential "baggage," S_∞—asymptote (16). The line B is the binodal. The following points are marked on B: B_0—the position of the binodal according to the estimates (22) ($\nu_0 = \sqrt{16.52/8\pi} = 0.81$), B_1—termination of the binodal in the range $\nu \to 0$ [estimate (19)]. The region of stability lies in the sector between the origin of coordinates and the binodal.

$$\nu^2 + (\varepsilon_+ + \varepsilon_-)^2 = 2, \quad \varepsilon_\pm = \frac{E_\pm}{4\pi\sigma_{max}}. \tag{12}$$

In the (ν, ε_-) phase diagram the curve $\nu(\varepsilon_-)$ (12) is the spinodal. If $\varepsilon_- \to 0$, then

$$\nu(\varepsilon_- \to 0) \to 1. \tag{12a}$$

In the opposite limit $\nu \to 0$

$$\varepsilon_-(\nu \to 0) = \varepsilon_+(\nu \to 0) \to 1/\sqrt{2}. \tag{12b}$$

The symbols S_0 and S_1 mark the positions of the points (12a) and (12b) on the spinodal "S" (Fig. 3).

The limit (12b) in the definition (12) actually has no real meaning, since on the path toward this limit the deformed helium surface ceases to be equipotential. Different estimates of the position of this boundary have been made, though specific calculations of the dispersion law in the transitional range have not been performed. As a point of reference, it can be assumed that equipotentiality vanishes in the range

$$V_C \lesssim T, \quad V_C \sim e^2 \sqrt{n_s}. \tag{13}$$

For $T \lesssim 1$ K the transitional range for the electron density is $n_s^* \lesssim 10^6$ cm^{-2}.

For $n_s < n_s^*$ the problem of the oscillations of a charged helium surface must be solved anew without using the equipotentiality property. A suitable alternative, which takes account of the influence of the deformation of the liquid boundary on the electron density $n(x)$, is the requirement

$$n(x) = n_s \exp[-eE_\perp \xi(x)/T], \tag{14}$$

where $\xi(x)$ is the amplitude of the oscillations of the charged surface and $E_\perp$ is the clamping electric field.

Using Eq. (14) (more accurately, its linear expansion, when $eE_\perp \xi(x) < T$) and the electronic pressure $P_{el} = eE_\perp n(x)$ acting on the helium surface, the dispersion law for small oscillations of the charge surface becomes

$$\frac{\rho\omega^2}{\alpha} = (\kappa^2 - \eta^2)q + \alpha q^3, \quad \eta^2 = \frac{n_s E_\perp^2}{\alpha T}. \tag{15}$$

Just as in the Frenkel–Tonks problem, oscillations with the dispersion law (15) become unstable. But this happens in a different range, specifically,

$$\eta^2 > \kappa^2, \quad E_\perp \simeq V/h. \tag{16}$$

According to Eqs. (16), a field which increases with decreasing n_s as $E_\perp \propto n_s^{-1/2}$ must be used in order for a weakly charged helium surface to become unstable. This assertion is qualitatively different from "equipotential" predictions [see the asymptotic behavior (12b)]. Therefore the spinodal asymptote for small ν does not terminate at the point S_1 but rather it extends as a square-root function right up to $\varepsilon_- \to \infty$. The ordinate ν_* in Fig. 3 marks the level near which the transition from Eq. (12b) to Eq. (16) occurs.

It should be noted that the instability (16) develops primarily at small wave numbers [and not at the capillary length, as in the case (9)].

2. In contrast to a spinodal, the binodal of the reconstruction process cannot be determined very reliably. Here the competitors are the dimple energy and the electrostatic energy of a capacitor with $2D$ electrons where fluctuations have produced a dimple. The uncertainty lies in the estimate of the optimal charge forming the critical dimple. The situation is relatively simple only for $\nu \ll 1$. Here, taking account of the development of an instability (16) at small wave numbers, all free electrons "roll down" into the dimple at the moment of the transition. This occurs when the Coulomb energy V_C of the electronic system occupying a circle of radius L between the capacitor plates (Fig. 2) reaches the energy W of a multielectron dimple with the same charge Q:

$$V_C = Q^2 \frac{(h-d)d}{L^2 h}, \quad Q = \pi L^2 e n_s, \tag{17}$$

$$W = Q^2 \kappa \left[s \exp\left(\frac{x^2}{2}\right) \mathrm{Ei}\left(-\frac{x^2}{2}\right) - \frac{1}{x} \right], \tag{18}$$

$$s = \frac{2}{2\kappa R_*}, \quad x = \kappa R, \quad R_*^2 = \frac{\sqrt{\pi}\alpha}{e E_\perp^2}, \quad E_\perp \simeq \frac{V}{h},$$

and $\mathrm{Ei}(x)$ is the integral exponential function. The quantity R in Eq. (18) is found from the condition for the energy W to be minimum as a function of R.

For $L \gg h$ the energy V_C (17) is quite low and instead of a general expression for W (18), competing with V_C, its expansion near the zero point can be used:

$$W(s_0, x_0) = 0, \quad s_0 = 1.05, \quad x_0 = 0.72,$$

$$W(s, x_0) \simeq \frac{\partial W}{\partial s_0}(s - s_0). \tag{18a}$$

Equating the competing energies gives

$$Q^2 \frac{(h-d)d}{L^2 h} = \frac{\partial W}{\partial s_0}(s_{max} - s_0), \tag{19}$$

determining the value of s_{max}. Since the left-hand side of Eq. (19) is small, we find that s_{max} is close to s_0.

The electric field $E_-^{\max}$, related with $s_{\max}$ by the formulas (18), determines the abscissa in Fig. 3 into which the binodal "butts" as $n_s \to 0$. This field is finite and is independent of n_s [n_s drops out of the definition (19)]. Therefore in the limit $n_s \to 0$ the binodal lies "under" the asymptotic spinodal (16).

In the opposite limit $E_- \to 0$ the characteristic fluctuations develop near wave numbers $q \sim \kappa$. Therefore the optimal charge Q_κ per dimple is

$$Q_\kappa \simeq \pi \kappa^{-2} e n_s. \tag{20}$$

The dipole energy V_C^κ for a charge distribution in the form of a flat disk with radius κ^{-1}, electron density n_s, and a compensating positive charge localized near the center impedes the appearance of a dimple. Just as in the case (19), the equality

$$V_C^\kappa = W_\kappa \tag{21}$$

is independent of n_s. Its left-hand side, by analogy to (19), contains an additional smallness $(\kappa R)^2$ compared with the Coulomb energy of the dimple, though not so serious as in Eq. (19). As a result the solution of Eq. (21) for s once again, [just as in the case (19)] gives a value close to s_0, i.e. the field threshold essentially remains on the entire binodal. In dimensional units this field is

$$(E_+^0)^2 = (2\pi)^{3/2} s_0 \kappa \alpha \simeq (16.52 \pm 0.005) \kappa \alpha. \tag{22}$$

The field $(E_+^0)^2$ is somewhat weaker than the critical field $E_+^{\max}$ (9), (10) for a spinodal.

Focusing on the two characteristic binodal points (19), (21), and (22) and assuming that the desired curve in the (n_s, E_-) plane has no special features in the interval between its limiting values, the binodal of the reconstruction of a charged helium surface can be represented in the form shown in Fig. 3 (line B).

3. We note that two dimples can be in equilibrium at a finite distance from one another. The interaction W_{dd}^b between them contains Coulomb and deformation parts

$$W_{dd}^b = -\frac{Q^2 E_\perp^2}{2\pi\alpha} K_0(\kappa r) + \frac{Q^2}{r}. \tag{23}$$

Here, just as above, Q is the total charge of the dimple, $E_\perp$ is the clamping field, r is distance between the dimples, and $K_0(x)$ is a modified Bessel function. The energy (23) has a minimum $\partial W_{dd}^b / \partial r = 0$ at the point $r_{\min}$, which can be determined from

$$K_1(x_m) - x_m^{-2} = 0, \quad x_m = \kappa r_{\min}, \quad x_m \gtrsim 1. \tag{24}$$

The presence of the metastable coupling (24) between dimples qualitatively explains why an assembly of dimples arising during binodal decomposition of a $2D$ charged system forms clusters with internal periodicity with characteristic length of the order of the capillary length.

Summarizing, the qualitatively new contribution of our analysis is an explanation of the data presented in Fig. 1, which attest to the possibility of aperiodic reconstruction of a charged helium surface. Another point of interest is that binodal (spinodal) motifs can be seen in the reconstruction of a charged helium surface, which served as a basis for the construction of the diagram (Fig. 3).

[*]E-mail: shikin@issp.ac.ru

[1] Ja. Frenkel, Z. Sowietunion **8**, 675 (1935).
[2] L. Tonks, Phys. Rev. **48**, 562 (1935).
[3] Ya. Frenkel', Zh. Éksp. Teor. Fiz. **6**, 347 (1936).
[4] L. Gor'kov and D. Chernikova, JETP Lett. **18**, 68 (1973).
[5] D. Chernikova, Fiz. Nizk. Temp. **2**, 1374 (1976) [Sov. J. Low Temp. Phys. **2**, 669 (1976)].
[6] L. Gor'kov and D. Chernikova, Dokl. Akad. Nauk SSSR **228**, 829 (1976) [Sov. Phys. Dokl. **21**, 328 (1976)].
[7] V. Shikin and P. Leĭderer, JETP Lett. **32**, 416 (1981).
[8] V. Mel'nikov and S. Meshkov, JETP Lett. **33**, 211 (1981).
[9] A. Volodin, M. Khaĭkin, and V. Édel'man, JETP Lett. **26**, 543 (1977).
[10] P. Leiderer, Phys. Rev. B **20**, 4511 (1979).
[11] W. Wanner and P. Leiderer, Phys. Rev. Lett. **42**, 315 (1979).
[12] P. Leiderer, W. Ebner, and V. Shikin, Surf. Sci. **113**, 405 (1982).

Translated by M. E. Alferieff

LOW-DIMENSIONAL AND DISORDERED SYSTEMS

Atomic dynamics and the problem of the structural stability of free clusters of solidified inert gases

É. T. Verkhovtseva, I. A. Gospodarev, A. V. Grishaev, S. I. Kovalenko, D. D. Solnyshkin, E. S. Syrkin, and S. B. Feodos'ev*

B. Verkin Institute for Low Temperature Physics and Engineering, National Academy of Sciences of Ukraine, pr. Lenina, 47, 61103 Khar'kov, Ukraine

The dependence of the rms amplitudes of atoms in free clusters of solidified inert gases on the cluster size is investigated theoretically and experimentally. Free clusters are produced by homogeneous nucleation in an adiabatically expanding supersonic stream. Electron diffraction is used to measure the rms amplitudes of the atoms; the Jacobi-matrix method is used for theoretical calculations. A series of distinguishing features of the atomic dynamics of microclusters was found. This was necessary to determine the character of the formation and the stability conditions of the crystal structure. It wass shown that for clusters consisting of less than $N \sim 10^3$ atoms, as the cluster size decreases, the rms amplitudes grow much more rapidly than expected from the increase in the specific contribution of the surface. It is also established that an fcc structure of a free cluster, as a rule, contains twinning defects (nuclei of an hcp phase). One reason for the appearance of such defects is the so-called vertex instability (anomalously large oscillation amplitudes) of the atoms in coordination spheres. © *2003 American Institute of Physics.* [DOI: 10.1063/1.1542502]

1. INTRODUCTION

The rapid advancement which the physics of nanostructures and nanocomposite materials is currently undergoing is due to the exceptional importance of these objects in fundamental research and modern technological applications. On the one hand it is precisely when a minimum number of atoms combine together that the basic properties of a solid appear while on the other hand small particles (clusters) possess their own distinguishing features which vanish as the cluster grows in size. In recent years, after the publication of the well-known monographs Refs. 1 and 2, an entire series of new and interesting features has been discovered in clusters: the melting temperature of small metallic particles differences strongly from the value in the bulk;[3,4] the laws governing the appearance of more stable clusters with so-called "critical" numbers in the structure of solidified insert gases have been predicted;[5] the existence of a roton cluster in He II, providing the conditions for the existence of rotons, has been proposed;[6] optical surface modes have been observed in pure defect-free clusters;[7] and, a surface plasmon has been observed in a cluster.[8] Interesting features of the physics of clusters on the surface of solids have been analyzed in Ref. 9. Two of the main informative characteristics for clusters are the density of vibrational states and the rms displacements of the atoms. As a rule, the size dependences of the physical characteristics of a solid are studied experimentally, in most cases, on films (solid or island) condensed on a substrate. The drawbacks of such investigations are: a high probability of quenching of nonequilibrium states, interaction of the sample with the substrate, and contamination of the

sample by impurities. Observations performed on clusters free of a substrate are more accurate. At the same time, to construct a a theoretical description of the atomic dynamics it is desirable to study models with the smallest possible number of parameters, and experimental studies should employ methods which do not affect the interior structure of clusters. In this sense it is of special interest to study a new class of physical objects—clusters of inert gases. For such clusters the important problem is the evolution of the structural and dynamical properties with a quasicontinuous transition from atom to solid.

In the present work the problem of the stability of the crystal structure of free clusters is studied. To this end the size dependence of the rms displacements of atoms in clusters of inert gases is studied experimentally and theoretically. The experimental objects are substrate-free Ar and Kr clusters produced by homogeneous nucleation in an isentropically expanding supersonic stream of gas. In this case an equilibrium structure is obtained, there is no interaction with the substrate, and uncontrollable impurities do not contaminate the experimental objects. Electron diffraction is used to determine the rms amplitudes of the atoms. Sharp, well-recorded diffraction patterns are obtained in electron-diffraction cameras with primary-beam current densities j not exceeding 10^{-2} A/m^2. For such densities an electron beam has virtually no bolometric effect on the experimental object. Observations performed on condensed films of cryocrystals (see, for example, Refs. 12 and 13) and theoretical estimates, obtained for metallic nanoparticles on a substrate,[12] which showed no effect due to the beam even for

$j \approx 0.1$ A/m^2, have confirmed this. In electron-diffraction investigations of clusters moving with supersonic velocities, the short residence time ($\approx 10^{-7}$ sec) of a cluster in the irradiation zone makes heating by the electron beam even less likely.

In the theoretical calculations, the method of Jacobi matrices (J matrices), developed by V. I. Peresada and his students,[13–15] was used to analyze the experimental data. This method makes it possible to clarify the physics of the question in detail, does not require voluminous computer calculations, and provides greater clarity than the molecular-dynamics and similar methods which have been employed in the last few years to calculate the physical properties of clusters (see, for example, Ref. 5). A detailed exposition of this method is given in Ref. 16 (unfortunately, without references to the author). In application to clusters, V. I. Peresada's method makes it possible to investigate the behavior of each atom. As shown in the present paper, this is extremely important because each atom in small particles plays an individual role.

The combination of experimental investigations and theoretical calculations has revealed new laws in the atomic dynamics of clusters of solidified gases. Specifically, the rapid growth[17] of the rms displacements of atoms with decreasing cluster size is explained. This fact could not be explained by a simple increase in the fractional contribution of the surface. It has been shown theoretically and experimentally that the special features of the atomic dynamics of clusters with decreasing cluster size are due not so much to the increasing role of the surface as to the special structural features of clusters.

2. EXPERIMENTAL PROCEDURE AND RESULTS

The observations were performed using a setup whose main components are a liquid-hydrogen-cooled apparatus that generates a supersonic cluster beam, a cryogenic condensation pump for evacuating the stream gas, and a standard ÉMR-100M electron-diffraction camera. A detailed description of the entire setup is given in Ref. 18. The supersonic cluster beam generator is described in detail in Ref. 19. The average size N (the number of atoms per cluster) of the clusters investigated was varied by varying the gas pressure P_0 at the entrance into the nozzle at constant gas temperature T_0. The average characteristic size δ of the crystalline clusters was determined, using the Selyakov–Scherrer relation,[20] from the broadening of the diffraction peaks taking account of their additional smearing due to stacking faults. It should be noted that as the average size of the aggregates in a cluster beam increases, the fraction of icosahedral formations decreases. For example, for $N \approx 1400 - 1500$ the number of clusters with icosahedral structure is $\approx 25\%$, whereas for $N \sim 3 \times 10^3$ virtually all clusters possess fcc structure.

When small atomic aggregations with icosahedral structure predominated in cluster beams, the characteristic size was established by extrapolating to low pressures the relation $\delta = \varphi(P_0)_{T_0 = \text{const}}$ obtained for average-size crystalline clusters. Statistical analysis of the observational results showed that δ was determined to within $\pm 10\%$.

The diffraction patterns were photographed to find the lattice parameters a of the crystal clusters of argon and krypton. In this case, depending on the quality of the electron-diffraction pictures, a was determined to within $\pm (0.1 - 0.3)\%$.

Data on the value and temperature dependence of the lattice parameter[21] were used to determine the temperature of the clusters. The intensity I of the diffraction peaks was determined by analyzing the diffraction patterns obtained by electrometric recording. The relative error in determining the intensity usually did not exceed $\pm 3\%$. The method for determining the instrumental constant $2L\lambda$ (L is the distance between the diffraction region and the detector and λ is the electron wavelength) and the instrumental width of the diffraction peaks are described in Ref. 22. These quantities are needed to determine the lattice parameter and the characteristic size of the clusters.

The rms displacements of the atoms from their equilibrium positions were found using the dependence of the temperature factor, the intensity of the diffracted rays, exp $(-2M)$, on the diffraction angle θ.

For an fcc lattice

$$M = 8\pi\lambda^{-2}\langle u^2 \rangle \sin^2\frac{\theta}{3},$$

where $\langle u^2 \rangle$ is the mean-squared total displacement of an atom from its equilibrium position.[23]

Thus, the total intensity of the diffracted rays reflected by a system of planes $\{hkl\}$, can be written as

$$I_{hkl} = I_0 A_{hkl} \exp\left(\frac{-16\pi^2 \sin^2\theta}{\lambda^2} \frac{\langle u^2 \rangle}{3}\right) \tag{1}$$

or

$$I_{hkl} = I_0 A_{hkl} \exp\left(-\frac{S_{hkl}^2 \langle u^2 \rangle}{3}\right), \tag{2}$$

where $S_{hkl} = 4\pi\lambda^{-1}\sin\theta$ is the diffraction vector; A_{hkl} is the product of all constant factors in the intensity (for a particular system of reflecting planes) with the exception of the temperature factor; and, I_0 is the intensity of the primary electron beam. Since I_0 can vary appreciably from one experiment to another, it is desirable to normalize the intensity of the diffraction peaks to a well-distinguished peak. One such peak for an fcc structure is the diffraction maximum (220). Thus, in what follows, the following relation was used to determine $\langle u^2 \rangle$:

$$\ln\left(\frac{I_{hkl}}{I_{220}} \frac{A_{220}}{A_{hkl}}\right) = \frac{\langle u^2 \rangle}{3}(S_{220}^2 - S_{hkl}^2), \tag{3}$$

which establishes a relation between the logarithm of the normalized intensity of the diffraction peak and the difference of the squared diffraction vectors. Plots illustrating the dependence of the logarithm of the normalized intensity of the diffraction peaks for argon and krypton on the difference of the squared diffraction vectors are presented in Figs. 1 and 2. These plots were constructed for clusters of different size, but to simplify the figures only three plots are presented here.

According to Figs. 1 and 2, the slope angle of the experimental straight lines increases with decreasing average size of the clusters. Since the tangent of the slope angle is
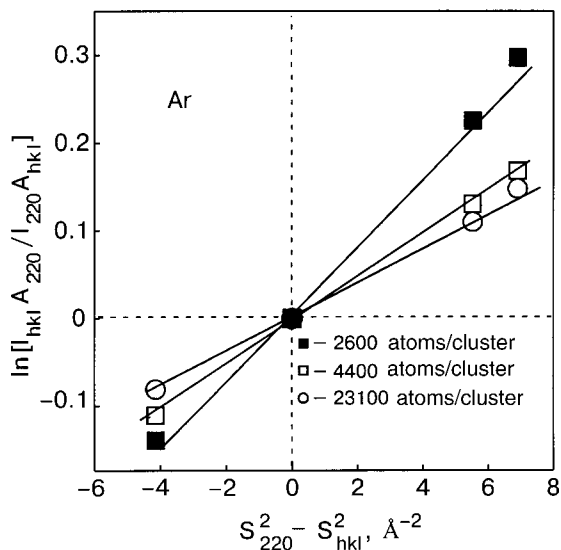
FIG. 1. Logarithm of the normalized intensity of the diffraction peaks from Ar clusters with 2600, 4400, and 23100 atoms/cluster versus the difference of the squared diffraction vectors $S_{220}^2 - S_{hkl}^2$, Å^{-2}. The reflections (111), (200), (220), and (311) were used to construct the plots.

proportional to the mean-squared atomic amplitude (3), the observed behavior shows that $\langle u^2 \rangle$ increases as cluster size decreases. The curve *1* in Figs. 3 and 4 shows for argon and krypton clusters, respectively, the size dependence of the rms displacements of the atoms. In these plots, a quantity which is the inverse of the cube root of the average cluster size is plotted along the abscissa and the quantity Ω—the rms amplitude $\sqrt{\langle u^2 \rangle}$ normalized to the rms displacement of atoms in the bulk $\sqrt{\langle u^2 \rangle_v}$—is plotted along the ordinate.

On the basis of the x-ray data the Debye temperatures $\Theta_D^{Ar} = 93.3$ K and $\Theta_D^{Kr} = 71.9$ K for argon and krypton were used in the calculations. The cluster temperatures, determined using the method indicated at the beginning of this section, were found to be $T_{Ar} = (37 \pm 4)$ K and $T_{Kr} = (55$
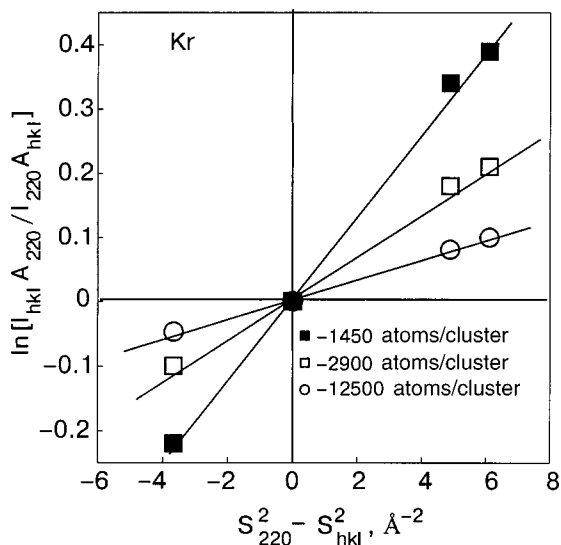

FIG. 2. Logarithm of the normalized intensity of the diffraction peaks from Kr clusters with 1450, 2900, and 12500 atoms/cluster versus the difference of the squared diffraction vectors $S_{220}^2 - S_{hkl}^2$, Å^{-2}. The reflections (111), (200), (220), and (311) were used to construct the plots.
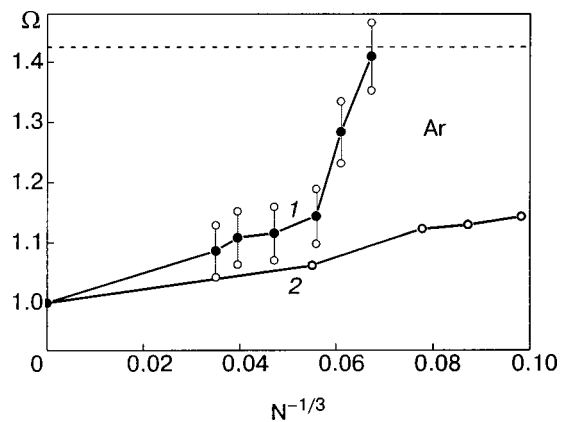

FIG. 3. Evolution of Ω—the ratio of the rms atomic vibrational amplitudes, averaged over all directions and all possible positions of atoms in a cluster, to the rms amplitude in a bulk sample—as a function of the size of a free Ar cluster: experimental result (*1*); theoretical calculation for a *proper* cluster (*2*); $\Omega_m \approx 1.4252$ (dashed line); number of atoms in the cluster N; $T_{Ar} = 37 \pm 4$ K.

± 4) K. The experimental values of the normalized rms amplitudes are shown in Figs. 3 and 4 (circles). For large clusters the experimental values of $\sqrt{\langle u^2 \rangle}$ fall quite well on straight lines corresponding to an increase in the relative contribution of the surface (see Ref. 17). Hence it follows that the increase in the mean-square atomic amplitude with decreasing number of atoms in a cluster (for clusters with $N \gtrsim 4 \times 10^3$ atoms/cluster) is due primarily to an increase in the relative number of surface atoms. However, as the cluster size decreases further ($N \lesssim 3 \times 10^3$ atoms/cluster), $\langle u \rangle^2$ increases very rapidly, which cannot be explained only by an increase in the fractional contribution of the surface. In this case, other factors, whose effectiveness needs to be analyzed, probably come into play. The same figures show (curves *2*) the results of theoretical calculations (at the microscopic level) of the rms vibrational amplitudes of the atoms in clusters of various sizes. The computational method and results and a detailed comparison of theory with experiment are given in the next section.
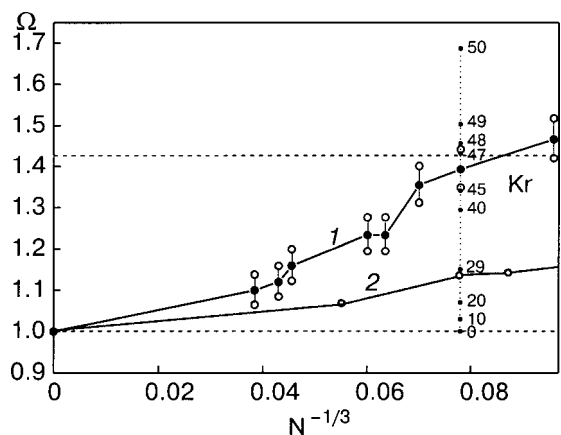

FIG. 4. Evolution of Ω as a function of the size of a free Kr cluster: experimental result (*1*); theoretical calculation for a *proper* cluster (*2*); $\Omega_m \approx 1.4258$ (dashed line); number of atoms in the cluster N; $T_{Kr} = 55 \pm 4$ K.

3. ATOMIC DYNAMICS OF FREE MICROCLUSTERS

Let us consider the temperature dependences of the relative rms amplitudes $\mathcal{U}_i$, i.e. the quantities

$$\mathcal{U}_i(\mathbf{r},T) \equiv \frac{\langle |u_i|(T,\mathbf{r})\rangle}{a} = \frac{\sqrt{\langle u_i^2(\mathbf{r},T)\rangle}}{a} \qquad (4)$$

for Ar, Kr, and Xe crystals, unbounded and bounded by one or several flat surfaces. These crystals are regarded as fcc crystal lattices with a central interaction between nearest neighbors. In Eq. (4) a is the equilibrium interatomic distance in the crystal (which in an fcc lattice is $\sqrt{2}$ times shorter than the edge length l of a cube). The function $\langle u^2(\mathbf{r},T)\rangle$ is the temperature dependence of the mean-squared displacement of an atom with radius vector $\mathbf{r}$ in the crystallographic direction i[1)] and is defined as (see, for example, Refs. 13 and 24)

$$\langle u_i^2(\mathbf{r},T)\rangle = \frac{\hbar}{2m(\mathbf{r})} \int_0^\infty \frac{\rho_i(\varepsilon,\mathbf{r})}{\sqrt{\varepsilon}} \coth\left(\frac{\hbar\sqrt{\varepsilon}}{2kT}\right) d\varepsilon. \qquad (5)$$

Here $m(\mathbf{r})$ is the mass of an atom whose radius vector is $\mathbf{r}$; the integration variable ε is the squared frequency of a normal vibration; $\hbar$ and k are, respectively, the Planck and Boltzmann constants; the function $\rho_i(\varepsilon,\mathbf{r})$ is the spectral density characterizing the distribution over vibrational frequencies in the crystallographic direction i of an atom with radius vector $\mathbf{r}$. In the general case, when the frequency spectrum of an atom consists of a region in the continuous spectrum $\mathcal{D}$ (generally speaking, multiply connected) and a set of discrete levels outside this region, this function can be represented in the form[13,24–26]

$$\rho_i(\varepsilon,\mathbf{r}) = \pi^{-1} \operatorname{Im} \mathcal{G}_{ii}(\mathbf{r},\mathbf{r},\varepsilon)$$

$$+ \sum_d \operatorname{rés}_{\varepsilon=\varepsilon_d} \mathcal{G}_{ii}(\mathbf{r},\mathbf{r},\varepsilon)\,\delta(\varepsilon-\varepsilon_d), \qquad (6)$$

where $\mathcal{G}_{ik}(\mathbf{r},\mathbf{r}',\varepsilon)$ is the Green's tensor of the system [no summation over repeated indices in Eq. (6)]. The condition that the imaginary part of the Green's function $\mathcal{G}_{ii}(\mathbf{r},\mathbf{r}',\varepsilon)$ is different from zero determines a region of the continuous spectrum $\mathcal{D}$ and the discrete levels ε_d are poles of this function, which can lie only outside $\mathcal{D}$. For $\varepsilon \notin \mathcal{D}$, the Green's function is real and piecewise-smooth. The spectral density is normalized to 1, i.e.

$$\int_0^\infty \rho_i(\varepsilon)\,d\varepsilon = 1. \qquad (7)$$

If the crystal lattice contains one atom per unit cell, then the region of the continuous spectrum is the interval $[0,\varepsilon_{\max}]$. In our case there are no discrete levels outside this interval.

The upper limit $\varepsilon_{\max}$ of the band in the continuous spectrum of the crystal can be associated to a characteristic temperature $\Theta_p \equiv \hbar\sqrt{\varepsilon_{\max}}/k$; this quantity is identical to the Debye temperature Θ_D at high temperatures and equals 0.95–$0.96\,\Theta_D$ at low temperatures. Then the expression (5) can be put into the form

$$\langle u_i^2(\mathbf{r},T)\rangle = (\mathcal{A}_\alpha a)^2 \,{}_i\!\left(\frac{T}{\Theta_p},\mathbf{r}\right), \qquad (8)$$

where ${}_i(z,\mathbf{r})$ is the integral ($\varepsilon \equiv \varepsilon_{\max} x$)

TABLE I. Physical properties of Ar, Kr, and Xe.

α	μ, amu	T_m, K	Θ_D, K	$l = a\sqrt{2}$, Å	$\mathcal{A}$	$\mathcal{U}_m$
Ar	39.948	83.806	93.3	5.40	$2.1545\cdot10^{-2}$	$5.3614\cdot10^{-2}$
Kr	83.80	115.76	71.9	5.59	$1.6369\cdot10^{-2}$	$5.3908\cdot10^{-2}$
Xe	131.30	161.39	64.0	6.20	$1.2497\cdot10^{-2}$	$5.1274\cdot10^{-2}$

$${}_i(z,\mathbf{r}) = \int_0^1 \frac{\rho_i(x,\mathbf{r})}{\sqrt{x}} \coth\left(\frac{\hbar\sqrt{x}}{2z}\right) dx \qquad (9)$$

which in our case is independent of the parameters of the specific material, and the constant

$$\mathcal{A}_\alpha \equiv \frac{\hbar}{a_\alpha \sqrt{2km_\alpha \Theta_p^{(\alpha)}}}$$

(the index α enumerates the material) describes all characteristics of a particular material. The basic characteristics of the crystal lattices of Ar, Kr, and Xe[27,28] which we require are given in Table I.

The spectral densities (6) and the integrals (9) are calculated using the Jacobi-matrix technique[13,14] and continued fractions (Refs. 15 and 16)[2)]

Figure 5 shows the temperature dependences of $\mathcal{U}$ for unbounded Ar, Kr, and Xe crystals in the range from zero up to the melting point. The rms amplitudes for an unbounded ideal lattice are identical for all directions and all atoms in the same crystal. For different crystals they differ by the preintegral factors $\mathcal{A}_\alpha$. We note that at the melting temperature T_m the values of $\mathcal{U}$ are essentially the same for all three cryocrystals. These values $\mathcal{U}_m = \mathcal{U}(T_m)$ are also presented in Table I.

The ratio of $\mathcal{U}_i(\mathbf{r},T)$ to $\mathcal{U}_m$, conventionally, serves as a stability criterion for the crystal lattice or atoms located, for example, at the boundaries of the sample (surfaces, edges, vertices).

The temperature dependences $\mathcal{U}_i(\mathbf{r},T)$ for all types of boundary atoms mentioned above are presented in Fig. 6. In this and subsequent figures the scale for krypton is the ordinate on the left-hand side and the scale for argon is the ordinate on the right-hand side (the ratio of the scale divisions equals the ratio of the quantities $\mathcal{A}_\alpha$; see Table I). The curve
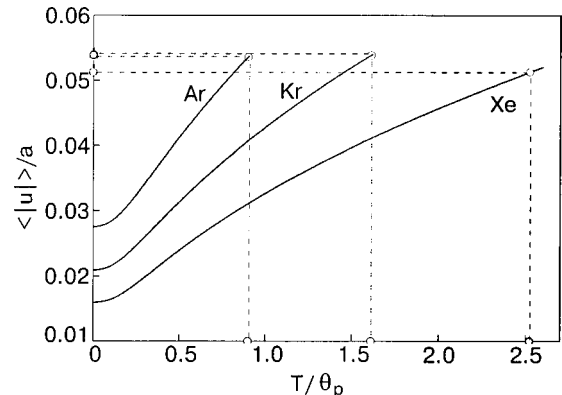

FIG. 5. Temperature dependences of $\mathcal{U} = \langle |u|\rangle/a \equiv \langle u^2\rangle$.
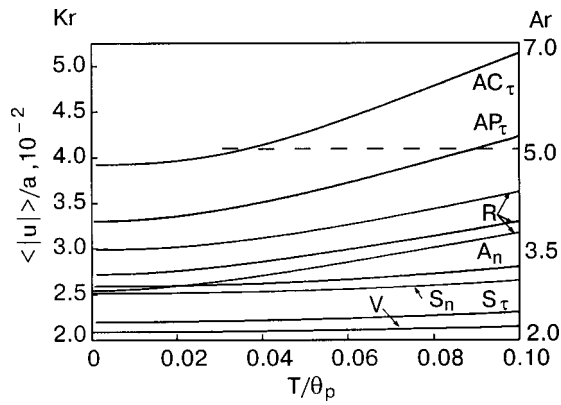
FIG. 6. Temperature dependences of $\mathcal{U}=\langle|u|\rangle/a$ for volume (V), surface (S), edge (R), and vertex (A) atoms. AC—corresponds to the vertex of a cube, AP—vertex of an octahedron; the indices τ and n indicate tangential and normal displacements of vertex atoms.

S_n corresponds to a displacement in a direction normal to the close-packed flat surface (111). The first moment of the corresponding spectral density (square of the corresponding Einstein frequency)[3)] is $\langle\varepsilon\rangle_n^{(S)}=\varepsilon_{\max}/4$. The curve S_τ corresponds to a displacement in the direction in this plane. For such a displacement $\langle\varepsilon\rangle_\tau^{(S)}=\varepsilon_{\max}/2$, just as for a bulk atom V, so that the curve S_τ lies appreciably below the curve S_n.

The curves AC correspond to a vertex of a cube and the curves AP correspond to a vertex of a pyramid formed by the intersection of close-packed planes (four such planes intersect at a single point). The curves AC_n and AP_n, corresponding to normal displacements of vertex atoms, i.e. displacements of atoms at AC vertices in the [111] direction and atoms at vertices of the type AP in the [100] direction, are virtually identical and are denoted by the same symbol A_n. For normal displacements of both types of vertex atoms studied here, just as for S_n, the squared Einstein frequency $\langle\varepsilon\rangle_n^{(AP)}=\langle\varepsilon\rangle_n^{(AC)}=\langle\varepsilon\rangle_n^{(S)}=\varepsilon_{\max}/4$. Consequently, the curve A_n lies near the curve S_n (somewhat above it).

The curves AC_τ and AP_τ, corresponding to displacements of the vertex atoms in directions perpendicular to AC_n and AP_n, differ substantially from one another: the curve AC_τ, corresponding to displacements for which the squared Einstein frequency $\langle\varepsilon\rangle_\tau^{(AC)}=\varepsilon_{\max}/16$, substantially above the curve AP_τ, which corresponds to displacements engendering a spectral density with the first moment $\langle\varepsilon\rangle_\tau^{(AP)}=\varepsilon_{\max}/8$. The rms displacement amplitudes of the AC atoms are $\sim\mathcal{U}_m$ even at low temperatures (for Ar they exceed $\mathcal{U}_m$, denoted in Fig. 6 by the dashed line, even for $T\lesssim0.04\,\Theta_p$). This shows that the position of the atoms at vertices of this type is unstable. Since the vibrational amplitudes of these atoms in the normal direction are comparatively small, the most likely outcome will not be detachment of these atoms from a monolithic sample but rather a transfer of the atoms into a neighboring position—AC vertices will be smoothed. The atoms at AP vertices are somewhat more stable but their stability is still weak, especially for argon.

The curves R corresponds to displacements of edge atoms. For them $\langle\varepsilon\rangle$ can assume values from $\varepsilon_{\max}/8$ to $(7/16)\varepsilon_{\max}$, depending on the direction of displacement and on the planes whose intersection forms the given edge. The

corresponding values of $\mathcal{U}$ lie between the values of the rms amplitudes of the surface and vertex atoms.

A. Stability of atoms in proper free clusters

We shall say that a free cluster is a *proper* cluster if it is formed by complete filling of several coordination spheres. We shall consider the evolution of the temperature dependences of the rms vibrational amplitudes in different crystallographic directions i of the atoms located in different positions of such a *proper* cluster as a function of the number of these coordination spheres n, i.e. the quantities $\mathcal{U}_i(\mathbf{r},T)$.

Since the number of atoms in a cluster is finite, the vibrational spectrum of a cluster is discrete, and it becomes impossible to calculate the temperature dependences $\mathcal{U}_i(\mathbf{r},T)$ using an analytical approximation of the spectral density. The subsequent calculations are performed using the so-called *quadrature method* in the Jacobi-matrix method.[13,14] It has been shown, for example, in Ref. 31, that the rms displacements calculated using this method converge very rapidly as the rank of the Jacobi matrix increases, and this method gives quite accurate results even for Jacobi-matrix rank $\mathcal{N}\geq10$. The characteristic vibrational frequencies of atoms in a free cluster have zero frequencies which correspond to displacements and rotations of a cluster as a whole. The quadrature method makes it possible to separate quite accurately these displacements for a cluster with $n\leq\mathcal{N}$ (where $\mathcal{N}$ is the rank of the computed Jacobi matrix). Our computers and software make it possible to calculate for the systems considered Jacobi matrices of rank $\mathcal{N}=40$, so that we shall confine our attention to clusters with $5\leq n\leq50-100$ (it is shown in Ref. 33 that smaller clusters do not have a crystalline structure).

The rms amplitudes of atoms in the least stable (i.e. vibrating with the highest amplitudes) surface coordination sphere Σ_n are of greatest interest from the standpoint of studying the stability of a cluster. We denote these amplitudes as $\mathcal{U}_i^{\Sigma_n}(T)=\mathcal{U}_i(\mathbf{r},T)|_{\mathbf{r}\in\Sigma_n}$. These quantities will be nonmonotonic functions of n, since atoms of various types will be present on the surface.

1) Surface atoms (P-S type), where $n=5,7,10,\ldots$ and so on. Displacements of this type correspond to the squared Einstein frequencies:
   – for normal displacements $\langle\varepsilon\rangle_n=\varepsilon_{\max}/4$;
   – for tangential displacements (in a plane tangent to the surface of a cluster) $\varepsilon_{\max}/4\leq\langle\varepsilon\rangle_\tau\leq\varepsilon_{\max}/2$.
2) Edge atoms (R-type), where $n=8,9,16,25$:
   – $\langle\varepsilon\rangle_n=\varepsilon_{\max}/4$;
   – $\langle\varepsilon\rangle_\tau=\varepsilon_{\max}/8$.
3) Vertex atoms (A-type), where $n=6m^2$ (m is an integer):
   – $\langle\varepsilon\rangle_n=\varepsilon_{\max}/4$;
   – $\langle\varepsilon\rangle_\tau=\varepsilon_{\max}/16$.

The corresponding curves for the normal and tangential atomic displacements are presented in Figs. 7 and 8.

The rms amplitudes of atomic displacements normal to the surface (Fig. 7) lie near the curve S_n in the preceding figure (transferred to this figure and shown by the long dashes). Only the rms amplitudes of type-A atoms ($n=6,24,54$) and certain type-R atoms in an extreme low-temperature range lie somewhat above the curve S_n, so that the probability of an atom becoming detached from a free
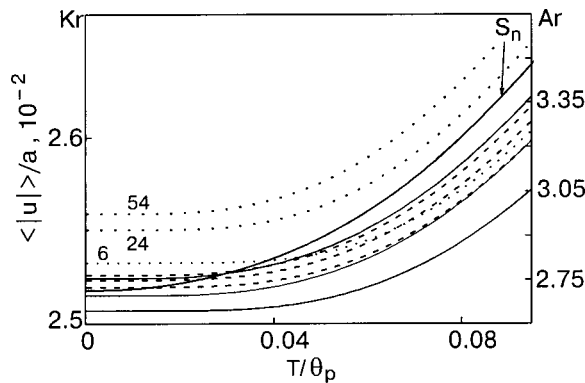
FIG. 7. Temperature dependences of the relative rms vibrational amplitudes of surface atoms in *proper* clusters of various sizes in a direction normal to the surface. *A* atoms, $n=6, 24, 54$ ($\cdots$); *R* atoms, $n=9, 16, 25$ ($- - -$); *P*-*S* atoms, $n=5, 15, 25$ (——).

cluster, generally speaking, does not exceed the probability of detachment from a free surface of the type (111).

As the cluster increases in size, the quantities $\mathcal{U}_n^{(\Sigma_n)}(T)$ increase and the corresponding curves tend toward the curve S_n from below (except for the curves corresponding to type-*A* atoms, lying somewhat above S_n, but even these dependences increase appreciably with n). Such evolution of the temperature dependences $\mathcal{U}_n^{(\Sigma_n)}(T)$ is due primarily to an increase in the contribution of the recoil energy to the total energy of a free cluster as the size of the cluster decreases, i.e. the kinetic energy of displacement of an atom as a whole. In addition, an increase in the surface curvature decreases, but to a much lesser degree, $\mathcal{U}_n^{(\Sigma_n)}(T)$ as n increases. As the curvature increases, the differences of the projections of neighboring surface atoms on the direction of the normal increase and hence the normal component of the restoring force, which neighboring surface atoms exert on the surface atom, increases somewhat. However, this increase is negligible in our range of values of n.

The rms amplitudes of the tangential displacements of surface atoms (Fig. 8) are, on the average, much greater than those of the normal displacements (this agrees with calculations of the rms displacements of atoms adsorbed on a flat surface of a crystal[32]). The values of $\mathcal{U}_\tau^{(\Sigma_n)}(T)$ are especially large for *A*-type atoms. The corresponding curves lie be-

tween the curves AP_τ and AC_τ [Fig. 6, these curves, just as the curves S_n, are shown in Fig. 8 (long dashes)]. We note that for *A*- and *R*-type atoms $\mathcal{U}_\tau^{(\Sigma_n)}(T)$ are essentially independent of the cluster size. For *P*–*S*-type atoms, as the cluster size increases, the rms amplitudes decrease slowly, exhibiting nonmonotonicity for small values of n. As $n \to \infty$ these curves tend toward S_τ (Fig. 6) from above.

The anomalously high ($\sim \mathcal{U}_m$) values of the rms amplitudes $\mathcal{U}_\tau^{(\Sigma_n)}(T)$ for *A*-type atoms attest to the instability of coordination spheres with $n=6, 24, 54, \ldots, 6m^2$. The atoms should not detach from the surface of a free cluster, since $\mathcal{U}_\tau^{(\Sigma_n)}(T)$ for these atoms are small (Fig. 7), but rather they will move along the surface of the cluster and settle in points where their values of $\langle \varepsilon \rangle_\tau$ will be higher (the value of this quantity for type-*A* atoms—one sixteenth of ε_{max}—is its minimum possible value) and the rms amplitude, therefore, lower. However, these points will no longer correspond to filling of coordination spheres in a *proper* free cluster. Specifically, such improper filling of coordination spheres will give rise to twins and local nuclei of phases with hcp crystal structure; this will be manifested in the diffraction patterns.[33,34] It should be expected, with a high degree of probability, that the fcc structure will remain as free clusters grow, as a collection of octahedra formed by the intersection of close-packed planes of the fcc lattice, since the curve AP_τ lies appreciably below the curve AC_τ (Fig. 6).

B. Dependence of the average total-displacement amplitudes of atoms in a cluster on the cluster size

The increase in the contribution of the recoil energy to the total energy of a cluster as the size of the cluster decreases is most clearly seen in the evolution of the rms amplitudes of the central atoms of clusters $\mathcal{U}(0,T) = \mathcal{U}(\mathbf{r},T)|_{\mathbf{r}=0}$ (this quantity is isotropic and is independent of i). A collection of temperature dependences $\mathcal{U}(0,T)$ is displayed in Fig. 9. It is evident that these curves all lie below $\mathcal{U}(T)$—the rms amplitude of an atom of an unbound fcc crystal (the curve *V* in Fig. 6, which we transferred to this figure), and they tend toward this curve from below as n increases. The somewhat high value of $\mathcal{U}(0,T)$ for $n=6$ is due to the general "looseness" of this cluster with an unstable surface, whose contribution to all characteristics of such a small cluster is very large.

FIG. 9. Temperature dependences of the relative rms vibrational amplitudes of the central atoms in *proper* free clusters of various sizes.
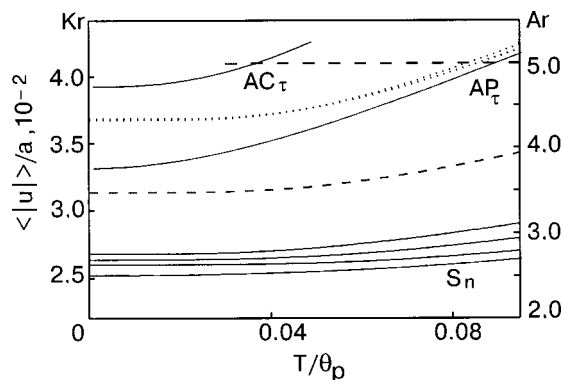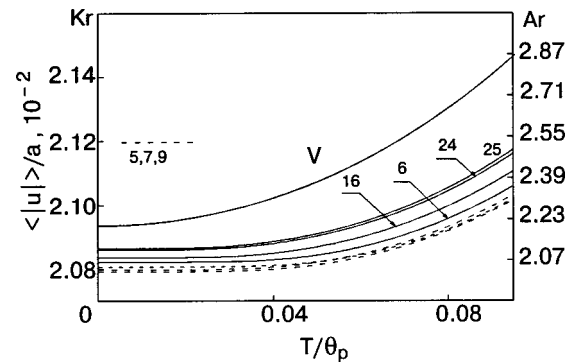

FIG. 8. Temperature dependences of the relative rms vibrational amplitudes of surface atoms in *proper* clusters of various sizes in directions tangent to the surface. *A* atoms, $n=6, 24, 54$ ($\cdots$); *R* atoms, $n=9, 16, 25$ ($- - -$); *P*-*S* atoms, $n=5, 15, 25$ (——).
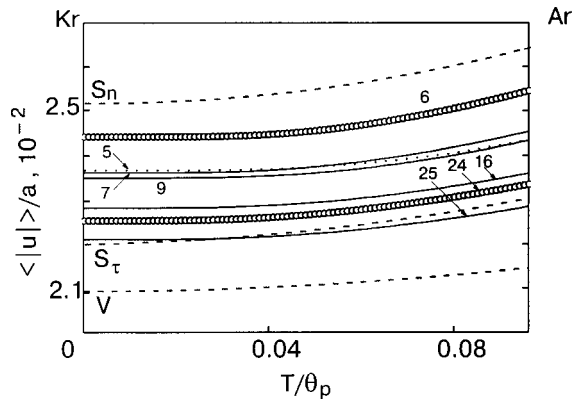
FIG. 10. Evolution of the temperature dependences of the relative rms amplitudes of atomic vibrations averaged over all directions and all possible positions of atoms for various sizes of a *proper* free cluster.

The melting temperature of a cluster can be estimated from the relation

$$\langle \mathcal{U} \rangle(T) \sim \mathcal{U}_m,$$

where $\langle \mathcal{U} \rangle(T) = a^{-1}\sqrt{\langle u^2 \rangle}$ is the average amplitude of the total displacement of the atoms in a cluster, i.e. the rms amplitude $\mathcal{U}_i(\mathbf{r}, T)$ averaged over all directions of atomic displacements and all positions $\mathbf{r}$ of an atom in the cluster. The evolution of these quantities as a function of the cluster size is presented in Fig. 10. It is evident that the values of these quantities increase appreciably as the cluster size decreases, i.e. the increase in the rms amplitudes as a result of an increase in the contribution of different types of boundary atoms is greater than the decrease of these quantities due to an increase in the contribution of the recoil energy. The anomalously large value of $\langle \mathcal{U} \rangle(T)$ for $n=6$ is due to, just as the anomalously large value of $\mathcal{U}(0,T)$ for the same cluster, the relatively large number of A-type atoms. Such a cluster is not realized as a *proper* cluster. We note that for $n=24$ $\langle \mathcal{U} \rangle(T)$ is only negligibly greater than for $n=25$, since this cluster consists of 683 atoms, of which only eight are type-A, while the cluster with $n=6$ also has eight type-A atoms but consists of only 87 atoms.

For clusters of all sizes considered the values of $\langle \mathcal{U} \rangle \times (T)$ fall between the curves S_τ and S_n, i.e. for such clusters the increase of the rms amplitudes (and therefore, for example, the decrease of the melting temperature) is much greater than expected simply from an increase in the contribution of the surface. We underscore once again that this is due to the contribution of edge and vertex atoms and the finite relaxation length of the amplitudes of atomic vibrations from the boundary to the interior volume (the vibrational amplitudes of atoms located near the boundaries are still appreciably greater than those of interior atoms).

Figures 3 and 4 (curves *2*) show the results of a theoretical calculation of the rms amplitudes of the vibrations of atoms in *proper* clusters of the same size (same number of atoms) as in the experiment; curves *2*, just as the experimental curves *1*, deviate upwards from the straight lines corresponding to an increase of the rms amplitudes as a result of the simple increase of the surface contribution.

At the same time, the experimental curves lie appreciably above the theoretical curves (the deviation is 20%). To

explain this behavior it should be noted first that the vibrational amplitudes of the atoms in a cluster are strongly nonuniform. Figure 4 shows values of Ω_n—the ratios of the rms vibrational amplitudes of atoms in various coordination spheres of a *proper* cluster, consisting of 50 such completely filled spheres ($N=2123$; $N^{-1/3} \approx 0.0778$), to the rms vibrational amplitude of an atom in a bulk sample at the same temperature. The ratio $\Omega_{50}/\Omega_0 \approx 1.8$. Thus, the deviation of the shape of a cluster from a *proper* shape, resulting in an increase in the specific contribution of the surface or near-surface atoms (in a *proper* cluster such a specific contribution for a fixed size is minimal), can easily explain the observed difference between the experimental and theoretical values of Ω.

In addition, the temperatures at which the rms amplitudes, shown in Figs. 3 and 4, were measured are quite high, ≈ 0.442 and ≈ 0.475 times the melting temperature for argon for krypton, respectively. Consequently, Ω_n for $n \geq 47$ lie above (and sometimes quite substantially) the dashed line corresponding to Ω_m determined on the basis of the data in Table I and Fig. 5 ($\Omega_m \approx 1.452$ for Ar and ≈ 1.4258 for Kr). Therefore it can be supposed that the surface of a given cluster is no longer, generally speaking, in a crystalline state. This can weaken the interatomic interaction and therefore increase the vibrational amplitudes of the atoms (and not only for atoms close to the surface), and it can give rise to additional scattering of electrons and decrease the corresponding peaks, interpreted in the experiment as an additional increase in amplitude. The additional electron scattering is indicated by, among other things, the fact that values of Ω above Ω_m were recorded experimentally for a free cluster (Fig. 4).

4. CONCLUSIONS

There exists a complete qualitative and more than satisfactory quantitative agreement between the experimental data and the results of theoretical calculations performed at the microscopic level for the model of a *proper* cluster. The strong nonuniformity of the rms amplitudes which is obtained in these calculations makes it possible to explain adequately not only the main experimental results but also the observed discrepancies between the theoretical and experimental curves; these discrepancies are due to the complexity of the experimental object itself. Virtually complete quantitative agreement can be obtained by taking into account the shape of free clusters which are actually formed in a supersonic stream.

Comparing the theoretical and experimental results makes it possible to draw two important conclusions which determine the basic distinguishing features of the atomic dynamics of free clusters and the stability of their crystal structure:

(1) The dependence of the rms amplitude of atomic vibrations, averaged over all atomic positions and all directions of atomic displacements, on cluster size is determined by the increase of the contributions of *all types—vertex, edge, and surface*—of boundary atoms, vibrating with large amplitudes, as the cluster size decreases. The consequent increase in $\langle \mathcal{U} \rangle$ is much greater than the

contribution of the vibrations of atoms located in the interior volume of a cluster. The vibrational amplitudes of such atoms are somewhat smaller than those of atoms in bulk samples because of the recoil energy—the kinetic energy of the motion of a cluster as a whole. As cluster size decreases, these amplitudes decrease, since the contribution of the recoil energy increases.

As a result, for clusters consisting of less than $N \sim 10^3$ atoms, as cluster size decreases, $\langle \mathcal{U} \rangle$, which determines the stability of the crystal structure of a cluster (specifically, the melting temperature of the cluster), increases much more rapidly than should be expected simply on the basis of the increase in the specific surface contribution.

(2) The crystal structure of a free cluster, as a rule, contains twinning-type stacking faults (nuclei of an hcp phase). They appear because of the instability (anomalously large vibrational amplitudes) of the atoms in the vertex coordination spheres.

The vertex atoms in free clusters with octahedral structure, i.e. bounded by intersecting close-packed planes of the fcc structure, will be more stable. Consequently, nuclei of an hcp phase are less likely to form in such clusters.

We thank V. N. Samovarov for a fruitful discussion of the results and A. G. Danil'chenko for assisting in the experiment.

---

[*]E-mail: feodosiev@ilt.kharkov.ua

[1)]The temperature dependence of the quantity $\langle u \rangle^2$ introduced in the preceding section is obtained by averaging $\langle u^2(\mathbf{r}, T) \rangle$ over all positions $\mathbf{r}$ and displacement directions i.

[2)]A succinct description of this method can be found in Ref. 29 or in the Appendix in Ref. 30.

[3)]This quantity equals the first diagonal component of the corresponding Jacobi matrix.[13,14]

---

[1] M. A. Vasil'ev, *Surface Structure and Dynamics of Transition Metals*, Naukova dumka, Kiev (1988).

[2] Yu. I. Petrov, *Physics of Small Particles*, Nauka, Moscow (1982).

[3] K. F. Peters, J. B. Cohen, and Yip-Wao Chung, Phys. Rev. B **57**, 1340 (1998).

[4] S. A. Gorban', S. A. Nepijko, and B. M. Tomchuk, Int. J. Electron. **70**, 485 (1991).

[5] F. Calvo, J. P. K. Doye, and D. J. Wales, J. Chem. Phys. **114**, 7312 (2001).

[6] V. I. Kruglov and M. J. Collet, Phys. Rev. Lett. **87**, 185302 (2001).

[7] A. Ya. Blank, L. V. Garanina, and L. G. Grechko, Fiz. Nizk. Temp. **25**, 1067 (1999) [Low Temp. Phys. **25**, 797 (1999)].

[8] Yu. N. Ovchinnikov, Zh. Éksp. Teor. Fiz. **121**, 1384 (2002) [JETP **121**, 1188 (2002)].

[9] A. G. Naumovets, Fiz. Nizk. Temp. **20**, 1091 (1994) [Low Temp. Phys. **20**, 857 (1994)].

[10] S. I. Kovalenko and N. N. Bagrov, Fiz. Tver. Tela (Leningrad) **11**, 2724 (1969) [Sov. Phys. Solid State **11**, 2207 (1969)].

[11] S. I. Kovalenko, E. I. Indan, and A. A. Khudotyoplaya, Phys. Status Solidi **20**, 629 (1973).

[12] V. G. Gryaznov, A. M. Kaprelov, and A. Yu. Belov, Philos. Mag. Lett. **63**, 275 (1991).

[13] V. I. Peresada, *New Computational Method in the Theory of Harmonic Oscillations of a Crystal Lattice*, Doctoral Dissertation in Physical and Mathematical Sciences, Institute for Low Temperature Physics and Engineering, Ukrainian SSR Academy of Sciences, Khar'kov (1972).

[14] V. I. Peresada, "New computational method in crystal lattice theory," in *Condensed State Physics*, Institute for Low Temperature Physics and Engineering, Ukrainian SSR Academy of Sciences, Khar'kov (1968), p. 172.

[15] V. I. Peresada, V. N. Afanas'ev, and V. S. Borovikov, Fiz. Nizk. Temp. **1**, 461 (1975) [Sov. J. Low Temp. Phys. **1**, 227 (1975)].

[16] R. Haydock, "The recursive solution of the Schrödinger equation," in *Solid State Physics*, edited by H. Ehrenreich, F. Seitz, and D. Turnbull, Academic Press, New York (1980), p. 215.

[17] V. V. Eremenko, S. I. Kovalenko, and D. D. Solnyshkin, Fiz. Nizk. Temp. **29**, 469 (2003) [Low Temp. Phys. **29**, 353 (2003)].

[18] S. I. Kovalenko, D. D. Solnyshkin, É. T. Verkhovtseva, and V. V. Eremenko, Fiz. Nizk. Temp. **20**, 961 (1994) [Low Temp. Phys. **20**, 758 (1994)].

[19] E. A. Katrunova, A. P. Voĭtenko, G. V. Dobrovol'skaya, V. I. Yaremenko, and É. T. Verkhovtseva, Prib. Tekh. Éksp., No. 3, 208 (1977).

[20] S. S. Gorelik, L. N. Rastorguev, and Yu. A. Skakov, *X-Ray Diffraction and Electron-Optical Analysis of Metals*, Metallurgiya, Moscow (1970).

[21] S. I. Kovalenko and N. N. Bagrov, in *Condensed State Physics*, Institute for Low Temperature Physics and Engineering, Ukrainian SSR Academy of Sciences, Khar'kov (1971), No. 11, p. 44.

[22] S. I. Kovalenko, D. D. Solnyshkin, E. A. Bondarenko, and É. T. Verkhovtseva, Fiz. Nizk. Temp. **23**, 190 (1997) [Low Temp. Phys. **23**, 140 (1997)].

[23] A. Guinier, *X-Ray Diffraction Analysis of Crystals* [Russian trans.], Fizmatgiz, Moscow (1961).

[24] H. Böttger, *Principles of the Theory of Lattice Dynamics*, Physik-Verlag, Weinheim (1983) [Russian trans.], Mir, Moscow (1986).

[25] A. M. Kosevich, *Crystal Lattice Theory (The Physical Mechanics of Crystals)*, Vishcha shkola, Khar'kov (1988).

[26] A. M. Kosevich, *The Crystal Lattice (Phonons, Solitons, Dislocations)*, WILEY-VCH Verlag Berlin GmbH, Berlin (1999).

[27] A. G. Prikhot'ko, V. G. Manzheliĭ, I. Ya. Fugol', Yu. B. Gaĭdideĭ, I. N. Krupskiĭ, V. M. Loktev, E. V. Savchenko, V. A. Slyusarev, M. A. Strzhemechnyĭ, Yu. A. Freĭman, and L. I. Shanskiĭ, *Cryocrystals*, Naukova dumka, Kiev (1983).

[28] Yu. A. Freiman and V. G. Manzhelii, *Physics of Cryocrystals*, Woodbury, New York (1998).

[29] S. B. Feodosyev, I. A. Gospodarev, M. A. Strzhemechny, and R. J. Hemley, Physica B **300**, 186 (2001).

[30] I. A. Gospodarev, A. V. Grishaev, E. S. Syrkin, and S. B. Feodos'ev, Fiz. Tver. Tela **42**, 2153 (2000) [Sov. Phys. Solid State **42**, 2217 (2000)].

[31] E. S. Syrkin and S. B. Feodos'ev, "Investigation of the temperature dependence of the rms displacements and rms velocities of ideal and impurity atoms in anisotropic crystals," in *Functional Analysis and Applied Mathematics*, Naukova dumka, Kiev (1983), p. 173.

[32] A. M. Kosevich, A. Mayer, S. B. Feodosyev, I. A. Gospodarev, V. I. Grishaev, and E. S. Syrkin, Superlatt. Microstruct. **27**, 7 (2000).

[33] S. I. Kovalenko, D. D. Solnyshkin, E. T. Verkhovtseva, O. G. Danylchenko, and V. V. Eremenko, in *CC'2002 Book of Abstracts*, Freising, Germany (2002).

[34] B. W. van de Waal, G. Torchet, and M. de Feraudy, Chem. Phys. Lett. **331**, 57 (2000).

Translated by M. E. Alferieff

Nonlinear Rayleigh waves in a medium with a monatomic nonlinear coating

A. S. Kovalev* and E. S. Sokolova

*B. Verkin Institute for Low Temperature Physics and Engineering, National Academy of Sciences
of Ukraine, pr. Lenina, 47, 61103 Khar'kov, Ukraine*

A. P. Mayer

Institut für Theoretische Physik, Universität Regensburg, D-93040, Regensburg, Germany

G. A. Maugin

Laboratoire de Modélisation en Mècanique, Université Pierre et Marie Curie, 75252, Paris, France
(Submitted March 3, 2003)

The nonlinear dynamics of surface acoustic waves at the surface of a linear elastic half-space coated with a monolayer of a nonlinear material is investigated. A one-dimensional nonlinear integrodifferential equation describing the dynamics of such a system is derived. The model proposed is used to study Rayleigh solitons with a stationary profile. The possible phenomenological generalizations of the equations derived and their exact soliton solutions are discussed. © *2003 American Institute of Physics.* [DOI: 10.1063/1.1542503]

The theory of nonlinear acoustic waves in one-dimensional atomic chains has been developed in detail.[1,2] The problem of nonlinear acoustic surface waves at the surface of an anharmonic half-space is much more complicated because it is two-dimensional.[3–12] However, this problem became especially topical immediately after a series of experiments were performed on the propagation of nonlinear surface waves[13,14] and high-intensity acoustic surface pulses.[15–17] Most experiments were performed on samples consisting of a substrate coated with a film of a different material. The presence of a film coating is very important because it results in the appearance of an additional strong dispersion of linear waves and the competition between this dispersion and the nonlinearity gives rise to stationary non-linear surface waves and surface solitons with a stationary profile. The analytic study of these nonlinear waves simplifies somewhat when the substrate can be treated in the linear approximation.[18] The two-dimensional problem for the substrate can be solved exactly. It is important to underscore that such a formulation of the problem (a linear half-space with a nonlinear coating) is fully realizable experimentally. For example, in Ref. 19 experimental data are presented for anharmonic surface phonon effects in systems with a metallic substrate coated with a monolayer of inert-gas atoms (Ar or Xe). A similar situation arises for an inert-gas monolayer on a graphite surface.

1. FORMULATION OF THE MODEL

We shall consider the propagation of a nonlinear surface acoustic wave in the X direction along the surface of the half-space $Z<0$ coated with a monatomic layer. (The displacements are independent of the coordinate Y and the problem is effectively two-dimensional.) We shall confine our attention to the particular case where the nonlinear interaction of the atoms in the surface monolayer with one another and with atoms of the substrate surface is central. Each atom of the monolayer interacts with its nearest neighbors in the direction of the X axis in the monolayer and with the nearest neighbor and next two neighboring atoms in the substrate surface (see Fig. 1). Keeping only the first nonlinear terms in the expression for the interaction of the atoms in the surface film with one another and with substrate atoms we obtain the following expression for the total energy of the monatomic coating:

$$E = \sum_n \frac{M}{2}\left[\left(\frac{dU_n}{dt}\right)^2 + \left(\frac{dV_n}{dt}\right)^2\right]$$

$$+ \sum_n \left\{\frac{\alpha}{2}\xi_{n,n+1}^2 - \frac{\beta}{3}\xi_{n,n+1}^3 + \frac{\gamma}{2}\eta_n^2 - \frac{\delta}{3}\eta_n^3\right.$$

$$\left.+ \frac{\lambda}{2}\zeta_{n,n+1}^2 - \frac{\mu}{3}\zeta_{n,n+1}^3 + \frac{\lambda}{2}\zeta_{n,n-1}^2 - \frac{\mu}{3}\zeta_{n,n-1}^3\right\}, \quad (1)$$

where U_n and V_n are the displacements of the nth atom in the monolayer in the X and Z directions;

$$\xi_{n,n+1} = \sqrt{(U_n - U_{n+1} - a)^2 + (V_n - V_{n+1})^2} - a = \tilde{\xi}_{n,n+1} - a$$

is the deviation of the interneighbor distances in the surface film from their values a in equilibrium; M is the mass of an atom in the monolayer;
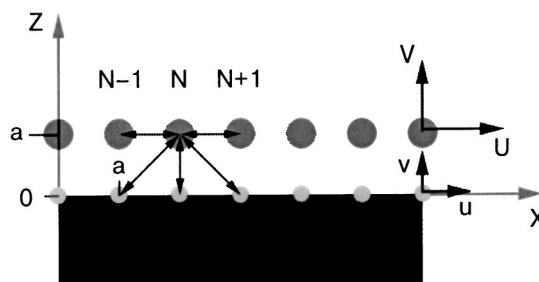

FIG. 1. Geometry of the problem.

$$\eta_n = \sqrt{(U_n - u_n)^2 + (V_n - v_n + a)^2} - a = \tilde{\eta}_n - a$$

and

$$\zeta_{n,n\pm1} = \sqrt{(U_n - u_{n\pm1}\mp a)^2 + (V_n - v_{n\pm1}+a)^2}$$
$$- a\sqrt{2} = \tilde{\zeta}_{n,n\pm1} - a\sqrt{2}$$

are the deviations from the equilibrium distances between atoms in the monolayer and neighboring atoms on the surface of the substrate (the nearest and next two neighboring atoms, respectively); u_n and v_n are the displacements of surface atoms in the substrate in the X and Z directions; α, β, γ, δ, λ, and μ are the linear and nonlinear elastic moduli. For simplicity, we assume that the interatomic distances equal a in all directions. As will be shown below, in the leading approximation the nonlinear interaction only between neighboring atoms in the covering monolayer is important.

The dynamical equations for the monolayer atoms are:

$$M\frac{d^2 U_n}{dt^2} + \left\{ \frac{\xi_{n,n+1}}{\tilde{\xi}_{n,n+1}}(U_n - U_{n+1} - a)(\alpha - \beta\xi_{n,n+1}) \right.$$
$$+ \left. \frac{\xi_{n,n-1}}{\tilde{\xi}_{n,n-1}}(U_n - U_{n-1}+a)(\alpha - \beta\xi_{n,n-1}) \right\}$$
$$+ \left\{ \frac{\zeta_{n,n+1}}{\tilde{\zeta}_{n,n+1}}(U_n - u_{n+1}-a)(\lambda - \mu\zeta_{n,n+1}) \right.$$
$$+ \left. \frac{\zeta_{n,n-1}}{\tilde{\zeta}_{n,n-1}}(U_n - u_{n-1}+a)(\lambda - \mu\xi_{n,n-1}) \right\}$$
$$+ \left\{ \frac{\eta_n}{\tilde{\eta}_n}(U_n - u_n)(\gamma - \delta\eta_n) \right\} = 0; \qquad (2)$$

$$M\frac{d^2 V_n}{dt^2} + \left\{ \frac{\xi_{n,n+1}}{\tilde{\xi}_{n,n+1}}(V_n - V_{n+1})(\alpha - \beta\xi_{n,n+1}) \right.$$
$$+ \left. \frac{\xi_{n,n-1}}{\tilde{\xi}_{n,n-1}}(V_n - V_{n-1})(\alpha - \beta\xi_{n,n-1}) \right\}$$
$$+ \left\{ \frac{\zeta_{n,n+1}}{\tilde{\zeta}_{n,n+1}}(V_n - v_{n+1}+a)(\lambda - \mu\zeta_{n,n+1}) \right.$$
$$+ \left. \frac{\zeta_{n,n-1}}{\tilde{\zeta}_{n,n-1}}(V_n - v_{n-1}+a)(\lambda - \mu\xi_{n,n-1}) \right\}$$
$$+ \left\{ \frac{\eta_n}{\tilde{\eta}_n}(V_n - v_n+a)(\gamma - \delta\eta_n) \right\} = 0. \qquad (3)$$

In what follows, we shall use the continuum approximation to describe the elastic properties of the substrate and the monolayer coating. However, we shall use a discrete description of the relative displacements of the atoms on the substrate surface and in the covering monolayer. (Although, as will be shown below, in the leading approximation these displacements are identical.) In the long-wavelength approximation we retain in the dynamical equations the linear terms with spatial derivatives up to fourth order and the leading

nonlinear terms which are quadratic in the displacements of the medium. In this approximation Eqs. (2) and (3) are

$$M U_{tt} - \alpha\left(U_{xx} + \frac{1}{12}U_{xxxx} \right) + 2\beta U_x U_{xx} - \alpha V_x V_{xx}$$

$$= \lambda(u - U) - \left(\gamma - \frac{\lambda}{2} + \sqrt{2}\mu \right)(u - U)(v - V)$$

$$+ \lambda\left(-v_x + \frac{1}{2}u_{xx} - \frac{1}{6}v_{xxx} + \frac{1}{24}u_{xxxx} \right)$$

$$+ \left(\frac{\lambda}{2} - \sqrt{2}\mu \right)u_x v_x + \left(\frac{3\lambda}{2} - \sqrt{2}\mu \right)(u - U)u_x$$

$$- \left(\frac{\lambda}{2} + \sqrt{2}\mu \right)(v - V)v_x - \frac{\mu}{\sqrt{2}}(u_x u_{xx} + v_x v_{xx}); \qquad (4)$$

$$M V_{tt} - \alpha(V_x U_{xx} + U_x V_{xx})$$

$$= (\lambda - \gamma)(v - V) + \left(\frac{\lambda}{4} - \frac{\gamma}{2} + \frac{\mu}{\sqrt{2}} \right)(u - U)^2$$

$$+ \left(\delta - \frac{3\lambda}{4} + \frac{\mu}{\sqrt{2}} \right)(v - V)^2 + \lambda\left(-u_x + \frac{1}{2}v_{xx} \right)$$

$$- \frac{1}{6}u_{xxx} + \frac{1}{24}v_{xxxx} \right) + \left(\frac{\lambda}{4} + \frac{\mu}{\sqrt{2}} \right)u_x^2$$

$$+ \left(-\frac{3\lambda}{4} + \frac{\mu}{\sqrt{2}} \right)v_x^2 - \left(\frac{\lambda}{2} + \sqrt{2}\mu \right)(v - V)u_x$$

$$- \left(\frac{\lambda}{2} + \sqrt{2}\mu \right)(u - U)v_x. \qquad (5)$$

The equations for the displacements of the atoms in the covering monolayer must be supplemented with dynamical equations for the displacements in the substrate volume. For simplicity we shall assume that the medium in the substrate half–space is linear and isotropic and the corresponding equations of motion are

$$\rho \mathbf{y}_{tt} \rho c_t^2 \Delta\mathbf{y} + \rho(c_l^2 - c_t^2) \ \text{grad} \ \text{div} \ \mathbf{y}, \qquad (6)$$

where $\mathbf{y} = (u,v)$ are the displacements in the sagittal plane of the substrate volume (the plane XZ); c_l and c_t are the longitudinal and transverse velocities in the substrate; and, ρ is the substrate density. The nonzero components of the stress tensor are

$$\sigma_{xz} = \rho(c_l^2 - 2c_t^2)u_x + \rho c_l^2 v_z, \qquad (7)$$

$$\sigma_{zz} = \rho c_t^2(u_z + v_x). \qquad (8)$$

The right-hand sides of Eqs. (4) and (5) are the forces which the substrate exerts on the monolayer. These forces can be found from the expressions (7) and (8). Thus, the system of equations (4)–(8) completely describes the problem posed.

2. DERIVATION OF THE EFFECTIVE ONE-DIMENSIONAL EQUATIONS FOR THE DYNAMICS OF RAYLEIGH WAVES WITH A STATIONARY PROFILE

It is convenient to represent the displacement vector **y** as a sum of transverse $\mathbf{y}_t$ and longitudinal $\mathbf{y}_l$ components, each of which for waves with a stationary profile $\mathbf{y} = \mathbf{y}(x - ct, z)$ satisfies a two-dimensional Laplace equation. The spatial derivatives of all components of $\mathbf{y}_t$ and $\mathbf{y}_l$ on the half-space surface (in the plane $Z = 0$) are coupled by the relation (see, for example, Ref. 20)

$$\left.\frac{\partial y}{\partial z}\right|_s = \sqrt{1 - \frac{c^2}{b^2}} \hat{H} \left.\frac{\partial y}{\partial x}\right|_s, \tag{9}$$

where $b = c_l$ and $b = c_t$ for longitudinal and transverse components, respectively, and $\hat{H}$ is the integral Hilbert transform operator (see Appendix, Part 1). Using the obvious relations between the displacement components $\partial u^t/\partial x = -\partial v^t/\partial z$ and $\partial u^l/\partial z = \partial v^l/\partial z$ all components of the deformation can be easily expressed in terms of u_x^l and v_x^t (see Appendix, Part 2). Using these relations in Eqs. (7) and (8) we rewrite Eqs. (4) and (5) in the form

$$M(1 - c_f^2/c^2)U_{xx} - \alpha(U_{xxxx}/12 + V_x V_{xx}) + 2\beta U_x U_{xx}$$
$$= 2\rho a^3 c_t^2 [(s^2 - 1)u^l + \kappa_t \hat{H}v^t]_x, \tag{10}$$

$$MV_{xx} - \alpha(U_x V_{xx} + U_{xx}V_x)$$
$$= \rho a^3 [(2c_t^2 - c^2)v^t + 2c_t^2 \kappa_l \hat{H}u^l]_x, \tag{11}$$

where u and v are displacements on the substrate surface (in what follows we assume that $a = 1$), $\mathrm{M} = Mc^2$, $\kappa_t = \sqrt{1 - c^2/c_t^2}$, $\kappa_l = \sqrt{1 - c^2/c_l^2}$, $s = c^2/2c_t^2$, and $c_f = \sqrt{\alpha/M}$ is the sound velocity in the monolayer. Integrating Eqs. (10) and (11) with respect to x we obtain the final expressions for the displacements u and v on the substrate surface in terms of the displacements of the atoms in the covering monolayer:

$$u = \frac{1}{\varepsilon} \left\{ A[V_x - c_f^2/c^2 U_x V_x] + B\hat{H} \left[U_x - \frac{\alpha/2 V_x^2 + \beta U_x^2}{M(1 - c_f^2/c^2)} \right] \right\}, \tag{12}$$

$$v = \frac{1}{\varepsilon} \left\{ C \left[U_x - \frac{\alpha/2 V_x^2 + \beta U_x^2}{M(1 - c_f^2/c^2)} \right] + D\hat{H} \left[V_x - \frac{c_f^2}{c^2 U_x V_x} \right] \right\}. \tag{13}$$

where

$$\varepsilon = (1 - s)^2 - \kappa_t \kappa_l, \tag{14}$$

$$A = -[(1 - s) - \kappa_t \kappa_l]s(M/\rho), \quad C = -A(1 - c_f^2/c^2),$$

$$D = s^2 \kappa_l (M/\rho), \quad B = s^2 \kappa_t (M/\rho)(1 - c_f^2/c^2).$$

It follows from Eq. (14) that

$$AC + BD = \varepsilon s^2 (M/\rho)^2 (1 - c_f^2/c^2)(\kappa_l \kappa_t - 1) \sim \varepsilon.$$

It is obvious from the definition of the parameter ε that ε is small if the deviation of the velocity of a surface wave from the velocity for a linear Rayleigh wave in a half-space with no film coating is small. The relation (14) gives an expression for the Rayleigh wave velocity $c = c_R$ in the limit $\varepsilon \to 0$. In what follows we shall study nonlinear surface waves with velocities close to the Rayleigh velocity, and to derive the effective dynamical equations we shall employ ε

as a small parameter. Using the relations (12) and (13) for $u = u(U, V)$ and $v = v(U, V)$ on the right-hand sides of Eqs. (4) and (5), we obtain the final closed equations for the functions $U(x - ct)$ and $V(x - ct)$.

We examine first linear Rayleigh waves in a half-space covered with a monolayer. In the long-wavelength limit, only the linear terms with the smallest derivative indices need be retained in Eqs. (4) and (5). Then Eqs. (4) and (5) yield

$$U \approx u - v_x, \quad V \approx v - \frac{\lambda}{\lambda + \gamma} u_x. \tag{15}$$

Substituting the relations (15) into the linearized expressions (12) and (13) we obtain the following closed system of linear equations for u and v:

$$\varepsilon u - B\hat{H}u_x = Av_x, \quad \varepsilon v - D\hat{H}v_x = Cu_x, \tag{16}$$

which can be rewritten in the form

$$\varepsilon u - (B + D)\hat{H}u_x - BDu_{xx}(1 - s)^2 = 0. \tag{17}$$

In the absence of a monolayer (with $M = A = B = C = D = 0$) the relation $\varepsilon = 0$ follows from Eq. (17) and the dispersion law for nondispersive Rayleigh waves of the form $u = u_0 \sin(kx - \omega t)$ with $\omega = ck$ and $c = c_R$ is obtained from Eq. (14). In the presence of a monolayer the additional terms in Eq. (17) engender dispersion for Rayleigh waves. In the leading approximation the dispersion relation now has the form

$$\omega \approx c_R k(1 - d\tilde{\beta}|k|), \tag{18}$$

where the parameter $\tilde{\beta} = (s^2/c_R^2)(\kappa_t^{-1} + \kappa_l^{-1})/(\kappa_t^{-2}c_t^{-2} + \kappa_l^{-2}c_l^{-2} - 2(1-s)^{-1}c_t^{-2})$ and has the same form as for a half-space with a thin but not monatomic film coating.[18] The influence of a monolayer is similar to that of a thin film with the effective thickness

$$d = \frac{M}{\rho} \left(1 - \frac{c_f^2}{c_R^2} \frac{\tilde{\kappa}_t}{\tilde{\kappa}_t + \tilde{\kappa}_l} \right), \tag{19}$$

where

$\tilde{\kappa}_t = \sqrt{1 - c_R^2/c_t^2}$ and $\tilde{\kappa}_l = \sqrt{1 - c_R^2/c_l^2}$ [i.e. $d \sim a(\rho_f/\rho)$].

It is well known that the properties of nonlinear waves and solitons in a specific dynamical system depend strongly on the dispersion properties of linear waves in it. In our case the dispersion of linear waves $D = \partial^2 \omega/\partial k^2$ remains finite in the long-wave limit $k \to 0$: $D \to -2c_R d\tilde{\beta}$, i.e. Rayleigh waves in a system with a film coating are strongly dispersive. Here the question of the character of the nonlinear terms in the dynamical equations becomes very important.

Let us now return to nonlinear surface waves in a half-space covered with a monolayer of a material with nonlinear properties. To obtain an effective one-dimensional dynamical equation for these waves we shall employ the smallness of the parameter ε and introduce the "slow" coordinate $r = \varepsilon(x - ct)$, where c is the velocity of the center of a soliton (close to the velocity of a linear Rayleigh wave in a half-space with no covering layer). Then, for the new variables $p = u_x$, $q = v_x$, $P = U_x$, and $Q = V_x$ the relations (12) and (13) in the leading approximation in the small parameter ε can be rewritten as

$$p = \frac{\partial}{\partial r}\left\{ AQ + B\hat{H}P - A\frac{c_f^2}{c^2}PQ - \frac{B}{2}\frac{1}{c^2/c_f^2 - 1} \right.$$

$$\left. \times \hat{H}\left(Q^2 - \frac{2\beta}{\alpha}P^2 \right) \right\}, \tag{20}$$

$$q = \frac{\partial}{\partial r}\left\{ CP + D\hat{H}Q - D\frac{c_f^2}{c^2}\hat{H}PQ - \frac{C}{2}\frac{1}{c^2/c_f^2 - 1} \right.$$

$$\left. \times \left(Q^2 - \frac{2\beta}{\alpha}P^2 \right) \right\}, \tag{21}$$

and in the same leading approximation in the small parameter ε from Eqs. (4), (5), and (15) follows

$$q = Q + O(\varepsilon), \quad p = P + O(\varepsilon), \tag{22}$$

and we can set $q = Q$ and $p = P$ in Eqs. (20) and (21) to obtain the final closed-form equations for the variables P and Q. Since it was shown previously that $BD + CA \sim O(\varepsilon)$, in the leading approximation in ε from Eqs. (20) and (21) follows a relation between the two components of the deformation in the monolayer P and Q:

$$Q = -(C/B)\hat{H}P. \tag{23}$$

Using the relation (23) we find the final equation for $P = P(r)$:

$$P - \eta\frac{\partial}{\partial r}\hat{H}P - \psi\frac{\partial}{\partial r}\hat{H}P^2 = 0, \tag{24}$$

where

$$\eta = (M/\rho)s^2[\tilde{\kappa}_t(1 - c_f^2/c_R^2) + \tilde{\kappa}_l].$$

$$\psi = (M/2\rho)(c_f^2 s^2/c_R^2)(2\beta/\alpha\tilde{\kappa}_t + \tilde{\kappa}_l).$$

In the initial variables this equation becomes

$$\varepsilon U - \eta\hat{H}U_x - \psi\hat{H}U_x^2 = 0. \tag{25}$$

The structure of Eq. (25) is similar to that of the equation obtained in Ref. 18 for an elastic half-space with an ideal boundary where the nonlinear properties decrease with distance away from the surface. Since the other component of the surface deformation $Q = \partial V/\partial x$ is ordinarily measured experimentally, we shall rewrite Eq. (24) in terms of this component:

$$Q - \eta\frac{\partial}{\partial r}\hat{H}Q - \psi\frac{B}{C}\frac{\partial}{\partial r}(\hat{H}Q)^2 = 0. \tag{26}$$

It is simple to take the next step in the approximating procedure in terms of the small parameter ε and find a correction of the order of ε to η. But it is important to point out that this does not change structure of Eqs. (2)–(26), and in this approximation additional nonlinear terms of a different type do not appear in the equations.

3. EQUATIONS FOR SLOWLY TIME-VARYING NONLINEAR RAYLEIGH WAVES

Thus far we have discussed only nonlinear surface waves with a stationary profile. Now we shall extend Eq. (24) to nonlinear Rayleigh waves with a slowly varying profile and we shall introduce an additional dependence of the

displacements on the "slow time" $\tau = \xi t$ ($\xi = (c - c_R)/c_R \ll 1$). in a coordinate system moving with the velocity $c = c_R$: $\mathbf{y} = \mathbf{y}(x - c_R t, z, \tau)$. The new parameter ξ is related with the previously introduced small parameter ε as $\xi = \varepsilon/[(2(1 - \tilde{s})/c_t^2 - \tilde{\kappa}_t/(\tilde{\kappa}_l c_l^2) - \tilde{\kappa}_l/(\kappa_l c_l^2))c_R^2]$ and $\tilde{s} = c_R^2/(2c_t^2)$. In the leading approximation in the small parameter ξ the Laplace equations for the transverse and longitudinal components of the displacements are replaced by the equations

$$(1 - c_R^2/b^2)\mathbf{y}_{xx} + \mathbf{y}_{zz} = -\xi(2c_R/b^2)\mathbf{y}_{xx}, \tag{27}$$

where, just as above, $b = c_l$ for $\mathbf{y} = \mathbf{y}_l$ and $b = c_t$ for $\mathbf{y} = \mathbf{y}_t$. From Eq. (27) follows a relation, which generalizes the expression (9), between the different components of the deformation on the surface:

$$\left.\frac{\partial y}{\partial z}\right|_s - \sqrt{1 - \frac{c_R^2}{b^2}}\,\hat{H}\left.\frac{\partial y}{\partial x}\right|_s \approx \xi\frac{c_R}{b\sqrt{b^2 - c_R^2}}\hat{H}\left.\frac{\partial y}{\partial \tau}\right|_s. \tag{28}$$

Using the relations $\partial u^t/\partial x = -\partial v^t/\partial z$ and $\partial u^l/\partial z = \partial v^l/\partial x$ and differentiating the boundary conditions (7) and (8) with respect to the coordinate x, all components of the deformation on the right-hand sides of Eqs. (7) and (8) can be expressed in terms of u_x^l and v_x^t (see Appendix, Part 3):

$$\frac{\partial}{\partial x}\sigma_{xz} = 2\rho\left[c_t^2(1 - \tilde{s})v_{xx}^t + c_t^2\tilde{\kappa}_l\hat{H}u_{xx}^l + \xi c_R \right.$$

$$\left. \times \left(\frac{c_t^2}{c_l^2\tilde{\kappa}_l}\hat{H}u_{x\tau}^l + v_{xz}^t \right) \right], \tag{29}$$

$$\frac{\partial}{\partial x}\sigma_{zz} = 2\rho\left[-c_t^2(1 - \tilde{s})u_{xx}^l + c_t^2\kappa_t\hat{H}v_{xx}^t + \xi c_R \right.$$

$$\left. \times \left(\frac{1}{\tilde{\kappa}_l}\hat{H}v_{x\tau}^t - u_{x\tau}^l \right) \right]. \tag{30}$$

Performing calculations similar to the preceding ones and using the relations (15) the components u_x^l and v_x^t of the displacements can be expressed in terms of the displacements of the atoms in the monolayer

$$v_x^t = c_t^2 c_l^2\tilde{\kappa}_l\tilde{\kappa}_t\theta[(-\tilde{\kappa}_l + \tilde{\kappa}_l^2\tilde{\kappa}_t)\hat{H}U_x + (1 - \tilde{\kappa}_l\tilde{\kappa}_t)V_x]$$

$$+ \xi c_R\theta\{-[(c_l^2 - c_t^2)\tilde{\kappa}_l + c_t^2\tilde{\kappa}_t]\hat{H}U_\tau + (c_l^2 + c_t^2)$$

$$- 2c_R^2)V_\tau\}, \tag{31}$$

$$u_x^l = c_t^2 c_l^2\tilde{\kappa}_l\tilde{\kappa}_t\theta[(\tilde{\kappa}_t - \tilde{\kappa}_l\tilde{\kappa}_t^2)\hat{H}V_x + (1 - \tilde{\kappa}_l\tilde{\kappa}_t)U_x]$$

$$+ \xi c_R\theta\{[(c_t^2 - c_R^2)\tilde{\kappa}_t + c_l^2\tilde{\kappa}_l]\hat{H}V_\tau + (c_l^2 + c_t^2)$$

$$- 2c_R^2)U_\tau\}, \tag{32}$$

where $1/\theta = \tilde{\kappa}_l\tilde{\kappa}_t c_t^2 c_l^2(1 - \tilde{\kappa}_l\tilde{\kappa})^2$. This makes it possible to obtain a closed system of equations which, after introducing the variable $\varphi = x\sqrt{\xi}$ and using the notations P and Q, become

$$\sqrt{\xi}[Mc_R^2 Q_{\varphi\varphi} - \alpha(PQ)_{\varphi\varphi} - \tilde{d}P_\tau - \tilde{e}\hat{H}Q_\tau]$$

$$= -\tilde{a}P_\varphi + \tilde{b}\hat{H}Q_\varphi, \tag{33}$$

$$\sqrt{\xi}\left[(Mc_R^2-\alpha)P_{\varphi\varphi}-\frac{\alpha}{2}(Q^2)_{\varphi\varphi}+\beta(P^2)_{\varphi\varphi}-\tilde{g}P_{\tau}\right.$$

$$\left.+\tilde{d}\tilde{H}Q_{\tau}\right]=\tilde{c}\hat{H}P_{\varphi}+\tilde{a}Q_{\varphi}, \tag{34}$$

where

$$\tilde{a}=(1-s-\tilde{\kappa}_l\tilde{\kappa}_t)2c_t^2\tilde{\theta}\rho, \quad \tilde{b}=c_R^2\tilde{\kappa}_t\tilde{\theta}\rho,$$

$$\tilde{c}=\tilde{b}\tilde{\kappa}_l/\tilde{\kappa}_t, \quad \tilde{d}=(\tilde{\kappa}_t-\tilde{\kappa}_l)^2c_l^2c_t^2\theta\rho c_R,$$

$$\tilde{e}=[(3c_R^2-2c_l^2)c_t^2\tilde{\kappa}_l+(2c_t^2-c_R^2)c_t^2\tilde{\kappa}_l^3]\theta\rho c_R,$$

$$\tilde{g}=[(3c_R^2-2c_l^2)c_t^2\tilde{\kappa}_t+(2c_t^2-c_R^2)c_l^2\tilde{\kappa}_l^3]\theta\rho c_R,$$

$$1/\tilde{\theta}=1-\kappa_l\kappa_t,$$

and $\tilde{a}^2-\tilde{c}\tilde{b}=0$. Using these relations we obtain a relation between the components of the deformations of the surface layer that is similar to the relation obtained above: $Q=-(\tilde{a}/\tilde{b})\hat{H}P$.

The final equation which extends Eq. (24) to the case of slowly evolving nonlinear waves, close to Rayleigh waves, is

$$P_{\tau}-\eta\frac{\partial^2}{\partial m^2}\hat{H}P-\psi\frac{\partial}{\partial m}\hat{H}(PP_m)=0, \tag{35}$$

where the parameters η and ψ were determined above, and $m=x[-\xi(2\tilde{a}\tilde{d}+\tilde{b}\tilde{g}+\tilde{c}\tilde{e})/(\tilde{\theta}\rho(2c_t^2)^2)]^{1/2}$. It is obvious from Eq. (35) that if the dependence on $(x-c_Rt,\tau)$ is sought in the stationary form $f(x-c_Rt,\tau)=f(x-c_Rt-c_R\tau)=f(x-ct)$, we arrive at Eq. (24).

The derivation of Eq. (35) is the main result of this paper.

4. SOLITON SOLUTIONS FOR NONLINEAR RAYLEIGH WAVES

In Sec. 3 we obtained an explicit form of the nonlinear terms in the one-dimensional evolutionary equations describing the dynamics of nonlinear Rayleigh waves in a halfspace with a monatomic coating [the last terms in Eqs. (24) and (35)]. According to Eq. (35), the nonlinearity which arises is very weak: it is quadratic in the field amplitude and contains the same number of spatial derivatives as the linear dispersion term in this equation. Ordinarily, localized soliton excitations arise in "nonlinear physics" as a result of competition between nonlinearity and dispersion of the waves. In the present case strong dispersion [the number of spatial derivatives in the dispersion term—the second term in Eq. (35)] cannot be compensated by nonlinearity. (The nonlinear term contains the same number of spatial derivatives.) Consequently, in the general case Eqs. (24) and (35) probably do not possess stationary soliton solutions because these equations possess such large gradients that their description on the basis of the long-wavelength approximation is unjustified. However, the situation can change when the parameter η in the leading dispersion term is anomalously small. This can happen for certain definite ratios of the parameters of the substrate half-space and the monolayer covering it: the inequality

$$s^2(M/\rho)(\kappa_l+\kappa_t(1-c_f^2/c^2))\ll 1 \tag{36}$$

must hold.

Since all parameters appearing in this relation are of the order of 1, the indicated inequality can in principle be satisfied. In this case, the leading dispersion term in the evolutionary equations, which is due to the presence of the adsorbed surface layer, becomes anomalously small and the additional weak dispersion arising in the next order of perturbation theory in the small parameter ε must be taken into account. Then the relations (22) must be written to a higher order of accuracy:

$$q=Q-\varepsilon\frac{\lambda}{\lambda+\gamma}P_r+O(\varepsilon^2), \quad p=P-\varepsilon Q_r+O(\varepsilon^2). \tag{37}$$

As a result, the relation (23) between the various components of the deformation becomes more complicated:

$$Q=-(C/B)\hat{H}P-\varepsilon LP_r+\varepsilon N\hat{H}(P\hat{H}P)_r,$$

$$L=-\lambda/(\lambda+\gamma)-(C+K) \quad B^2, \quad N=CKc_f^2/(B^2c_R^2),$$

$$K=(M/2\rho)^2(c_R/c_t)^4(1-c_f^2/c_R^2)(\tilde{\kappa}_t\tilde{\kappa}_l-1). \tag{38}$$

The equation (24) is modified and becomes

$$P-\tilde{\eta}\frac{\partial}{\partial r}\hat{H}P-\varepsilon LD\frac{B}{C}\frac{\partial^2}{\partial r^2}P-\psi\frac{\partial}{\partial r}\hat{H}P^2=0, \tag{39}$$

where $\tilde{\eta}=\eta-\varepsilon(C+K)/B$. A similar equation has been discussed in Ref. 18, but the derivation of the equation using a certain asymptotic procedure required a definite ratio between the small parameters in the expansion (actually, the wave amplitude) and the thickness of the film covering the surface of the crystal. In the model proposed the derivation of the dynamical equations is free of this drawback and is exact at the theoretical-physics level.

Let us now reexamine a weakly dispersive system when the parameter $\tilde{\eta}$ in Eq. (39) is anomalously small and can be dropped. Then Eq. (39) in dimensionless form becomes

$$W-W_{\zeta\zeta}-\hat{H}(W^2)_{\zeta}=0, \tag{40}$$

where $W=P\sqrt{C\psi/LDB}\ \sqrt{\varepsilon}$ and $\zeta=\sqrt{\varepsilon}\sqrt{CLDB}(x-ct)$. In this equation the nonlinear and dispersion terms can no longer compensate one another and Rayleigh solitons with a stationary profile can exist. Unfortunately, such solutions could not be found in analytic form. However, the form of Eq. (40) reveals some unusual properties of these solitons. Integrating Eq. (40) with respect to ζ over infinite limits and assuming zero deformation at infinity, we find that the total longitudinal deformation in a Rayleigh soliton should be zero:

$$\int_{-\infty}^{+\infty}dxP(x)=0,$$

and therefore the profile of the soliton should be signchanging. Indeed, the numerical solution which we obtained for Eq. (40) for this soliton looks like a "Mexican sombrero" (see Fig. 2). It should be noted that actually the numerical calculation was performed for a nonlinear periodic Rayleigh wave consisting of a train of Rayleigh solitons. However, as the period l of this wave increased, the wave indeed transformed into a periodic structure of strongly localized solitons spread over a large distance. Figure 2 shows the solution of
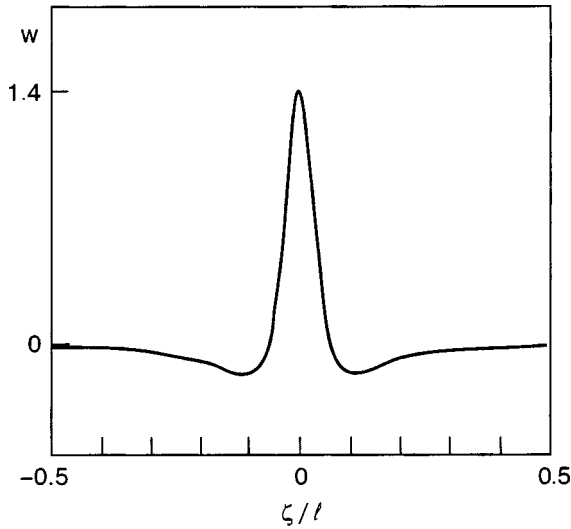
FIG. 2. Numerical solution of Eq. (40) for one period of the profile of a nonlinear Rayleigh wave with wavelength $l \approx 16$.

Eq. (40) for a nonlinear Rayleigh wave with wavelength $l = 2\pi\sqrt{0.15} \approx 16$. The width Δ of an individual soliton (the distance between the minima of the soliton profile) was approximately one tenth the period of the wave.

The possible phenomenological generalizations of Eq. (39) admitting analytic solutions for Rayleigh solitons are discussed in the Appendix (Part 4).

5. APPENDIX

1. The Hilbert transform is defined as

$$\hat{H}f(x) = \frac{1}{\pi}\int_{-\infty}^{\infty}\frac{dx}{x'-x}f(x') \tag{A1}$$

and possesses the following properties which we used in this paper:

$$\hat{H}\hat{H}f(x) = -f(x), \tag{A2}$$

$$\hat{H}(fg) = f\hat{H}g + g\hat{H}f + \hat{H}((\hat{H}f)(\hat{H}g)). \tag{A3}$$

2. The relation between the various components of the deformation on the surface of a linear isotropic half-space are:

$$u_x^t = -\kappa_t \hat{H}v_x^t, \quad u_z^l = -\kappa_l \hat{H}u_x^l, \quad u_2^t = \kappa_t^2 v_x^t,$$

$$v_x^l = \kappa_l \hat{H}u_x^l, \quad v_z^l = -\kappa_l^2 u_x^l, \quad v_z^t = \kappa_t \hat{H}v_x^t. \tag{A4}$$

3. The relations between the deformation components for slowly varying waves are:

$$u_x^t = -\tilde{\kappa}_t \hat{H}v_x^t - \xi\frac{c_R}{c_t^2\tilde{\kappa}_t}\hat{H}v_\tau^t,$$

$$u_z^l = \tilde{\kappa}_l \hat{H}u_x^l + \xi\frac{c_R}{c_l^2\tilde{\kappa}_l}\hat{H}u_\tau^l,$$

$$u_z^t = \tilde{\kappa}_t^2 v_x^t + 2\xi\frac{c_R}{c_t^2}v_\tau^t,$$

$$v_x^l = \tilde{\kappa}_l \hat{H}u_x^l + \xi\frac{c_R}{c_l^2\tilde{\kappa}}\hat{H}u_\tau^l, \quad v_z^l = -\tilde{\kappa}_l^2 u_x^l - 2\xi\frac{c_R}{c_l^2}u_\tau^l,$$

$$v_z^t = \tilde{\kappa}_l \hat{H}v_x^t + \xi\frac{c_R}{c_t^2\tilde{\kappa}_t}\hat{H}v_\tau^t. \tag{A5}$$

4. We now return to Eq. (24), which we derived rigorously in the leading approximation in the small parameter ε, and rewrite it in the dimensionless form

$$F - \hat{H}F_\chi - \hat{H}(FF_\chi) = 0, \tag{A6}$$

introducing the new field variable $F = 2\psi P/\eta$ and the coordinate $\chi = r/\eta$. It is now possible to consider generalizations of this equation. The linear dispersion term is the only possible combination that is linear in the field variable and contains one spatial derivative and one Hilbert transform. However, the independent nonlinear terms quadratic in the field variable and containing one Hilbert transform and one spatial derivative could be, in principle, of three types. Using the relations (A2) and (A3) it is easy to show that the independent combinations are $\hat{H}(FF_\chi)$, $F\hat{H}F_\chi$, and $F_\chi\hat{H}F$. Consequently, as a phenomenological equation extending Eq. (A6) we suggest an equation that contains all three possible types of nonlocal nonlinear terms, since such an analysis yields interesting mathematical results. We hope that such equations can also arise in other physical formulations of the problem. The generalized phenomenological equation will have the form

$$F - \hat{H}F_\chi - \alpha_1 F_\chi\hat{H}F - \alpha_2 F\hat{H}F_\chi - \alpha_3\hat{H}(FF_\chi) = 0, \tag{A7}$$

where α_i are arbitrary constants. This equation looks much more complicated than Eq. (A6), but for certain definite ratios of the parameters α_i it admits exact analytical solutions for surface solitons.

We consider first the case $\alpha_3 = 0$ and $\alpha_1 = -\alpha_2$. (Renormalizing the amplitude of the solution we can set $\alpha_1 = -\alpha_2 = 1$.) The equation obtained

$$F - \hat{H}F_\chi - F_\chi\hat{H}F + F\hat{H}F_\chi = 0 \tag{A8}$$

possesses the exact soliton solution

$$F = \frac{2}{1+\chi^2}, \tag{A9}$$

which has the same form as the well-known solution of the Benjamin–Ono equation for nonlinear waves on the surface of an infinitely deep liquid.[21] We note that in this solution, in contrast to the solution presented in Fig. 2, the deformation is everywhere positive and the total deformation in the crystal is different from zero. It is also easy to find an extension of the solution (A9) for a periodic train of solitons:

$$F = \frac{1-b^2}{1-b\cos(\chi/\tilde{l})}, \tag{A10}$$

where $\tilde{l} = b^2/\sqrt{1-b^2}$ and $b \leqslant 1$.

A more interesting case is $\alpha_1 = \alpha_2 = -\alpha_3/2$. Here there arises the equation

$$F - \hat{H}F_\chi - F_\chi\hat{H}F - F\hat{H}F_\chi + 2\hat{H}(FF_\chi) = 0, \tag{A11}$$

which also possesses exact soliton solutions; the set of such solutions is infinite. The first and simplest soliton solution of Eq. (A11) is
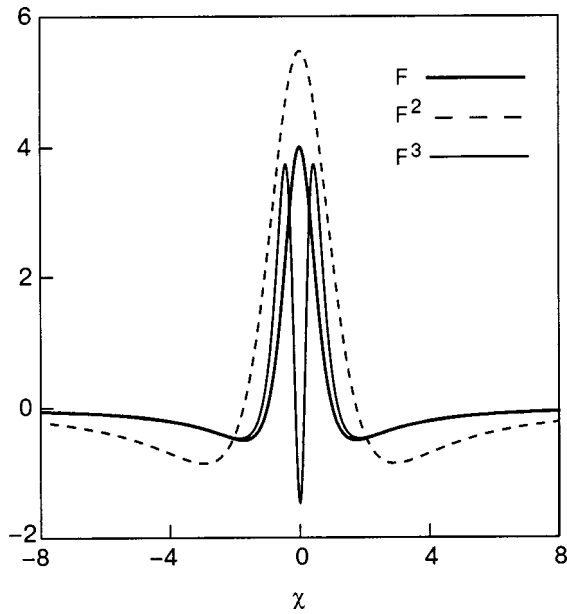
FIG. 3. Profiles of the soliton solutions of Eq. (A12) (F) and Eq. (A13) ($F^{(2)}$ and $F^{(3)}$).

$$F = \frac{8}{(1+\chi^2)^2} - \frac{4}{1+\chi^2}. \tag{A12}$$

This solution has qualitatively the same form as the solution of Eq. (40) derived above and shown in Fig. 2. The total deformation corresponding to this solution likewise is strictly equal to zero. However, in this case the soliton profile is not as narrow as the profile of the solution of Eq. (40).

The most interesting circumstance is the existence of other more complicated solutions of Eq. (A11) for surface Rayleigh solitons. For example, the solutions of Eq. (A11) which are next in terms of the complexity are

$$F^{(2,3)} = \lambda_1^{(1,2)}\left\{\frac{2\beta^{(1,2)2}}{(\chi^2+\beta^{(1,2)2})^2} - \frac{1}{\chi^2+\beta^{(1,2)2}}\right\}$$
$$+ \lambda_2^{(12)}\left\{\frac{8\beta^{(1,2)3}}{(\chi^2+\beta^{(1,2)2})^3} - \frac{6\beta^{(1,2)}}{(\chi^2+\beta^{(1,2)2})^2}\right\} \tag{A13}$$

with $\lambda_1^{(1)} = 3(3+\sqrt{3})$, $\lambda_2^{(1)} = 3(3+2\sqrt{3})$, and $\beta^{(1)} = (3+\sqrt{3})/2$ for the solution $F^{(2)}$ and $\lambda_1^{(2)} = 3(3-\sqrt{3})$, $\lambda_2^{(2)} = 3(3-2\sqrt{3})$, and $\beta^{(2)} = (3-\sqrt{3})/2$ for the solution $F^{(3)}$. The profile of the solution $F^{(2)}$ is similar to that of the solution (A12), whereas the profile of the solution $F^{(3)}$ has two

large maxima and three minima. The profiles of the solutions for F, $F^{(2)}$, and $F^{(3)}$ are presented in Fig. 3.

More complicated soliton solutions can be written in the unified form

$$F^{(N)}(\chi) = \sum_{n=1}^{N} \lambda_n^{(N)}\left(-\hat{H}\frac{d}{d\chi}\right)^n \frac{\beta^{(N)}}{\chi^2+\beta^{(N)2}}, \tag{A14}$$

where the parameters $\lambda_n^{(N)}$ and $\beta^{(N)}$ for each N are found as solutions of a system of algebraic equations. Of course, for large N the solutions can be found only numerically, but with arbitrary accuracy. The solutions of Eq. (A11) are exact to this accuracy. The evolutionary analog of Eq. (A11) with a spatiotemporal derivative replacing the first term and with additional differentiation of all other terms with respect to the coordinate could be exactly integrable.

*E-mail: kovalev@ilt.kharkov.ua

[1] A. D. Navaco, Phys. Rev. B **19**, 6493 (1979); **46**, 8178 (1992).

[2] T. M. Hakim, M. F. Bertino, F. Hofmann, J. P. Toennies, and Ch. Woll, J. Chem. Phys. **106**, 6194 (1997); **107**, 4445 (1997).

[3] D. F. Parker and F. M. Talbot, J. Elast. **15**, 389 (1985).

[4] M. F. Hamilton, Yu. A. Il'insky, and E. A. Zabolotskaya, J. Acoust. Soc. Am. **93**, 3089 (1993).

[5] D. Bonart, A. P. Mayer, and V. G. Mozhaev, Il Vuoto, Scienza e Tecnologia **3/96**, 21 (1996).

[6] J. K. Hunter, Contemp. Math. **100**, 185 (1989).

[7] V. G. Mozhaev, Phys. Lett. A **139**, 333 (1989).

[8] H. Hadouaj and G. A. Maugin, C. R. Acad. Sci. Paris **2−309**, 1877 (1989); J. Phys. (Paris), Suppl., **51**, C2-57 (1989); Wave Motion **16**, 115 (1992).

[9] A. S. Kovalev and E. S. Syrkin, Surf. Sci. **346**, 337 (1996).

[10] A. S. Kovalev, E. S. Syrkin, and G. A. Maugin, Fiz. Nizk. Temp. **28**, 635 (2002) [Low Temp. Phys. **28**, 452 (2002)].

[11] C. Eckl, A. P. Mayer, and A. S. Kovalev, Phys. Rev. Lett. **81**, 983 (1998).

[12] V. E. Gusev, W. Lauiks, and J. Thoen, Phys. Rev. B **55**, 9344 (1997).

[13] V. I. Nayanov, JETP Lett. **44**, 314 (1986).

[14] V. Kavalerov, T. Fujii, and M. Inoue, J. Appl. Phys. **87**, 907 (2000).

[15] Al. A. Kolomenskii, A. M. Lomonosov, R. Kischnereit, P. Hess, and V. E. Gusev, Phys. Rev. Lett. **79**, 1325 (1997).

[16] A. M. Lomonosov and P. Hess, Phys. Rev. Lett. **83**, 3876 (1999).

[17] A. M. Lomonosov, P. Hess, and A. P. Mayer, Phys. Rev. Lett. **88**, 076104 (2002).

[18] A. S. Kovalev, A. P. Mayer, C. Eckl, and G. A. Maugin, Phys. Rev. E **66**, 036615 (2002).

[19] L. W. Bruch and A. D. Novaco, Phys. Rev. B **61**, 5786 (2000).

[20] H. D. Greenberg, *Application of Green's Functions in Science and Engineering*, New Jersey (1971).

[21] H. Ono, J. Phys. Soc. Jpn. **39**, 1082 (1975).

Translated by M. E. Alferieff

PHYSICAL PROPERTIES OF CRYOCRYSTALS

Local excitations in the conduction band of crystalline xenon

A. G. Belov, E. I. Tarasova,* and E. M. Yurtaeva

B. Verkin Institute for Low Temperature Physics and Engineering, pr. Lenina, 47, 61103 Khar'kov, Ukraine
(Submitted March 17, 2003)

A detailed experimental investigation of the basic characteristics of the radiation of crystalline xenon with $E_{max} = 2$ eV (*A* band) is performed as a function of temperature, impurity concentration, lattice perfection, and irradiation dose. The radiation parameters of this band are compared with the same parameters of the radiation of free excitons, localized holes $Xe_2^+ *$, and impurity centers Xe_2O^*, whose bands were recorded in parallel. The photoexcitation spectra of the *A* band and the time decay curves of luminescence are analyzed. Radiation with similar structure with $E_{max} = 2.05$ eV is also found in the binary crystals Ar + Xe with high ($\sim 10\%$) xenon concentrations. It is concluded that the observed radiation is due to intrinsic molecular-type excited states of localized in the interior volume of the crystal and lyingnear 10 eV in the conduction band. © *2003 American Institute of Physics.*
[DOI: 10.1063/1.1542504]

1. INTRODUCTION

Irradiation of a dielectric crystal by light or high-energy particles can result in the excitation of excitons and free electron–hole pairs, depending on the energy and spectral width of the exciting beam. The energy transfer and relaxation processes occurring in the conduction band of a crystal and in other high-energy states need to be investigated in order to construct the complete scheme of channels for the distribution of the initial excitation energy over the radiating states—both intrinsic and impurity. The problem is more complicated for crystals of inert elements because free and self-localized excitations coexist with one another, and the effect is observed for excitons and holes. A complicated pattern of branching of the relaxation of the excitation energy over states of free, self-localized, and surface excitations and excitations localized on defects arises. The band gap E_g in crystals of inert elements exceeds 9 eV, and the lowest relaxation step are excitonic states with radiation energy $E > 7$ eV, which determine the entire quantum yield of luminescence of crystals in the VUV region of the spectrum. The radiative transitions from the lowest free and localized excitonic states and the dependence of their characteristics on the excitation energy, temperature, and defect density of the crystal served as a basis for many experimental investigations of the dynamics and localization of excitons and energy transfer.[1–3] Special attention is devoted to xenon crystals, which offer the best conditions for stability and radiation of free excitons.

As a result of the strong resonance coupling in the valence *p* states, the hole and excitonic bands in Xe are wider than in the crystals of other inert elements. Exciton and hole self-localization occurs only in two-center (quasimolecular) states, which have a large depth ($D_e \sim 0.5$ eV) because of this resonance coupling. In the last few years a theory of mixing of free-exciton states with the vibrational states of a molecular self-localized exciton in the region of overlapping of the excitonic band and local states as a result of the strong exciton–phonon coupling[4,5] has been developed, and new stability[6] and self-localization[7] criteria have been proposed for the lowest free $\Gamma(3/2)$ excitons. However, the more the properties of the lowest excitons were studied, the more obvious it became that their radiation is affected by the dynamics of higher-energy excitations and the properties of the energy relaxation processes from the moment of excitation in the range of higher-energy excitons or the continuum of unbound electron–hole pairs to the lowest radiating states. Consequently, the focus has now shifted to radiation from higher-energy excitation states. The most interesting question is how important the problem of the coexistence of free and self–localized excitations is for them. The possibility of hole self-localization can be regarded as proven, but neither the fraction of the band quasiparticles capable of reaching the bottom of the hole band nor their contribution to energy transfer and relaxation processes is known. For excitons with energies above E_g only one characteristic is known thus far—their contribution to the absorption spectrum. In Xe the problem complicated by the fact that such excitations include all singlet excitons in the $\Gamma(1/2)$ series (including also the lowest state $n = 1$ with a large oscillator strength). The main question in this situation is how stable these excitonic states are with respect to decay into free electrons and holes and whether or not their self-localization or localization on defects is, in principle, possible if the corresponding local states lie above E_g.

Investigations of the photoexcitation spectra of free excitons at energies above E_g have shown[8,9] that the initial excitations decay into free electrons and holes in a time much shorter than the electron relaxation time in the band with excitation E_v at high energies ($E_v - E_g \sim 1$ eV). Subsequently, the hole self-localizes in a quite short time, and the

much lighter electron thermalizes in a time almost an order of magnitude longer. The recombination process is much more efficient for low electron kinetic energies and occurs primarily near the bottom of the conduction band. The effect is observed as a long-lived component in the photoexcitation spectra and as a time shift of the radiation peak of a free exciton relative to the peak of the exciting photopulse.

Data showing that the contribution of the recombination channel to the formation of two-center local excitations[10] and free excitons[8] depends strongly on the density of defects and impurities, which initially play the role of traps for holes and electrons and after recombination for free excitons, have also appeared.

An important recent achievement is the investigation of the visible radiation of local excited hole centers.[10–12] It has been shown that radiative centers corresponding to a quite shallow (as is known from the gas phase) potential of a two-center ion in the excited state Xe_2^+*, appearing when a singlet hole with orbital angular momentum $J=1/2$ becomes localized, arise in a crystal. Here there are two surprises. First, this shallow molecular potential is somehow capable of becoming a stable state in a crystal, which on the basis of energy considerations should lie in the corresponding hole band (see, for example, Ref. 2). Second, if the state still lies above the bottom of its own band, then there arises the question of whether or not the excitation is stable with respect to relaxation into a lower-lying triplet ($J=3/2$) hole band, since the singlet band essentially overlaps with the latter. However, the radiation of such centers is still observed, and there are grounds for believing that the similar effects can also be observed for neutral local excitations which lie in the range of band states.

Investigations of the visible radiation from crystals of inert elements pursue two important goals. The first (and trivial) one reduces to identifying impurity radiation in order to monitor the presence of impurities and the effect of impurities on the filling of the intrinsic radiating states of a crystal. The second one is to search for possible relatively stable intrinsic excited states which lie at higher energies and can radiate in accordance with transitions between excited states. Such investigations could yield direct information about relaxation processes in the range of higher-energy excitations.

The radiation bands of the lowest-lying ($n=1$) $\Gamma(3/2)$ free exciton (FE) with energy $E_{FE}=8.36$ eV in xenon and the quasimolecular band (M) Xe_2^* $E_M\approx7.2$ eV have been investigated in detail in many works[1–3] The range of states that corresponds to higher-energy excitations is conventionally identified with fast nonradiative relaxation processes, since no VUV radiation has been observed from states above $n=1$ $\Gamma(3/2)$. This supposition seemed especially valid for xenon, where the width B of exciton bands $n=1, 2, 3, \dots$ (~1 eV), which overlap with one another and with the states of free electron–hole pairs right up to the center of the conduction band ($E_g=9.30$ eV in Xe[13]), is greater than in crystals of other inert elements.

Nonetheless, even the first investigations of the visible luminescence of xenon crystals revealed two intrinsic radiation bands with peaks E_{max} near 4.0 and 2.0 eV and with half-widths $\Delta\approx1.3$ and 0.08 eV, respectively.[14–16] It was suggested that quite long-lived radiative centers exist in the

conduction band above E_g, in the range where the band states overlap. Synchrotron photoexcitation of more perfect xenon crystals revealed bands with $E_{max}=4.29$, 4.44, and 2.16 eV and $\Delta=0.25$, 0.09, and 0.3 eV, identified as intrinsic radiation of crystalline xenon.[17] A luminescence band with $E_{max}\approx2.15$ eV and $\Delta=0.27$ eV has been investigated in xenon crystals grown by condensation of a gas from an electric discharge.[13,14]

Suggestions have now been made about the nature of some of the radiation bands mentioned above. In Refs. 14 and 15 the band with $E_{max}\approx4.0$ eV is attributed to a radiative transition from high-energy molecular states Xe_2^{**} to the dissociative terms $^{1,3}\Pi_u$ and $^{1,3}\Sigma_g^+$, associated with the lowest excited states $Xe*6s[3/2]_{1,2}$. In Ref. 17 the bands with $E_{max}=4.29$, 4.44, and 2.16 eV were initially identified as recombination radiation, i.e. the excess energy released as a result of the recombination of localized holes and electrons accompanying a transition into the ground state of the crystal. However, it was shown subsequently that the band with $E_{max}\approx2.15$ eV is associated with the radiation of excited localized ionic centers Xe_2^+* and is due to a radiative transition from the excited ionic state Xe_2^+* $2(1/2)_g$ (the depth of the potential in the gas phase is $D_e=0.03$ eV) into the ground state Xe_2^+ $1(1/2)_u$. The position of the maximum of this band varies within 0.07 eV, depending on the excitation energy. Thus, the discrepancy $\delta E_{max}=0.01$ eV in Refs. 17 and 12 is not fundamentally important for identifying the band. Raising the temperature of the crystal above 30 K deactivated the Xe_2^+ centers as a result of recombination processes with electrons freed from crystalline traps.[12]

The interpretation of the band with $E_{max}=2$ eV (A band) presented the greatest difficulty. Initially, the A band of xenon was attributed, on the basis of its high sensitivity to the presence of impurities in the crystal and the perfection of the lattice structure, to a transition from a free X-type $n=1$ excitonic state near 11 eV into a Γ-type $n=1$ excitonic state near 9 eV at the X point of the Brillouin zone.[14,15]

The A band has also been observed with photoexcitation of xenon by synchrotron radiation,[17,18] but the authors of the work did not give any explanation or alternative interpretation of the origin of this band. We note that under synchrotron excitation this band was weak and it was only weakly distinguished against the background of a neighboring, wider band with $E_{max}=2.16$ eV. The A band hs not observed at all with laser photoexcitation of frozen ionic centers Xe_2^+.[11,12]

The first attempts to measure the excitation spectra using a synchrotron source of VUV radiation were made to determine the origin of the A band.[16] However, the inadequate spectral resolution and the strong overlapping of this band with neighboring bands made it impossible to draw definite conclusions about its origin. The photoexcitation spectrum of the xenon band with $E_{max}=2$ eV was obtained in Ref. 18 with better spectral resolution. Aside from the high-energy part, above the conduction band bottom E_g a substantial component in the $n=1$ $\Gamma(3/2)$ exciton range, i.e. 1 eV below E_g, was also observed in the spectrum. The existence of this section cast doubt on the correctness of the initial identification of the A band ($E_{max}=2.0$ eV) with a transition from high-energy free excitons with energy ~11 eV.

In summary, the existing information is clearly inad-

equate for determining the origin of radiation with E_{max} =2.0 eV. We decided to use a combined approach and undertake a series of additional multifaceted and systematic investigations which would help to establish the nature of the *A* band in xenon radiation. First and foremost, it was necessary to rule out the simplest assumption logically following from the fact that this band is excited by low-lying excitons—trapping of an exciton by an impurity and radiation from a low-lying impurity state. To this end the initial xenon gas was additionally purified. Next, the question was posed as to whether the *A* band is due to radiation from surface or volume states and whether the emitting states are free or local excitations. In solving this problem the dependence of the radiation intensity on the quality of the crystal structure, the irradiation dose, and the temperature of the crystal was decisive. The radiation of Xe as an impurity in the matrix of another inert gas was also investigated, since the intensity of free excitons is extremely sensitive to the introduction of an impurity. The next important question is to determine if the radiating state is associated with charged or neutral states. Consequently, in this work a comparative analysis was made of the behavior of the radiation band with E_{max}=2.0 eV and the luminescence of self-localized holes $Xe_2^+{}^*$(E_{max}=2.15 eV) as a function of the parameters enumerated above. In addition, we obtained the first time decay spectra of the luminescence of the *A* band for three substantially different energies of the excitation pulse. Combined with the analysis of previously obtained photoexcitation spectra these investigations made it possible to attribute radiation with E_{max}=2.0 eV to an intrinsic, neutral, localized, molecular-type volume state formed inside the lowest conduction band of the xenon crystal.

2. EXPERIMENTAL PROCEDURE

The luminescence of pure Xe crystals and Ar crystals with xenon as an impurity was investigated by using monochromatic electrons with energy $E_e \approx 2$ keV to excite the samples. The current density j was 0.04 mA/cm^2. The electron flux was directed along the normal to the surface of the sample.

The initial, nominally pure, xenon gas contained residual impurities with concentration $C_i \sim 10^{-3}\%$, as stated on the supplier's data sheet. After prepurification in a special apparatus, using liquid lithium at $T=200\,^\circ$C, the purity of the initial gas was improved by more than an order of magnitude to $C_i < 10^{-4}\%$. Nominally pure xenon gas with impurity concentration $C_i \sim 10^{-3}\%$ and the additionally purified Xe were used in the experiments. A continuous-flow helium cryostat with substrate temperature regulatable from 2.5 to 78 K was used for growing and performing optical investigations on the crystals. The crystals were grown by deposition from the gas phase at condensation temperatures $T_c = 5$, 35, or 80 K, followed by slow cooling to lower temperatures. The polycrystals obtained were $\sim 1\,\mu$m thick and were optically completely transparent. The highest-quality crystals were obtained by condensation of prepurified gas on a substrate at $T=80$ K. Crystal quality was checked according to the intensity and shape of the free $\Gamma(3/2)$ exciton luminescence band. Argon crystals with xenon impurity concentration $C_{Xe}=1\%$ and 10% were grown at 30 K. The working

vacuum in the cryostat was maintained at 10^{-10} bar. Radiation at angles $\pm 45°$ was detected simultaneously in the visible and VUV regions of the spectrum using DFS–24 and VMR–2 spectral instruments. The spectral resolution was 0.015 and 0.05 nm for the visible and VUV regions, respectively. The procedure used for the luminescence investigations is described in greater detail in Ref. 19.

The photoexcitation of Xe crystals in the S–60 synchrotron was performed under the following experimental conditions. Xenon polycrystals were grown at 65 K and irradiated at the same temperature. The spectrum of the exciting synchrotron radiation was scanned from 25 to 5 eV with 0.5 eV resolution. The time interval between the peaks of the light pulses was 49 ns, and the half-width of a pulse was 8 ns. The experimental spectral interval of luminescence was extracted using the following interference light filters: IF–625 (E_{max} =2 eV), IF–550 (E_{max}=2.25 eV), and IF–500 (E_{max} =2.5 eV). The working transmission range of the light filters was 0.05 eV. The setup used for the optical investigations in the S–60 synchrotron is described in greater detail in Ref. 20.

3. EXPERIMENTAL RESULTS

A. Luminescence of Xe crystals

The visible-range luminescence of xenon crystals grown from purified gas consists of two partially overlapping bands *A* and *B* with maxima E_{max}=2.0 and 2.15 eV and half-widths $\Delta = 0.055$ and 0.26 eV, respectively. The *A* and *B* bands lie adjacent to one another but because they have different widths their contours are well separated, which makes it possible to reproduce their spectral distribution in the region of overlapping. The *B*-band maximum lies within 0.01 eV of the maximum of the radiation band of Xe_2^+ in a crystal matrix $2(1/2)_g \rightarrow 1(1/2)_u$ (E_{max}=2.147 eV), which was obtained in Ref. 1 by excitation with $E_\nu=3.72$ eV photons. The intensities, the positions of the maxima, and the half-widths of the *A* and *B* bands exhibit different behavior as functions of the crystal structure, impurity concentration, temperature, and irradiation duration.

Sensitivity of the spectrum to the impurity concentration. Figure 1 shows the radiation spectrum of xenon crystals for different degrees of purification of the initial gas. The quite well-known band near 1.7 eV, which belongs to the excimeric compounds XeO* and Xe_2O^* in an Xe matrix (see, for example, Ref. 21), can serve as a spectral indicator of the presence of impurities. The band near 1.7 eV is completely absent in the radiation of the purified samples. The *A* band was not observed in samples grown from unpurified gas. In the radiation spectra of the most perfect crystals obtained from purified xenon, the *A* band is much stronger than the *B* band. In the intermediate case, where the initial gas was not purified adequately, the *A* band is weak and is observed as a small peak on the low-energy shoulder of the *B* band.

Two parameters were used to monitor the *effect of defects in the crystal on the luminescence spectrum*: the growth temperature T_c of the crystal and the electron irradiation duration t_i. The first parameter determines the damage (stacking faults) produced in the crystal lattice during growth. As the condensation temperature decreases, the single-crystal
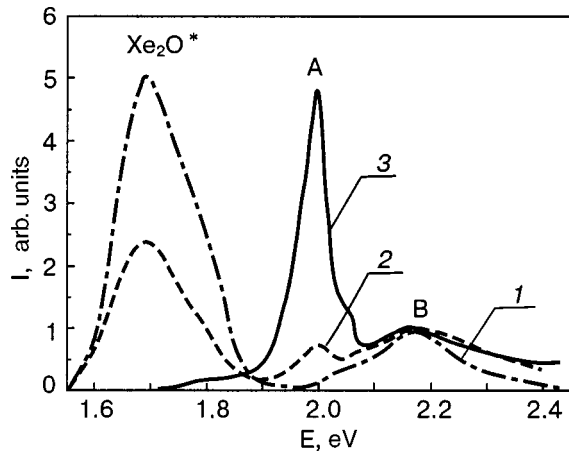
FIG. 1. Xe luminescence spectra as a function of the impurity concentration in the initial gas: *1*—unpurified Xe ($C_i \approx 10^{-3}$ at.%), *2*—purified Xe ($C_i < 10^{-4}$ at.%), and *3*—1:100 mixture of these gases. $T = 5$ K. The spectra are normalized to the maximum *B*-band intensity.

grains decrease in size and the total extent of the grain boundaries increases. The second parameter determines the generation of radiation point defects, whose concentration increases with the irradiation time. Figure 2 shows the spectra of crystals grown from purified gas at condensation temperatures $T_c = 35$ and 80 K. The ratio (I_A/I_B) of the *A*- and *B*-band intensities increases with condensation temperature by approximately a factor of 2. The *A* band is virtually absent in the luminescence spectra of crystals grown at temperatures $T_c < 30$ K; the intensity of the *B* band likewise decreases, but this band is still observed. Therefore it can be concluded that the *A* band is more sensitive than the *B* band to the sizes of the single-crystal grains.

Figure 3a shows the change in the radiation spectrum of *A* and *B* bands with increasing irradiation time t_i and therefore increasing concentration of radiation defects. The irradiation doses $N_e(t)$ are approximately $N_e(t_1) = 4 \times 10^8$, $N_e(t_2) = 2 \times 10^9$, $N_e(t_3) = 4 \times 10^9$, $N_e(t_4) = 8 \times 10^9$ electrons with energy $E_e = 2$ keV. The *A*- and *B*-band intensities increase with t_i. The intensity of the radiation spectrum of a free exciton changes in the opposite direction (Fig. 3b). Initially, I_{FE} decreases rapidly and reaches its lowest value for
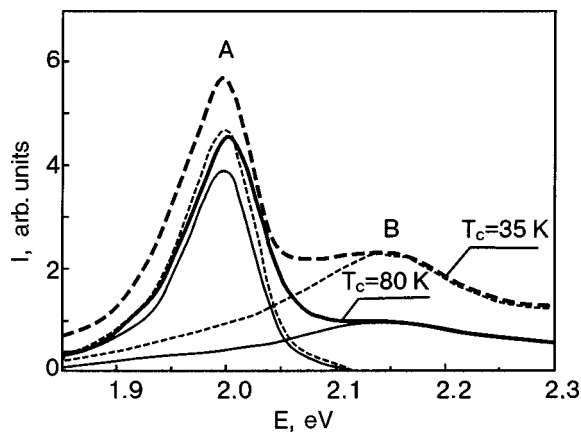

FIG. 2. Radiation spectra of samples grown from purified xenon at different condensation temperatures. The spectra are represented as a superposition of *A* and *B* components.
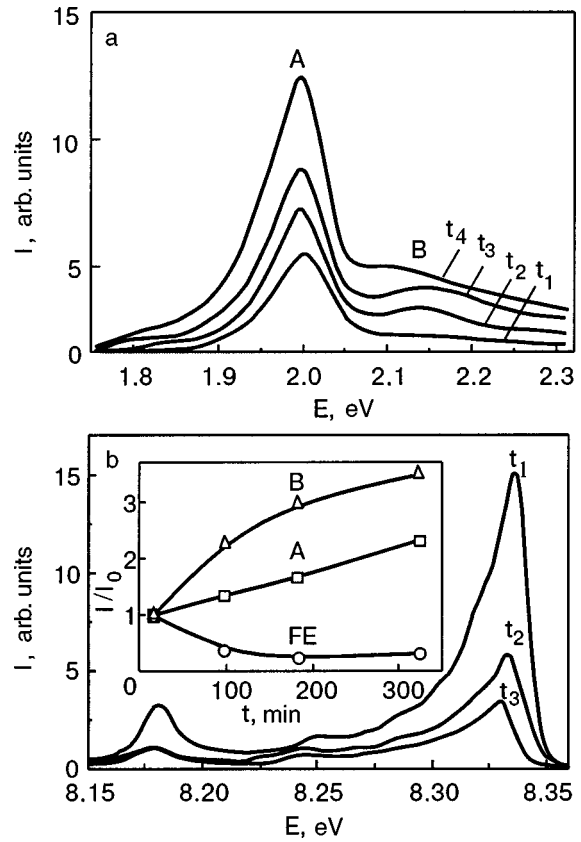

FIG. 3. Variations of the luminescence spectrum of crystalline Xe as a function of the electron irradiation dose. $T_c = 80$ K, $T = 5$ K, $I_e = 13$ μA, $t_1 < t_2 < t_3 < t_4$. a—Visible range, b—VUV range, spectrum of a $\Gamma(3/2)$ free exciton. Inset—band intensities I_A, I_B, and I_{FE}, normalized at the initial point of measurements t_1. The spectra *A*, *B*, and *FE* were recorded simultaneously.

$t_i > 200$ min. The dose dependences of the band intensities I_{FE}, I_A, and I_B are displayed in Fig. 3b (inset).

The temperature variations of the spectrum of the combined contour of the *A* and *B* bands are quite complicated. These bands were spectrally separated in order to determine the behavior of each one; the separation was done using as a reference the shape of a band in these spectra which is least affected by neighboring bands. The *A*-band shape was extracted from the spectrum of the most perfect crystal with a minimal impurity concentration, and the *B*-band shape was extracted from the spectrum of a crystal with a low impurity concentration, corresponding to curve *3* in Fig. 1. The extracted *A* band is displayed in Fig. 4. To see the changes in the band shape more clearly the spectra are normalized to the maximum point. The position of the *A*-band maximum remains virtually unchanged in the entire experimental temperature range, and the half-width of this band decreases with temperature from $\Delta_A = 0.079$ eV at $T = 66$ K to $\Delta_A = 0.052$ eV at $T = 5$ K.

The temperature dependences of the intensities of the *A* and *B* bands and the free-exciton band are displayed in Fig. 5. The intensity $I_A(T)$ almost doubles as temperature decreases from 66 to 5 K. The function $I_A(T)$ is flatter from 20 to 50 K than at low and high temperatures. A maximum is observed in $I_B(T)$ at $T \approx 40$ K (we note that a maximum has been observed in the thermal luminescence spectrum at this temperature[22]). In most of the temperature range—right up to
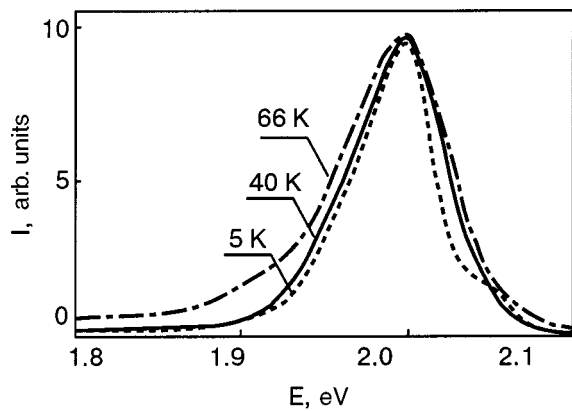
FIG. 4. *A*-band shape at different temperatures. The intensities are normalized at the point of the maximum.

60 K—practically an anticorrelation is observed in the behavior of the *A* and free-exciton bands, while the *B* band exhibits weak intermediate behavior.

A superposition of three narrow Gaussian components A_1, A_2, and A_3 with $E_{max}=1.97$, 2.0, and 2.05 eV describes the *A*-band shape quite well (see Fig. 6). The highest-energy, weak component A_3 is clearly observed only at low temperatures. As temperature increases, the relative intensity $I(A_1)/I(A_2)$ of the bands decreases and both bands are broadened. The parameters of the A_1 and A_2 bands as a function of temperature are presented in Table I. These data agree with the information presented in Ref. 18 on the existence of two bands with maxima $E_{max}=1.98$ and 2.0 eV and half-widths $\Delta=0.08$ and 0.05 eV.

B. Luminescence of Ar crystals with Xe impurity

The luminescence spectrum of Xe impurity in an Ar matrix with concentrations $C_{Xe}=1$ and 10% is shown in Fig. 7. The figure also shows the radiation spectra of the *A* and *B* bands for pure Xe with quite prolonged irradiation. Analysis of the spectra in Fig. 7 shows that for sufficiently high concentrations ($C_{Xe}\simeq10\%$) a superposition of the *A* and *B* bands could account for most of the impurity radiation spectrum.
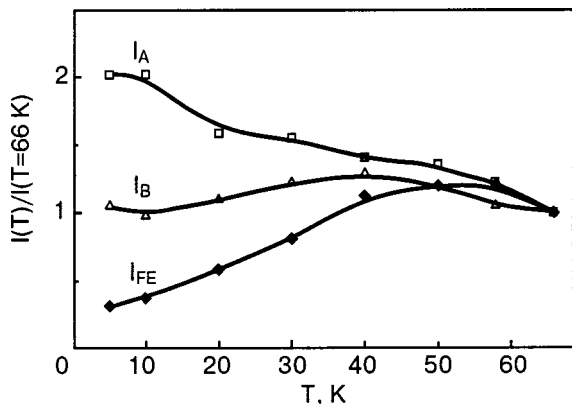

FIG. 5. Temperature dependence of the intensities of xenon radiation bands. The normalization is done at the initial point at 66 K.
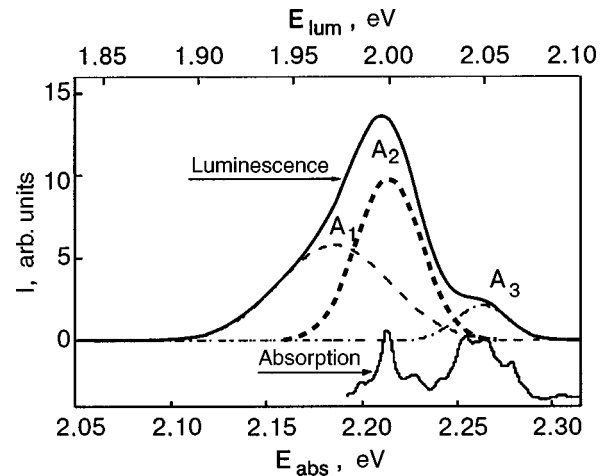

FIG. 6. Representation of the *A* band as a superposition of three separate Gaussian bands (top energy scale). To facilitate comparison the nonstationary absorption spectrum of xenon gas from the states of $Xe_2^+{}^*$ $(1)0_u^-/6s\,^3P_2$, $(1)1_u/6s\,^3P_2$, and $(1)0_u^+/6s\,^3P_1$ into the states $(9)1_g$, $(10)1_g$, $(11)1_g$, $(4)2_g$, and $(7)0_g^-$[34] is shifted downward in energy by 0.215 eV (bottom energy scale).

C. Luminescence excitation spectra and decay curves

The *A*-band photoexcitation spectra are presented in Fig. 8. Figure 8a shows the data required for comparative analysis; these date were obtained by other authors. The top spectrum[23] shows which states absorb light (top scale) and explains a number of minima in the excitation spectra by the anticorrelation effect, since reflection maxima are observed in the region of the resonance-absorption peaks, in consequence of which the excitation efficiency decreases. We note that the photoexcitation spectra of the radiation band M_1 (7.05 eV) of the lowest exciton $Xe_2^+{}^*$, localized on a defect, and the band M_3 (7.6 eV) at 60 K, when the M_3 band dominates in the spectrum of quasimolecular radiation, were recently obtained in Ref. 24. The last spectrum in Fig. 8a is the two-photon excitation spectrum of the *M* band, where transitions which are forbidden in the one-photon regime appear.[25] Figure 8b shows the complete *A*-band excitation spectrum which we obtained at $T=60$ K, using the S–60 synchrotron, and the free-exciton photoexcitation spectrum from Ref. 18.

A clear similarity between the excitation spectra of the *A* band and the quasimolecular band *M* is observed below the conduction band bottom E_g. The *A*-band excitation spectrum[18] with $E_1=8.9$ eV$\sim E_{ex}(n=2)$ has a feature (labeled with the number 1 in the figure) which is essentially identical in this region to the behavior of the high-temperature component M_3, previously ascribed to radiation

TABLE I. Structure of the *A* band and variation of the parameters of its components as a function of the crystal temperature.

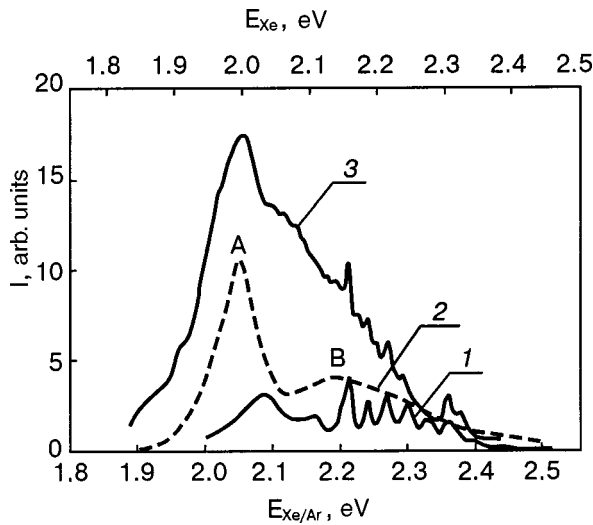| T, K	A_1		A_2		$\dfrac{I(A_1)}{I(A_2)}$
	E_{max}, eV	Δ, eV	E_{max}, eV	Δ, eV	
5	1.971	0.058	2.0	0.033	0.58
40	1.963	0.068	2.0	0.049	0.35
66	1.957	0.122	2.0	0.054	0.36

FIG. 7. Luminescence spectrum of Xe in Ar, $C_{Xe}=1\%$ (*1*) and $C_{Xe}=10\%$ (*3*). The series of narrow bands in the region 2.2–2.3 eV is the luminescence of XeO* from the residual oxygen impurity in argon. The spectrum of the *A* and *B* bands, which is observed in pure xenon (top energy scale), shifted upwards in energy by 0.05 eV (*2*) is presented for comparison.

from triatomic quasimolecular complexes.[26] The spectrum in the region of the $\Gamma(3/2)$ $n=1$ exciton resonance[18] looks more like the excitation of the standard *M* band (the sum $M_1 + M_2$) of self-localized exciton Xe_2^*. We note that in Ref. 18 the measurements were performed at $T=5$ K, and the spectrum displayed in Fig. 8b was obtained at 60 K. In our spectrum the feature 1 is somewhat stronger and the $n=1$ resonance is somewhat weaker, and on the whole our spectrum is almost completely identical to the excitation spectrum of M_3 at 60 K. Above E_g good agreement is observed between the structure of the excitation spectra of the *A*-band[18] and the free-exciton band, recorded 49 ns after the excitation pulse;[8] in addition, on the whole, both dependences reflect the character of the absorption spectrum. The spectrum *A* is distinguished by the presence of the feature 2 ($E_2 \approx 10.3$ eV) in the region of absorption of excitons engendered by electrons and holes whose states lie close to the edge points *L* and *X* of the Brillouin zone.[27] We denoted the corresponding very strong band in the absorption spectrum as *L,X* excitons. This same feature is also observed in the excitation spectrum of the *A* band (Fig. 8b). Above 12 eV a certain similarity is observed between the excitation spectra of the *A* and *FE* bands. The feature 3 ($E_3 \approx 13$ eV) in the spectrum of the *A* band should be noted; its energy corresponds approximately to the interband transition $X_6^- \rightarrow X_7^+$. Substantial intensity growth is observed at high energies (the threshold near 18 eV); this growth, taking account of the feature at $E_1 = 8.9$ eV, can be explained by an increase in the probability of excitation of two excitons with energy E_1.

The lifetime of the *A* band was measured on the S–60 synchrotron with photon energies $E_\nu = 9$, 13, and 21 eV, which correspond to the features 1 and 3 and the maximum energy of the spectrum in Fig. 8b. The curves showing the time decay of the luminescence are presented in Fig. 9. The two top curves correspond to excitation by photons with energy $E_\nu = 21$ eV and $E_\nu = 9$ eV. A special feature of these decay curves is the time shift of the maximum of the radia-
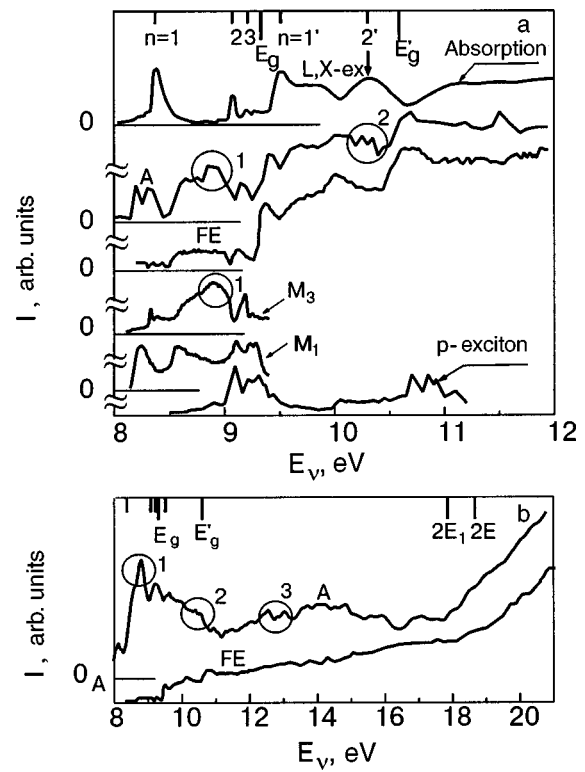

FIG. 8. Xenon spectra. (a) Curves from top to bottom: absorption spectrum,[40] the position of the bottom of the excitonic bands $n=1$, 2, 3 $\Gamma(3/2)$, (1/2) and the conduction bands E_g, E_g' are marked at the top. *A*—excitation spectrum of the *A* band at $T=5$ K,[18] the numbered circles mark the peaks which have no analogs on the *FE* curve. *FE*—excitation spectrum of a $\Gamma(3/2)$ free exciton, recorded in a time window with duration $\tau=49$ ns at $T=5$ K.[18] M_1—excitation spectrum of the band of two-center excitons Xe_2^* with $E_{max}=7.15$ eV localized on defects, M_3—excitation spectrum of the $E_{max}=7.6$ eV band, both spectra were obtained at $T=60$ K.[24] *p* excitons—excitation spectrum of the *M* band at $T=158$ K,[25] the features are attributed to *p* excitons. (b) *A*—excitation spectrum of the *A* band; we obtained the spectrum in the S–60 synchrotron at $T=60$ K, *FE*—excitation spectrum of free excitons.[18]

tion decay curve relative to the maximum of the photoexcitation pulse. This is characteristic for a cascade process. The simplest cascade scheme for the change in the number of particles with time is described by the equations

$$\frac{dn_0(t)}{dt}=I_0(t)-\frac{n_0(t)}{\tau_0}; \quad \frac{dn_{A(t)}}{dt}=\frac{n_0(t)}{\tau_0}-\frac{n_A(t)}{\tau_A}, \quad (1)$$

where $I_0(t)=I_0\delta(t-t_0)$ is the excitation pulse (in our case $t_0=5$ ns corresponds to the maximum of the excitation pulse, curve *3* in Fig. 9). In this process the primary centers with concentration $n_0(t)$ transform over their lifetime τ_0 into radiating centers with concentration $n_A(t)$ and lifetime τ_A. Then the *A*-band intensity is $I_A(t)=\tau_A^{-1}n_A(t)$. The solution of the system of equations (1) is presented in Fig. 9 as the curve *1* with the parameters $\tau_0=3$ ns and $\tau_A=6$ ns. The strong background with excitation period 48 ns (15 scale units in the figure) is explained by the presence of a long-lived radiation component whose time can be estimated as $\tau_A^l \sim 200$ ns. The discrepancy between the computed curve and the experimental points on the initial section is explained by the large actual width of the exciting pulse. The computed shift of the maximum of the curve relative to the initial pulse ($t=5$ ns) is $\Delta t \simeq 4$ ns. A similar shift has been observed on
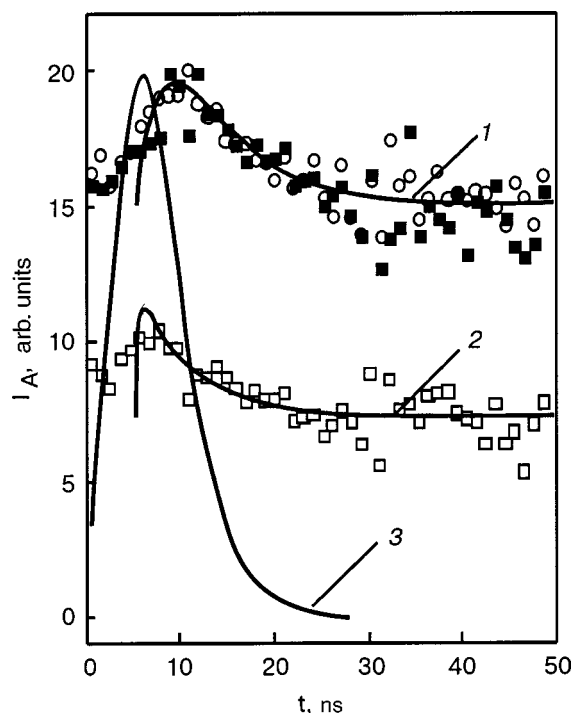
FIG. 9. *A*-band intensity as a function of the time elapsed after the excitation pulse: *1*—excitation energy $E_\nu = 21$ and 9 eV (open and filled circles, respectively), *2*—$E_\nu = 13$ eV, *3*—shape of the exciting light pulse. To facilitate comparison the experimental curve *2* is shifted downwards relative to curve *1*. The solid curves *1* and *2* were calculated using the model (1).

the luminescence decay curves of a free exciton excited by photons with energy $E_\nu > (E_g + 0.5)$ eV.[9] The delay is explained by the fact that as the excitation energy increases, the relaxation time of an electron relaxing to the bottom of the conduction band in a single-phonon scattering process increases.

A shift in the maximum of curve *2* in Fig. 9, obtained with excitation energy $E_\nu = 13$ eV, is not observed; this corresponds to $\tau_0 \leqslant 3$ ns ($\tau_0 = 0.3$ ns was used in the calculation); the lifetime $\tau_A = 6$ ns did not change. The short filling time is manifested in the fact that the shape of the curve *2* at the initial stage is virtually identical to that of the curve *3* of the exciting pulse.

The fact that the maximum on the decay curve shifts once again as the excitation energy decreases to 9 eV attests to the existence of intermediate delay processes with excitation in the excitonic region E_1.

4. DISCUSSION

A. General description of the radiating states

To clarify the origin of the *A*-band radiation with $E_{max} = 2$ eV we shall analyze the results obtained, comparing the dependence of this band on various parameters with the same dependences for reliably identified radiation bands—impurity centers XeO*, free excitons, molecular excited centers Xe_2^*, and ionic excitations $Xe_2^+{}^*$.

First, the sharp increase in the *A*-band radiation intensity simultaneously with quenching of the impurity band XeO* after additional purification of the initial xenon gas definitely rules out the version where the radiating states are attributed to impurities.

The version where the *A* states are surface states can be immediately ruled out on the basis of the following three facts. First, when fine-grained samples are grown and the total surface area increases, the intensity of the *A* band decreases (for $T_c < 35$ K) virtually to zero. Second, the photoexcitation spectrum has the so-called inverted form (anticorrelation with the absorption spectrum). This signifies that the energies at which the absorption coefficient is small (the "wings" of the resonance absorption band) correspond to a larger penetration depth of light in the crystal and more efficient excitation of volume excitons. Third, similar, quite strong radiation due to Xe impurity states in an Ar matrix, where at concentrations $C_{Xe} = 10\%$ the fraction of surface states of xenon atoms (molecules) becomes much smaller, is observed. Therefore the *A* band should be attributed to intrinsic volume states.

Let us discuss whether or not the *A* band could be due to a transition from free (band) exciton states with higher energies into the lowest-lying $n = 1$ $\Gamma(3/2)$ dipole-active exciton band. The 2 eV radiation band should correspond to transitions from excitonic states far above the conduction band bottom $E_g = 9.3$ eV (they are called resonance states). According to the general theory,[28] excitonic states in the continuous spectrum are not bound states in the usual sense, but rather they are characterized by an imaginary energy $E - i\Gamma$, where Γ describes the probability that an exciton decays into free charges and their wave function is a wave whose amplitude diverges at infinity. These states can be relatively stable if the symmetry of the wave functions of the excitonic electron (or hole) is different from that of a free electron. Eexcitons in the $\Gamma(1/2)$ series are distinguished by the hole state (the lowest conduction band corresponds to a triplet hole with $J = 3/2$) and X, L excitons are distinguished by a change in the configuration of the electronic band wave function as the band edge is approached. The interaction with defects can result either in localization of an exciton on a defect or it can stimulate decomposition of the exciton into free charges. In either case it results in rapid quenching of free excitons (just as happens with the *FE* band in Fig. 3) and therefore flare-up of radiation from localized states. The increase in the intensity of *A*-band radiation with increasing irradiation dose, i.e. with increasing concentration of point defects, clearly points to local excitation. On the other hand, in impurity systems ($C_{Xe} \sim 10\%$) the *A*-band intensity increases and free xenon excitons cannot exist, since translational symmetry is absent. Therefore it must be acknowledged that the excitation responsible for the *A*-band radiation is local.

The next question is whether or not the *A* band corresponds to the radiation of an excited ionic center. The fact that its energy is close to that of the *B* band, corresponding to the excitation $Xe_2^+{}^*$, suggests, first and foremost, the idea that their origins could be similar, but our data show that these bands behave differently. The intensity of the *B* band saturates in a characteristic time ~ 300 min, depending on the irradiation dose. In an experimental investigation of photoconductivity due to ionization of excitons in krypton,[29] where it was shown that charges accumulate on the surface of the crystal, the characteristic time was ~ 100 min. The saturation of the photocurrent was attributed to the electro-

static limit on the accumulation of charge centers in the sample. In our case the increase in the saturation time of the crystal by ionic centers is due to the specific nature of the excitation of the crystal by an electron beam. In contrast to the *B* band, the *A*-band intensity does not saturate over the detection time; this shows that there is no charge on an *A* center. In addition, as already mentioned, in experiments on samples with a specially created high concentration of ionic centers, efficient excitation of the *B* band by 4.5 eV light was observed, but in this case the *A*-band radiation was completely absent.[11,12] These facts show that the *A* band belongs to a neutral radiation center.

Let us consider the next variant of the origin of the observed band: the *A* band is due to the excess energy released when localized electrons and holes recombine with one another. When this happens, a transition occurs into the ground state of the crystal. This interpretation was proposed in Ref. 17 for a number of visible-range bands with energy $\sim 3–4$ eV. The energy released as a result of recombination is described by the equation

$$E(r) = E_g - (E_h + E_e) - \frac{e^2}{4\pi\varepsilon_r\varepsilon_0}\frac{1}{r} - \Delta V_L, \qquad (2)$$

where $E_h \approx 0.6$ eV is the depth of the self-localized hole; E_e is the binding energy of an electron in a trap; r is the electron–ion distance; $\varepsilon_r = 2.2$ is the dielectric constant of solid Xe; e is the electron charge; and, ΔV_L is the difference of the lattice energies between the excited and ground states, taking account of the contribution of hole and electron centers. We note that an equation where the third term in Eq. (2) is taken with the opposite sign is used in Ref. 17 by analogy to known recombination effects in semiconductors.[30] However, an excited state in semiconductors consists filled (neutral) states of hole and electron traps, and the ground state consists emptied (charged) acceptor and donor centers. When a local hole recombines with a local electron Coulomb coupling exists in the excited state (local analog of an exciton) and the ground state contains neutral atoms, which is what gives the corresponding sign of the Coulomb energy in Eq. (2).

The formation of local charge centers in crystals of inert elements could be due to a large deformation of the lattice. A two-center hole ion consists of two closely spaced atoms whose repulsion energy in the ground state gives for Xe $\Delta V_L \approx 0.8$ eV.[31] Clearly, there are still not enough experimental data on actually existing electronic traps. In shallow pore-type (a large cluster of vacancies) traps the repulsion of an electron from the nearest-neighbor environment is essentially compensated by polarization attraction. Deep traps can be only of an impurity origin, and the electronic level in this case must correspond to a strongly bound state with a small radius. In both cases the lattice deformation due to the presence of an electron in a trap is small. Neglecting the electronic contribution to ΔV_L, we obtain from Eq. (2) that the recombination radiation energy $E(r)$ can be 2 eV only if the depths E_e of the electron traps are $\sim 5–6$ eV with the distances r between the charged centers ranging from a_0 to $r \gg a_0$ (the lattice constant in xenon $a_0 = 0.613$ nm). In Ref. 17 it was noted that in experiments on the photoyield of electrons an effect corresponding to electron-trap depths

ranging from 2 to 7 eV and lifetimes up to several hours was observed. The authors could not explain the nature of such deep states. It is known that the binding energies of electronic traps estimated on the basis of thermal luminescence data are 60, 72, and 86 meV.[22] The main uncontrollable impurities in inert gases are other atmospheric gases and water. The binding energy of electrons on impurity traps of atmospheric gases cannot exceed the electron affinity. Oxygen has the highest electron affinity among known impurities—1.47 eV. We remind the reader that we specially investigated the influence of the impurity oxygen concentration; this was discussed above.

Another very important argument against the recombination radiation version is the small width of the *A* band (see Table I). When the contribution of the last term in Eq. (2) is taken into account, an effect which is well known from the quasimolecular radiation of the *M* band obtains—a transition to a repulsive term of the ground state gives a band of width ~ 0.5 eV. Therefore the version of the *A*-band radiation where such a recombination transition occurs into the ground state of the crystal seems to us to be groundless.

Let us now examine the conjecture that local excitations exist in the conduction band of the crystal. Transitions between excited states are supported by the fact that the position of the *A*-band maximum is essentially temperature-independent (see Table I). As temperature increases, an appreciable shift is observed in the maximum of the radiation of atoms and excitons. This shift is due to the fact that the change in the electron–lattice interaction in the excited state (large radius of the electron state) is different from that in the ground state (much smaller radius) as the crystal expands. In the deformation-potential approximation the shift is given by the expression

$$E(T') - E(T) = C\beta(T)(T - T'), \qquad (3)$$

where $E(T)$ is the position of maximum luminescence; $\beta(T)$ is the dilation; $C = C_1 - C_2$ is the deformation potential corresponding to a transition from the state 1 into the state 2. Crystals of inert elements possess a strong exciton–phonon coupling; $C = 1.3$ eV corresponds to an exciton with $n = 1$ ($\Gamma(3/2)$. As temperature increases, the maximum of the $\Gamma(3/2)$ excitonic luminescence shifts appreciably to lower energies.[2] A similar effect is also observed for atomic excitations of Xe in a matrix with a change in its density.[1] In contrast to excitonic luminescence, the position of the main maximum of the *A* band remains unchanged as temperature changes. This situation corresponds to transitions between local excited states, when $C_1 \approx C_2 \approx C_e$—the deformation potential of the electronic state in the limit of a large radius. For a molecular local state there exists an additional condition that the position of maximum radiation is independent of temperature: the states 1 and 2 must have potentials of a similar form with the same internuclear distances.

Since intrinsic local quasiatomic excitations in Xe do not occur either for the lowest excitons or for holes, the *A*-band radiation is most likely due to quasimolecular excitation. The increase in the intensity of the *A* band in the luminescence spectrum of mixed Ar–Xe crystals with the Xe concentration increasing to 10% confirms the supposition that the radiating

A centers are of a molecular type. For such a xenon concentration the probability that Xe–Xe pairs are formed in the crystal grown is about 75%.[32]

The energy $E_A = 2$ eV of the luminescence transition between the excited states of a molecule establishes the lower limit of the energy of the radiative state:

$$E_{\min} = T_e(I_u) + E_A \approx 7.95 + 2 = 9.95 \text{ eV}, \tag{4}$$

where $T_e(I_u) \approx 7.95$ eV is the zero-point vibrational energy of the lowest excited state of the Xe_2^* molecule in a crystal.[2] This limit lies approximately 0.7 eV above the conduction band bottom in the crystal ($E_g = 9.30$ eV).

The possibility that local electronic–vibrational molecular excitons are formed at the center of the excitonic band has been shown theoretically in Ref. 4. The necessary condition for this process is the presence of deep molecular states, lying in the same energy range, and defects of the crystal structure which stimulate exciton localization. Energy relaxation of an exciton in a band is branching process, which results in deexcitation of free and localized excitons. Therefore it can be supposed that resonance excitations in the conduction band likewise form mixed states with the vibrational levels of high-energy molecular states Xe_2^{**} lying in the same energy range. The interaction of these excitonic polarons with defects results in relaxation of excitation along a local system of vibrational levels and deexcitation of their local centers.

B. Identification of radiating states

Proceeding to the analysis of the excited states that could be responsible for the 2-eV *A*-band radiation of xenon, we recall that the temperature dependences of the band width and position of the band maximum support the ideas that the internuclear distance r_e is close for the upper and lower molecular potentials and that these potentials have a similar shape. The scheme of molecular and atomic states of xenon is displayed in Fig. 10. The lowest bound molecular states of Xe are the states 1_u, $0_u^-(6s\,^3P_2)$, and $0_u^+(6s\,^3P_1)$. The parameters of these potentials in the gas phase have been well-determined ($D_e = 0.53$ eV, $r_e = 0.31$ nm).[33] These potentials converge to the atomic terms $6s[3/2]_{2,1}$ with energies 8.315 and 8.436 eV. Thus if a radiative transition occurs to the lowest vibrational level of Xe_2^*, then the internuclear distance of the upper potential should be $r_e \approx 0.3$ nm and this potential should lie about 2 eV above the zeroth vibrational level of the lowest state of the excited molecule Xe_2^*.

Calculations of the potential energy of Xe_2^* molecules[34] show that bound states satisfying these conditions do indeed exist. The close-lying potentials $(6)0_g^-$, $(7)0_g^+$, $(9)1_g$, $(4)2_g$, $(10)1_g$, $(11)1_g$, $(7)0_g^-$, and $(8)0_g^+$, arranged in order of increasing energy, correspond to these conditions (see Fig. 10). The states $(6)0_g^-$, $(7)0_g^+$, $(9)1_g$, $(4)2_g$, and $(10)1_g$ correlate with the $7p$ atomic asymptote and are described by the configuration $A\pi_u 7p$ (they are shown in the inset in Fig. 10; the numbers 1–3 denote the first three states). The lowest four states possess the $^3\Pi_g$ configuration and $(10)1_g$ possesses the $^1\Pi_g$ configuration. The higher-lying states $(7)0_g^-$, $(11)1_g$, and $(8)0_g^+$ possess $^3\Sigma_g^+$ and $^1\Sigma_g^+$ configurations, and they correlate with the $7s$ atomic states and are quasibound. They possess a high barrier to
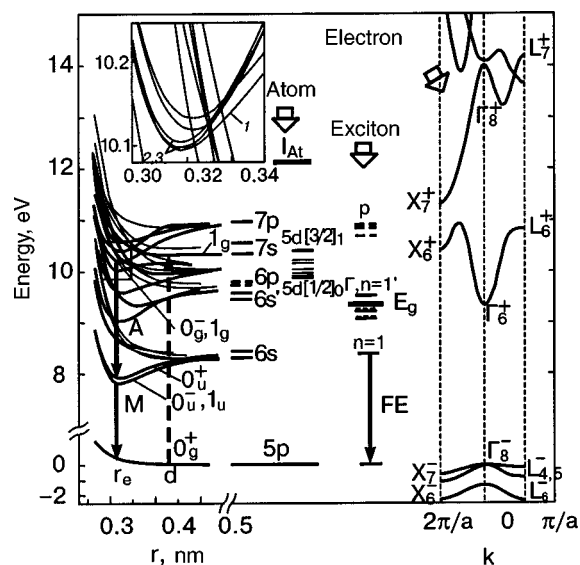

FIG. 10. Energy scheme of molecular potentials and atomic states of xenon (left-hand side). The atomic states $6p$, $7s$, and $7p$ are designated for simplicity by a single level corresponding to their average value; the $5d$ levels are presented completely. The solid arrows denote *A*-band and localized-exciton (*M*) radiation, the dashed arrow denotes the absorption from the ground state, corresponding to the closest internuclear distance in the crystal *d*. Inset: molecular potentials of Xe near 10.2 eV,[32] the potential curves denoted by the numbers *1–3* correspond to the states $(6)0_g^-$, $(9)1_g$, and $(7)0_g^+$ in order of increasing energy. Center—the excitonic states of xenon. The position of the Γ excitons is designated by solid lines, the position of *p* excitons by dotted lines,[25] and the conduction band bottom E_g by the heavy line. The arrow shows a radiative transition of a free exciton (*FE*). Right-hand side—computed valence-band and conduction-band states of xenon.[38]

dissociation to the lower-lying $5d$ atomic terms. The calculations show that the right-hand branch of the molecular potentials $(6)0_g^-$, $(9)1_g$, $(7)0_g^+$, $(4)2_g$, and $(10)1_g$ is intersected by repulsive terms, but the lowest vibrational levels can have quite long predissociation lifetimes.[34] The transition dipole moment for the indicated molecular states is nonzero for a transition to the lower bound states of the molecule Xe_2^* $0_u^+(6s\,^3P_1)$ and $1_u, 0_u^-(6s\,^3P_2)$.

The presence of such states in the gas phase was confirmed experimentally by the nonstationary absorption of the molecule Xe_2^* from the lowest excited states $0_u^+(6s\,^3P_1)$ and $1_u, 0_u^-(6s\,^3P_2)$. The absorption spectrum near 2.22 eV consists of two structured bands, which themselves consist of a set of overlapping components.[34] The first band was attributed to a transition from the lower excited molecular state $0_u^+(6s\,^3P_1)$ into the excited states $(9)1_g$, $(10)1_g$, and $(11)1_g$. The second was attributed to transitions from $1_u, 0_u^-(6s\,^3P_2)$ into the states $(9)1_g$, $(10)1_g$, $(11)1_g$, $(4)2_g$, and $(7)0_g^-$. The nonstationary absorption spectrum of the Xe_2^* molecule in the gas phase is compared in Fig. 6 with radiation in the *A* band. We performed a simple reconstruction of the spectrum of a group of bands near 2.21 eV, representing them as a sum of three Gaussians with half-width 0.007 eV. The contour obtained describes well the central component A_2 while at the same time the relative intensity of the individual components is preserved and the width of each band increases to 0.03 eV as a result of the interaction with the lattice. The magnitude of the shift $\Delta E_S = 0.15$ eV of the band maximum to lower energies corresponds to a crystalline shift due to the difference of the po-

larization interaction with the environment in the upper (radiating) state and the lower molecular term.

In crystalline xenon, as a result of the the Franck–Condon principle, absorption from the ground state can excite only band states or local states with $r_e \sim d = 0.43$ nm, and for nonstationary absorption in Xe_2^* localized excitons with $r_e \sim 0.3$ nm can be occupied. The nonstationary absorption in inert-gas crystals has been investigated in Refs. 35 and 36. For Xe it was found in Ref. 35 that the energy of the allowed transition $^3\Sigma_u^+ - ^3\Pi_g$ from the lowest excited state is less than 1.1 eV. Continuum absorption is observed in the energy range of interest to us 1.1–3 eV. This absorption is quite strong, but the resolution in detecting this spectrum in Ref. 35 (0.1 eV) was too low to separate the fine structure in it. For krypton, whose structure and properties are closest to xenon, the absorption with $E_{max} = 1.2$ eV between the lowest excited molecular terms $^3\Sigma_u^+ - ^3\Pi_g$ and the additional structure at 1.6 and 2.5 eV were observed. The matrix shift of nonstationary absorption in krypton is $\Delta E_S \approx 0.1$ eV. This small value of ΔE_S shows that the molecular terms in the gas phase are close to those of the crystalline phase. The shift between the absorption spectrum and the luminescence spectrum in crystalline krypton is 0.11 eV, i.e. the change in the relaxation energy of the environment makes a comparatively small contribution to the transition energy. These data can serve as reference points for estimating the magnitude and direction of a possible shift of various molecular potentials of Xe_2^{**} accompanying a transition from the gas into the crystalline phase.

In the crystalline state the energies of the $7s$ and $7p$ levels of Xe*, which have a large excitation radius, decrease as a result of the polarization interaction with the environment. The polarization interaction energy of an electron occupying an interstice is $\Phi_e = -2.26$ eV, and for a hole occupying a site $\Phi_h = -1.35$ eV.[37] If an electron in an excited atom possesses an intermediate radius, as in the case of the excitations Xe* $5p^56s$, $5p^66p$, then its interaction is determined more by the repulsion with the environment, which is only compensated to some extent by the polarization attraction. Correspondingly, the local crystalline atomic level (approximately the center of the band) of $\Gamma(3/2)$ and $\Gamma(1/2)$ excitons, genetically related with the excited atomic states $5p^56s$ and $5p^56s'$, is shifted to higher energies by ~ 0.4 eV. For s states with large radii of the electronic orbit, i.e. ns with $n > 6$, the polarization interaction is in full play and a lowering of the levels compared with the levels in the spectrum of a gas and compression of the spectrum should be observed. This corresponds to lowering of the atomic ionization potential for triplet states $I_A = 12.13$ eV to the conduction band bottom in the crystal $E_g = 9.3$ eV at the point Γ_6^+ of the Brillouin zone, which is the convergence limit for s excitons (see Fig. 10). For $\Gamma(1/2)$ excitons the convergence limit E_g' can be estimated as

$$E_g' = E_g + \Delta E_{SO} = 9.3 + 1.3 = 10.6 \text{ eV},\qquad(5)$$

where ΔE_{SO} is the spin-orbital splitting.

The conduction band whose minimum lies at the point X_7^+ of the Brillouin zone corresponds to electronic states with p-symmetry wave functions in the crystal. For single-photon excitation, transitions from the $5p$ ground state into

the p excited states of atoms and excitons are forbidden. Investigations of the excitation of the M band in the two-photon absorption regime at $T = 158$ K revealed a series of absorption bands whose limit is $E_g(p) = 10.98 \pm 0.08$ eV (see Fig. 8a).[25] Since the $X_7^- \rightarrow X_7^+$ transition energy is ~ 11 eV,[38] these states lie in the bottom conduction band and probably are of the same origin as the L, X excitons. On the basis of the symmetry of the electronic wave function and the energy these excitations can be regarded as the crystalline analog of the atomic $7p$ terms. Then, as is evident in Fig. 10 the molecular levels associated with the atomic $7p$ states, lying in the range 10.9–11 eV, remains virtually unshifted at the transition into the solid phase. Incidentally, this signifies that the polarization interaction with the crystal for p states does not correspond to a model of two point charges, as assumed in the estimates of Φ_e and Φ_h given in Ref. 37. The states associated with $7s$ and $7s'$ will be shifted by a larger amount into the region of E_g and E_g', respectively.[1] The molecular terms associated with small-radius $5d$ excitations and intermediate-radius $6p$ excitations should remain approximately at the same energies as in the gas phase. Localization of high-energy excitons can occur with the participation of different potentials in the indicated energy range, which relax nonradiatively to the lowest molecular terms, designated by 1–3 in Fig. 10. On account of the different configuration of these states in the crystal a difference can arise in the crystalline shift, which is manifested as a splitting of the A band into components $A_1 - A_3$.

In addition to the maxima corresponding to p excitations, a local maximum (labeled by the number 2) is observed near 10.3 eV in the photoexcitation spectrum of the A band; this maximum is absent in the excitation spectrum of a free exciton (see Fig. 8b). In all probability the states near 10.3 eV have relaxation channels with direct filling of localized states associated with A centers. The most likely local excitations corresponding to this energy are molecular states converging to the atomic limit $5d[3/2]_1$ near 10.4 eV. The selection rules allow transitions into these states. Moreover, Xe_2 absorption bands associated with this atomic state are observed in the gas phase of Xe.[33] As a rule, the levels $5d[3/2]_1$ are filled as a result of dissociative recombination of molecular ions.[39] The weakly bound molecular term converging to the atomic level $5d[3/2]_1$ possesses 1_g symmetry and a shallow potential with $D_e = 0.06$ eV and $r_e = 0.4$ nm, close to the nearest-neighbor distance in the crystal ($d = 0.43$ nm).[40] Consequently, under photon excitation this molecular term can be efficiently filled from the ground state. In the crystal the $5d$ states are converted into narrow bands and their coupling with the lattice can be much stronger than for other excitations. Subsequently, nonradiative relaxation is possible and can result in filling of deeper molecular potentials with different symmetry, since the weakly bound state $1g$ ($5d[3/2]_1$) is intersected by many deeper potentials, including potentials associated with $6p'$ and $7p$ atomic excitations. Ultimately, radiative transitions with energy near 2 eV ($A_1 - A_3$ bands) can occur from states with a deep minimum (1–3 in Fig. 10). The decrease in the intensity of the blue component A_3 with increasing temperature can be explained by thermal activation above a barrier sepa-

rating the minimum of the potential and repulsive terms intersecting it.

C. Formation of high-energy radiating states in the conduction band of crystalline xenon

The character of the absorption spectrum of crystalline xenon reflects the Coulomb interaction force between an electron and a hole.[27] In light crystals (Ne, Ar) with low permittivity ($\varepsilon_0 \sim 1.5$) the screening of the Coulomb interaction is weak and the exciton binding energy is high. In absorption, most of the intensity (contribution to the oscillator strength) lies in the exciton region ($E < E_g$) and the fraction of interband transitions ($E > E_g$) (in the two-band approximation) in Ar is about 40%, half of them are due to L, X exciton type resonance states. In heavy crystals (Kr, Xe) the Coulomb interaction is weaker ($\varepsilon_0 \sim 2$), the exciton binding energy is smaller and the exciton contribution to absorption for $E < E_g$ is less than half (in Xe—30%). The fraction of resonance states is 62% and only 8% goes into in continuum absorption of free electron–hole pairs. Thus, as the atomic number increases, the role of interband transitions in the excitation of a crystal increases and the question of the mechanisms of shedding (transformation) of the energy of the initially arising excitations and channels for filling the radiative excitonic states becomes more critical.

One of the most important questions is to determine the lifetime of resonance states taking account of the decay into electrons and holes, the character of electron–hole pair recombination, and the recombination efficiency for particles with different energies. Investigation of the excitation spectra of the luminescence bands of the lowest free and self-localized excitons in perfect crystals has shown that even though light absorption in the region of interband transitions is efficient the excitation of the M band (Xe_2^*) for $E > E_g$ decreases strongly. (We recall that the radiation of quasimolecular states usually strongly predominates in luminescence; luminescence of free excitons comparable to M luminescence is observed only in the most perfect crystals.) This means that, on the whole, for low defect densities the recombination process is inefficient, i.e. excitons in the region of the conduction band either leave the crystal (quenching on a substrate, and so on) or are quenched on impurities. The probability of these processes is determined by the long mean-free path length of quasiparticles, since it is assumed that a quite large crystal is grown with the lowest possible impurity concentration. It is still unclear whether or not resonance states in the conduction band can possess such large diffusion lengths. At the same time the observation of a direct channel (no delay) for the formation of a localized state of a singlet (excited) hole state followed by B-band radiation with $E_{max} = 2.15$ eV could serve as an indicator of the decay of excitons above $E_g' = 10.6$ eV.

An especially intriguing fact obtained in this work is the absence of a time shift of the A-band luminescence relative to the photoexcitation maximum at 13 eV. This could signify that localized molecular states are filled directly from high-energy free exciton states in this region. Although, in accordance with the relatively smooth variation of the photoexcitation spectrum near 13 eV, the contribution of direct processes filling A centers from the conduction band does

not predominate, it is important to show that such a process is, in principle, possible and to determine the energy range of its excitation. This requires more accurate measurements of A-band quenching with a small excitation energy step.

With the exception of local maxima (see Fig. 10, *1–3*), a high degree of correlation is observed between the excitation spectrum of the A band and the long-time recombination component of free excitons in defective crystals (see Fig. 8a). This shows that aside from the channel for direct excitation of high-energy excitons, a second channel for filling the A band is recombination of self-localized holes and free electrons, which also can result in filling of high-energy excitonic states localized in high-energy molecular excitons. This process proceeds in two steps and requires additional time for energy relaxation of holes and electrons. This conclusion agrees with the existence of a time delay $\Delta t \approx 5$ ns between the photoexcitation maximum with energy $E_\nu = 21$ eV for the A band and the A-band radiation maximum (see Fig. 9). The time shift Δt is of the same order of magnitude as for excitation of free excitons by photons with excess energy $E_\nu - E_g \sim 1.5$ eV above the conduction band bottom. The delay Δt depends on the defect density in the crystal and is $\sim 5 - 10$ ns.[8,9] The shift Δt is observed only in crystals with defects and is determined by the time required for the energy of the electrons participating in recombination with holes localized on defects to relax.[9]

As shown in Ref. 9, recombination of a thermalized electron with a localized hole is rapid and the subsequent relaxation of excitations into the region of the top ($n > 2$) band excitons likewise occurs without a delay. The fact that the excitation by light with $E_\nu = 8.9$ eV results in a time delay of A-band radiation can be explained by the following scheme for the process: the recombination of holes and thermalized electrons results in a channel for filling free excitons without a delay, and subsequently the exciton should be absorbed by another (localized) excited state (to increase the probability of the process, this state should be long-lived), the excitation lies in the high-energy range, and the delay occurs along the relaxation path to an A-center state.

The very high sensitivity of the A band, just as of free excitons, to the presence of even a small amount of impurities shows that band excitations with a long mean-free path, i.e. electrons and excitons, the former at the stage of recombination of electrons and localized holes and the latter for excitonic excitation of local long-lived states, participate in the filling of the states responsible for A-band radiation. Impurity oxygen traps both with high efficiency. The positive electron affinity of the oxygen atom and the lower energy of the excimeric terms Xe^+O^- compared with excitonic states facilitates this.[21] Since the sensitivity of local centers Xe_2^+* (B band) to impurities is much weaker, it can be concluded that the cross section for trapping of excitons on local centers corresponding to A-band excitation is smaller than for ionic centers, and the concentration of such centers is lower than that of impurities in nominally pure xenon. This situation corresponds to trapping of excitons by neutral long-lived excited centers. These long-lived states can be the lowest long-lived terms of the Xe_2^* molecule or three-center excitations whose radiation (M_3) appears in the form of a band with $E_{max} = 7.6$ eV only at temperatures $T > 50$ K. This is con-

firmed by the fact that the maximum 1 of the A-band excitation with $E = 8.9$ eV coincides with the analogous maximum of the M_3 band excitation (see Fig. 8). We note that the energy range near 8.9 eV corresponds to excitation of $n = 2$ excitons, the radius of whose excited state is four times larger ($r_{ex} \sim 2a_0$) than that of $n = 1$ excitons. As shown in Ref. 10, the polarization attraction of such an exciton to a different excitation is much stronger than for the lowest exciton and, hence, the capture cross section is larger.

A different nature of the formation of the radiation in the A and B bands is observed in the luminescence of crystals precipitated at different temperatures. In finely dispersed samples large defects most likely form on the grain boundaries; these defects can become traps for electrons (an electron in a perfect Xe crystal cannot become localized). Since electron localization only increases the lifetime of localized holes Xe_2^+, preventing their recombination with an electron, this increases the B-band intensity. Conversely, the efficiency with which states associated with recombination processes are filled decreases substantially, and the A-band intensity in finely dispersed crystals drops virtually to zero.

For the electronic method of excitation, excess electrons are formed in the crystal. As a result, the recombination probability is higher than with photoexcitation. Correspondingly, for electronic excitation the A-band intensity clearly predominates over the ionic B band compared with photoexcitation.

5. CONCLUSIONS

The basic properties of the radiation band of crystalline xenon with $E_{max} = 2$ eV (A band) was studied experimentally in detail as a function of temperature, impurity concentration, lattice perfection, and irradiation dose. The radiation parameters of this band were compared with the analogous parameters of the radiation bands of free excitons, localized on holes $Xe_2^+{}^*$ and impurity centers Xe_2O^*; the latter bands were detected simultaneously in the same samples. Radiation with $E_{max} = 2.05$ eV and the analogous structure was also observed in Ar+Xe binary crystals with high ($\sim 10\%$) xenon concentrations. The photoexcitation spectra of the A band and the time decay curves of the luminescence were analyzed. It was concluded that the observed radiation is associated with molecular-type intrinsic excited states, which are localized in the interior volume of the crystal and lie in the conduction band near 10 eV. It is possible that these states are the terms $(6)0_g^-$, $(9)1_g$, and $(7)0_g^+$, associated with the atomic $7p$ excitations.[34] They lie in the corresponding energy range, possess quite deep minima in the potentials $D_e \approx 0.7$ eV, and are not intersected by the repulsive branches of other states directly at the minimum of the potential. A radiative transition occurs to the lowest bound excited molecular terms 1_u, $0_u^-(6s^3P_2)$.

An intriguing result was an indication that there exists a direct (no delay) channel filling radiating states when the crystal is excited in the region of the conduction band. It was shown that the excitation of A centers can occur as a result of the recombination of a free electron with a localized hole. Below the conduction band radiating states are most likely formed with the participation of two excitations. One is a free exciton and the other should be a long-lived local ex-

cited state. It could be that this is a specific three-center state responsible for high-temperature 7.6 eV radiation. The results obtained show that long-lived excited centers accumulate in a xenon crystal during irradiation.

*E-mail: tarasova@ilt.kharkov.ua

[1] N. Schwenter, E. E. Koch, and J. Jortner, *Electronic Excitations in Condensed Rare Gases*, Springer-Verlag, Berlin (1985).

[2] I. Ya. Fugol', Adv. Phys. **27**, 1 (1978); **37**, 1 (1988).

[3] G. Zimmerer, in *Excited-State Spectroscopy in Solids*, XCVI Corso Societa Italiana di Fisica, Bologna (1987), p. 37.

[4] A. M. Ratner, J. Lumin. **81**, 271 (1999).

[5] A. M. Ratner, Phys. Lett. A **265**, 411 (2000).

[6] I. Ya. Fugol' and E. I. Tarasova, Fiz. Nizk. Temp. **23**, 767 (1997) [Low Temp. Phys. **23**, 578 (1997)].

[7] A. M. Ratner and E. I. Tarasova, Phys. Status Solidi B **170**, 135 (1992).

[8] B. Steeg, E. Gminder, M. Kirm, V. Kisand, S. Vielhauer, and G. Zimmer, J. Electron Spectrosc. Relat. Phenom. **101–103**, 879 (1999).

[9] I. Reimand, E. Gminder, M. Kirm, V. Kisand, B. Steeg, D. Varding, and G. Zimmerer, Phys. Status Solidi B **214**, 81 (1999).

[10] A. N. Ogurtsov, A. M. Ratner, E. V. Savchenko, V. Kisand, and S. Viclhauer, J. Phys.: Condens. Matter **12**, 2769 (2000).

[11] E. V. Savchenko, O. N. Grigorashchenko, O. M. Sokolov, J. Agreiter, N. Caspary, A. Lammers, and V. E. Bondybey, J. Electron Spectrosc. Relat. Phenom. **101–103**, 377 (1999).

[12] O. N. Grigorashchenko, E. V. Savchenko, O. M. Sokolov, J. Agreiter, N. Caspary, A. Lammers, and V. E. Bondybey, J. Mol. Struct. **480**, 523 (1999).

[13] G. Zimmerer, J. Low Temp. Phys. **11**, 629 (1998).

[14] A. G. Belov, V. N. Svishchev, I. Ya. Fugol', and E. M. Yurtaeva, Fiz. Nizk. Temp. **9**, 1206 (1983) [Low Temp. Phys. **9**, 623 (1983)].

[15] A. G. Belov, V. N. Svishchev, and E. M. Yurtaeva, Izv. Akad. Nauk SSSR, Ser. Fiz. **47**, 1380 (1983).

[16] I. Ya. Fugol', A. G. Belov, V. N. Svishchev, E. M. Yurtaeva, M. N. Yakimenko, Yu. M. Aleksandrov, V. N. Makhov, and T. I. Syreĭshchikova, in *Proceedings of the 6th All-Union Conference on the Applications of SI-84 Synchrotron Radiation*, Institute of Nuclear Physics, Siberian Branch of the Soviet Academy of Sciences, Novosibirsk (1984), p. 315.

[17] M. Havecker, M. Runne, and G. Zimmerer, J. Electron Spectrosc. Relat. Phenom. **79**, 103 (1996).

[18] M. Havecker, Diploma Thesis, University of Hamburg (1996).

[19] E. M. Yurtaeva, I. Ya. Fugol', and A. G. Belov, Fiz. Nizk. Temp. **16**, 101 (1990) [Low Temp. Phys. **16**, 54 (1990)].

[20] Yu. M. Aleksandrov, V. N. Kolobanov, V. N. Makhov, T. I. Syreĭshchikova, and M. N. Yakimenko, Zh. Prikl. Spektrosk. **36**, 941 (1982).

[21] A. G. Belov and E. M. Yurtaeva, Fiz. Nizk. Temp. **27**, 1268 (2001) [Low Temp. Phys. **27**, 938 (2001)].

[22] M. Kink, R. Kink, V. Risand, J. Maksimov, and M. Selg, Nucl. Instrum. Methods Phys. Res. B **122**, 668 (1997).

[23] G. Baldini, Phys. Rev. **128**, 1562 (1962).

[24] A. N. Ogurtsov, E. V. Savchenko, E. Gminder, S. Vielhauer, and G. Zimmerer, in *Book of Abstracts of the 4th International Conference on Cryocrystals and Quantum Crystals CC'2002*, Friesing, Germany (2002), B-21.

[25] H. Pournasr, J. P. Holder, and J. W. Keto, Phys. Rev. B **54**, 864 (1996).

[26] A. M. Ratner, I. Ya. Fugol', A. G. Belov, and U. L. Steshenko, Phys. Lett. A **137**, 403 (1989).

[27] U. Rossler and O. Schutz, Phys. Status Solidi B **56**, 483 (1973).

[28] L. D. Landau and E. M. Lifshitz, *Quantum Mechanics: Nonrelativistic Theory*, Pergamon Press, New York [Russian original, Nauka, Moscow (1974)].

[29] J. Kraft, A. Schrimpf, B. Schweitzer, K. Ibbeken, and H.-J. Stockmann, Europhys. Lett. **39**, 459 (1997).

[30] F. Williams, Phys. Status Solidi **25**, 493 (1968).

[31] *Crysocrystals*, edited by B. I. Verkin and A. F. Prikhot'ko, Naukova dumka, Kiev (1983).

[32] S. Craydok and A. Hincliff, *Matrix Isolation* [Russian trans.], Mir, Moscow (1978).

[33] K. P. Huber and G. Herzberg, *Constants of Diatomic Molecules* [Russian trans.], Mir, Moscow (1984).

[34] C. Jonin, P. Laporte, and F. Spiegelmann, Chem. Phys. Lett. **308**, 13 (1999).

[35] T. Suemoto, Y. Kondo, and H. Kanzaki, Solid State Commun. **225**, 669 (1978).

[36] T. Suemoto and H. Kanzaki, J. Phys. Soc. Jpn. **46**, 1554 (1979).

[37] A. M. Ratner, Phys. Rep. **269**, 198 (1996).

[38] U. Rossler, in *Rare Gas Solids*, edited by M. L. Klein and J. A. Venables, Academic Press, New York (1976), Vol. 1, p. 505.

[39] A. F. Borghesani, G. Bressi, G. Carugno, E. Conti, and D. Iannuzzi, J. Chem. Phys. **115**, 6042 (2001).

[40] X. K. Hu, D. M. Mao, S. S. Simov, and R. H. Lipson, J. Chem. Phys. **106**, 9411 (1997).

Translated by M. E. Alferieff

LATTICE DYNAMICS

Surface and quasisurface states in a strongly anisotropic layered crystal

A. M. Kosevich, P. A. Minaev, and E. S. Syrkin*

B. Verkin Institute for Low Temperature Physics and Engineering, pr. Lenina, 47, 61103 Khar'kov, Ukaine

M. L. Polyakov

1153 Baker Ave., Schenectady, NY 12309, USA

In Part 1 a relatively simple model of a strongly anisotropic layered crystal is use to study various types of surface waves in the long-wavelength approximation. Particular solutions are obtained for the lattice-dynamics equations in the presence of a surface impurity monolayer. The solutions have frequencies that lying outside (surface states) and inside (quasisurface states) a band in the continuous spectrum of an ideal lattice. In Part 2 shear waves localized near a monatomic layer adsorbed on the free surface of a strongly anisotropic layered crystal are studied at the microscopic level using a vector laltice model with translational and rotational invariance and elastic stability. It is shown that in some cases a noncentral interatomic interaction results in the appearance of surface shear waves of a special type with one or two termination points and a damping parameter that is a nonmonotonic function the two-dimensional wave vector. © *2003 American Institute of Physics.* [DOI: 10.1063/1.1542505]

Strongly anisotropic layered crystals comprise a large class of substances which include semiconductors, dielectrics, magnetically ordered systems, polymers, and other materials.[1,2] A characteristic feature of these crystals is the presence of a weak interlayer bond which strongly influences various types of excitations. It is unquestionably of interest to study the surface acoustic waves that can propagate in such compounds. It is known that Rayleigh surface waves are modified in strongly anisotropic systems (or in crystals near a structural phase transition associated with softening of acoustic phonons): these waves become retarded and deeply penetrating.[3–5] The latter property has technological applications (for example, in acoustoelectronics). Together with Rayleigh-type surface waves, purely shear surface waves with horizontal polarization (*SH* waves)—an analog of surface Gulyaev–Blyusteĭn waves in piezoelectric crystals[6,7]—are also modified. In the long-wavelength limit the penetration depth of *SH* elastic waves (in contrast to Rayleigh waves) is much greater than the wavelength,[8,9] and the characteristics of the waves become extremely sensitive to external actions.[10] In recent years *SH* waves have been intensively studied and are now finding increasing applications.[11,12] The fact that single-component *SH* waves are structurally simpler than two-component Rayleigh waves can be used in experimental research, for example, for measuring the density of the normal component of superfluid helium[13] or for studying Langmuir–Blodgett films.[14] The present paper is devoted to clarifying the basic characteristics of these waves in the presence of strong anisotropy.

The following questions are studied. In Part 1 the long-wavelength case for a relatively simple model of a strongly anisotropic layered crystal is analyzed to determine the general properties of the surface states. Particular solutions are obtained for the equations of lattice dynamics in the presence of a planar defect. These solutions have frequencies outside (surface states) and inside (quasisurface) the continuous spectrum of an ideal lattice. In Part 2 the formation conditions and characteristics of the vibrational states for purely shear waves localized near a monatomic layer on the surface of a strongly anisotropic layered crystal are discussed. It is shown that, among other things, when the noncentral interaction in such crystals is taken into account, deeply penetrating surface waves, which exist only in a definite range of values of the two-dimensional quasiwave vector, can appear.

1. LONG-WAVELENGTH APPROXIMATION FOR A SIMPLE MODEL OF A STRONGLY ANISOTROPIC LAYERED CRYSTAL

The long-wavelength approximation for a scalar model of a semibounded, strongly anisotropic, layered crystal with an adsorbed layer of impurity atoms on the surface is studied. It is assumed that the crystal lattice is body-centered tetragonal and the crystal surface is perpendicular to a four-fold symmetry axis. To describe such a lattice it is convenient to use a rectangular coordinate system whose OX and OY axes lie in the plane of the monatomic layer on the surface of the crystal and the OZ axis is directed into the crystal. Let a be the distance between the nearest-neighbor atoms in the XOY plane and $b/2$ the distance between neighboring atomic layers perpendicular to the OZ axis. The smallest number of different types types of interatomic interactions that can be consequential for the structures studied is taken into account in this model—the interlayer interaction is taken into account in the nearest-neighbors approximation

and is characterized by the parameter γ and the interaction within the layers of the crystal is also taken into account in the nearest-neighbors approximation (the parameter α). Strong anisotropy means that $\gamma \ll \alpha$. We introduce parameters characterizing the adsorbed monolayer: $\varepsilon = \tilde{m}/m - 1$ and $\zeta_0 = \tilde{\alpha}/\alpha - 1$. Here $\tilde{m}$ and m are the masses of the atoms in a layer and in the main lattice; $\tilde{\alpha}$ and α are the interaction parameters of the nearest neighbors in the adsorbed monolayer and in the layers of the main lattice, respectively. It is assumed that the interaction of the surface layer with the main lattice, being quite weak, is the same as the interlayer interaction in the interior volume of the crystal. Since the crystal is structurally uniform in the XOY plane, it is convenient to switch in the equations of motion from a site representation in the plane of the layers to a two-dimensional k representation, retaining the site representation along the z axis. This yields difference equations describing stationary oscillations of the atomic layers in the interior volume of the crystal:

$$\lambda u(z) + \frac{2\alpha}{m}[\cos k_x + \cos k_y - 2u(z)] + \frac{4\gamma}{m}[(u(z+b/2)$$

$$+ u(z-b/2))\cos(k_x/2)\cos(k_y/2) - 2u(z)] = 0, \quad (1)$$

where $\lambda \equiv \omega^2$ and ω^2 is the squared characteristic frequency of the oscillations. Using the standard form for the solution $u(z) = u_0 \exp[ik_z z/(b/2)]$ we obtain the dispersion law for the vibrations of an ideal lattice. In this part of our exposition we shall examine the low-frequency range $\omega \ll \sqrt{\alpha/m}$, which makes it possible to take into account approximately the dispersion of the waves propagating along the layers. To take account of the the influence of a weak interlayer interaction on the propagation of such waves in the long-wavelength limit, it is sufficient to use in the terms containing the factor γ in the dispersion law the quadratic approximation with respect to the magnitude of the two-dimensional wave vector k. However, since the anisotropy of the system is assumed to be strong ($\gamma \ll \alpha$), the fourth power of k must be taken into account in addition to the second power in the terms containing as a factor the constant α of the strongest interaction in the lattice. The dispersion of the waves propagating perpendicular to the lattice layers must be taken into account more accurately, since the frequencies of these oscillations are of the order of $\sqrt{\gamma/m} \ll \sqrt{\alpha/m}$ and, generally speaking, fall into the frequency range which are studying. In this approximation the dispersion law for waves of an ideal crystal in the direction [100] is

$$\lambda = \frac{1}{m}(\alpha + \gamma \cos k_z)k^2 - \frac{\alpha}{12m}k^4 + \frac{16\gamma}{m}(\sin(k_z/2))^2,$$
$$(2)$$

where $k = k_x$ is the modulus of the two-dimensional wave vector. It is evident from this expression that taking account of terms of the order of $(\gamma/m)k^2$ and $(\alpha/m)^4$ is important in the long-wavelength limit for two-dimensional wave vectors such that $k \lesssim \sqrt{\gamma/\alpha}$. This distinguishes the dispersion law (2) from the dispersion law presented in Ref. 17 for a strongly anisotropic crystal.
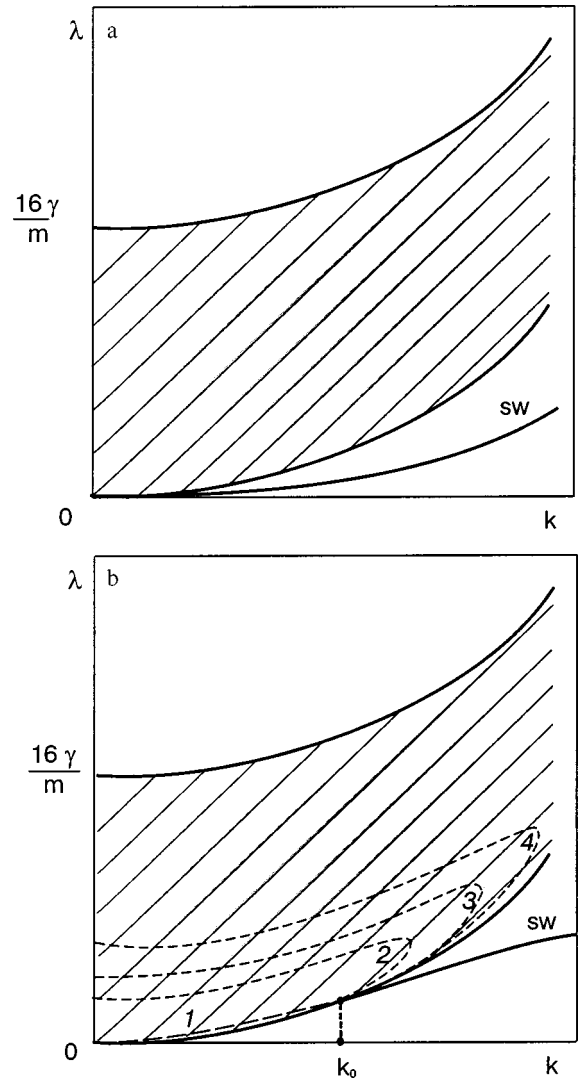

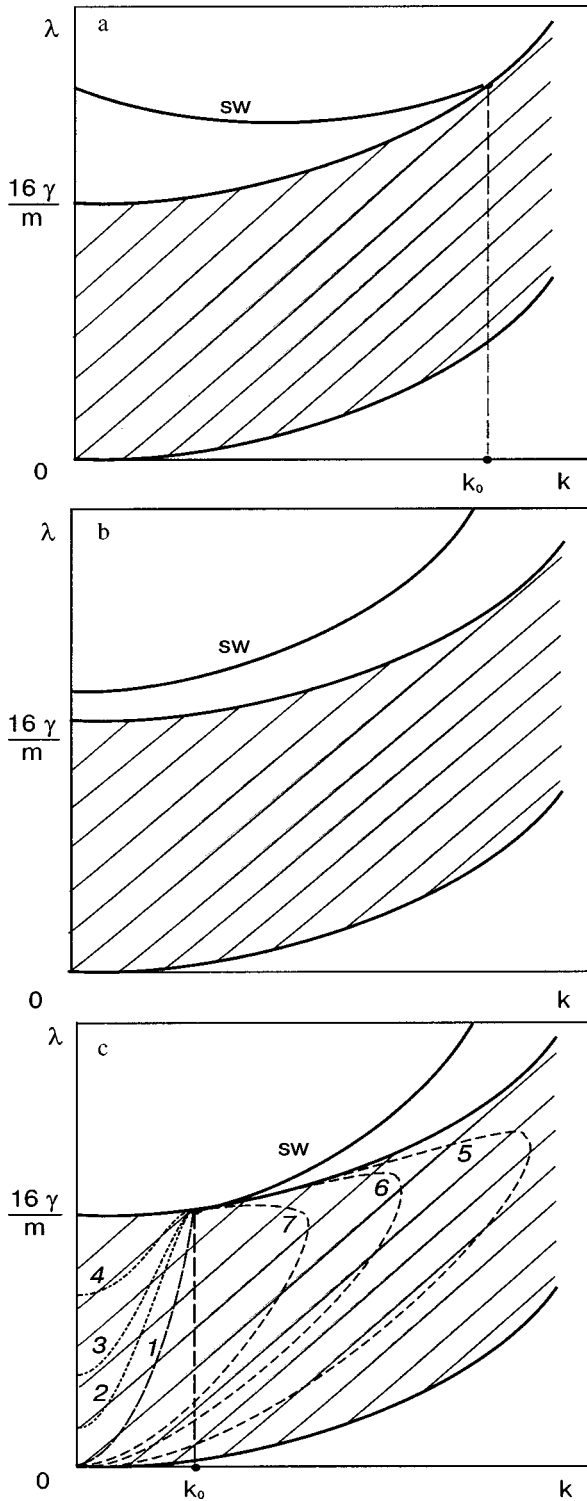FIG. 1. Dispersion curve (SW) corresponding to a surface wave where neighboring layers of the lattice oscillate in phase: a surface wave exists for two-dimensional wave numbers $k > 0$ (a); $k > k_0$ (b). The hatching marks the region of the continuous spectrum of an ideal crystal.

To analyze localized states it is convenient to construct a band in the continuous spectrum of oscillations of an ideal crystal as a function of the two-dimensional wave vector (k_x, k_y) for all possible values of k_z (2). A characteristic feature of such bands in strongly anisotropic layered crystals is that the band width (for any value of k) is determined by the weak interlayer interaction, and the maximum frequency of the oscillations is determined by the strong intralayer interaction, i.e. the band is very narrow and strongly elongated.[18] In Figs. 1 and 2 the hatched region corresponds to a band in the continuous spectrum of oscillations of an ideal crystal in the present model. The bottom $\lambda_{\text{low}}(k)$ and top $\lambda_{\text{top}}(k)$ boundaries of this band are given by the expressions

$$\lambda_{\text{low}}(k) = \frac{1}{m}(\alpha + \gamma)k^2 - \frac{\alpha}{12m}k^4,$$

$$\lambda_{\text{up}}(k) = \frac{1}{m}(\alpha - \gamma)k^2 - \frac{\alpha}{12m}k^4 + \frac{16\gamma}{m}. \quad (3)$$

FIG. 2. Dispersion curve (SW) corresponding to a surface wave where neighboring layers of the lattice oscillate in antiphase: a surface wave exists for two-dimensional wave numbers $k < k_0$ (a); $k > 0$, a gap between the top boundary of the continuous spectrum and the frequency of the localized state exists at $k = 0$ (b); $k > k_0$ (c).

Let us analyze the characteristics of localized states in our geometry. The system of equations which describe the oscillations of an adsorbed monolayer ($z=0$) and the next layer ($z=b/2$) and play the role of boundary conditions for the volume equations (1) has the form

$$\left[\lambda - \frac{\alpha(\zeta_0+1)}{m(\varepsilon+1)}\left(k^2 - \frac{k^4}{12}\right) - \frac{4\gamma}{m(\varepsilon+1)}\right]u(0)$$

$$+ \frac{4\gamma}{m(\varepsilon+1)}\left(1 - \frac{k^2}{8}\right)u\left(\frac{b}{2}\right) = 0,$$

$$\frac{4\gamma}{m}\left(1 - \frac{k^2}{8}\right)u(0) + \left[\lambda - \frac{\alpha}{m}\left(k^2 - \frac{k^4}{12}\right) - \frac{8\gamma}{m}\right]u\left(\frac{b}{2}\right)$$

$$+ \frac{4\gamma}{m}\left(1 - \frac{k^2}{8}\right)u(b) = 0. \tag{4}$$

The solutions decaying into the crystal are

$$u(0) = w,$$

$$u(z) = v q^{(z-b/2)/(b/2)}, \quad z \geq b/2. \tag{5}$$

Here w is the displacement of the adsorbed monolayer, $u(z)$ is the displacement of the layers in the main lattice, and q is a parameter characterizing the damping of the solutions in a direction into the crystal ($|q| < 1$).

Analyzing Eqs. (1) and (4) we obtain surface states of the following types:

1. Surface states with frequencies lying below the band in the continuous spectrum of oscillations of an ideal crystal. Such states can appear if the lattice parameters of the crystal and the defect satisfy $\gamma(2\varepsilon+1) \sim 2\alpha(\zeta_0-\varepsilon)$. For this case the function $q(k)$ in the approximation considered is

$$q(k) = 1 + \frac{2\alpha(\zeta_0-\varepsilon) - \gamma(2\varepsilon+1)}{8\gamma}k^2 - \frac{\alpha(\zeta_0-\varepsilon)}{64\gamma}k^4, \tag{6}$$

and the splitting of the squared frequency of a surface state from the bottom boundary of the band in the continuous spectrum is

$$\Delta\lambda = \lambda_{\text{low}} - \lambda_{\text{loc}} = \frac{4\gamma(1-q)^2}{mq}\cos(k/2). \tag{7}$$

According to the expressions (6) and (7) the magnitude of the splitting $\Delta\lambda$ in the long-wavelength limit is proportional to k^4. This is characteristic for the type of waves under consideration.[16]

The neighboring atoms in the lattice layers oscillate in phase, since $q(k) > 0$. If $\gamma(2\varepsilon+1) > 2\alpha(\zeta_0-\varepsilon)$, then a surface wave exists for all $k > 0$ (Fig. 1a). However, if the opposite inequality holds (i.e. $\gamma(2\varepsilon+1) < 2\alpha(\zeta_0-\varepsilon)$), then a surface wave can exist only for $k > k_0$, where

$$k_0 = 2\sqrt{2\frac{2\alpha(\zeta_0-\varepsilon) - \gamma(2\varepsilon+1)}{\alpha(\zeta_0-\varepsilon)}}. \tag{8}$$

The dispersion curve corresponding to this case is shown in Fig. 1b.

2. Surface states with frequencies lying above the band in the continuous spectrum of oscillations of an ideal crystal. Such states correspond to antiphase displacements of neighboring lattice layers and occur when $\gamma(2\varepsilon+1) \ll 2\alpha(\zeta_0-\varepsilon)$. The corresponding value of the parameter $q(k)$ (in this case $q(k) < 0$) is

$$q(k) = \frac{\varepsilon+1}{\varepsilon} - \frac{\alpha(\zeta_0-\varepsilon)}{8\gamma\varepsilon}k^2, \tag{9}$$

and the splitting of the squared frequency of the surface state from the top boundary of the band in the continuous spectrum is

$$\Delta\lambda = \lambda_{\text{loc}} - \lambda_{\text{up}} = \frac{4\gamma(1+q)^2}{k|q|}\cos(k/2). \tag{10}$$

If the mass of the atoms in the layer on the surface of the crystal is less than half that of the atoms of the crystal itself (i.e. $\varepsilon < -1/2$), then for $k=0$ there is a gap between the frequency of the surface state and the band in the continuous spectrum. Depending on the ratios of the parameters characterizing the adsorbed monolayer, surface states can exist either for wave numbers $k < k_0$ (Fig. 2a) or for all $k > 0$ (Fig. 2b). The first possibility occurs when $\zeta_0 < \varepsilon$ and the second occurs in the opposite case $\zeta_0 > \varepsilon$. The value of k_0 for which the dispersion curve corresponding to a surface wave touches the top boundary of the band in the continuous spectrum is given by

$$k_0 = 2\sqrt{2\frac{\gamma(2\varepsilon+1)}{\alpha(\zeta_0-\varepsilon)}}. \tag{11}$$

However, if the mass of the atoms in the layer is such that $\varepsilon \geq -1/2$, then there is no gap at $k=0$ and surface states can exist only for $k > k_0$ (Fig. 2c). In addition, the same expression (11) determines k_0.

It is also of interest to examine the solutions of Eqs. (1) and (4) that possess frequencies inside the band in the vibrational spectrum of an ideal crystal. These solutions are standing waves (with respect to the coordinate z) and can be written as

$$u(z) = \tilde{w}\cos\left(\frac{z}{(b/2)}k_z + \phi\right). \tag{12}$$

In these expressions $\tilde{w}$ is the amplitude of the vibrations of the crystal layers and ϕ is the phase (an independent parameter of the solutions). The characteristic frequencies corresponding to these solutions are functions of the two variables k and ϕ and can be obtained from the system of equations

$$\lambda m = 2\alpha(1-\cos k) + 8\gamma(1-\cos k_z \cos(k/2));$$

$$(\lambda m(\varepsilon+1) - 2\alpha(\zeta_0+1)(1-\cos k) - 4\gamma)\cos\phi$$

$$+ 4\gamma\cos(k_2+\phi)\cos(k/2) = 0. \tag{13}$$

It is of interest to analyze qualitatively the possible dispersion relations obtained from Eqs. (13) for ϕ in the range $(0,\pi)$. We shall do this for the two cases already examined, when surface states exist with $k > k_0$ (8), (11). First we consider the case corresponding to Fig. 1b. For $\phi=0,\pi$ the dispersion curves are identical to the curve *1* given by the expression

$$\lambda = \frac{4\alpha(2\zeta_0+1)}{m(2\varepsilon+1)}(\sin(k/2))^2. \tag{14}$$

The curves *2*, *3*, and *4*, which approach the top boundary of the continuous spectrum, correspond to systematically increasing ϕ in the range $0 < \phi < \pi/2$. For $\phi = \pi/2$ the dispersion curves merge with the top and bottom boundaries of the continuous spectrum (3). As the parameter ϕ increases further in the range $\pi/2 < \phi < \pi$ dispersion curves will exist only for $0 < k < k_0$ and the corresponding frequencies will be lower than on the curve *1*. As ϕ approaches the limiting value π these curves will tend asymptotically toward the curve *1*.

We shall now consider the case corresponding to Fig. 2c. For $\phi=0,\pi$ the dispersion curves merge with the curve 1 determined by the same expression (14). The typical form of the dispersion curves corresponding to increasing values of the parameter ϕ in the range $0 < \phi < \pi/2$ is presented in this figure for $0 < \phi_1 < \phi_2 < \phi_3 < \pi/2$ (curves *2*, *3*, and *4*). For $\phi = \pi/2$ the dispersion curves merge with the top and bottom boundaries of the continuous spectrum (3). As ϕ increases further in the range $\pi/2 < \phi < \pi$ the curves assume a form similar to that shown in Fig. 2c for $\pi/2 < \phi_4 < \phi_5 < \phi_6 < \pi$ (curves *5*, *6*, and *7*), and as ϕ approaches π these curves asymptotically approach the curve *1*.

Various types of surface waves will be investigated in greater detail in Part 2 below for a vector model of a strongly anisotropic layered crystal exhibiting elastic stability and translational and rotational invariance.

2. SHEAR SURFACE WAVES IN A SEMI-INFINITE, STRONGLY ANISOTROPIC, LAYERED CRYSTAL WITH AN ADSORBED LAYER

In this part of our exposition the formation conditions for and the characteristics of purely shear surface waves localized near a monolayer adsorbed on the surface of a strongly anisotropic layered crystal are studied. We take as a model of the main lattice a body-centered tetragonal structure where the interlayer interaction, being relatively weak, can be described in the nearest-neighbors approximation and is purely central, while the central and noncentral interactions of the nearest and next-to-nearest neighbors are taken into account in the planes of the layers. The force-constants matrices of such a model have the form (the z axis is directed along a four-fold symmetry axis and the x and y axes lie in the plane of the layers)[19,20]

$$\Phi_{ik}(a,0,0) = -\delta_{ik}[\alpha\delta_{i,x} + \beta(\delta_{i,y} + \delta_{i,z})];$$

$$\Phi_{ik}(a,a,0) = -\begin{pmatrix} \alpha' & \xi & 0 \\ \xi & \alpha' & 0 \\ 0 & 0 & \beta' \end{pmatrix};$$

$$\Phi_{ik}\left(\frac{a}{2},\frac{a}{2},\frac{a\Delta}{2}\right) = -\gamma\begin{pmatrix} 1 & 1 & \Delta \\ 1 & 1 & \Delta \\ \Delta & \Delta & \Delta^2 \end{pmatrix}.$$

Here a is the interatomic distance in the plane of the layer; $a\Delta$ is the interatomic distance along the z axis (this axis is perpendicular to the plane of the layers). The parameters β and β' describe the noncentral interaction in the plane of a layer. The condition for the transition to the long-wavelength limit of the lattice-dynamics equations in the equations of the theory of elasticity gives the following relation between these parameters: $\beta = -2\beta'$.[19] The same relation obtains when the boundary oriented along the plane of the layer is stress-free; this allows us to study such a free surface without taking into account the relaxation of the force constants on it.

The parameter γ describes the weak interlayer interaction, and the parameter α describes the strongest (in the crystal) central interaction of nearest neighbors in the plane of

the layer. The quantity α' characterizes the central interaction of the next-to-nearest neighbors in the same plane, and $\xi = \alpha' + \beta/2$.

The matrix $\Phi_{ik}(0,0,0)$ is determined from the translational invariance of the lattice and is given by

$$\Phi_{ik}(0,0,0) = 2(\alpha + 2\alpha' + \beta + 4\gamma)(\delta_{i,x}\delta_{k,x} + \delta_{i,y}\delta_{k,y})$$
$$+ 2(\beta + 4\gamma\Delta^2)\delta_{i,z}\delta_{k,z}.$$

All other matrices can be obtained using the operations of the point symmetry group D_{4h}. The present model is mechanically stable for positive α, α', γ, and ξ and $0 < \beta < \alpha$.

The mass of the atoms in the adsorbed monolayer and the parameters characterizing the interaction in the plane of the layer differ from the corresponding values for the main lattice. The interlayer interaction, being relatively weak, is assumed to be the same for the entire structure. We introduce the following parameters describing the monolayer: $\varepsilon = \tilde{m}/m - 1$, $\zeta_0 = \tilde{\alpha}/\alpha - 1$, $\zeta_1 = \tilde{\alpha}'/\alpha' - 1$, and $\zeta_2 = \tilde{\beta}/\beta - 1$. Here m, α, α', and β denote, respectively, the mass of the atoms, the central interaction of the nearest and next-to-nearest neighbors, the noncentral interaction in the planes of the layers in the main lattice; $\tilde{m}$, $\tilde{\alpha}$, $\tilde{\alpha}'$, and $\tilde{\beta}$ are the analogous quantities for the monolayer.

The equation describing the characteristic oscillations of the crystal lattice can be written in the form

$$\lambda u_i(\mathbf{n}) - \sum_{k,\mathbf{n}'} L_{ik}(\mathbf{n}, \mathbf{n}') u_k(\mathbf{n}') = 0, \qquad (15)$$

where $\lambda \equiv \omega^2$ is the squared characteristic frequency; $u_i(\mathbf{n})$ is the ith component of the displacement of an atom whose position in the lattice is given by the vector $\mathbf{n}$;

$$L_{ik}(\mathbf{n},\mathbf{n}') = \frac{\Phi_{ik}(\mathbf{n},\mathbf{n}')}{(m(\mathbf{n})m(\mathbf{n}'))^{1/2}}$$

is the matrix of a dynamical operator ($\Phi_{ik}(\mathbf{n},\mathbf{n}')$ is the force-constants matrix of the crystal, $m(\mathbf{n})$ is the mass of an atom at the site $\mathbf{n}$). We shall use the translational periodicity of a defective crystal in the xy plane and represent the solution of Eq. (15) in the form

$$u_i(\mathbf{n}) = \chi_i(z)\exp\{i(k_x x + k_y y)\}.$$

This gives the following equation for the function $\chi_i(z)$:

$$\lambda \chi_i(z) - \sum_{k,z'} C_{ik}(k_x, k_y; zz') \chi_k(z') = 0, \qquad (16)$$

where

$$C_{ik}(k_x, k_y; zz') = \sum_{x,y} L_{ik}(x,y;zz')\exp\{-i(k_x x + k_y y)\}.$$

We shall use this approach to study the following problems.

Let the plane where the wave propagates also be a mirror symmetry plane of the crystal. Then, as is well known, the displacement field of the wave can be represented as two noninteracting modes—a single-component SH–type mode (or shear wave) and a two-component mode with Rayleigh polarization.

For single-component displacement fields in an SH wave Eq. (16) acquires the especially simple form $\lambda\chi(z)$

$-\sum_{z'}C(zz')\chi(z')=0$ and the displacement $\chi(z)$ is perpendicular to the direction of propagation of the wave.

For our model of a crystal the mirror symmetry planes are the planes that pass through the directions [10] and [11] of a two-dimensional Brillouin zone perpendicular to the surface of the crystal. We shall study SH waves whose phase velocity vector projected onto the surface of the crystal lies along one of the indicated directions.

A. The direction [10] in a two-dimensional Brillouin zone

The system of equations describing the motion of an adsorbed monolayer is

$$\lambda\chi(0) = C(00)\chi(0) + C(01)\chi(1),$$
$$\lambda\chi(1) = C(10)\chi(0) + C(11)\chi(1) + C(12)\chi(2),$$

where

$$C(00) = \frac{4}{m(\varepsilon + 1)}[\beta(\zeta_2 + 1) + 2\alpha'(\zeta_1 + 1)]$$

$$\times \sin^2(ka/2) + \frac{4\gamma}{m(\varepsilon + 1)},$$

$$C(01) = C(10) = -\frac{4\gamma}{m\sqrt{\varepsilon + 1}}\cos(ka/2),$$

$$C(11) = \frac{4}{m}(\beta + 2\alpha')\sin^2(ka/2) + \frac{8\gamma}{m},$$

$$C(12) = -\frac{4\gamma}{m}\cos(ka/2).$$

We shall seek a solution of these equations that is localized near the surface and has the form $\chi(0) = A$ and $\chi(n) = Bq^{n-1}$, $n > 0$. Here A and B are, respectively, the amplitudes of the vibrations of the adsorbed monolayer and the next layer in the main lattice, q characterizes the damping of the wave in a direction into the crystal ($|q| < 1$), and n is the number of the layer. Depending on the parameters of the adsorbed layer, the following types of localized waves can arise:

1. Localized waves with frequencies below the band in the continuous spectrum of an ideal lattice. Such waves arise if the parameters of the adsorbed layer and the main lattice satisfy the relation $\gamma(2\varepsilon + 1) > \beta(\zeta_2 - \varepsilon) + 2\alpha'(\zeta_1 - \varepsilon)$ (for example, a quite heavy monolayer, where the noncentral interaction and the interaction of next-to-nearest neighbors are weaker than in the interior volume of the crystal or only negligibly stronger, corresponds to this inequality). It is evident from this expression that since the central interaction α' of the next-to-nearest neighbors in the plane of the layer and the noncentral interaction β of nearest neighbors in the same plane appear additively in the formation condition for a localized wave, even though, as a rule, $\beta \sim 0.1\alpha'$, in some cases (for example, when $\zeta_1 \approx \varepsilon$) it may be inadequate to take account of only the stronger central interaction of the next-to-nearest neighbors when analyzing the conditions for the appearance of surface waves. The dependence of q on the monolayer parameters and the two-dimensional wave vector k is given by the relation
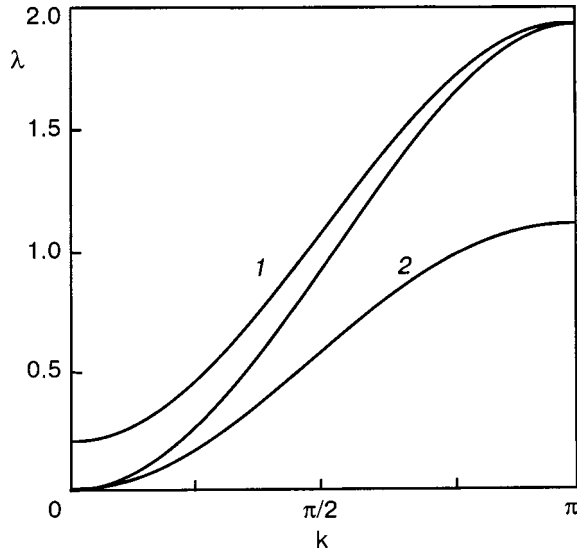
FIG. 3. Region of the continuous spectrum of *SH* oscillations (*1*) and the dispersion curve (*2*) corresponding to a wave localized at the adsorbed monolayer, where the displacements of atoms of neighboring layers in the lattice occur in phase in the wave (the direction [10] in the two-dimensional Brillouin zone).

$$q = \frac{1}{2\gamma\varepsilon\cos(ka/2)}[(\beta(\varepsilon-\zeta_2)+2\alpha'(\varepsilon-\zeta_1)$$

$$\times\sin^2(ka/2)+\gamma(2\varepsilon+1)]-\frac{1}{2\gamma\varepsilon\cos(ka/2)}$$

$$\times\{[(\beta(\varepsilon-\zeta_2)+2\alpha'(\varepsilon-\zeta_1))\sin^2(ka/2)$$

$$+\gamma(2\varepsilon+1)]^2-4\gamma^2\varepsilon(\varepsilon+1)\cos^2(ka/2)\}^{1/2}.$$

Under these conditions $q>0$, which corresponds to localized oscillations where the displacements of the atoms in neighboring layers of the lattice are in phase. The local frequency splits off the bottom boundary of the spectrum of volume *SH* waves (in Fig. 3 the region of the continuous spectrum of *SH* oscillations is labeled by the number *1*). This splitting is given by

$$\Delta\lambda=\lambda_{low}-\lambda_{loc}=\frac{4\gamma(q-1)^2}{mq}\cos(ka/2).$$

If the parameters of the adsorbed monolayer are such that

$$\varepsilon>-1/2; \quad \frac{\gamma(2\varepsilon+1)}{\beta(\zeta_2-\varepsilon)+2\alpha'(\zeta_1-\varepsilon)}<2, \tag{17}$$

then the dispersion curve corresponding to a wave localized in space splits off near $k=0$ (Fig. 3, curve *2*). In this region the expression for q is

$$q=1-\frac{k^2a^2}{8\gamma}[2\beta(\varepsilon-\zeta_2)+4\alpha'(\varepsilon-\zeta_1)+\gamma(2\varepsilon+1)],$$

and the corresponding splitting off of the frequency is

$$\Delta\lambda=\frac{k^4a^4}{16\gamma m}[2\beta(\varepsilon-\zeta_2)+4\alpha'(\varepsilon-\zeta_1)+\gamma(2\varepsilon+1)]^2.$$

The quantity $\Delta\lambda$ in the long-wavelength limit $(ka\ll1)$ is small enough $(\sim(ka)^4)$ so that a wave of the type we are considering here cannot be described on the basis of the or-

dinary local theory of elasticity. This is why surface waves penetrate deep into the crystal.[3] Conversely, if the inequalities (17) do hold, then the spectrum of surface waves terminates at a point different from $k=0$ (a termination point is a value of k from the range considered $(0,\pi/a)$ at which the dispersion curve corresponding to a localized wave enters the continuous spectrum of volume oscillations). This point is given by

$$k_0=(4/a)\arccos\left\{\frac{\gamma(2\varepsilon+1)}{2\beta(\zeta_2-\varepsilon)+4\alpha'(\zeta_1-\varepsilon)}\right\}^{1/2}.$$

The splitting-off $\Delta\lambda$ is determined primarily only by the weak interlayer interaction, and the corresponding surface waves are deeply penetrating waves. The maximum of the splitting-off

$$\Delta\lambda=\frac{4}{m(\varepsilon+1)}(\beta(\varepsilon-\zeta_2)+2\alpha'(\varepsilon-\zeta_1)+\gamma(2\varepsilon+1))$$

is reached at the boundary of a two-dimensional Brillouin zone $(k=\pi/a)$. Near this point q is given by

$$q=\frac{\gamma(\varepsilon+1)\cos(ka/2)}{\beta(\varepsilon-\zeta_2)+2\alpha'(\varepsilon-\zeta_1)+\gamma(2\varepsilon+1)}.$$

Vanishing of q at the boundary of the zone corresponds to complete localization of oscillations in the plane of the adsorbed monolayer.

2. Localized waves with frequencies above the band in the continuous spectrum of an ideal crystal. Such waves can arise if the parameters of the adsorbed layer and the main lattice satisfy the relation

$$\gamma(2\varepsilon+1)<\beta(\zeta_2-\varepsilon)+2\alpha'(\zeta_1-\varepsilon)$$

(for example, a light monolayer where noncentrality and the interaction of next-to-nearest neighbors are much stronger than in the main lattice). Then q is given by

$$q=\frac{1}{2\gamma\varepsilon\cos(ka/2)}[(\beta(\varepsilon-\zeta_2)+2\alpha'(\varepsilon-\zeta_1))$$

$$\times\sin^2(ka/2)+\gamma(2\varepsilon+1)]+\frac{1}{2\gamma\varepsilon\cos(ka/2)}$$

$$\times\{[(\beta(\varepsilon-\zeta_2)+2\alpha'(\varepsilon-\zeta_1))\sin^2(ka/2)$$

$$+\gamma(2\varepsilon+1)]^2-4\gamma^2\varepsilon(\varepsilon+1)\cos^2(ka/2)\}^{1/2}.$$

The function $q(k)$ is negative-definite in the entire range $(0,\pi/a)$ considered. This corresponds to localized oscillations where the displacements of the atoms in neighboring layers in the lattice occur in antiphase. The splitting-off from the dispersion curve corresponding to these oscillations occurs from the top boundary of volume *SH* oscillations and is given by

$$\Delta\lambda=\lambda_{loc}-\lambda_{up}=\frac{4\gamma(q+1)^2}{m|q|}\cos(ha/2).$$

If the crystal surface is covered with a light layer of adsorbed atoms and $\varepsilon\leqslant-1/2$, then the spectrum of surface waves has no termination point and $\lambda_{loc}\neq\lambda_{up}$ at $k=0$ [Fig. 4a, curve *2*; the band of volume oscillations (*1*)]. For wave numbers $k\to+0$ the behavior of q is given by
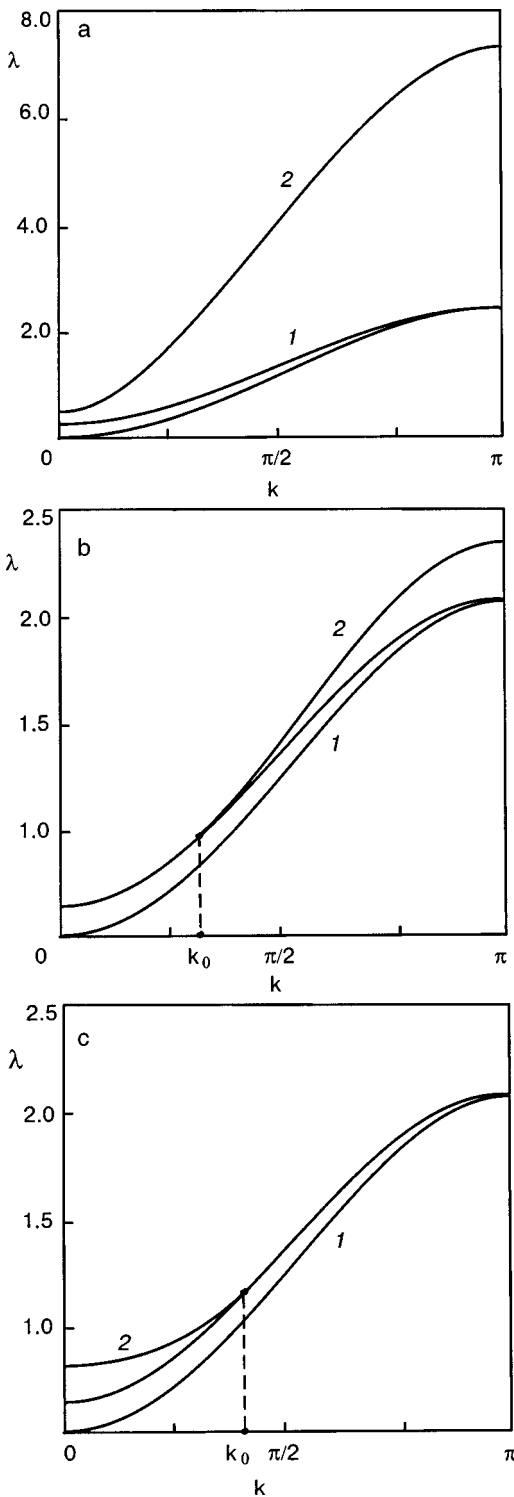
FIG. 4. Region of the continuous spectrum of *SH* oscillations (*1*) and the dispersion curve (2) corresponding to localized oscillations where the displacements of atoms in neighboring layers in the lattice occur in antiphase (the direction [10] in a two-dimensional Brillouin zone). The oscillations localized near a defect exist for all values of k (a); $k>k_0$ (b); $k<k_0$ (c).

$$q = \frac{\varepsilon+1}{\varepsilon} + \frac{\varepsilon+1}{8\gamma\varepsilon}[2\beta(\varepsilon-\zeta_2)+4\alpha'(\varepsilon-\zeta_1)$$

$$+ \gamma(2\varepsilon+1)](ka)^2. \qquad (18)$$

The splitting-off of the frequency in the same region is

$$\Delta\lambda = \frac{4\gamma(2\varepsilon+1)^2}{m|\varepsilon|(\varepsilon+1)} + (ka)^2\frac{2\varepsilon+1}{m|\varepsilon|(\varepsilon+1)}$$

$$\times[\beta(\varepsilon-\zeta_2)+2\alpha'(\varepsilon-\zeta_1)+\gamma(2\varepsilon+1)], \qquad (19)$$

and if $\varepsilon=-1/2$, then

$$\Delta\lambda = \frac{(ka)^4}{16\gamma m}[2\beta(\varepsilon-\zeta_2)+4\alpha'(\varepsilon-\zeta_1)+\gamma(2\varepsilon+1)]^2.$$

If $\varepsilon>-1/2$ (the mass of an atom in the adsorbed monolayer is greater than half the mass of an atom in the main crystal), then the spectrum has a termination point given by

$$k_0 = \frac{4}{a}\arcsin\left\{\frac{\gamma(2\varepsilon+1)}{2\beta(\zeta_2-\varepsilon)+4\alpha'(\zeta_1-\varepsilon)}\right\}^{1/2}. \qquad (20)$$

Oscillations localized near the surface of the crystal exist for $k>k_0$ (Fig. 4b, curve *2*). The splitting-off reaches its maximum magnitude at the boundary of a two-dimensional Brillouin zone ($k=\pi/a$) and is given by

$$\Delta\lambda = \frac{4}{m(\varepsilon+1)}(\beta(\zeta_2-\varepsilon)+2\alpha'(\zeta_1-\varepsilon)-\gamma(2\varepsilon+1)).$$

Near this point the behavior of q is identical to that when the frequency of localized waves lies below the band in the continuous spectrum of an ideal lattice.

Waves existing for two-dimensional wave vectors $0\leq k \leq k_0$ (Fig. 4c, curve *2*), where k_0 is given by the expression (20), also can appear. This situation is observed when the parameters of the monolayer and the crystal satisfy

$$\gamma(2\varepsilon+1)>\beta(\zeta_2-\varepsilon)+2\alpha'(\zeta_1-\varepsilon), \quad \varepsilon<-1/2.$$

The expressions (18) and (19) describe the behavior of q and $\Delta\lambda$ near the point $k=0$.

B. The direction [11] in a two-dimensional Brillouin zone

In the direction [11] in a two-dimensional Brillouin zone the conditions for the formation of waves localized near an adsorbed monolayer are more diverse than in the preceding case. But, generally speaking, there are no qualitative peculiarities compared with the analysis performed above. However, there is an interesting, in our opinion, exception where the spectrum of surface waves possesses two termination points in the continuous spectrum of volume *SH* oscillations. This feature of the spectrum is due to the specific manifestation of a noncentral interaction in the lattice and is not observed in the absence of such an interaction. This effect can exist only under special conditions where a number of limitations imposed on the parameters of the surface monatomic layer and the main lattice are satisfied. These limitations, incidently, are not too strong and can be easily satisfied for actually existing structures:

$$\begin{cases} \beta(\varepsilon-\zeta_2)>0, \ \gamma(2\varepsilon+1)\geq 0 \\ -3\beta(\varepsilon-\zeta_2<\alpha(\varepsilon-\zeta_0)<\beta(\varepsilon-\zeta_2) \\ \alpha(\varepsilon-\zeta_0)+\beta(\varepsilon-\zeta_2)+2\gamma(2\varepsilon+1)\geq 0 \\ 16\beta\gamma(\varepsilon-\zeta_2)(2\varepsilon+1)<[\alpha(\varepsilon-\zeta_0)-\beta(\varepsilon-\zeta_2)]^2. \end{cases}$$

A wave localized at an adsorbed layer exists in the range $k \in (k_1,k_2)$, where $k_i=(2/a)\arcsin(\sqrt{x_i})$, $i=1,2$; $x_i= -(B/2A)[1\mp\sqrt{1-(4AC/B^2)}]$ (here the $-$ and $+$ signs correspond to $i=1,2$). The parameters A and B in these ex-
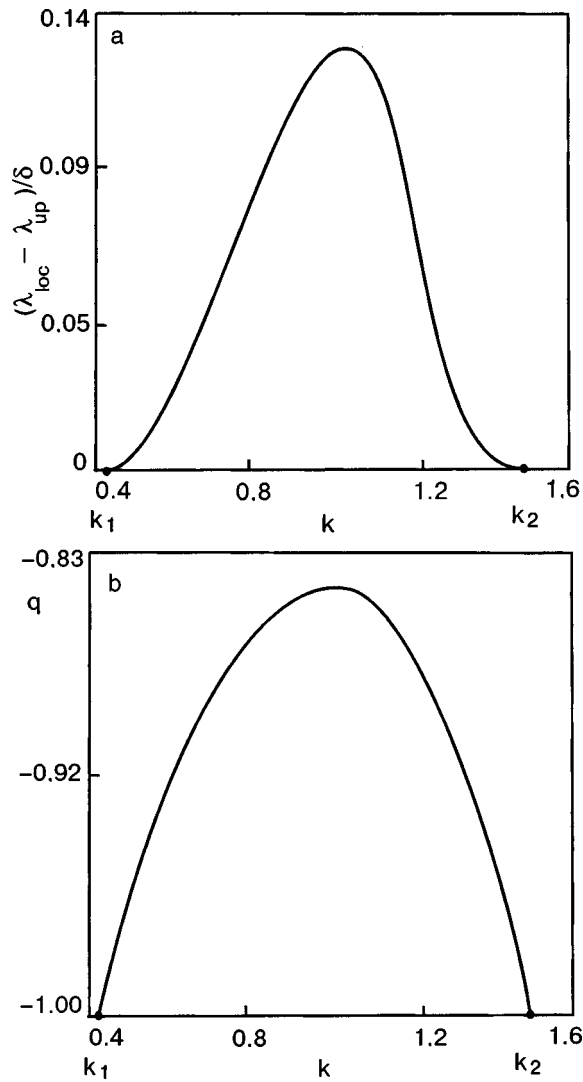
The magnitude of the splitting-off $\Delta\lambda$ is determined primarily by the noncentral and interlayer interaction and as a result it is relatively small. Its dependence on the two-dimensional wave vector k is shown in Fig. 5a ($\Delta\lambda = \lambda_{\text{loc}} - \lambda_{\text{up}}$ is normalized to $\delta = \gamma/m$). Figure 5b shows the dependence of the damping parameter $q(k)$ of the wave for the case in Fig. 5a. In this figure $q(k) = -1$ at the two points $k_1 \approx 0.4$ and $k_2 \approx 1.5$; this corresponds to a transition of an *SH* surface wave into a volume wave propagating undamped into the crystal. Thus, when the noncentral interaction is taken into account, for certain ratios of the parameters of the main lattice and the adsorbed layer an *SH* wave localized at the surface can exist only for a definite interval (k_1, k_2) of projections of the wave vector on the [11] direction in the two-dimensional Brillouin zone.

[*]E-mail: syrkin@ilt.kharkov.ua

FIG. 5. The magnitude of the splitting-off $\Delta\lambda$ versus the wave number k (the direction [11] in a two-dimensional Brillouin zone, $\Delta\lambda = \lambda_{\text{loc}} - \lambda_{\text{up}}$ is normalized to $\delta = \gamma/m$, $k_1 \approx 0.4$ and $k_2 \approx 1.5$ are termination points of the spectrum of a localized wave) (a). The damping parameter $q(k)$ for the case in panel a (b).

pressions are given by $A = 2\beta(\varepsilon - \zeta_2)$, $B = \alpha(\varepsilon - \zeta_0) - \beta(\varepsilon - \zeta_2)$, and $C = 2\gamma(2\varepsilon + 1)$. The damping constant of this wave is

$$q = \frac{1}{2\gamma\varepsilon}[(\alpha(\varepsilon - \zeta_0) - \beta(\varepsilon - \zeta_2)\cos(ka))\sin^2(ka/2)$$

$$+ \gamma 2\varepsilon + 1)] + \frac{1}{2\gamma\varepsilon}\{[(\alpha(\varepsilon - \zeta_0)$$

$$- \beta(\varepsilon - \zeta_2)\cos(ka))\sin^2(ka/2) + \gamma(2\varepsilon + 1)]^2$$

$$- 4\gamma^2\varepsilon(\varepsilon + 1)\}^{1/2}.$$

[1] *Dynamics of Solids and Liquids by Neutron Scattering*, edited by S. W. Lovesey and T. Springer, Springer-Verlag, New York (1977).
[2] G. Benedek, F. Hofmann, P. Ruggerone, G. Onida, and L. Miglio, Surf. Sci. Rep. **20**, 1 (1994).
[3] I. M. Gel'fgat and E. S. Syrkin, Fiz. Nizk. Temp. **4**, 672 (1978) [Sov. J. Low Temp. Phys. **4**, 324 (1978)].
[4] S. V. Gerus, I. E. Dikshteĭn, V. V. Tarasenko, and V. D. Kharitonov, Fiz. Tver. Tela (Leningrad) **19**, 218 (1977) [Sov. Phys. Solid State **19**, 124 (1977)].
[5] Yu. A. Kosevich, O. Yu. Serdobol'skaya, and E. S. Syrkin, Ferroelectrics **75**, 409 (1987).
[6] J. L. Bleustein, Appl. Phys. Lett. **13**, 412 (1968).
[7] Yu. V. Gulyaev, JETP Lett. **9**, 37 (1969).
[8] G. P. Alldredge, Phys. Lett. A **41**, 281 (1972).
[9] I. M. Gel'fgat, Fiz. Tver. Tela (Leningrad) **19**, 1711 (1977) [Sov. Phys. Solid State **19**, 998 (1977)].
[10] Yu. A. Kosevich and E. S. Syrkin, Pis'ma Zh. Tekh. Fiz. **13**, 1439 (1987) [Sov. Tech. Phys. Lett. **13**, 602 (1987)].
[11] A. N. Dariskii and W. Weinacht, J. Appl. Phys. **90**, 383 (2001).
[12] Ken-ya Hashimoto, *Surface Acoustic Wave Devices in Telecommunications*, Springer-Verlag, Heidelberg (2000).
[13] Yu. A. Kosevich and E. S. Syrkin, J. Phys.: Condens. Matter **2**, 5047 (1990).
[14] M. V. Voĭnova, A. M. Kosevich, and E. S. Syrkin, Akust. Zh. **39**, 944 (1993) [Acoust. Phys. **39**, 500 (1993)].
[15] V. I. Peresada and E. S. Syrkin, Fiz. Nizk. Temp. **3**, 250 (1977) [Sov. J. Low Temp. Phys. **3**, 110 (1977)].
[16] I. M. Lifzhitz and A. M. Kosevich, Rep. Prog. Phys. **29**, 217 (1966); I. M. Lifshitz, *Selected Works. Physics of Real Crystals and Disordered Systems*, Nauka, Moscow (1987).
[17] A. M. Kosevich, *Crystal Lattice Theory*, Vishcha Shkola, Khar'kov (1988).
[18] E. S. Syrkin and I. M. Gel'fgat, Fiz. Nizk. Temp. **5**, 181 (1979) [Sov. J. Low Temp. Phys. **5**, 87 (1979)].
[19] E. S. Syrkin, S. B. Feodos'ev, and O. Ya. Shamfarova, Fiz. Nizk. Temp. **17**, 746 (1991) [Sov. J. Low Temp. Phys. **17**, 393 (1991)].
[20] A. M. Kosevich, E. S. Syrkin, and S. B. Feodosyev, Phys. Low-Dimens. Semicond. Struct. **3**, 47 (1994).

Translated by M. E. Alferieff

Heat transfer by low-frequency phonons and "diffusive" modes in molecular crystals

V. A. Konstantinov*

B. Verkin Institute for Low Temperature Physics and Engineering, National Academy of Sciences of Ukraine, pr. Lenian, 47, 61103 Khar'kov, Ukraine

A model where low-frequency phonons and, above the mobility limit, "diffusive" modes migrating randomly from site to site transfer heat is proposed to describe the behavior of the isochoric thermal conductivity of molecular crystals in orientationally ordered phases. The mobility limit ω_0 is found from the condition that the phonon mean-free path length determined by umklapp processes cannot become less than half the wavelength. The Bridgman coefficient $g = -(\partial \ln \Lambda / \partial \ln V)_T$ is the weighted-mean over these modes, whose volume dependence differs strongly. The model proposed here is used to analyze the thermal conductivity of CO_2, N_2O, naphthalene $C_{10}H_8$, anthracene $C_{14}H_{10}$, and hexamethylenetetramine $(CH_2)_6N_4$. It is shown that site-to-site rotational energy transfer must be taken into account in order to calculate the lower limit of the thermal conductivity of molecular crystals. © *2003 American Institute of Physics.* [DOI: 10.1063/1.1542506]

Dedicated to my teacher and the coauthor of most works V. G. Manzheliĭ, Academician of the Ukrainian National Academy of Sciences, who determined, in many respects, the development of this line of research.

1. INTRODUCTION

It is commonly supposed that phonons, which are the energy quanta of each vibrational mode, transfer heat in dielectric crystals; the rate of energy transfer between the phonons of different modes determines the mean-free path length. At temperatures of the order of and above the Debye temperatures ($T \geq \Theta_D$) the following expression is ordinarily used for the thermal conductivity:[1,2]

$$\Lambda = K \frac{ma\Theta_D^3}{\gamma^2 T}, \tag{1}$$

where m is the average atomic (molecular) mass, a^3 is the volume per atom (molecule), $\gamma = -(\partial \ln \Theta_D / \partial \ln V)_T$ is the Grüneisen parameter, and K is a structure factor. In order for the law $\Lambda \propto 1/T$ to hold the crystal volume must remain constant, otherwise the vibrational modes (and with them Θ_D, a, and γ) will change and this will change the temperature dependence of the thermal conductivity. This condition is especially important for molecular crystals, whose thermal expansion coefficients are large. The dependence of the thermal conductivity on the specific volume can be described using Bridgman's coefficient[2,3]

$$g = -(\partial \ln \Lambda / \partial \ln V)_T. \tag{2}$$

It follows from Eqs. (1) and (2) that for crystals

$$g = 3\gamma + 2q - 1/3, \tag{3}$$

where $q = (\partial \ln \gamma / \partial \ln V)_T$. Ordinarily, it is assumed that at temperatures of the order of and above the Debye temperatures $\gamma \propto V$ and the second Grüneisen coefficient $q \approx 1$.[2,3]

As the temperature increases, phonon–phonon scattering processes intensify and the mean-free path length l decreases but it cannot become less than half the phonon wavelength

$\lambda/2$.[4] If all vibrational modes disperse in a distance of the order of $\lambda/2$, the thermal conductivity reaches its lower limit Λ_{min}:

$$\Lambda_{min} = \frac{1}{2}\left(\frac{\pi}{6}\right)^{1/3} k_B n^{2/3}(v_l + 2v_t), \tag{4}$$

where v_l and v_t are, respectively, the longitudinal and transverse sound velocities and $n = 1/a^3$ is the number of atoms per unit volume. At constant volume the lower limit of the lattice thermal conductivity should not depend on temperature for $T \geq \Theta_D$, while at the saturated vapor pressure Λ_{min} can be weakly temperature-dependent because of the temperature dependence of n, v_l, and v_t. Using the polarization-averaged sound velocity and $\Theta_D = v(\hbar/k_B)(6\pi^2 n)^{1/3}$ we obtain $\Lambda_{min} \propto \Theta_D/a$ and

$$g = \gamma + 1/3. \tag{5}$$

The thermal conductivity reaches its lower limit Λ_{min} in amorphous solids and strongly disordered crystals.[2,4] The values of the Bridgman coefficient, on the whole, are correlated with the structure: as structural disorder increases, g decreases; the thermal conductivity is least density-dependent in glasses and polymers.[3] There arises the question of whether or not three-phonon scattering processes in themselves result in Λ_{min} in perfect crystals as temperature increases. To find an answer we shall compare the thermal conductivity Λ_{meas} of a number of crystals with different types of chemical bonds and the lower limit of the thermal conductivity Λ_{min} at the corresponding melting temperatures (Fig. 1). The data on the thermal conductivity of molecular crystals are taken from the works of the present author and Ref. 3; for all other substances the data are taken from Refs. 2 and 5–7. The densities and sound velocities required to calculate Λ_{min} are taken from Refs. 7–9.
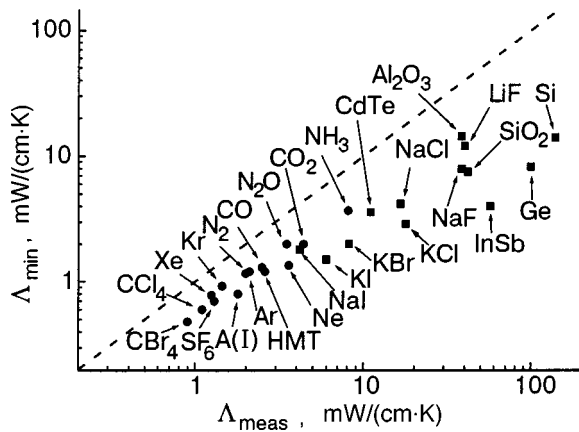
FIG. 1. Comparison of the thermal conductivity Λ_{meas} of a number of molecular crystals (●) and crystals with other types of chemical bond (■) with a lower limit of thermal conductivity Λ_{min} with the corresponding melting temperatures.

It is evident that the ratio $\Lambda_{meas}/\Lambda_{min}$ increases as the crystal bond becomes stronger. In van–der–Waals crystals $\Lambda_{meas}/\Lambda_{min} \approx 1.5$–2, while in crystals with diamond-type structure $\Lambda_{meas}/\Lambda_{min} \approx 10$–20, i.e. molecular crystals and solidified inert gases are the most suitable objects for observing the thermal conductivity "minimum" due only to umklapp processes. Strong deviations of the isochoric thermal conductivity from $\Lambda \propto 1/T$, which are associated with the thermal conductivity approaching its lower limit, have been observed in solidified inert gases, simple molecular crystals, and their solutions.[10–14] The behavior of the isochoric thermal conductivity of solidified inert gases Ar, Kr, and Xe and krypton–methane solid solutions has been described quantitatively on the basis of a simple model that takes account of the fact that the phonon mean-free path length cannot become less than half the wavelength.[13–15] In the present paper it is shown for CO_2, N_2O, hexamethylenetetramine $(CH_2)_6N_4$, naphthalene $C_{10}H_8$, and anthracene $C_{14}H_{10}$ that the proposed model describes well the temperature and volume dependences of the thermal conductivity of simple molecular crystals in orientationally ordered phases.

2. MODEL

The present calculations were performed on the basis of the Debye model of thermal conductivity[1,16] in the spirit of the approach used by Roufosse and Klemens,[17] who employed the idea of a lower limit for the phonon mean-free path. In the Debye model the thermal conductivity Λ is given by

$$\Lambda = \frac{k_B}{2\pi^2 v^2} \int_0^{\omega_D} l(\omega)\omega^2 d\omega, \tag{6}$$

where v is the velocity of sound, $\omega_D = (6\pi^2)^{1/3}v/a$ is the Debye frequency, $l(\omega)$ is the phonon mean-free path, which for an impurity-free crystal can be written as[1,18]

$$l_u(\omega) = v/A\omega^2 T, \tag{7}$$

$$A = \frac{18\pi^3}{\sqrt{2}}\frac{k_B\gamma^2}{ma^2\omega_D^3}. \tag{8}$$

The expression (7) is inapplicable if $l(\omega)$ is of the order of or less than half the phonon wavelength: $\lambda/2 = \pi v/\omega$. Such a situation has been discussed for U processes.[17] Let us assume that in general

$$l(\omega) = \begin{cases} v/A\omega^2 T, & 0 \leqslant \omega \leqslant \omega_0, \\ \alpha\pi v/\omega = \alpha\lambda/2, & \omega_0 < \omega \leqslant \omega_D, \end{cases} \tag{9}$$

where α is a numerical factor of the order of 1. The frequency ω_0 can be found from the condition

$$v/A\omega_0^2 T = \alpha\pi v/\omega_0. \tag{10}$$

It equals

$$\omega_0 = 1/\alpha\pi AT. \tag{11}$$

The condition (10) is the well-known Ioffe–Regel' criterion, which presumes localization, so that we shall assume excitations whose frequencies lie above the phonon mobility limit ω_0 to be "localized." Since completely localized states do not contribute to the thermal conductivity, localization is assumed to be weak and excitations can hop from site to site in a diffusion manner, as Cahill and Pohl supposed.[4] This point of view is, on the whole, consistent with the results of Ref. 19, where the theory for the intermediate case (where disorder is sufficient for oscillations not to propagate but insufficient for localization) was formulated for amorphous silicon. The idea was that the dominant scattering was correctly described by a harmonic Hamiltonian and reduced to a single-particle problem of decoupled oscillators. On this basis the thermal conductivity could be calculated exactly using a formula similar to the Kubo–Greenwood formula for the electric conductivity of disordered metals. The calculations performed by the authors showed that in this case it is incorrect to identify the Ioffe–Regel' threshold with localization. Although the oscillations dominating in high-temperature heat transfer lie near the Anderson localization threshold, with the exception of a narrow band of states they are not completely localized.

The Boltzmann theory assigns to each vibrational mode with wave vector **k** and propagation velocity $\mathbf{v} = \partial\omega/\partial\mathbf{k}$ a diffuseness $D_k = vl/3$, where l is the mean-free path length. The authors found that even though vibrations are not localized, a definite wave vector or velocity cannot be assigned to them. Nonetheless, they transfer heat and contribute to the thermal conductivity an amount of the order of $C_i(T)D_i/V$ for the ith mode, where the specific heat $C_i(T) = k_B$ for $T \geqslant \Theta_D$ and D_i is the temperature-independent "diffuseness" of the mode. The numerical calculation is in many respects similar to the calculation performed according to Boltzmann's theory and it confirms the concept of a "lower limit" for the thermal conductivity in the form in which it is discussed by Slack[2] and Cahill, Watson, and Pohl.[4]

If $\omega_0 > \omega_D$, then the mean-free path length of all modes is greater than $\lambda/2$ and the thermal conductivity is

$$\Lambda_{ph} = \frac{k_B\omega_D}{2\pi^2 vAT}. \tag{12}$$

It is easy to show that, to within a structure factor, it is identical to Eq. (1).

If $\omega \leqslant \omega_D$, the integral of the thermal conductivity (6) separates into two parts which describe the contributions of low-frequency phonons and high-frequency "diffusive" modes to heat transfer:

$$\Lambda = \Lambda_{ph} + \Lambda_{loc}. \tag{13}$$

In the high-temperature limit ($T \geqslant \Theta_D$) these contributions are

$$\Lambda_{ph} = \frac{k_B \omega_0}{2 \pi^2 v A T}, \tag{14}$$

$$\Lambda_{loc} = \frac{\alpha k_B}{4 \pi v} (\omega_D^2 - \omega_0^2). \tag{15}$$

The problem of determining the Bridgman coefficient in the present model reduces to finding the volume derivative of the expression (13). Since $(\partial \ln A / \ln V)_T = 3\gamma + 2q - 2/3$, we obtain

$$g = \frac{\Lambda_{ph}}{\Lambda} g_{ph} + \frac{\Lambda_{loc}}{\Lambda} g_{loc}, \tag{16}$$

where

$$g_{ph} = 5\gamma + 4q - 1, \tag{17}$$

$$g_{loc} = -\left(\frac{\partial \ln \Lambda_{loc}}{\partial \ln V} \right)_T$$

$$= -\gamma + \frac{1}{3} + \frac{2}{\omega_D^2 - \omega_0^2} (\omega_D^2 \gamma - \omega_0^2 \gamma_0), \tag{18}$$

$$\gamma_0 = 3\gamma + 2q - 1/3. \tag{19}$$

For $\omega_0 \geqslant \omega_D$ the expression (3) gives the volume dependence of the thermal conductivity.

Substituting the expression (11) into Eq. (15), the thermal conductivity for $\omega_0 \leqslant \omega_D$ can be written as

$$\Lambda(T) = \frac{k_B}{4 \alpha \pi^3 v A^2 T^2} + \frac{(6\pi^2)^{2/3} \alpha k_B v}{4 \pi a^2}. \tag{20}$$

It is easy to show that the last term in the expression (20) is identical to the lower limit of the thermal conductivity (4), if the polarization-averaged sound velocity and $\alpha = 1$ are used.

3. RESULTS AND DISCUSSION

Crystals containing molecules or molecular ions are more complicated than crystals containing only atoms and ions, since the former possess translational and orientational degrees of freedom. They can form phases of a special type, for example, liquid crystals and orientationally disordered phases. If the noncentral forces are strong and the temperature sufficiently low, then long-range orientational order exists in the arrangement of the molecular axes. Molecules undergo small oscillations around selected axes (librations) in a manner so that the motion of neighboring molecules is correlated and collective orientational excitations (librons) propagate through the crystal. The main difficulty in describing the orientational subsystem is the strong anharmonicity of librational motions. Estimates of the libration amplitudes and analysis of the thermodynamic properties of molecular crystals show that anharmonic effects for the rotational sub-

system are strong even at temperatures much below the orientational ordering temperatures of these crystals, while translational vibrations can be described quite well in the harmonic approximation.[9]

In general, translational and orientational motions in molecular crystals are not independent of one another, but rather they occur as coupled translational–orientational vibrations. Nonetheless, at sufficiently low temperatures a simplified model where the translational and orientational subsystems are described independently is often used. In such a description it is assumed that the translational–orientational interaction results only in a renormalization of the dispersion law for the rotational excitations and, correspondingly, the sound velocities. In this approximation the librational oscillations result in an additional contribution to the thermal resistivity of the crystal $W = 1/\Lambda$, which increases as temperature so that their contribution can be taken into account by a simple renormalization of the coefficient A in the expression (7).[20]

If noncentral forces are relatively weak and the temperature is sufficiently high, then the molecules can possess substantial orientational freedom. In this case a number of orientations are accessible to a molecule, which can pass from one orientation to another. In individual cases the limit of such reorientational motion can be a continuous rotation. Unfreezing of the rotational motion of molecules is accompanied by an increase in the isochoric thermal conductivity,[21] and the simple expression (7) no longer describes the mean-free path length. We shall illustrate this for some specific examples.

Crystals of CO_2 and N_2O consist of linear molecules and have a $Pa3$ structure. The unit cell contains four molecules, whose centers of gravity lie at the sites of an fcc lattice, and the axes are oriented along the spatial diagonals of a cube. The noncentral part of the intermolecular interaction in these crystals is determined primarily by the quadrupole–quadrupole interaction. In CO_2 and N_2O this interaction is so strong that orientational ordering remains right up to the melting temperatures. The high-temperature values Θ_D^∞ for CO_2 and N_2O are 128 and 120 K, respectively, and the triple-point temperatures are 216.6 and 182.4 K.[9]

The isochoric thermal conductivity of CO_2 and N_2O for crystals with molar volumes $V_m = 25.8$ and 27.02 cm^3/mole are shown in Fig. 2 (filled squares), following Ref. 11. Such volumes correspond to equilibrium conditions at 0 K. The Bridgman coefficients for CO_2 and N_2O are 5.7 ± 0.8 and 6.2 ± 0.8 at the corresponding temperatures.

A least-squares computer fit using the expression (20) for the thermal conductivity was made by varying the coefficients A and α. The parameters a and v in the Debye model of thermal conductivity,[9] which are used in the fit and also obtained by adjusting A and α, are presented in Table I together with the computed and experimentally obtained Bridgman coefficients. The figure also shows the Grüneisen constants γ,[9] which were used to calculate g. The second Grüneisen constant q was assumed to be 1.[3]

Figure 2 shows the results of fitting the thermal conductivity, the contributions Λ_{ph} and Λ_{loc} of low-frequency phonons and high-frequency "diffusive" modes, respectively, calculated using Eqs. (14) and (15), to the heat transfer, and the lower limits Λ'_{min} obtained for the thermal con-
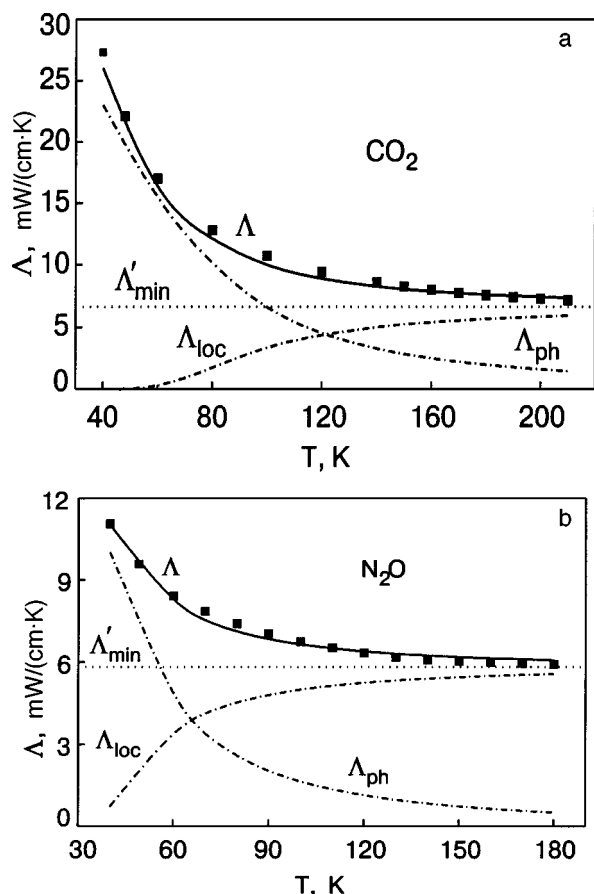
FIG. 2. Results of a fit of the isochoric thermal conductivity and calculation of Λ_{ph} and Λ_{loc} for CO_2 samples with molar volume $V_m = 25.8$ cm^3/mole (a) and N_2O with $V_m = 27.02$ cm^3/mole (b).

ductivity by fitting. It is evident that "localization" of high-frequency modes in CO_2 starts above 60 K and in N_2O appreciably sooner—at 30 K. Similar methods were used to calculate the contributions of low-frequency phonons and high-frequency "diffusive" modes to heat transfer in hexamethylenetetramine $(CH_2)_6N_4$, naphthalene $C_{10}H_8$, and anthracene $C_{14}H_{10}$.

Hexamethylenetetramine (HMT) is a high-symmetry organic crystal which is often compared to adamantane. Even though the molecules are similar (they are both globular), their crystal properties differ enormously. Right up to the
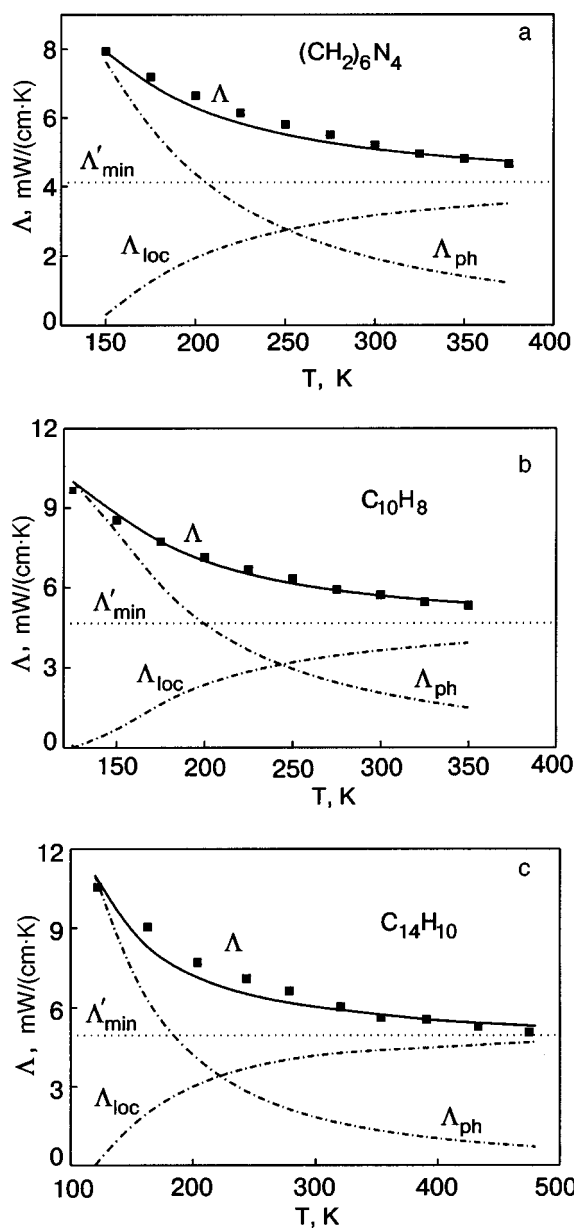

FIG. 3. Results of fitting the isochoric thermal conductivity and calculation of Λ_{ph} and Λ_{loc} for HMT samples with molar volume $V_m = 101.5$ cm^3/mole (a), naphthalene with $V_m = 103.3$ cm^3/mole (b), and anthracene with $V_m = 138.6$ cm^3/mole (c).

triple-point temperature $T_t \sim 540$ K HMT exists only in a single orientationally ordered crystalline phase with bcc structure of the space group $I\bar{4}3m$ and contains one molecule per unit cell.[22] Although HMT molecules are nonpolar, it is thought that there exist strictly directed forces between these molecules in the crystal as a result of local polarity concentrated on the nitrogen atoms. The Debye temperature of HMT is 170 K at absolute zero and $\Theta_D^\infty \sim 110$ K in the high-temperature limit.

Wigren and Andersson studied the thermal conductivity of solid HMT at 100 MPa.[23] Figure 3a shows the thermal conductivity converted to constant volume $V_m = 101.5$ cm^3/mole using thermal expansion data[24] and $g = 8.9$.[3] The values used for the sound velocities in making the fit were calculated for the elastic constants given in Ref. 25.
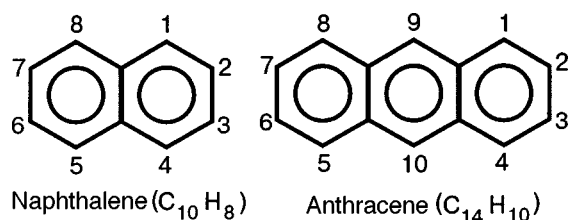
TABLE I. Parameters of the Debye model of thermal conductivity which were used in the fit: a and v,[9,28–31] obtained by fitting the quantities A and α, the Grüneisen constants γ,[9,28,29] the computed g_{th} and experimental g_{exp} values of the Bridgman coefficients.

Substance	a, 10^8 cm	v, km/s	γ	A, 10^{16} s/K	α	g_{exp}	g_{th}
CO_2	3.5	2.0	2.5	0.8	2.7	5.7	4.8
N_2O	3.6	1.9	2.5	1.73	2.3	6.2	4.4
$(CH_2)_6N_4$	5.5	2.5	3.0	0.42	3.1	8.9	8.9
$C_{10}H_8$	5.6	2.4	3.0	0.41	3.5	8.5	8.5
$C_{14}H_{10}$	6.1	2.2	3.0	0.35	4.3	8.9	9.3

FIG. 4. Structural formulas for naphthalene and anthracene.

TABLE II. Lower limits of the thermal conductivity: Λ'_{min}, obtained by fitting Eq. (20); Λ_{min}, calculated from Eq. (4) neglecting the rotational degrees of freedom; Λ^*_{min}, calculated according to Eq. (21) taking account of site-to-site rotational energy transfer (in mW/cm·K).

Substance	Λ'_{min}	Λ_{min}	Λ^*_{min}	$\Lambda'_{min}/\Lambda^*_{min}$
CO_2	6.5	2.7	4.5	1.4
N_2O	5.6	2.5	4.2	1.35
ГМТ	4.3	1.5	3.0	1.4
Naphthalene	3.8	1.4	2.8	1.35
Anthracene	4.5	1.3	2.6	1.7
Ar	1.7	1.3	1.3	1.3
Kr	1.5	1.1	1.1	1.4
Xe	1.4	1.0	1.0	1.4

Naphthalene and anthracene (see Fig. 4) are, respectively, the first and second members of a series of linear polyarenes. The molecules possess D_{2h} symmetry, the structure of both crystals is monoclinic, and the space group is $P2_1/a$ with $Z=2$ molecules per cell.[26] The melting temperatures of naphthalene and anthracene are 353.5 and 489 K, respectively.

Many thermophysical properties of these substances have been studied in detail. Naphthalene and anthracene are often used as model crystals for theoretical calculations. Specifically, a model of the lattice dynamics of crystalline naphthalene and anthracene is presented in Ref. 26, and the dispersion curves, density of states, and other constants are also calculated there.

The thermal conductivity of naphthalene and anthracene has been investigated at 100 MPa.[23] Figure 3b shows the thermal conductivity of naphthalene converted to constant volume $V_m = 103.3$ cm³/mole using thermal expansion data from Ref. 28 and $g = 8.5$ (Ref. 3). Figure 3c shows the thermal conductivity of anthracene converted to $V_m = 138.6$ cm³/mole using thermal expansion data from Ref. 29 and $g = 8.9$ (Ref. 3). The sound velocities used to make the fit were calculated from the elastic constants given in Refs. 30 and 31.

Figure 3 shows that the "localization" of the high-frequency modes in all three substances starts above 150 K. The parameters in the Debye model of the thermal conductivity of HMT, naphthalene, and anthracene are presented in Table I. The values of the coefficient α, which expresses the ratio of the lower limit Λ'_{min} of the thermal conductivity obtained by a fit using Eq. (20) to Λ_{min} calculated from Eq. (4), vary from 2 to 4. These values are much larger than for solidified inert gases and krypton–methane solid solutions, where α lies in the range 1.2–1.4.[13,14] The most obvious reason for this difference is that site-to-site rotational energy transfer must be taken into account. The expression (4) for the lower limit of the thermal conductivity is valid for substances consisting of atoms and not molecules with rotational degrees of freedom. Slack[2] has taken into account the possibility of thermal energy transfer by optical phonons in crystals consisting of atoms of different kinds. In molecular crystals heat is transferred by mixed translational–orientational modes, whose specific heat for $T \geqslant \Theta_D$ saturates in proportion to the number of degrees of freedom. On this basis the following expression can be suggested for the lower limit of the thermal conductivity of molecular crystal whose molecules have z rotational degrees of freedom:

$$\Lambda^*_{min} = \frac{1}{2}\left(\frac{\pi}{6}\right)^{1/3}\left(1+\frac{z}{3}\right)k_B n^{2/3}(v_1+2v_t). \qquad (21)$$

Table II gives the lower limits of the thermal conductivities Λ'_{min}, Λ_{min}, and Λ^*_{min}. It is evident that even taking account of the contribution of the rotational degrees of freedom of the molecules the ratio $\Lambda'_{min}/\Lambda^*_{min}$ on the average is 1.4 (with the exception of anthracene, where it is somewhat higher). For solidified inert gases which do not possess rotational degrees of freedom, this ratio is 1.3–1.4. It should be noted that although the expression (4) for Λ_{min} describes well, over all, the thermal conductivity of amorphous bodies and strongly disordered crystals,[4] it is nonetheless semi-empirical. The assumption that the minimum phonon mean-free path length equals half the wavelength is only one of many possibilities. Thus, Slack[2] assumed that it is equal to the phonon wavelength. In addition, the expression was obtained on the basis of a very simple model which neglects phonon dispersion and the real density of states. The coefficient α is an integral factor that effectively takes account of the imperfection of the model.

Figure 5 shows the Bridgman coefficients calculated according to Eqs. (16)–(19). The temperature dependence of g was not investigated experimentally. For CO_2 and N_2O the Bridgman coefficients were determined at the triple-point temperature[11] and for HMT, naphthalene, and anthracene at room temperature ($T \approx 300$ K).[3] The data in Table I show that the agreement between the experimental and computed values of g is completely satisfactory. The large values $g \approx 9$ for organic crystals are explained by the fact that they were measured at temperatures much lower than the melting points and low-frequency phonons transferred a large fraction of the heat. As temperature increases, the dependence of the thermal conductivity on the specific volume should decrease in accordance with the general trend described by the relations (16)–(19).

It can be conjectured (see Fig. 1) that the "localization" of high-frequency modes at $T \geqslant \Theta_D$ occurs, to one extent or another, in all molecular crystals, in orientationally ordered and orientationally disordered phases. In orientationally disordered phases, as a rule, the isochoric thermal conductivity increases; this increase is due to the weakening of phonon scattering by fluctuations of short-range orientational order
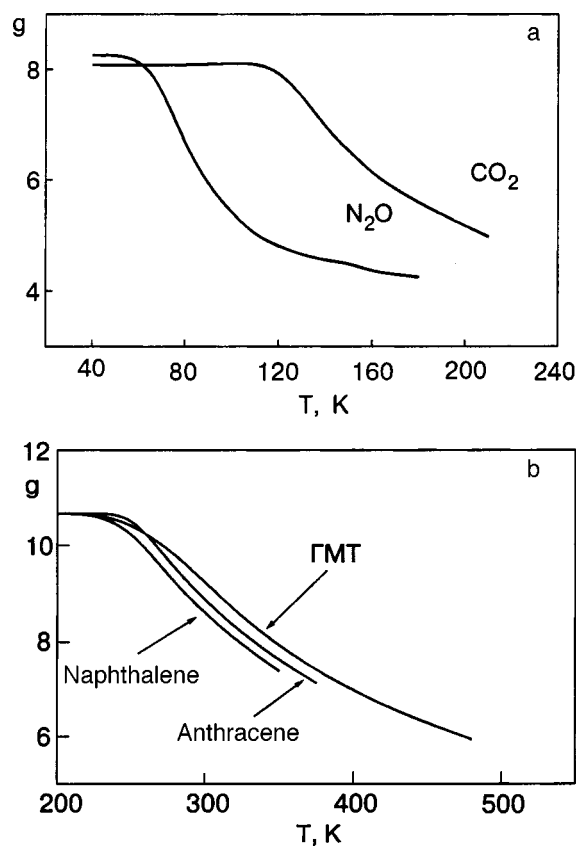
FIG. 5. Temperature dependence of the Bridgman coefficient $g = -(\partial \ln \Lambda / \partial \ln V)_T$ for solid CO_2 and N_2O (a) and HMT, naphthalene, and anthracene (b).

FIG. 6. Rate ν of reorientational jumps of molecules in crystalline adamantane.[22]

comparable to the time between the hops. This gives a basis for asserting that the molecules in crystalline adamantane near the melting point are close to a state of free rotation.

Wigren and Andersson studied the thermal conductivity of solid adamantane at pressures 0.1, 0.8, and 2.0 GPa.[32] Figure 7 shows the temperature dependences of the thermal conductivity referred to $P = 0$ and the isochoric thermal conductivity of A(II) and A(I) converted to molar volumes 107.5 and 121.5 $cm^3/mole$, respectively, using the thermal expansion data of Ref. 24. The Bridgman coefficients g for the phases A(II) and A(I) are 9.8 and 6.4.[3] The lower limit Λ_{min} of the thermal conductivity was calculated for the isobaric case ($P = 0$) neglecting the contribution of the rotational degrees of freedom. The temperature dependences of the longitudinal and transverse sound velocities were determined from the elastic constants given in Ref. 32.

It is evident that the isochoric thermal conductivity of adamantane in the orientationally disordered plastic phase increases with temperature. This effect could be due to weakening of phonon scattering by collective rotational excitations of molecules as the correlations between their rotations weakens. Unfortunately, the thermal conductivity of adamantane has been investigated only up to 400 K. It is very likely that it can pass through the characteristic maximum and then

with increasing temperature.[21] The lower limit of the thermal conductivity in this case can no longer be calculated by a direct fit using Eq. (20), since the simple expressions (7) and (8) do not describe the phonon mean-free path length. We shall illustrate this for adamantane.

The hydrocarbon adamantane $C_{10}H_{16}$ is one of the most carefully studied substances. It is a classic example of an orientationally disordered (plastic) phase. The adamantane molecule is almost spherical in shape with 16 hydrogen atoms distributed uniformly over the surface of the sphere. In the low-temperature ordered phase (II) adamantane molecules A(II) are distributed over two mutually perpendicular orientations, so that two neighboring molecules are perpendicular to one another ($P42_1c$ structure). On heating up to 208.6 K a transition occurs into an orientationally disordered fcc phase ($Fm3m$ structure) with an approximately 9% jump in density; this phase is stable right up to the triple-point temperature 543 K.[22] A detailed analysis of the relaxation times from the NMR spectra shows that in the ordered phase the rate of the reorientations of the molecules is 10^5 sec^{-1} at 170 K (see Fig. 6). As temperature increases, it increases and near the phase transition temperature T_{tr} it is of the order of 10^8 sec^{-1}. Above 208.6 K the reorientation rate increases abruptly to 10^{10} sec^{-1} and once again increases, reaching at the melting point T_m a value equal to approximately half the Debye frequency ν_D. The activation energy E_r of reorientations in the phases A(I) and A(II) is 13 and 27 kJ/mole, respectively. Since the time which the molecule spends in a hopping state is of the order of ν_D^{-1}, the reorientation time is
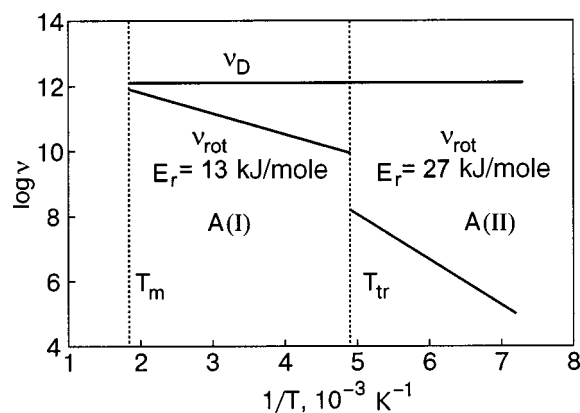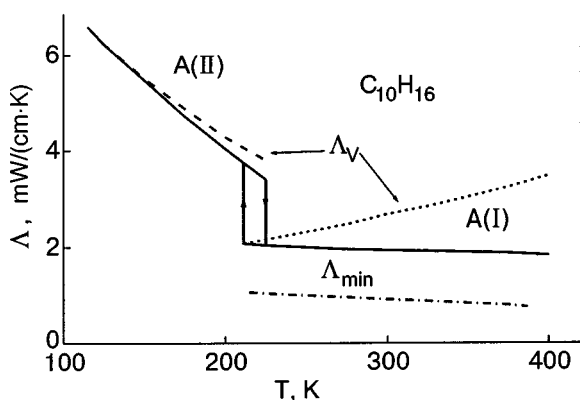

FIG. 7. Thermal conductivity of adamantane, scaled to $P = 0$, from the data of Ref. 23 (solid line), and the isochoric thermal conductivity of A(II) and A(I) for molar volumes 107.5 and 121.5 $cm^3/mole$, respectively, obtained using the data of Ref. 24 (dashed lines). The dot–dash line shows the lower limit Λ_{min} of the thermal conductivity of A(I) for the isobaric case ($P = 0$) neglecting the contribution of the rotational degrees of freedom.

decrease down to the melting point, just as in solid methane,[33] since in both crystals rotation is nearly free at premelting temperatures.

In certain cases a substantial orientational mobility of molecules and, correspondingly, an increase of isochoric thermal conductivity are observed long before a phase transition, for example, as in the case of the low-temperature phase of carbon tetrachloride.[34] The model discussed above is applicable for "normal" phases of molecular crystals in the absence of appreciable reorientational motion of the molecules. The lower limit of the thermal conductivity of molecular crystals must be estimated in accordance with Eq. (21) in all cases where site-to-site rotational energy transfer is possible.

4. CONCLUSIONS

It has been shown in this paper that the temperature and volume dependences of the thermal conductivity of molecular crystals in orientationally ordered phases at temperatures $T \geqslant \Theta_D$ can be described using a model where low-frequency phonons transfer heat and above the phonon mobility limit "diffusive" modes, which migrate randomly from site to site, transfer heat. The phonon mobility limit ω_0 can be found from the condition that the phonon mean-free path length, which is determined by umklapp processes, cannot become less than half the phonon wavelength. The Bridgman coefficient $g = -(\partial \ln \Lambda / \ln V)_T$ is the weighted-mean over these modes, whose volume dependence differs strongly. It has been shown that site-to-site rotational energy transfer must be taken into account when calculating the lower limit of the thermal conductivity of molecular crystals.

I thank V. G. Manzheliǐ, Academician of the Ukrainian National Academy of Sciences, and Professor R. O. Pohl for a fruitful discussion and V. P. Revyakin, Candidate of Physical and Mathematical Sciences, and engineer E. G. Orl for technical assistance.

*E-mail: konstantinov@ilt.kharkov.ua

[1] R. Berman, *Thermal Conduction in Solids*, Clarendon Press, Oxford (1976).

[2] G. A. Slack in *Solid State Physics*, edited by H. Ehrenreich, F. Seitz, and D. Turnbull, Academic Press, New York (1979), Vol. 34, p. 1.

[3] R. G. Ross, P. A. Andersson, B. Sundqvist, and G. Bäckström, Rep. Prog. Phys. **47**, 1347 (1984).

[4] D. G. Cahill, S. K. Watson, and R. O. Pohl, Phys. Rev. B **46**, 6163 (1992).

[5] S. Pettersson, J. Phys.: Condens. Matter **1**, 361 (1989).

[6] D. P. Spitzer, J. Phys. Chem. Solids **31**, 19 (1970).

[7] M. P. Shpol'skiǐ, *Acoustic Crystals*, Nauka, Moscow (1982).

[8] V. A. Shutilov, *Fundamental Physics of Ultrasound*, Gordon and Breach Science Publishes, New York (1988).

[9] V. G. Manzhelii, A. I. Prokvatilov, V. G. Gavrilko, and A. P. Isakina, *Handbook for Structure and Thermodynamic Properties of Cryocrystals*, Begell House Inc., New York (1999).

[10] V. A. Konstantinov, V. G. Manzheliǐ, M. A. Strzhemechnyǐ, and S. A. Smirnov, Fiz. Nizk. Temp. **14**, 90 (1988) [Sov. J. Low Temp. Phys. **14**, 48 (1988)].

[11] V. A. Konstantinov, V. G. Manzheliǐ, A. M. Tolkachev, and S. A. Smirnov, Fiz. Nizk. Temp. **14**, 189 (1988) [Sov. J. Low Temp. Phys. **14**, 104 (1988)].

[12] V. A. Konstantinov, V. G. Manzheliǐ, V. P. Revyakin, and S. A. Smirnov, Fiz. Nizk. Temp. **21**, 102 (1995) [Low Temp. Phys. **21**, 78 (1995)].

[13] V. A. Konstantinov, J. Low Temp. Phys. **122**, 459 (2001).

[14] V. A. Konstantinov, V. G. Manzhelii, R. O. Pohl, and V. P. Revyakin, Fiz. Nizk. Temp. **27**, 1159 (2001) [Low Temp. Phys. **27**, 858 (2001)].

[15] V. A. Konstantinov, V. P. Revyakin, and E. S. Orel, Fiz. Nizk. Temp. **28**, 194 (2002) [Low Temp. Phys. **28**, 136 (2002)].

[16] J. Callaway, Phys. Rev. **113**, 1046 (1959).

[17] M. C. Roufosse and P. G. Klemens, J. Geophys. Res. **79**, 703 (1974).

[18] P. G. Klemens, High Temp.-High Press. **5**, 249 (1983).

[19] J. L. Feldman, M. D. Kluge, P. B. Allen, and F. Wooten, Phys. Rev. B **48**, 12589 (1993).

[20] V. B. Koksenev, I. N. Krupskii, and Yu. G. Kravchenko, Braz. J. Phys. **27**, 510 (1997).

[21] V. A. Konstantinov and V. G. Manzhelii, in *Die Kunst of Phonons*, edited by T. Paskiewizc and T. Rapsewizc, Plenum Press, New York (1994).

[22] N. Parsonage and L. Staveley, *Disorder in Crystals*, Clarendon Press, Oxford (1978) [Russian trans., Mir, Moscow (1982)].

[23] J. Wigren and P. Andersson, Mol. Cryst. Liq. Cryst. **59**, 137 (1980).

[24] K. V. Mirskaya, Kristallografiya **8**, 225 (1963) [Sov. Phys. Crystallogr. **8**, 167 (1963)].

[25] V. S. Hausshe, Acta Crystallogr. **11**, 58 (1958).

[26] E. A. Silinch, *Organic Molecular Crystals*, Springer-Verlag, New York (1980).

[27] R. G. Ross, P. Andersson, and G. Bäckström, Mol. Phys. **38**, 527 (1979).

[28] A. P. Ryzhenkov and V. M. Kozhin, Kristallografiya **12**, 1079 (1967) [Sov. Phys. Crystallogr. **12**, 943 (1967)].

[29] A. P. Ryzhenkov, V. M. Kozhin, and R. M. Myasnikov, Kristallografiya **13**, 1028 (1968) [Sov. Phys. Crystallogr. **13**, 892 (1968)].

[30] G. K. Afanas'eva, Kristallografiya **13**, 1024 (1969) [Sov. Phys. Crystallogr. **13**, 892 (1969)].

[31] G. K. Afanas'eva and R. M. Mashnikov, Kristallografiya **15**, 189 (1970) [Sov. Phys. Crystallogr. **15**, 156 (1970)].

[32] J. C. Damien, Solid State Commun. **16**, 1271 (1975).

[33] V. A. Konstantinov, V. G. Manzhelii, V. P. Revyakin, and S. A. Smirnov, Physica B **262**, 421 (1999).

[34] O. I. Purs'kiǐ, M. M. Zholonko, and V. A. Konstantinov, Ukr. Fiz. Zh. **46**, 740 (2001).

Translated by M. E. Alferieff

On the orientational relief of the intermolecular potential and the structure of domain walls in fullerite C_{60}

J. M. Khalack[a)]

Bogolyubov Institute for Theoretical Physics of the National Academy of Sciences of Ukraine,
14b Metrologichna Str., Kiev-143, 03143 Ukraine; Stockholm University, Arrhenius Laboratory,
Division of Physical Chemistry, S-106 91 Stockholm, Sweden

V. M. Loktev[b)]

Bogolyubov Institute for Theoretical Physics of the National Academy of Sciences of Ukraine,
14b Metrologichna Str., Kiev-143, 03143 Ukraine

A simple planar model for an orientational ordering of threefold molecules on a triangular lattice modeling a close-packed (111) plane of fullerite is considered. The system has 3-sublattice ordered ground state which includes 3 different molecular orientations. There exist 6 kinds of orientational domains, which are related with a permutation or a mirror symmetry. Interdomain walls are found to be rather narrow. The model molecules have two-well orientational potential profiles, which are slightly effected by a presence of a straight domain wall. The reason is a stronger correlation between neighbor molecules in the triangular lattice versus the square lattice previously considered. A considerable reduction (up to one order) of the orientational interwell potential barrier is found in the core regions of essentially two-dimensional potential defects, such as a three-domain boundary or a kink in the domain wall. For ultimately uncorrelated nearest neighbors the height of the interwell barrier can be reduced even by a factor of 10^2. © *2003 American Institute of Physics.* [DOI: 10.1063/1.1542507]

1. INTRODUCTION

The elegant hollow cage structure of the C_{60} fullerene molecule has drawn the close attention of scientists because of its unique icosahedral symmetry I_h. The nearly spherical form of the molecule leads to very unusual physical properties of solid C_{60}, fullerite.[1–4] While at room temperature the molecules can be considered to be perfect spheres, the low-temperature properties of fullerite are determined by the deviation of the molecular geometry from spherical. At these temperatures an orientational molecular ordering takes place, which is a basic issue for understanding the results of recent He-temperature experiments on heat transport,[5,6] linear thermal expansion,[7,8] and the specific heat[9] of C_{60} fullerite.

The mass centers of the C_{60} molecules in fullerite are arranged in an fcc structure characteristic for close-packed spheres with isotropic interactions between them. At room temperature the molecules are found to be freely rotating. The resulting crystal space group is $Fm\bar{3}m$.

Upon lowering of the temperature, fullerite is undergoes two transitions. At $T \approx 260$ K, it undergoes first-order phase transition, after which the fcc crystal lattice is divided into four simple cubic sublattices. The molecules are now allowed to rotate about one of the 10 molecular threefold axes. The other two of the three rotational degrees of freedom are frozen. Within each of the four sublattices, the allowed molecular rotation axis is fixed along one of the four ([111], [1$\bar{1}\bar{1}$], [$\bar{1}\bar{1}$1], or [$\bar{1}$1$\bar{1}$]) threefold cubic axes, so that the crystal space group is $Pa\bar{3}$.

It is worth noting that the truncated icosahedral shape of

the C_{60} molecule allows for a more symmetric regular crystal structure with only one sublattice and with the four above-mentioned molecular threefold axes oriented along the three-fold crystal axes (usually regarded as the standard molecular orientation). But such a structure is energetically unfavorable for the anisotropic intermolecular interaction. Instead, the observed low-energy structure is obtained by a simultaneous 22° counterclockwise rotation of the C_{60} molecules from the initial standard orientation about their fixed $Pa\bar{3}$ threefold axes.

As a result of such a rotation, each C_{60} molecule is oriented in such away that one of the negatively charged double C=C bonds to each of the six neighbor molecules belonging to the same close-packed (111) plane is perpendicular to the molecular rotation axis. To the other six neighbors (belonging to two adjacent (111) planes) the molecule is oriented with the positively charged pentagons (P). Therefore, following a commonly used notation we denote this as the ''P orientation.'' For an ideal structure with all the molecules having a P orientation, every pair of nearest neighbors is characterized by having a pentagon from one molecule opposing a double bond from another molecule.

On the other hand, the potential profile of a fullerene molecule rotating about its fixed threefold axis has an additional metastable minimum[1)] corresponding to an 82° rotation from the standard orientation (and to a 60° rotation from the P orientation). In this minimum, the molecule opposes the neighbor molecules from the same (111) plane with the double bonds, and the molecules from adjacent planes are opposed with hexagons (H orientation[2)]). The energy differ-

ence between the P and H minima is about 11 meV (≈ 130 K) and the height of the potential barrier is 235–280 meV (≈ 2700–3200 K).[10,11]

At high enough temperatures, molecules are able to jump between the two energy minima due to the processes of a thermal activation. The average P/H ratio is given by the Boltzmann distribution law. Just below the high-temperature phase transition ($T \approx 260$ K) the fraction of H oriented molecules is close to 0.5, and for $T \approx 90$ K it tends to 0.15 (Ref. 12).

For temperatures below 90 K the situation changes drastically. The waiting time for a molecule to obtain sufficient energy for a jump between the P and H orientations reaches the order of several days (10^4–10^5 s) or even more. Therefore at some critical temperature (its exact value near 90 K depends slightly on the cooling conditions) the molecules become frozen in their current orientational minima, and a transition to an orientational glassy phase takes place. Below this transition the fraction of H oriented molecules remains practically unchanged and equal to its equilibrium value (about 15%) characteristic for the temperature of the glass transition. In other words, on the average every 7th molecule has the H orientation, and with a very high probability every C_{60} molecule has at least one misoriented neighbor.

While the orientational glass structure is believed to persist down to the lowest temperatures, some of the experimental data obtained at helium temperatures can not be explained in terms of the concept of H oriented molecules alone. For example, the data on heat conductivity[5,6] show a maximum phonon mean free path of about 50 intermolecular spacings, which implies only a 0.02 fraction of scattering ("wrong") molecules. Besides, the negative thermal expansion[7,8] and the linear contribution to the specific heat[9,13] of the fullerite samples at helium temperatures are explained in terms of the tunneling (i.e., quantum) transitions of the C_{60} molecules between nearly degenerate orientational minima. Such a possibility was firstly assumed in Ref. 14, where all the molecules in a crystal were assumed to be in tunneling states. However, the paper[13] accurately estimates the tunneling frequency to be about 5.5 K, and the number of tunneling degrees of freedom to be $\sim 4.8 \cdot 10^{-4}$ ($N/60$), where N is the number of carbon atoms in the crystal. Obviously, the number of a H oriented molecules is much larger, and the above-mentioned potential barrier between the H and P orientations is too high to provide such a low tunneling frequency. Therefore the defect states other than the simple H oriented molecules should be considered.

One of the possibilities for a realization of the low potential barrier for C_{60} molecule is indicated in our previous paper.[15] Relatively low barrier sites can appear within the orientational domain walls because of the superposition of the mutually compensating potential curves due to interaction with the neighbor molecules belonging to different domains. For the case of orientational ordering of hexagons on a square planar lattice considered in,[15] the height of the potential barrier in the wall is found to be 5 times less than in the regularly ordered lattice. Such a lowering seems to be insufficient to provide the necessary magnitude of tunneling frequency following from the available experimental data analysis.[13]

Meanwhile, most of the results obtained for a square lattice seem to be caused by the incompatibility of the molecular threefold C_3 symmetry axis with the lattice fourfold C_4 symmetry axis. In the case of fullerite, a fullerene molecule has the 4 threefold axes and 3 twofold axes intrinsic to the fcc lattice. Furthermore, the closest-packed (111) plane of the $Pa\overline{3}$ lattice has a hexagonal structure. Six of the 12 nearest neighbor molecules belong to a hexagonal plane, while only 4 of them belong to the same square (001) plane.

Therefore it is interesting and necessary to investigate the main features of orientational ordering for the case of a molecular symmetry identical to that of the lattice. In the present paper we are concerned with the possible orientational domain structures formed by simple flat hexagonal molecules arranged in a (more relevant to a real situation) hexagonal lattice, with both the molecule and the lattice symmetry axes being C_3. The main purpose of this paper is to estimate the intermolecular interaction energy barriers for both the regular close-packed planar structure and for the vicinity of extended orientational defects.

It is a pleasure and an honor for us to dedicate this paper to Prof. Vadim G. Manzhelii a Ukrainian low-temperature experimentalist of world-wide reputation whose contribution to the physics of cryocrystals in general and to the physics of fullerites and fullerides, in particular, is well known and cannot be overestimated.

2. MODEL

Let us consider a system of flat hexagonal molecules[3)] located at the sites of a rigid hexagonal planar lattice, modeling a (111) plane of the 3D fcc lattice.

Following the empirical potentials used for modeling the intermolecular fullerene interaction (see, for example, Ref. 16 and references therein), we suppose two kinds of negative charges, $-(1 \pm \alpha)$, to be located at the centers of the sides of the hexagon (see, the large and small filled circles in Fig. 1a). These negative charges recall single and double covalent bonds between carbon atoms at the hexagon edge of the truncated icosahedral fullerene molecule. Introduction of the charge parameter α reduces the C_6 hexagonal symmetry down to the C_3 symmetry intrinsic to real C_{60}. The requirement of electrical-neutrality of the model hexagon molecule stipulates the presence of unit positive charges at its vertices (shown with the open circles in Fig. 1a).

For the initial orientation (an analog of the standard orientation in fullerite) the molecules are chosen to be aligned with the positive charges along the lattice directions. The topmost (positive Y direction) negative charge has to be the larger one (see Fig. 1a). The molecular rotation angle φ is measured starting from the positive X direction.

The interaction between two nearest molecules is given by the superposition of the Coulomb interactions between the vertices and bonds of these molecules. The exact form of the resulting interaction function can be found in Ref. 15 [Eqs. (1)–(4)]. The interaction is multipolar, so it depends not only on the difference of molecules' rotation angles (as for the case of the spin systems with Heisenberg exchange coupling), but essentially on both the angles. So the energy of interaction of the two neighbor molecules characterized
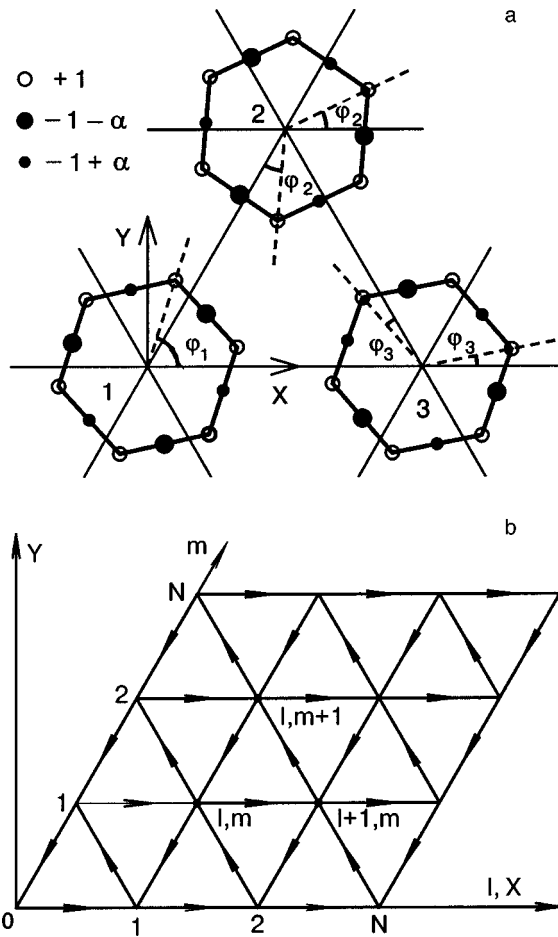
FIG. 1. (a) A local geometry of the model molecules on the triangular lattice. Note that molecular rotation angles (shown with the help of dashed lines) can be measured from any of the three lattice directions. (b) A geometry of the simulation cell. Arrows give the $1 \rightarrow 2$ order of the input parameters for the pair interaction function $W(\varphi_1; \varphi_2)$.

by rotation angles φ_1 and φ_2 has to be written as $W(\varphi_1; \varphi_2)$. The clockwise and counterclockwise rotations have different effects on the interaction:

$$W(\varphi_1; \varphi_2) \neq W(-\varphi_1; \varphi_2) \neq W(\varphi_1; -\varphi_2). \quad (1)$$

On the other hand, a clockwise rotation of the first molecule is somewhat equivalent to a counterclockwise rotation of the second molecule. Hence, the combination of the lattice mirror symmetry with the molecule mirror symmetry leads to the following symmetry relation for the interaction function:

$$W(\varphi_1; \varphi_2) \neq W(-\varphi_2; -\varphi_1). \quad (2)$$

Rotating the molecules shown in Fig. 1a by an angle $2\pi/3$ (or $4\pi/3$) about a threefold axis located at the center of the triangle 123, one can find that the pair interaction of the molecules $2, 3$ (or $3, 1$) is given by the same function $W(\varphi_2; \varphi_3)$ (or $W(\varphi_3; \varphi_1)$, respectively). The relative displacement (which was vertical or horizontal in the case of the square lattice considered in Ref. 15) of the two molecules does not have to be taken into account, but the order of the angle parameters is essential.

For a simulation of the possible domain structures, we consider a finite parallelepiped-shaped system, the geometry of which is shown in Fig. 1b. It consists of 20×20 hexagonal molecules labeled with the two indexes l and m. Arrows

show the order of the interaction function arguments for each pair of hexagons. The system Hamiltonian then reads:

$$H = \sum_{l,m=0}^{N-1} [W(\varphi_{lm}; \varphi_{l+1,m}) + W(\varphi_{l+1,m}; \varphi_{l,m+1})$$

$$+ W(\varphi_{l,m+1}; \varphi_{lm})] + \sum_{l=0}^{N-1} W(\varphi_{lN}; \varphi_{l+1,N})$$

$$+ \sum_{m=0}^{N-1} W(\varphi_{N,m+1}; \varphi_{Nm}), \quad (3)$$

where $N = 19$, and the last two terms are introduced to take into account the edge molecules. For numerical simulations, the charge parameter α is chosen to be $1/3$. A hexagon side makes 0.3 of the lattice spacing.

3. POSSIBLE ORDERING TYPES

For the general case of orientational ordering of identical molecules on a planar hexagonal lattice, structures with 1, 3, 4, and 7 sublattices are possible. The one-sublattice structure would correspond to a uniform rotation of all the molecules on a lattice. The three-sublattice structure is characteristic of antiferromagnetic systems (Loktev structure).[17] A close-packed (111) plane of the $Pa\bar{3}$ structure should contain the molecules belonging to four different sublattices. The results of STM imaging of the (111) fullerite surface[18] confirm this fact.[4] The more complicated case of seven sublattices could be expected for less symmetric molecules.

As to the C_3-symmetric hexagons considered, a rather aesthetic consideration of the threefold site symmetry[5] implies either the 1- or 3-sublattice case, or a 4-sublattice structure involving three identical rotations. Numerical calculations give for the ground state the three-sublattice structure shown in Fig. 2a. It is interesting to notice that in the 3-sublattice structure the energy minimum corresponds to molecule positions which do not provide the minimum of the pair potential. The molecular rotation angles obtained are ($\alpha = 1/3$):

$$\varphi_1 = 72.37209°; \quad \varphi_2 = 25.24477°; \quad \varphi_3 = 10.87533°. \quad (4)$$

Another possible (energy degenerate) ground state can be found with the help of the symmetry relation (2). The corresponding angles are given by

$$\varphi_1' = -\varphi_1; \quad \varphi_2' = -\varphi_2; \quad \varphi_3' = -\varphi_3. \quad (5)$$

This ground state is related by mirror symmetry to the state defined by Eq. (4).

The high symmetry of the hexagonal molecules makes it difficult to perceive the ordering pattern presented in Fig. 2a. The more complicated task of finding an orientational defect in this pattern becomes unfeasible. Therefore for the purpose of visualization, we implement a vector representation of hexagonal molecules, shown in Fig. 2b. The vector rotation angle is three times the hexagon rotation angle: $\varphi_{lm}^v = 3\varphi_{lm}^h$. A vector can be rotated from 0° to 360°. As a result, the difference between sublattices appears more clearly.

Figure 3 shows the change of the interaction of a molecule energy upon a change of its orientation for three molecules belonging to three different sublattices. It is clearly
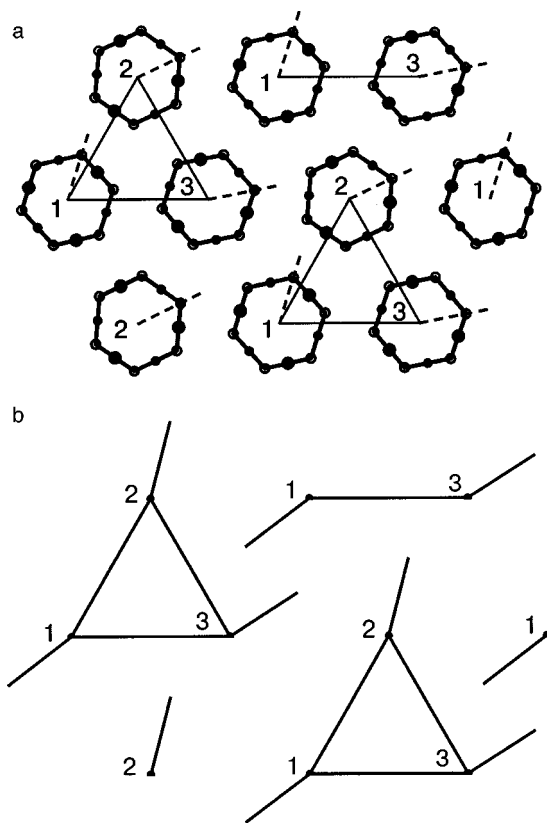
a

b

FIG. 2. A ground-state orientational ordering of the hexagonal molecules (a), and the same ordering patterned with vectors (b).

seen that the molecules are not identical. All of them have double-well energy profiles, but the height of the interwell energy barrier varies by a factor of 2. The potential minima of the 2nd molecule are almost energy-degenerate, the energy difference being only 1/20 of the barrier height (a situation similar to the case of fullerite).

For comparison, the same potential profiles are shown for the molecules from the edge of the simulated lattice (see Fig. 4). Such molecules keep only 4 of the 6 nearest neighbors (molecules from two different sublattices are missing). As a result, the overall potential profile is lowered by a factor of 6/4. The C_{60} molecule at the fullerite (111) edge surface is
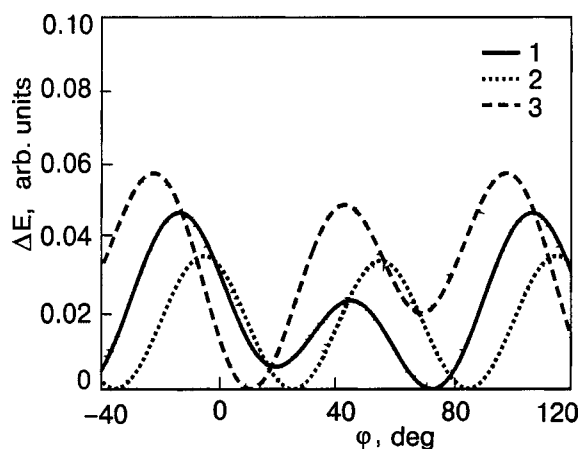
FIG. 3. Orientational potential profiles for regular molecules belonging to three different sublattices.
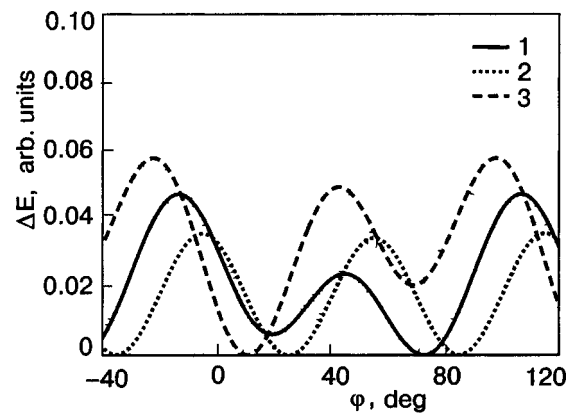
FIG. 4. Orientational potential profiles for the edge molecules belonging to different sublattices.

missing 3 neighbors from 3 different sublattices. Therefore one could expect a lowering of the orientational barriers by a factor of 12/9.[6]

But the real situation is even more complicated. The three-dimensional character of fullerite lattice leads to subdivision of the neighbors of an arbitrary bulk fullerene molecule into only two categories, denoted here as double-bond (for which the molecule is oriented with the double bond), and pentagon (for which the molecule is oriented with the pentagon or hexagon) neighbors. The six double-bond neighbors belong to the (111) plane normal to the molecule fixed C_3 axis. The other six pentagon neighbors, which give a major contribution to the molecular orientational profile, are located in the other (111) planes.

Therefore an edge molecule with a fixed C_3 axis normal to the edge surface is missing three pentagon neighbors, while the molecules with the other three directions of the allowed rotation axis are missing two double-bond and one pentagon neighbor each. As a result, the potential relief of a molecule with a normal rotation axis is shallower than the relief of the other molecules. In this way, the molecules from the four different sublattices which are identical in their rotational properties in the bulk fullerite become non-identical at the edge surface crystal defect due to a loss of symmetry. This non-identity evidently reveals itself in the presence of two additional lower-temperature order-disorder phase transitions reported in.[21]

4. LINEAR ORIENTATIONAL DEFECTS

A general kind three-sublattice two-dimensional triangular lattice allows for orientational ordering of three different types. Molecular orientations for these ordering types are related to each other by cyclic permutations of the rotation angles φ_i [$i=1, 2, 3$; cf. Eq. (4)] for the molecules located at the vertices of a lattice triangle (e.g., the triangle 123 shown by a solid line in Fig. 2). In the case of hexagonal molecules under consideration the existence of the mirror orientational twin defined by Eq. (5) leads to the appearance of three additional ordering types, which are related to the basic permutation ones in mirror symmetry.

As a result, the lattice under discussion allows for the simultaneous existence of orientational domains with 6 different ordering types. A boundary between two domains con-
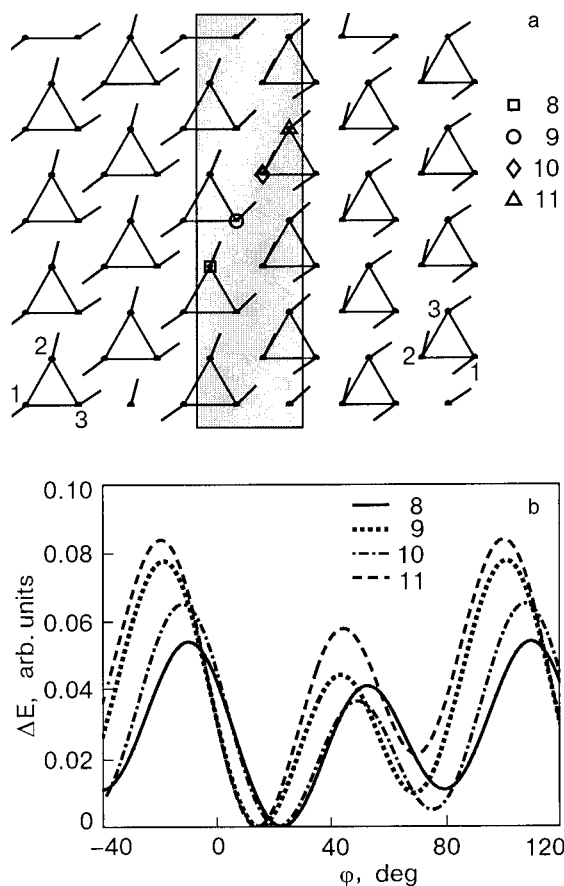
FIG. 5. Permutation domain wall (a) perpendicular to a close-packed row, and the orientational potential profiles (b) for the four marked molecules identified with the lattice index m ($l=10$).
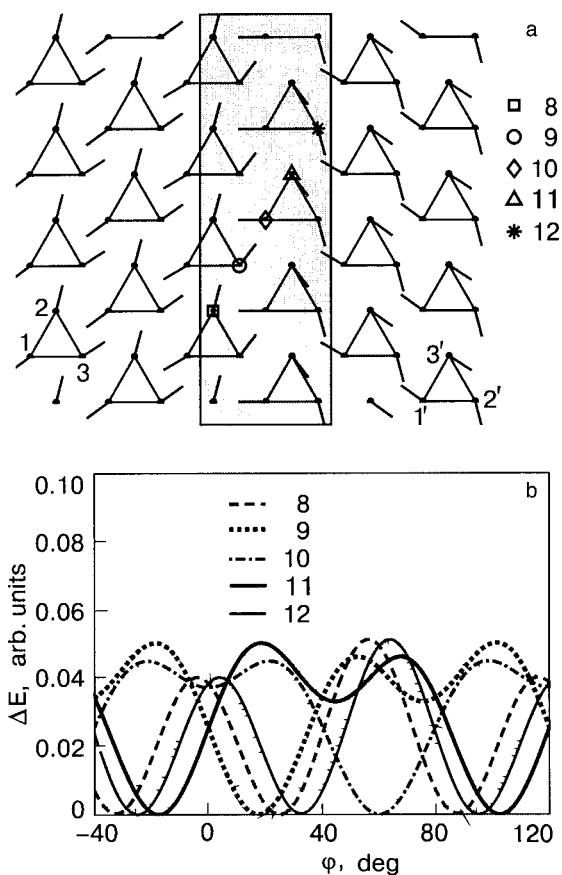

FIG. 6. Mirror domain wall (a) perpendicular to a close-packed row, and the potential profiles (b) for the five marked molecules with $l=10$ and with the indicated m value.

tains a linear orientational defect (domain wall). Such a defect can involve a permutation (clockwise or counterclockwise) or a mirror transformation (with a center at 3 different lattice sites) of molecular orientations.[7]

A domain wall of the permutation type is presented in Fig. 5a. The rotation angles of the molecules located at the vertices of a lattice triangle (shown with solid lines) have the values φ_1, φ_2, and φ_3 in the left domain. In the right domain they are equal to φ_2, φ_3, and φ_1, respectively. The domain wall (gray) is relatively narrow. Its width (measured along the horizontal close-packed l direction) is about one period of the 3-sublattice structure. As seen along the close-packed m direction, this defect can be regarded as obtained by the removal of one element from the ideal sequence ...1231231... of molecular orientations. The resulting sequence is ...123|231... .

The orientational dependence of the potential energy of the four central molecules from the domain wall is given in Fig. 5b. The molecules are marked in Fig. 5a and labeled with their m index, while l is taken to be 10. Molecules 8 and 10 have orientations of the type 2, and the rotation angles of molecules 9 and 11 are close to φ_3. The potential profiles are quite close in form to the profiles of the regular molecules (shown in Fig. 3), but one of the two potential barriers is lowered for each molecule.

Orientational domain walls of a mirror nature are wider than the permutation ones. Figure 6a gives an example of the mirror domain wall. For this wall, the sequence of molecular

orientations in the m direction is ...123?3'2'1'..., where the question mark stands for a molecule in the mirror plane. This molecule does not fit any regular orientation. Instead, it reflects the mirror symmetry of the wall. Figure 6b clearly shows the orientational potential minimum of the molecule 10 to be located at the rotation angle $\varphi=60°$. Such an orientation corresponds to aligning one of the mirror planes of the hexagonal molecule with the domain-wall mirror plane.

The mirror symmetry of an orientational defect is also manifested through the symmetry of the potential curves of other molecules. The potential profiles of molecules 9 and 11 (orientations 3 and 3') and 8 and 12 (orientations 2 and 2') are related through $\Delta E_9(\varphi)=\Delta E_{11}(-\varphi)$ and $\Delta E_8(\varphi)=\Delta E_{12}(-\varphi)$, respectively.

In the vector pattern of Fig. 6a, this symmetry is given with the clockwise—counterclockwise vector rotations on the two different sides of the wall. Since the rotation angles are measured form the X direction, the vectors representing rotation of molecules 9 and 11 (8 and 12) are related by a mirror plane parallel to the X direction.

The effect of the domain wall on the potential relief of molecules 8 and 12 (orientations 2 and 2') is found to consist in a slight lowering of one of the two barriers. For molecules 9 and 11 (orientations 3 and 3'), close to the center of the domain wall, both the potential barriers are lowered considerably. But the position and the relative height of the secondary minimum are unchanged, resulting in the shallow character of this minimum seen in Fig. 6b.
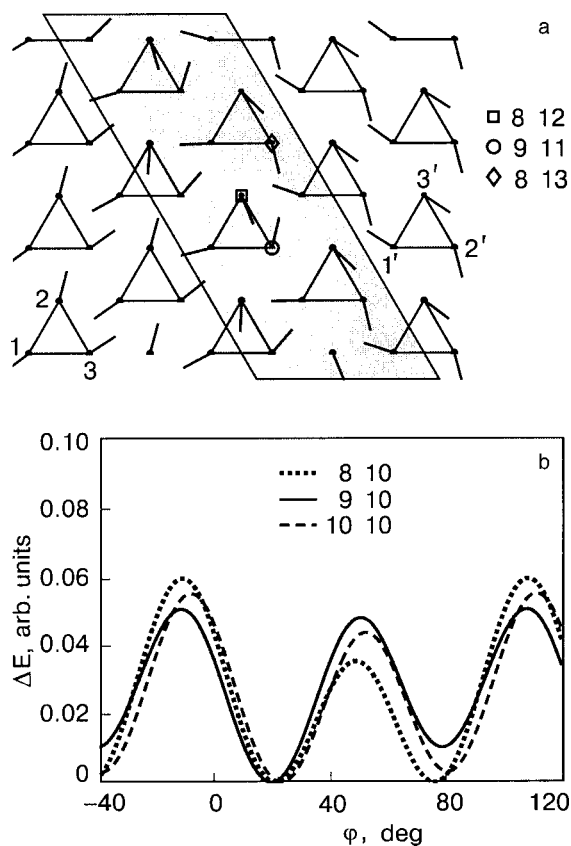
FIG. 7. Permutation domain wall parallel to a close-packed row (a), and the orientational potential profiles (b) for the marked molecules with the given lattice indices *l* and *m*.

FIG. 8. Mirror domain wall parallel to a close-packed row (a), and the potential profiles (b) for the marked molecules (the lattice indices *l* and *m* are indicated).

The domain walls given in Figs. 5 and 6 have their directions parallel to one of the sublattice period vectors, and perpendicular to one of the close-packed molecular row directions. At the same time, there is a possibility for a domain wall to lie along the close-packed molecular rows. An example of a permutation domain wall of this kind is presented in Fig. 7a. The relationship between the left and right domains here is the same as in Fig. 5, but the location of the domain wall line is different. As a result, the molecular orientation sequence along the *m*th molecular row can now read ...231|312... ($l=8$), ...312|123... ($l=9$), or ...123|231... ($l=10$). Therefore, the central part of the domain wall contains molecules with 6 different potential profiles (orientations 1, 2, and 3 from the left domain, and orientations 3, 1, 2 from the right domain). The three potential profiles with the lowest energy barriers are shown in Fig. 7b. It is noteworthy that here we gain a low barrier profile with almost energy-degenerate minima (see dotted curve).

A domain wall of a mirror nature parallel to a close-packed molecular row has the more complicated structure shown in Fig. 8a. It is again wider than the permutation wall, so that the molecules from *three* close-packed rows have substantially corrupted orientational potential relief. As a result, the number of intra-wall molecules with different orientational profiles increases up to 9, opposed to 6 different profiles for a permutation wall. Furthermore, the direction of the domain wall does not coincide with the lattice mirror plane, so there is no mirror symmetry in the pattern of Fig. 8a, and, accordingly, no symmetry relations for the potential
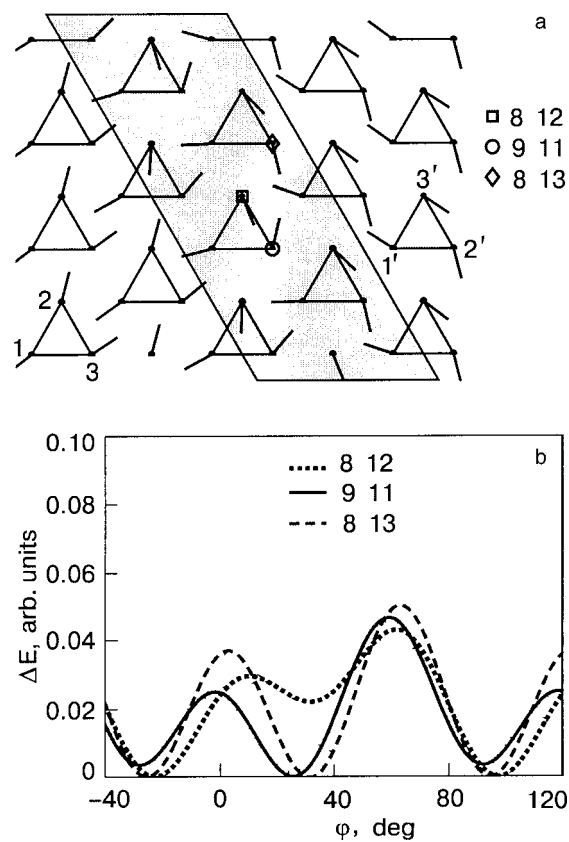
curves (cf. the mirror symmetry of the potential profiles shown in Fig. 6b for a domain wall perpendicular to a close-packed molecular row). In Fig. 8b we give the orientational potential profiles for the three molecules with the lowest interwell energy barriers. It is seen that there exists a molecule (○) for which the interwell barrier is about 1.4 times lower than the lowest of the interwell barriers of the regular molecules. The molecule is situated at the center of the domain wall and marked with a circle. The corresponding potential profile is plotted by the solid curve in Fig. 8b. The obtained reduction of the orientational interwell barrier is caused by a lower correlation between the nearest-neighbor molecules (every molecule within the considered wall has neighbors of six different orientations).

5. TWO-DIMENSIONAL DEFECTS

The results on the modeling of the straight domain walls in the system considered show that the molecules with the shallowest potential profile tend to appear at sites with the reduced correlation between the orientations of the neighbor molecules. For the straight walls this condition is met at the boundary of two domains with different sets of equilibrium molecular orientations (mirror domain walls).

Then it is straightforward to continue the search for the shallow-potential molecules in the core regions of essentially two-dimensional orientational defects. One of such promising two-dimensional defect is a meeting point of three different domains. Molecules at the center of this defect should have three pairs of neighbors belonging to three different
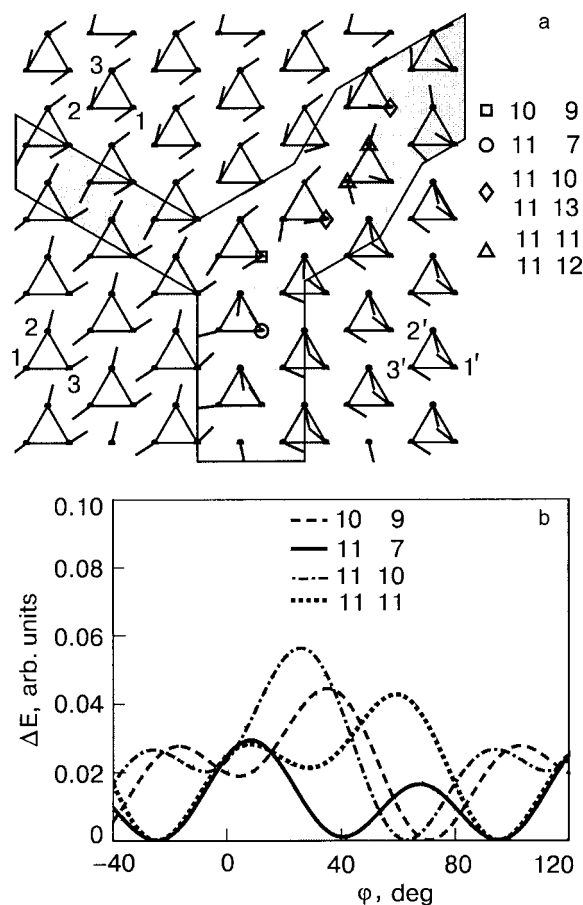
FIG. 9. Structure of orientational defect (a) formed at the boundary of three orientational domains, and the potential profiles (b) for some chosen molecules in the defect core region. Pairs of molecules marked with the same sign (△ or ◇) have symmetry-related potential profiles, so only one of the profiles is given for each pair. The molecules are labeled by the indices l and m.

domains, so one could expect an additional decrease of the interwell barriers in comparison to the two-domain boundary case.

The results of numerical calculations indeed show a further reduction of the interwell potential barriers at the boundary of three orientational domains. The most effective reduction is found to take place in the presence of mirror boundaries.

Figure 9a shows an example of an orientational defect formed at the intersection of three domain walls perpendicular to molecular rows. The left (narrow) domain wall is of a permutation type, while the other two (the bottom one and the right one) have a mirror nature and are much wider. The right domain wall incorporates a kink in order to minimize the surface spanned by the defect. The molecules with the lowest interwell barriers are marked.

As we have said no significant potential barrier reduction has been observed for straight domain walls perpendicular to close-packed molecular rows. Therefore the marked molecules can be seen only at the crossing of the three walls. The corresponding orientational potential profiles are plotted in Fig. 9b.

It is surprising that the potential profile with the least energy barrier belongs not to the molecule □ situated at the very center of the defect (potential curve plotted with a

dashed line) with totally different orientations of all the 6 nearest neighbors, but to the molecule located at the beginning of the bottom domain wall (○, solid line). For the last molecule the orientations of the nearest neighbors differ only slightly from that in the straight wall, but the interwell potential barrier is 2.3 times lower than the lowest regular molecule barrier.

The other four molecules that are marked in Fig. 9a are located within the center of the kink in the right domain wall. At a closer look, one can find a kind of symmetry center at the middle of the line between the molecules marked with △. The exact symmetry is as follows: if the centers of two molecules are related by inversion symmetry, these molecules have rotation angles which are equal in absolute value, but opposite sign. Therefore the two molecules marked with △ (as well as the two molecules marked with ◇) have the same orientational dependence of intermolecular interaction potential, the only difference being in the clockwise or counterclockwise direction of molecular rotation. This can be compared to the symmetry of the potential curves in Fig. 6b, but there is no mirror plane in the present case. To avoid having a very complicated picture, only one of the two symmetry-related curves is shown in Fig. 9b for each pair of molecules. Both the dotted and the dash-dotted curves have an interwell energy barrier which is less than the lowest energy barrier characteristic for regular molecules. This means that at the center of the kink in a domain wall (also a two-dimensional defect) the molecules have ill-correlated nearest neighbors. Therefore the case of a kinked domain wall has to be investigated more thoroughly.

Figure 10a shows the structure of the kink that contains the molecule with the lowest height of the orientational interwell barrier obtained in our simulations. This molecule (in fact, two molecules, since the kink has a center of symmetry of the kind described above) is located at the very center of the kink, and the corresponding potential curve is shown in Fig. 10b by a solid line. The height of the interwell potential barrier is 5 times less than for the case of regular molecules.

6. TOTALLY UNCORRELATED NEIGHBORHOOD CONFIGURATION

The three-dimensional defect structure of the real fullerite can be even more complicated. As a result, some molecule can have neighbors whose orientations are fixed by different elements of the defect network. In the framework of our simple two-dimensional model such a neighborhood would be totally uncorrelated, and the height of the interwell barriers could be further lowered. Therefore it is interesting to know the minimum possible height of the molecule interwell potential barrier for an arbitrary orientational configuration of its neighbor molecules.

For this purpose, let us consider a system of 7 hexagonal molecules located at the sites of hexagonal lattice, so that one central molecule has 6 nearest neighbors. The rotation angles of the outer molecules are fixed to be equal to 6 random numbers between 0° and 120°, and then the orientational potential profile of the central molecule is calculated. Configurations with the shallowest potential profiles obtained in the course of about 10^6 different realizations of the
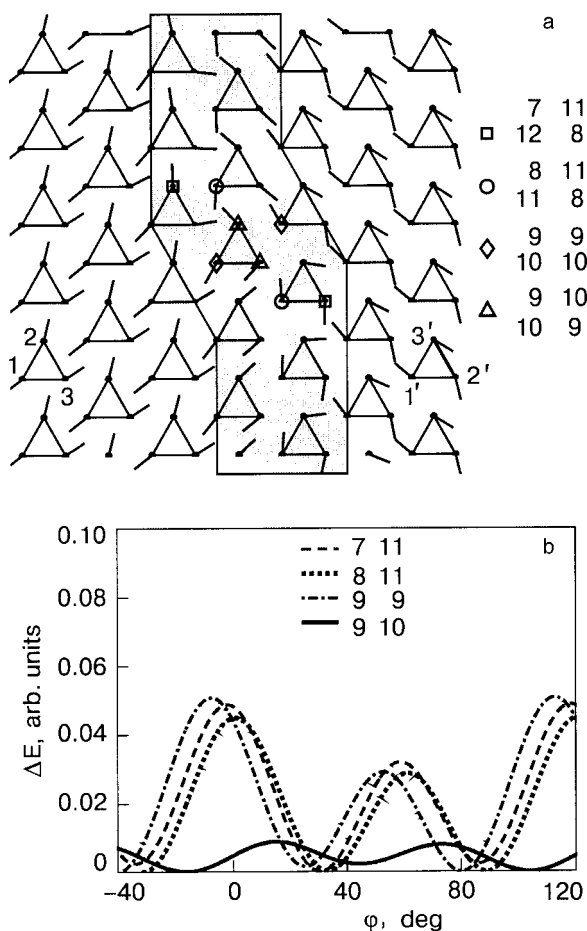
FIG. 10. The structure of a kink in a mirror domain wall (a), and the orientational potential profiles (b) for the marked molecules. Only one potential curve is given for every pair of symmetry-related molecules which are marked with identical signs. The indices l and m are indicated.
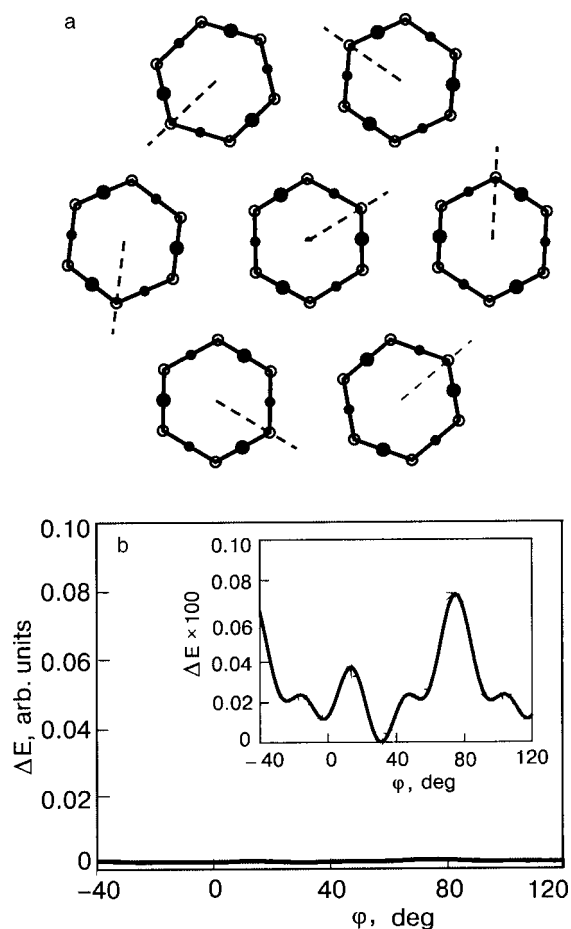

FIG. 11. A molecular configuration with nearly symmetric orientations of the outer molecules (a) and the corresponding shallow potential profile of the central molecule (b). The inset in the bottom panel shows a magnified potential curve.

random neighborhood configuration are shown in Figs. 11, 12, and 13.

Figure 11 gives an example of a molecular configuration with interwell potential barriers of a central molecule reduced by two orders of magnitude with respect to the case of the totally orientationally ordered lattice. This configuration is nearly symmetric (the outer molecules have rotation angles of about $\pm 30°$). The central molecule has a four-well orientational potential profile with the main minimum located close to $30°$. One could expect that a completely symmetric configuration might have an even shallower potential profile of the central molecule, because of the increase of the interaction energy at the minima of the potential. Contrary to the expectations, the exactly symmetric configuration (not shown) has an order of magnitude higher interwell barriers than the one shown in Fig. 11. Thus, interwell barriers prove to be extremely sensitive to even very small rotations of the molecules.

The case of the molecular configuration with a two-well orientational profile of the central molecule is presented in Fig. 12. If one does not take into account the difference between the values of the negative charges, this configuration seems to be close to having a mirror symmetry. It is probably this difference that leads to the increase of the interaction energy at the potential minima.

The molecular configuration with the lowest obtained

interwell potential barrier of the central molecule (shown in Fig. 13) has no symmetry at all. The orientational profile has three minima of different depth, and the lowest interwell barrier is about 200 times lower than the corresponding lowest barrier in the regularly ordered lattice.

Also it should be noted that the molecules of the regularly ordered lattice (namely, the molecules with the φ_1 orientation, see Fig. 3) have the neighborhood configuration with the highest possible interwell potential barrier. While minimizing the overall interaction energy, this configuration also minimizes the interaction energy at the minimum of the one molecule potential, and deepens this minimum.

7. DISCUSSION

The simple planar model considered recovers some of the features of the fullerite lattice. First of all, it predicts a multi-sublattice structure for a system which would be arranged in a more symmetric 1-sublattice manner in the absence of anisotropic intermolecular interactions.

Then, the model involves lowering of the orientation potential relief of the molecule at the crystal surface. This can be compared favorably to the absence of H-oriented molecules in the STM image of the fullerite surface.[18] Furthermore, at a closer look this image shows a slight difference in orientations of the fullerite molecules belonging to the three
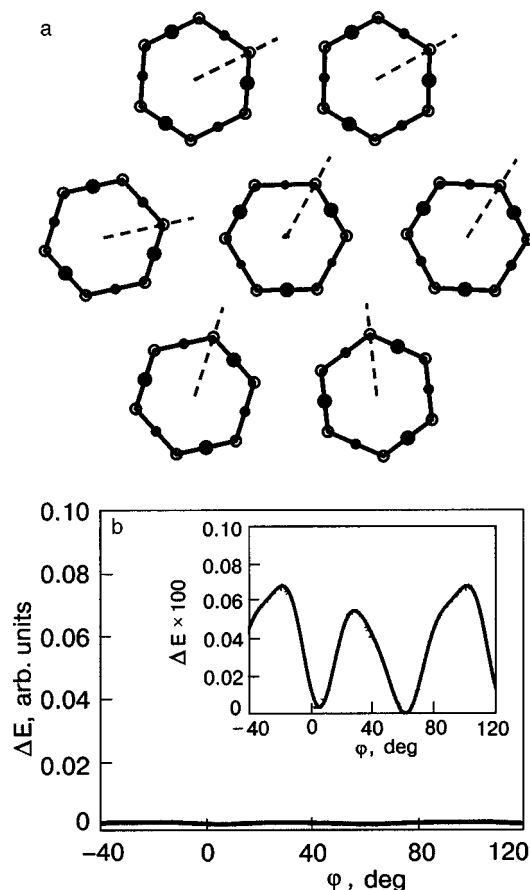
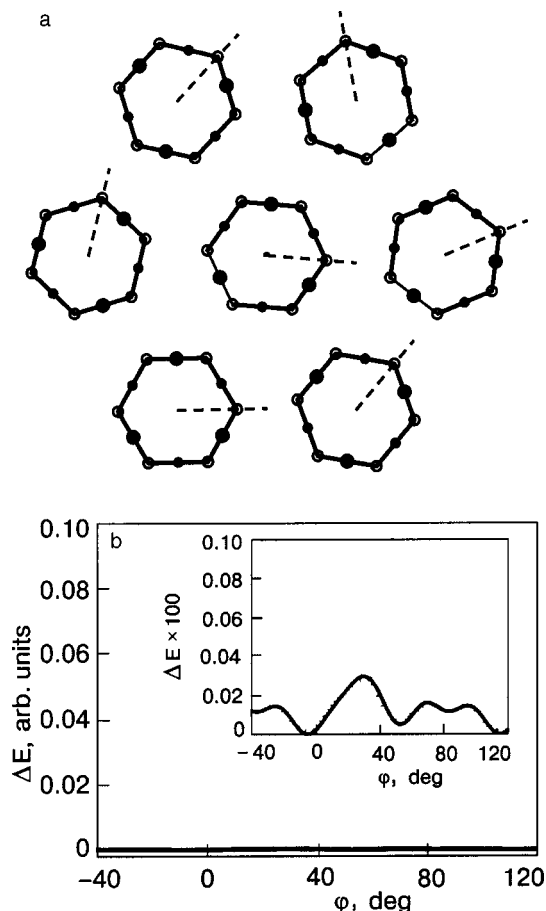FIG. 12. The same as in Fig. 11: Another nearly symmetric configuration with a two-well potential profile.

FIG. 13. The same as in Fig. 11: Nonsymmetryc configuration with the lowest interwell barriers found.

sublattices for which the molecular C_3 rotation axes are not perpendicular to the surface. This difference is due to a competition of the two-dimensional character of a surface (with probably another subdivision into sublattices) with the bulk equilibrium orientations of the molecules below the surface molecular layer.

The rather narrow character of the domain walls in the high-symmetry system considered is rather natural for a system with only one kind of interaction involved.[8] It agrees well with the very sharp character of the domain wall observed in a two-dimensional monolayer of C_{60} fullerene molecules.[22] This wall contains also a very sharp kink, which is a kind of essentially two-dimensional defect that can incorporate molecules with low orientational interwell barriers.

The sharp character of the observed kink implies the possibility of existence of strongly localized orientational defects also in the bulk of the three-dimensional fullerite. Some of these strongly localized defects with necessarily uncorrelated orientations of the neighbor molecules' orientations should involve molecules with an orientational potential which is sufficiently shallow to give a reasonable frequency of tunneling transitions. As to the rather high C_{60} molecule mass, the recent molecular dynamics simulations of dislocation-kink tunneling[23] in Ag show an efficient of tunneling of complex heavy objects under certain conditions.

The idea of explaining negative thermal expansion of solids by the double-well tunneling statistics was suggested by Freiman in 1983 for the case of solid methane.[24] In the

range of temperatures where the conventional phonon mechanism does not work the thermal expansion is established as a result of the competition of two factors. The first factor is a lattice contraction due to the process of populating the tunnel states with an increase of temperature. Shrinking the distances between molecules increases the height of the orientational interwell barriers, which leads to a decrease of the tunneling energy splitting and, as a result, to a decrease of the system free energy. The contraction of the lattice is stabilized by an increase of the elastic part of the free energy for every fixed value of crystal temperature.

Since the population of tunnel states has a very strong exponential temperature dependence, the thermal expansion resulting from the competition of the two factors is always negative. At $T \approx 0$ K it is practically absent (no molecules on excited tunnel levels). With an increase of temperature the population of the excited state grows, and therefore the lattice is contracted. But at $T > \Delta$, where Δ is the tunnel state energy splitting, both the ground and the excited states become almost equally populated, so that the effect becomes much less pronounced. This means that there should exist a maximum in the magnitude of the negative thermal expansion coefficient.

With a simple differentiation of expression (6) of Ref. 24 one can find that this maximum takes place at the temperature T_{max} satisfying the equation

$$\frac{2T_{max}}{\Delta} = \tanh\left(\frac{\Delta}{2T_{max}} + \frac{1}{2}\ln\frac{f_1}{f_2}\right),$$

where f_1 and f_2 are the degeneracies of the ground and excited states, respectively. It is easy to see that $T_{max} < \Delta/2$ holds for any ratio f_1/f_2.

Therefore the tunneling energy splitting in fullerite can be estimated from the T_{max} position in Refs. 7 and 8 to be more than 8 K. On the other hand, the positive thermal expansion of pure fullerite at $T < 2$ K implies the presence of processes other than two-well tunneling (probably, the conventional phonon mechanism is still valid) at this low temperature.

The possibility of detecting experimentally the negative contribution to thermal expansion due to the tunneling objects depends strongly on the relative magnitude of the positive (conventional) and negative (tunneling in this case) contributions. In the case of fullerite, the negative contribution is more pronounced, but one still encounters difficulty in determining the tunneling object. The first hypothesis of a tunneling of regular C_{60} molecules between P and H orientations[14] had the drawback of a high interwell potential barrier. The subsequent introduction of the idea of a competition of the isotropic and anisotropic parts of intermolecular interaction potential (though in orientational glass)[25] has lead to the current understanding (given in our previous paper[15] and the present one) that the tunneling objects are strongly localized orientational defects of the fullerite structure. A more detailed description of such defects could be obtained with the help of a more realistic three-dimensional modeling of the C_{60} crystal structure, which should be a subject for future studies.

a)E-mail: julia@physc.su.se
b)E-mail: vloktev@bitp.kiev.ua

1)We do not consider to be distinct the energy-degenerate minima obtained by 120° rotation about the threefold molecular axis.

2)Strictly speaking, the term "H (or P) configuration" is more adequate for describing a mutual orientation of two neighboring molecules. Nevertheless, for every chosen pair of neighboring molecules (let us denote them as A and B) with fixed directions of the allowed rotation axes, the mutual orientation depends strongly only on the rotation angle of one molecule (say, A). The other molecule (B) is always (at any angle of its rotation) turned to the first one (A) with a double bond. Therefore, the interaction energy of the pair weakly depends on the rotation angle of the second molecule. As to the molecule A, it is at any rotations always turned to B with a belt of pentagons and hexagons interconnected by single bonds. Thus it is the molecule A of the pair A, B that is responsible for the mutual orientation. Aside from this, upon the rotation of the molecule A from orientation P to orientation H this molecule becomes turned with hexagons (instead of pentagons) to five more its nearest neighbors. At the same time, the energy of its interaction with the other 6 nearest neighbors remains

practically unchanged, because the energy depends mainly on the orientation of those latter molecules. For the reasons mentioned above, we follow the common notations and use the letters "P" and "H" to denote the orientation of a single molecule, while keeping in mind those 6 pair orientations for which this molecule rotation angle is crucial.

3)In some sense, they can be regarded as imitating the C_{60} molecules viewed along the C_3 axis. Strictly speaking, such imitation is realistic only for the fullerene molecules with the fixed C_3 axis perpendicular to the considered (111) plane. The C_{60} molecules belonging to other three $Pa\bar{3}$ sublattices have their fixed threefold axes tilted to this plane.

4)At the beginning of the fullerene era, there were some publications[19,20] reporting an 8-sublattice fcc structure for the low-temperature fullerite. This structure could be obtained by division of each of the four sc $Pa\bar{3}$ sublattices into two fcc sublattices with different (P and H) molecular orientations. However, the 8-sublattice structure has not been confirmed by further investigations. Therefore, we do not consider it here.

5)The absence of site symmetry would induce a distortion of the lattice.

6)Nevertheless, it should be emphasized that the change (or relatively weak lowering) of the intermolecular rotational barriers appears to be too small for all the cases of the regular structure to allow for the orientational tunneling which is necessary for a number of physical phenomena. One has to remember that the mass of the C_{60} fullerene molecule is 720 a.u. This makes a very strong constraint for the height and width of the energy barriers which are able to give the observed probability (or frequencies)[13] of orientational tunneling transitions.

7)For the case of fullerite, there are $4+4$ different ordering types and $3+4$ different interdomain boundaries (not related with the symmetry operations).

8)For the case of ferromagnets the domain wall width is of the order of $a\sqrt{J/A}$, where a is the lattice spacing, J is the exchange, and A is the anisotropy. Since A is a relativistic correction, the ratio J/A can be increased up to 10^6. But for the present case of one interaction this ratio is about 1.

[1] V. M. Loktev, Fiz. Nizk. Temp. **18**, 217 (1992) [Low Temp. Phys. **18**, 149 (1992)].

[2] A. P. Ramirez, Condens. Matter News **3**, 6 (1994).

[3] O. Gunnarsson, Rev. Mod. Phys. **69**, 575 (1997).

[4] H. Kuzmany, B. Burger, and J. Kurty, in *Optical and Electronic Properties of Fullerenes and Fullerene-based Materials*, J. Shinar, Z. V. Vardeny, and Z. H. Kaffafi (Eds.), Marsel Dekker, New York (2000).

[5] V. B. Efimov, L. P. Mezhov-Deglin, and R. K. Nikolaev, JETP Lett. **65**, 687 (1997).

[6] V. B. Efimov and L. P. Mezhov-Deglin, Physica B **263–264**, 705 (1999).

[7] A. N. Aleksandrovskii, V. B. Esel'son, V. G. Manzhelii, A. V. Soldatov, B. Sundqvist, and B. G. Udovidchenko, Fiz. Nizk. Temp. **23**, 1256 (1997) [Low Temp. Phys. **23**, 943 (1997)]; *ibid.* **26**, 100 (2000) [**26**, 75 (2000)].

[8] A. N. Aleksandrovskii, V. G. Gavrilko, V. B. Esel'son, V. G. Manzhelii, B. Sundqvist, B. G. Udovidchenko, and V. P. Maletskiy, Fiz. Nizk. Temp. **27**, 333 (2001) [Low Temp. Phys. **27**, 245 (2001)]; *ibid.* **27**, 1401, 1033 (2001).

[9] J. P. Olson, K. A. Topp, and R. O. Pohl, Science (Washington, DC, U.S.) **259**, 1145 (1993).

[10] R. C. Yu, N. Tea, M. B. Salamon, D. Lorents, and R. Malhotra, Phys. Rev. Lett. **23**, 2050 (1992).

[11] S. Savin, A. B. Harris, and T. Yildirim, Phys. Rev. B **55**, 14182 (1997).

[12] M. David, R. Ibberson, T. Dennis, and K. Prassides, Europhys. Lett. **18**, 219 (1992).

[13] S. P. Tewari, P. Silotia, and K. Bera, Solid State Commun. **107**, 129 (1998).

[14] M. A. Ivanov and V. M. Loktev, Fiz. Nizk. Temp. **19**, 618 (1993) [Low Temp. Phys. **19**, 442 (1993)].

[15] V. M. Loktev, Yu. G. Pogorelov, and Ju. M. Khalack, Fiz. Nizk. Temp. **27**, 539 (2001) [Low Temp. Phys. **27**, 397 (2001)].

[16] P. Launois, S. Ravy, and R. Moret, Phys. Rev. B **55**, 2651 (1997).

[17] V. M. Loktev, Fiz. Nizk. Temp. **5**, 295 (1979) [Sov. J. Low Temp. Phys. **5**, 142 (1979)].

[18] H. Wang, C. Zeng, B. Wang, J. G. Hou, Q. Li, and J. Yang, Phys. Rev. B **63**, 085417 (2001).

[19] G. Van Tendeloo, S. Amelinckx, M. A. Verheijen, P. H. M. van Loosdrecht, and G. Meijer, Phys. Rev. Lett. **69**, 1065 (1992).

[20] E. J. J. Groenen, O. G. Poluektov, M. Matsushita, J. Schmidt, J. H. van der Waals, and G. Meijer, Chem. Phys. Lett. **197**, 314 (1992).

[21] C. Laforge, D. Passerone, A. B. Harris, P. Lambin, and E. Tosatti, Phys. Rev. Lett. **87**, 085503 (2001).

[22] J. G. Hou, J. Yang, H. Wang, Q. Li, C. Zeng, I. Yuan, B. Wang, D. M. Chen, and Q. Zhu, Nature (London) **409**, 304 (2001).

[23] T. Vegge, J. P. Sethna, S. A. Cheong, K. W. Jacobsen, C. R. Myers, and D. C. Ralph, Phys. Rev. Lett. **86**, 1546 (2001).

[24] Yu. A. Freiman, Fiz. Nizk. Temp. **9**, 657 (1983) [Sov. J. Low Temp. Phys. **9**, 335 (1983)].

[25] V. M. Loktev, Fiz. Nizk. Temp. **25**, 1099 (1999) [Low Temp. Phys. **25**, 823 (1999)].

Interaction between C_{60} and gases under pressure

B. Sundqvist[a]

Department of Physics, Umea University, S-90187 Umea, Sweden
(Submitted December 2, 2002)
Fiz. Nizk. Temp. **29**, 590–596 (May 2003)

A brief review is given of the interaction between fullerite C_{60} and various gases under elevated pressure. Subjects discussed include the formation of ordered interstitial gas-fullerene compounds, reactions between intercalated gases and fullerene molecules to form new endohedral and exohedral compounds, and changes in the structure and properties of C_{60} because of intercalated gas atoms or molecules. © *2003 American Institute of Physics.*
[DOI: 10.1063/1.1542508]

INTRODUCTION

Solid fullerites, such as C_{60} and C_{70}, have very interesting physical properties. However, in many cases the understanding of these properties has been hindered or delayed because interactions between the fullerene molecules and their environment have led to significant changes. Although the fullerene molecule is not very reactive, the intermolecular interactions are very weak and many simple properties change easily when the fullerite lattice is structurally deformed, or when small amounts of impurities are introduced.

A particular case in point is the study of fullerites under high pressure.[1,2] Pressure is a very useful parameter in the study of carbon-based materials. Although the graphite sheet structure has a higher interatomic binding energy than diamond, the weak interplane interaction in the three-dimensional graphite lattice implies that graphite is easily deformed by moderate pressures, and the equilibrium pressure between diamond and graphite at room temperature is only about 2 GPa.[3] Similarly, carbon nanotubes in bundles begin deforming radially at similar pressures, about 1.7 GPa.[4,5] Although fullerene molecules do not deform noticeably under these pressures, their orientation and rotation properties change radically with pressure in the range below 2 GPa,[1] and many studies have been carried out to map these changes as functions of pressure p and temperature T.

Because C_{60} and other fullerenes are "weak", easily deformable solids, it is important to use a pressure transmitting medium which does not cause a large shear stress in the specimens studied. This is most easily done using fluid media. However, most fluids that are in the liquid state at room temperature have a rather limited pressure and temperature range before they either crystallize or vitrify into the solid state (at low T or high p), begin breaking down (pyrolyze), or react with the sample material, both usually at high T. In many cases, gases, such as the rare gases, are therefore considered the "ideal" pressure media. Unfortunately, gases often strongly change the properties of fullerites by intercalating into the large interstitials in the lattice.

In this paper I briefly review the interaction of gases with C_{60}, and the changes brought about in the properties of C_{60} when the material has interacted with the gas. The review is mainly motivated by my own need to understand the interactions between fullerites and pressure media, and will be colored by this background, but the subject is also an interesting field of study in itself. The subject has been included before as part of larger reviews,[1,6] but since this was some time ago, new material will be presented here. First, a very short introduction is given to the structure of pure C_{60}. This is followed by a review of how solid C_{60} interacts with various kinds of gases by intercalation, chemical reactions, and the formation of endohedral compounds.

BACKGROUND: THE ORIENTATIONAL STRUCTURE OF C_{60}

The structure of C_{60} has been very well discussed in the literature,[7,8] and only a brief overview will be given here. At low pressures, C_{60} has three structurally different phases which, however, are all very similar. The room-temperature structure can be described as face-centered cubic (fcc). Both the molecules and the interstitial spaces in the lattice are relatively large, compared to most inorganic atoms or molecules. For each C_{60} molecule in the lattice there are three interstitial sites: two small tetragonal sites with an effective radius of 1.1 Å and one large octahedral site with a radius of 2.1 Å. For comparison, the thresholds or channels between sites have an effective radius of 0.7 Å.

Above $T_0 = 260$ K, the C_{60} molecules carry out quasi-free rotation because of their highly symmetrical shape, and thus the structure can be approximated as a fcc lattice of spherical molecules with a space group $Fm3m$. With decreasing T the correlation between the rotation of neighboring molecules increases, and near T_c large, co-rotating clusters are formed. On cooling through T_0 the molecular rotation stops and a simple cubic (sc) phase with space group $Pa\bar{3}$ and a temperature-dependent degree of orientational order is formed. In this phase the molecular rotation has stopped but the molecules can still jump between different molecular orientations. Finally, below the glassy crystal transition at $T_g \approx 90$ K, molecular motion is very slow and the remaining orientational disorder can be considered frozen; an orientational glass is formed. With increasing pressure both T_0 and T_g increase, as might be expected. The phase lines have slopes of $dT_0/dp = 160$ K·GPa^{-1} and $dT_g/dp = 62$ K·GPa^{-1}, respectively,[1] and on compression of C_{60} at room temperature the fcc-sc (or "rotational") transition oc-

curs already near 0.2 GPa. In practice, almost all high pressure studies are thus carried out on sc (rotationally hindered) C_{60}.

In spite of its high symmetry the C_{60} molecule can be orientationally ordered because it must have 12 carbon atom pentagons, in addition to the "normal" hexagons, in order to have a closed surface. This gives an anisotropic surface charge distribution and thus an electrostatic driving force for orientation. The two possible orientational states will here be denoted descriptively as the P (pentagon) and H (hexagon) orientations, since they correspond to the orientation of a double bond on one molecule towards the center of a pentagon or a hexagon, respectively, on a neighboring molecule.[7,8] At atmospheric pressure the energy difference between these states is only about 12 meV, with the P orientation being lower in energy, but compression of the lattice shifts this energy difference so that at 150 K the two orientations have the same energy near 0.19 GPa.[9] However, the energy threshold for reorientation between these states is quite high, and at atmospheric pressure no orientationally ordered state exists in pure C_{60}. When the material is cooled to below T_0 the orientational order improves with decreasing T, but the glass transition intervenes at about 90 K, when the fraction of P-oriented molecules is still only about 85%. At sufficiently high pressures, however, a completely H-ordered phase should exist.

The evolution of orientational order in the pressure-temperature phase diagram of molecular C_{60} is shown in Fig. 1. This figure shows the fcc-sc phase line and the glass transition line as solid lines. In the fcc phase there is no orientational order, and in the low-T "orientational glass" the orientational structure (i.e., the average number of P- and H-oriented molecules) will be frozen at the particular value present when the sample was cooled through the glass transition line. In the intermediate simple cubic phase, the approximate equilibrium fraction of H-oriented molecules is indicated by several (dotted) lines, corresponding to orientational states with 30, 50, 75 and 90% H-oriented molecules.
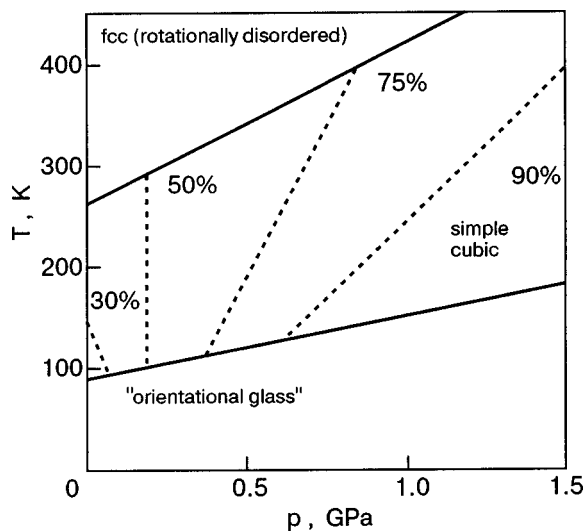

FIG. 1. Pressure-temperature phase diagram of pure C_{60}, showing the three structural phases. In the simple cubic range, the orientational structure under various conditions is shown as calculated from Eq. (1). Numbers indicate the fraction of H-oriented molecules along each of the dotted lines shown.

In the simplest possible model the fraction of H-oriented molecules is given by

$$f(T) = [1 + \exp(-\Delta/k_B T)]^{-1}, \qquad (1)$$

where Δ is the energy difference between the two states. Assuming that Δ is linear in p and independent of T, $f(T,p)$ will be constant on lines in the p-T plane. The dotted lines in Fig. 1 have been calculated assuming that the two states have equal energies at 0.19 GPa.[9] (An alternative model, which might be in better agreement with experiment,[1] assumes that the energies are always identical at the molecular volume corresponding to 0.19 GPa and 150 K.)

INTERCALATION OF C_{60} WITH GASES

Atomic (rare) gases

The chemical reactivity of the fullerene molecules is low, and many atomic or molecular species can diffuse into the cavities in the fullerite lattice without forming chemical bonds with individual fullerene molecules. As might be expected, there is also a strong correlation between the dimensions of the intercalant atoms or molecules and their ability to intercalate into the interstitial sites in the fullerite lattice. Very careful neutron scattering studies of the intercalation of rare gases into these sites have been carried out by Morosin et al.[10,11] At room temperature they were unable to measure the very high diffusion rate of He, which has an effective atomic radius of 0.93 Å and probably fills all available sites. While He is reported to penetrate the lattice completely within a few minutes, even at quite low applied pressure, Ar, with a radius of 1.54 Å, did not intercalate noticeably even after six days at 0.6 GPa. As expected, Ne is an intermediate case because of its atomic radius of 1.12 Å, and, as such is an excellent model substance to illustrate the general behavior of many gases. The presence of Ne atoms in the octahedral sites leads to a small expansion of the lattice. Using neutron diffraction, Morosin et al. were able to use this effect to show that Ne diffuses into the lattice with a time constant of a few hours, finally reaching a saturated state in which the Ne occupancy in the octahedral sites was about 20% at atmospheric pressure and increased to about 100% above 0.2 GPa.[10] Interestingly, the rate of Ne diffusion into the C_{60} lattice depends very strongly on the applied Ne pressure. In the fcc phase the diffusion time constant increases linearly from a few minutes (as for He) at zero pressure to about 90 min at 0.2 GPa, while in the sc phase the time constant for diffusion is approximately 5 h, independent of p over the range studied.[11] It should be noted that while pressure increases the driving force for diffusion, it also decreases the size of the interstitials and channels, but this decrease is much too small to explain the changes in the diffusion rate. On relieving of the Ne pressure, the diffusion of Ne out of the C_{60} lattice was always very rapid except at very low temperatures (200 K).

To explain these observations, Morosin et al. suggest that the main transport mechanism for the Ne atoms is a paddlewheel effect.[11] Ne atoms are slightly too large to pass through the static channels in the structure, but when the C_{60} molecules rotate, Ne atoms may follow the movement and be swept in. In particular, it is speculated that Ne atoms may

attach to the electron-poor centers of the pentagons and hexagons, which form dimples or buckets in the molecular structure and which would temporarily afford larger space for atomic transport through the intermolecular channels during rotation. Such a mechanism would explain the observation that Ne transport slows down significantly with increasing pressure, which leads to a larger interaction between the C_{60} molecules and thus to a slowing down of the molecular rotation. In the sc phase, diffusion slows down even more because rotation is replaced by a stepwise, much slower ratcheting movement of the molecules. On relief of the external pressure, the presence of Ne atoms in the interstitial sites should result in a larger lattice parameter than normal and thus also a smaller molecular interaction, a more rapid molecular rotation, and a very large diffusion coefficient.

The same model should be applicable over a large interval in T, and also to other gases that interact weakly with the fullerene molecules. We would expect the diffusion rate to be high and to increase very strongly with increasing T in the fcc phase (with "free" molecular rotation) and to be smaller and decrease very rapidly with decreasing T in the sc phase as the orientational ratcheting dies out. These predictions agree well with experimental results. At temperatures below 180 K, even He diffusion becomes too slow to be detectable over several hours or days even at 0.5 GPa,[12] and at temperatures above 475 K the heavy rare gases (R−Ar, Xe, and Kr) may all diffuse into C_{60} at 0.17 GPa to form compounds[13] $R_x C_{60}$ with $0.6 < x < 1$. After cooling and pressure relief these compounds are stable over long times at room temperature.

Although NMR shows that the intermolecular interactions and molecular dynamics of intercalated C_{60} differ little from those of the pristine material, intercalation into the interstitial sites still changes the lattice properties of the material in several subtle ways. In general, the presence of foreign atomic or molecular species in the lattice makes both the central interactions between the C_{60} molecules and the orientational interaction weaker, because intercalation expands the C_{60} lattice. The effects are particularly large in the case of the heavy rare gases and molecular gases. For $Kr_x C_{60}$ and $Xe_x C_{60}$ this leads to a decrease in T_0 from 260 K for pure C_{60} to 240 K and 200 K, respectively. Compressibility studies on C_{60} using the (intercalating) lighter rare gases as pressure media showed that the presence of intercalated atoms (He or Ne) made the lattice less compressible.[14] However, the fcc-sc transition still occurred at approximately the same molecular volume as for pure C_{60} (i.e., at a slightly higher pressure), showing that the orientational interaction had changed little. This was not the case for compounds with the heavy rare gases, for which T_0 at atmospheric pressure occurred at a larger molecular volume than for pure C_{60}, indicating a more complicated effect on the intermolecular potential. As mentioned above, the orientational state in the lattice changes with pressure (or, equivalently, volume) in such a way that compression favors the H orientation.[1,9] Conversely, expansion should favor the P orientation, and in principle the expanded lattices should have a higher fraction of P-oriented molecules at low T than pure C_{60}. This effect has not been observed in rare gas compounds, but we return to this question below.

Because intercalation changes the intermolecular inter-

action it also affects the low-energy vibrations and librations in the lattice, and thus the low-temperature properties. Aleksandrovskii *et al.* have carried out extensive studies of the low-temperature thermal expansion of C_{60}, which, surprisingly, shows a large negative peak[15] below 4 K. The magnitude of this effect is also very sensitive to the presence of intercalated gases, even rare gases,[16] showing again that intercalation leads to subtle effects in the lattice properties of C_{60}.

Molecular gases

Many other gases have molecules small enough to diffuse into the C_{60} lattice, especially under low pressures at high temperatures. Many studies have been carried out on the atmospheric components N_2 and O_2, because of their obvious presence in most practical experiments. Other gases that form stable intercalation compounds with C_{60} are, for example, H_2, CH_4, CO, CO_2, and NO.

Gases with relatively large molecules show many interesting effects, when confined to the octahedral interstitial sites in C_{60}. Complete filling of the octahedral sites is usually not observed, except for (Ref. 17) H_2 above 75 MPa, but all gases expand the original C_{60} lattice, and both molecular shape and size are important in determining the properties of the intercalated material. While the very symmetrical CH_4 (or CD_4) molecules continue to rotate freely inside the C_{60} interstitial sites[18] even at 210 K, far below the "freezing" temperature T_0 for the C_{60} lattice, the linear CO_2 molecules must be oriented along the $\langle 111 \rangle$ directions of the C_{60} lattice to fit inside the cavities at all, and the interaction between the C_{60} and the rod-like CO_2 molecules induces large structural differences[19] between pure C_{60} and the intercalated compound at low T. The smaller H_2, CO and NO molecules are also free to vibrate and rotate in their cavities. The dynamic behavior of CO has been observed by NMR and IR spectroscopy over large ranges in temperature and pressure (or "prison cell" volume), and the interaction between the guest molecules and the C_{60} host lattice has been analyzed in detail. With a decrease in temperature the motion gradually changes from basically free rotation at room temperature to tunneling between a few orientational states at low temperatures,[20] and with an increase in pressure a similar restriction in the motion is observed as the available volume decreases.[21] At the highest pressures studied, 3.2 GPa, the molecules must take up oriented positions in the C_{60} lattice in much the same way as does CO_2, and theoretical calculations indicate that the observed spectra agree well with a purely H-oriented C_{60} lattice. The dynamic behavior of trapped H_2 in C_{60} has also been studied.[17] Studies of the interaction between hydrogen and the carbon atoms in C_{60} are important from the point of view of understanding fully the interaction of hydrogen with carbon-based storage media, but C_{60} itself is not a practical storage host since only one H_2 molecule can be stored interstitially per C_{60} molecule, limiting the maximum storage capacity to well below one percent in pure C_{60}.

As in the case of heavy rare gases, intercalation of molecular gases leads to significant downward shifts in T_0, usually down to 240–250 K, and to large increases in the bulk moduli.[22] The lattice expansion should also in principle im-

prove the orientational order, as discussed above, and such an effect has indeed been observed in C_{60} intercalated with CO (Ref. 23) and NO.[24] For NO, Gu, Tang and Feng[24] claim to identify a completely pentagon-oriented lattice with $T_0 = 230$ K from dielectric measurements, but no structural evidence is shown. However, a very careful structural study on CO shows[23] a significant enhancement of the fraction of P-oriented molecules at both intermediate (150 K) and low temperatures. The improved order is believed to arise from a combination of three effects. In addition to the lattice expansion effect already discussed, the glass transition temperature is depressed by about 5 K, and the CO molecules are structurally correlated with the C_{60} molecules at low T through electrostatic interactions. The dipolar CO molecule prefers to bind weakly to the electron-poor single C–C bonds on P-oriented C_{60} molecules, resulting in an almost completely P-oriented structure.

Because of its practical importance, the interaction of C_{60} with N_2 and O_2 has received much attention. Early NMR studies showed that oxygen diffused reversibly into the octahedral sites at atmospheric pressure and room temperature with equilibrium filling fractions of at most a few percent.[25,26] At high pressures, 10–100 MPa, both O_2 and N_2 diffuse slowly into the C_{60} lattice, so that they may fill a large fraction of the octahedral sites over a time of several days.[27,28] However, for N_2 an elevated temperature (500 K) is needed to reach high filling fractions. Because diffusion is slow (and slower for nitrogen than for oxygen), grain size is important, and finely ground powder reaches the highest filling fractions, while the inner parts of crystallites probably always have a lower filling fraction. Evacuation at slightly elevated temperature (see the next Section) is reported to restore the C_{60} to a pure state. The intercalation compounds of oxygen have been studied by many methods. NMR can give information on the average number of filled octahedral sites[25–27,29] and also shows that the oxygen resides at the center of the interstitial sites with no sign of charge transfer or chemical bonding.[26] Inelastic neutron scattering and Raman scattering also shows that although some vibration modes of the intercalated molecules soften appreciably when the molecules are confined within the C_{60} interstitial sites, this has no measurable effect on the vibrational and librational properties of the C_{60} lattice.[28] In spite of this, calorimetry, structural studies, and dielectric studies[27–29] all show that the rotational transition temperature T_0 is strongly depressed by both O_2 and N_2, by up to -20 K in $(O_2)_x C_{60}$ and -22 K in $(N_2)_x C_{60}$ (Ref. 28). Again, these figures are much larger than can be explained by the intercalation-induced lattice expansion (the negative pressure effect).[27] To explain this anomaly, Gu *et al.*[29] suggest that the local strain set up by diffusing intercalant molecules enhances fluctuations in the order parameter close to T_0, while Renker *et al.*[28] suggest that the observed slowing down of molecular motion in the guest molecules transfers energy to the C_{60} lattice by anharmonic interaction with librational modes, thus reducing the effective height of the energy threshold for molecular rotation.

REACTIONS WITH INTERCALATED GASES

As reported above, treatment of intercalated C_{60} under vacuum usually removes the intercalated gas and restores the material to a pure state. However, this is not true for all gases, and in particular reactions may occur between the C_{60} and the gas if the temperature is raised. Two gases are particularly likely to react, hydrogen and oxygen. Hydrogen easily intercalates into C_{60} under pressure, but is also easily desorbed by pumping at room temperature.[17] However, if a high hydrogen pressure is applied to C_{60} at elevated temperature, a reaction occurs between C_{60} and intercalated hydrogen, transforming the material into an intercalation compound of H_2 in $C_{60}H_x$. At a pressure of 600 MPa and a temperature of 620 K, $x \approx 24$ has been reported.[30] The intercalated hydrogen could again be removed by pumping, leaving the new compound behind, and with a long enough reaction time the conversion of C_{60} into hydrofullerite was more or less complete.

All forms of carbon, including diamond and fullerites, burn in oxygen at sufficiently high temperatures. Although no oxidation of C_{60} seems to occur at room temperature, measurements at 370 K shows that reactions have occurred and that oxides have formed.[31] At higher temperatures the oxidation increases rapidly. At 470 K strong IR evidence for oxidation is seen, with traces of trapped CO and strong absorption bands from C–O and C=O bonds. The fullerene molecules have started breaking down or have been transformed into $C_{60}O_x$. At 570 K, the material breaks down further with the formation of both oxides and amorphous residues from broken cages; in simple terms, it slowly burns. Any fullerite sample exposed to air should thus be kept at temperatures well below 400 K to protect it from permanent changes by oxidation.

C_{60} can also react with oxygen without heating. In the discussions above, it has implicitly been assumed that the material has been protected from visible or UV light, since it is well known that both C_{60} and C_{70} polymerize if irradiated with such light in an oxygen-free environment.[32] Oxygen inhibits this polymerization process, but C_{60} irradiated in the presence of oxygen shows other characteristic changes (''photo-transformation'').[33,34] First, radiation with visible or UV light enhances the oxygen diffusion rate in C_{60} by at least an order of magnitude, so that thin films in air rapidly become oxygen saturated (most octahedral sites filled, at least within the light penetration depth), or oxygen-rich films lose oxygen in a vacuum. Films (or, equivalently, the surface layers of irradiated bulk material) irradiated for a short time do not differ from the materials discussed above, i.e., the oxygen interacts only weakly with the lattice. After longer times, however, an increasing amount of photo-induced oxidation of C_{60} to $C_{60}O_x$ becomes evident. After long time exposure the films become insoluble in toluene like photo-polymerized C_{60}, suggesting the presence of cross-linked carbon-oxygen clusters in the film. Fullerites should therefore also be protected from light, whether in air, vacuum, or under inert gas.

FORMATION OF ENDOHEDRAL COMPOUNDS

Fullerenes like C_{60} and C_{70} are hollow shells, which can be used as containers for other atoms, and several methods have been found to produce such materials. Here it will only be noted that the formation of such endohedral compounds has been reported during treatment of fullerenes under rea-

sonably high rare-gas pressure at high temperatures. Saunders *et al.*[35] reported that under 0.3 GPa at temperatures near 925 K, about 0.1% of the C_{60} molecules captured rare-gas guest atoms such as He, Ne, Ar, and Kr. The larger Xe molecule, however, did not enter into C_{60}. At high temperatures, C–C bonds on the C_{60} molecules are believed to break spontaneously and the rare-gas atoms then have a chance to enter and get trapped inside when the "window" closes. Endohedral compounds are usually stable for long times under ambient conditions. The method, the properties of the resulting endohedral compounds, and their possible applications have been thoroughly discussed in Ref. 36.

CONCLUSIONS

Intercalation of atomic and molecular gases gives rise to many novel and interesting phenomena in fullerite lattices. Some of these are well understood, while for others our understanding is still only in the early stages. Because intercalation may lead to significant changes in the properties of fullerite materials both directly and, in some cases, through chemical reactions induced by temperature or pressure, it is important to understand these effects in order to sort out which properties are intrinsic to C_{60} or other fullerites and which depend on the presence of intercalated impurity atoms or molecules. Since intercalation can also be used as a physical tool to study the properties of single molecules or their interactions with carbon or each other, research into intercalation compounds of fullerites will probably continue to be of interest for many years to come.

a)E-mail: bertil.sundqvist@physics.umu.se

[1] B. Sundqvist, Adv. Phys. **48**, 1 (1999).

[2] V. D. Blank, S. G. Buga, G. A. Dubitsky, N. R. Serebryanaya, M. Yu. Popov, and B. Sundqvist, Carbon **36**, 319 (1998).

[3] F. P. Bundy, W. A. Bassett, M. S. Weathers, R. J. Hemley, H. K. Mao, and A. F. Goncharov, Carbon **34**, 141 (1996).

[4] U. D. Venkateswaran, A. M. Rao, E. Richter, M. Menon, A. Rinzler, R. E. Smalley, and P. C. Eklund, Phys. Rev. B **59**, 10928 (1999).

[5] S. Rols, I. N. Goncharenko, R. Almairac, J. L. Sauvajol, and I. Mirabeau, Phys. Rev. B **64**, 153401 (2001).

[6] B. Sundqvist, in *Fullerenes: Chemistry, Physics and Technology*, edited by K. M. Kadish and R. S. Ruoff, J. Wiley & Sons, New York (2000), p. 611.

[7] M. S. Dresselhaus, G. Dresselhaus, and P. C. Eklund, *Science of Fullerenes and Carbon Nanotubes*, Academic Press, San Diego (1996).

[8] P. Launois, S. Ravy, and R. Moret, Int. J. Mod. Phys. B **13**, 253 (1999).

[9] W. I. F. David and R. M. Ibberson, J. Phys.: Condens. Matter **5**, 7923 (1993).

[10] B. Morosin, J. D. Jorgensen, S. Short, G. H. Kwei, and J. E. Schirber, Phys. Rev. B **53**, 1675 (1996).

[11] B. Morosin, Z. Hu, J. D. Jorgensen, S. Short, and G. H. Kwei, Phys. Rev. B **59**, 6051 (1999).

[12] L. Pintschovius, O. Blaschko, G. Krexner, and N. Pyka, Phys. Rev. B **59**, 11020 (1999).

[13] G. Gadd, S. Moricca, S. J. Kennedy, M. M. Elcombe, P. J. Evans, M. Blackford, D. Cassidy, C. J. Howard, P. Prasad, J. V. Hanna, A. Burchwood, and D. Levy, J. Phys. Chem. Solids **58**, 1823 (1997).

[14] J. E. Schirber, G. H. Kwei, J. D. Jorgensen, R. L. Hitterman, and B. Morosin, Phys. Rev. B **51**, 12014 (1995).

[15] A. N. Aleksandrovskii, V. B. Esel'son, V. G. Manzhelii, A. Soldatov, B. Sundqvist, and B. G. Udovidchenko, Fiz. Nizk. Temp. **26**, 100 (2000) [Low Temp. Phys. **26**, 75 (2000)].

[16] A. N. Aleksandrovskii, V. G. Gavrilko, V. B. Esel'son, V. G. Manzhelii, B. G. Udovidchenko, V. P. Maletskiy, and B. Sundqvist, Fiz. Nizk. Temp. **27**, 1401 (2001) [Low Temp. Phys. **27**, 1033 (2001)].

[17] S. A. Fitzgerald, T. Yildirim, L. J. Santodonato, D. A. Neumann, J. R. D. Copley, J. J. Rush, and F. Trouw, Phys. Rev. B **60**, 6439 (1999).

[18] B. Morosin, R. A. Assink, R. G. Dunn, T. M. Massis, J. E. Schirber, and G. H. Kwei, Phys. Rev. B **56**, 13611 (1997).

[19] M. James, S. J. Kennedy, M. M. Elcombe, and G. E. Gadd, Phys. Rev. B **58**, 14780 (1998).

[20] I. Holleman, G. von Helden, E. H. T. Olthof, P. J. M. van Bentum, R. Engeln, G. H. Nachtegaal, A. P. M. Kentgens, B. H. Meier, A. van der Avoird, and G. Meijer, Phys. Rev. Lett. **79**, 1138 (1997).

[21] I. Holleman, G. von Helden, A. van der Avoird, and G. Meijer, Phys. Rev. Lett. **80**, 4899 (1998).

[22] S. van Smaalen, R. E. Dinnebier, R. Milletich, M. Kunz, I. Holleman, G. von Helden, and G. Meijer, Chem. Phys. Lett. **319**, 283 (2000).

[23] S. van Smaalen, R. E. Dinnebier, W. Schnelle, I. Holleman, G. von Helden, and G. Meijer, Europhys. Lett. **43**, 302 (1998).

[24] M. Gu, T. B. Tang, and D. Feng, Phys. Rev. B **66**, 073404 (2002).

[25] R. A. Assink, J. E. Schirber, D. A. Loy, B. Morosin, and G. A. Carlson, J. Mater. Res. **7**, 2136 (1992).

[26] P. Bernier, I. Luk'yanchuk, Z. Belahmer, M. Ribet, and L. Firlej, Phys. Rev. B **53**, 7535 (1996).

[27] J. E. Schirber, R. A. Assink, G. A. Samara, B. Morosin, and D. Loy, Phys. Rev. B **51**, 15552 (1995).

[28] B. Renker, H. Schober, M. T. Fernandez-Diaz, and R. Heid, Phys. Rev. B **61**, 13960 (2000).

[29] M. Gu, T. B. Tang, C. Hu, and D. Feng, Phys. Rev. B **58**, 659 (1998).

[30] A. I. Kolesnikov, V. E. Antonov, I. O. Bashkin, G. Grosse, A. P. Moravsky, A. Yu. Muzychka, E. G. Ponyatovsky, and F. E. Wagner, J. Phys.: Condens. Matter **9**, 2831 (1997).

[31] M. Wohlers, H. Werner, D. Herein, T. Schedel-Niedrig, A. Bauer, and R. Schlögl, Synth. Met. **77**, 299 (1996).

[32] A. M. Rao, P. Zhou, K.-A. Wang, G. T. Hager, J. M. Holden, Y. Wang, W.-T. Lee, X.-X. Bi, P. C. Eklund, D. S. Cornett, M. A. Duncan, and I. J. Amster, Science (Washington, DC, U.S.) **259**, 955 (1993).

[33] P. C. Eklund, A. M. Rao, P. Zhou, Y. Wang, and J. M. Holden, Thin Solid Films **257**, 185 (1995).

[34] T. L. Makarova, V. I. Sakharov, I. T. Serenkov, and A. Ya. Vul', Fiz. Tverd. Tela (St. Petersburg) **41**, 554 (1999) [Phys. Solid State **41**, 497 (1999)].

[35] M. Saunders, H. A. Jiménez-Vazquez, R. J. Cross, S. Mroczkowski, M. L. Gross, D. E. Giblin, and R. J. Poreda, J. Am. Chem. Soc. **116**, 2193 (1994).

[36] M. Saunders, R. J. Cross, H. A. Jimenez-Vazquez, R. Shimshi, and A. Khong, Science (Washington, DC, U.S.) **271**, 1693 (1996).

Intercalation of C$_{60}$ fullerite with helium and argon at normal temperature and pressure

Yu. E. Stetsenko, I. V. Legchenkova,* K. A. Yagotintsev, A. I. Prokhvatilov, and M. A. Strzhemechnyĭ

B. Verkin Institute for Low Temperature Physics and Engineering, National Academy of Sciences of Ukaine, pr. Lenina 47, 61103 Khar'kov, Ukraine
(Submitted January 30, 2003)
Fiz. Nizk. Temp. **29**, 597–602 (May 2003)

Powder x-ray diffractometry was used to study the effect of intercalating C$_{60}$ fullerite with helium and argon atoms on the fullerite structure. The samples were saturated at room temperature and normal pressure. The dependences obtained for the lattice parameter and half-width of certain reflections on the intercalation time with helium atoms showed that the voids in the C$_{60}$ lattice were filled in two stages. Helium filled the octahedral voids relatively rapidly first and then the tetrahedral subsystem, but much more slowly. Both intercalants affected the half-width and intensity of the reflections, the matrix lattice parameters, the phase transition temperature, the volume jump at the transition, and the thermal expansion coefficients of C$_{60}$ fullerite. © *2003 American Institute of Physics.* [DOI: 10.1063/1.1542509]

1. INTRODUCTION

The saturation of new carbon materials (fullerites, nanotubes) with atoms and molecules that enter into a different kind of interaction with the matrix is now under intensive investigation. One reason for this interest is the desire to understand the microscopic details of the infusion in order to learn how to the control the technology for obtaining new substances on based on carbon materials. In this respect C$_{60}$ fullerite as a matrix is nearly the most often-studied substance. The intercalation C$_{60}$ fullerite with atoms of alkali metals was performed[1-11] soon after its discovery and organic superconductors of a new kind with relatively high superconducting transition temperatures were obtained.[5-8]

According to the arrangement of the centers of gravity of the molecules, C$_{60}$ fullerite has a face-centered cubic lattice with quite large tetrahedral and octahedral voids in the entire range of existence of the solid phase. For each C$_{60}$ molecule in the lattice there are two tetrahedral voids and one octahedral void, whose average diameters are 2.2 Å and 4.2 Å, respectively.[12,13] This makes it possible to obtain diverse interstitial solutions based on C$_{60}$ fullerite in a wide concentration range.

Intercalation with particles which do not form a homopolar bond with the matrix occupies a special place. Atoms of inert elements and simple di- and triatomic molecules possess gas-kinetic diameters which are much larger than the tetrahedral voids and comparable in size to octahedral voids. Consequently, intercalation often fills only the octahedral voids. However, without a forming chemical bond with the matrix, such interstitial impurities appreciably affect the lattice energy and the thermodynamic properties of fullerite. As a result, the orientational phase transition temperature is shifted[14-17] and changes occur in the lattice parameters and volume,[14,15,18,19] compressibility,[20] thermal expansion coefficients,[21] diffusion kinetics,[22] and the vitrification process.[19] However, if there is a large difference in size and symmetry between the impurity component and the octahedral voids, as happens, for example, for intercalation of C$_{60}$

with carbon dioxide CO$_2$,[23] then the impurity molecules strongly influence the orientational order of the molecules and the crystal symmetry of the matrix. In the process the structural symmetry of the low-temperature phase of pure C$_{60}$ fullerite can be lowered from cubic $Pa3$ to monoclinic $P2_1/n$. C$_{60}$ fullerite intercalated with molecules of nitrogen and oxygen has been investigated in Refs. 24 and 25 using prece methods—dilatometry, neutron diffraction, and inelastic neutron scattering. It has been shown that even though the bond between the N$_2$(O$_2$) molecules placed into octahedral voids is weak, substantial structural changes are observed and not only the orientational high-temperature transition but also the low-temperature vitrification process are affected. Intercalation with CO molecules virtually completely precludes the formation of a glassy state in C$_{60}$.[19]

In the works above-mentioned polycrystalline samples intercalated at quite high pressures (from several to several tens of kilobars) and at temperatures of several hundreds of degrees celsius[14-16] or samples compacted under pressures up to 10 kbar at room temperature[21] were investigated. Under these conditions partial polymerization of C$_{60}$ fullerite is possible[20] and defects in the form of polymer complexes or chains can form in the samples. In studying the physical properties of such objects it is, of course, difficult to separate the effect of intercalation in a pure form. Consequently, it is important to perform experiments on samples which are stress-free and intercalated with atoms of inert elements or simple molecular substances at normal pressure and temperature. It should also be noted that even though the number of works on intercalation of C$_{60}$ with simple molecular substances is relatively large, the physical nature of the effect of these substances on the lattice still remains unclear. Consequently, any information on the behavior of an impurity in voids is very important. In this respect the results obtained in Refs. 26–28 on the influence of temperature and pressure on the dynamics of the rotational motion of molecules in octahedral voids and their interaction with the surrounding C$_{60}$ molecules are definitely of interest.

On the basis of the arguments presented above and the reasonable assumption that helium most easily penetrates into voids in the fullerite crystal lattice, the infusion of He atoms into C_{60} crystallites was studied under relatively low pressures (~ 1 bar) and temperatures $\sim(300 \pm 10)$ K. Powder x-ray diffractometry was used to study the saturation process. Special attention was devoted to determining how helium impurity affects the orientational phase transition and the orientational vitrification process. Some preliminary results obtained on the effect of helium on the structure of C_{60} have been published in a brief communication.[29] We note that for $T < 20$ K measurements were performed in Ref. 30 of the linear thermal expansion coefficients of C_{60} fullerite intercalated, just as in the present investigation, with He atoms at room temperature and pressure 1 atm. In the present paper results for samples of C_{60} fullerite intercalated with the heavier inert element argon are also presented.

2. EXPERIMENTAL PROCEDURE

The experiments were performed using ultrapure (99.98%) polycrystalline C_{60} fullerite. Fullerite powder was first allowed to stand for several days in a 10^{-3} mm Hg vacuum at 100 °C in order for degassing to occur. Next, the chamber with the sample was filled with He gas at room temperature up to pressure 1 atm, and C_{60} fullerite was allowed to stand in this atmosphere for several months. Quite complete x-ray diffraction patterns were obtained and the lattice parameter of C_{60} at room temperature was determined every 0.5–10 h at the beginning of intercalation and every 100–200 h at later stages. The measurements were performed periodically in a limited range of angles with temperature varyied from ~ 50 K to room temperature with a 10–20 K step. Specifically, such measurements were performed after the first stage of rapid saturation of the sample (see below) was completed. Such x-ray diffraction patterns were obtained with heating and cooling of the samples. The temperature range chosen for the investigations made it possible to follow the change in the structural characteristics of intercalated C_{60} near the temperature T_c of the orientational phase transition and the vitrification temperature T_g.

In addition to determining the lattice parameters, the temperature dependences of the half-widths of x-ray reflections were also investigated. These characteristics served as independent data making it possible to judge very reliably the state and distribution of the intercalant in the C_{60} matrix and the local effect of the intercalant on the crystal lattice.

The investigations were performed using the DRON-3 x-ray diffractometer, which was automated using a PC-286 personal computer, in a special x-ray gas-flow cryostat, which made it possible to stabilize the temperature of the samples to within ± 0.1 K at each point in the temperature range 15–300 K. The $K\alpha$ radiation of a nickel anode ($\lambda = 1.6591$ Å) was used. The lattice parameter of pure and intercalated fullerite was determined to within 0.02%. The lattice parameters at the reference points—at room temperature and 15 K, where the complete diffraction patterns were obtained—were measured to the same accuracy. This made it possible to average the data at these temperatures very reliably. The investigation of the temperature dependence of the lattice parameter in the intermediate range was based on
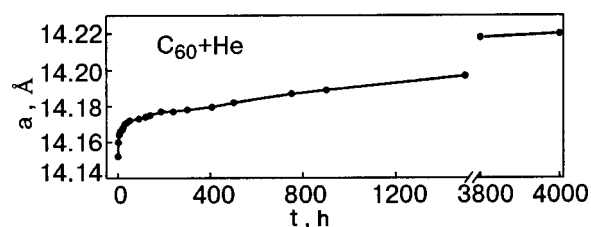

FIG. 1. Variation of the lattice parameter of the cubic fcc lattice of C_{60} fullerite as a function of the holding time in a helium atmosphere at pressure 1 atm and $T = 295$ K.

measurements of the temperature shift of the three strongest lines (111), (220), and (311) relative to their positions at the reference points.

We judged the kinetics of void filling in the C_{60} lattice according to the effect of the impurity on the lattice parameter and the half-width and intensity of the x-ray reflections during the saturation process. Independent measurements of these quantities performed by other authors at high pressures and temperatures were used.[16,18,31] Neutron spectroscopy data[32,33] and the results of adsorption and desorption investigations,[34,35] making it possible to estimate the upper limit of void filling by atoms and simple molecules, were taken into account. The data on the change in the half-width and intensity of x-ray reflections during the saturation of the samples also enabled us to draw certain conclusions about the kinetics of the diffusion of He atoms in C_{60} crystals.

3. RESULTS AND DISCUSSION

A. Intercalation with helium

The saturation of polycrystalline samples of C_{60} fullerites with He atoms was conducted at room temperature and pressure 1 atm over a quite long period of time (up to 4000 h). The lattice parameter of fullerite was observed to increase continually with time. Figure 1 shows a typical curve of the time variation of the fullerite lattice parameter $a(t)$ with the samples held in a helium atmosphere. It is evident that the intercalation process characterized by the curve $a(t)$ consists of two distinct stages. During the first stage $a(t)$ reaches relatively rapidly (in $\sim 50-60$ h) a section of relatively weak but almost linear temperature dependence. The lattice parameter at the first stage increases approximately by 0.022 Å (or 0.16%). During further holding up to 4000 h the increase in $a(t)$ is almost twice that at the first stage, i.e. 0.045 Å (or 0.32%), with reasonable extrapolation. The conjecture that the process occurs in two stages is unequivocally supported by the time dependence of the half-width Δ_{hkl} of the reflections. Figure 2 shows the most typical time dependences $\Delta_{hkl}(t)$. It is evident that at the first intercalation step the half-width of the lines (111), (220), and (311) increases by more than 50% relative to the value ordinarily observed for pure fullerite. This attests to a high level of static local distortions which appear in the matrix during intercalation and are due to the nonuniformity of the lattice deformation near the voids occupied by impurity atoms. The observation of a sharp decrease in the half-width of the lines at intercalation times 50–100 h (Fig. 2) and the slower dropoff of the half-width at longer times were very unexpected. The structural data taken as a whole and, especially, the presence of
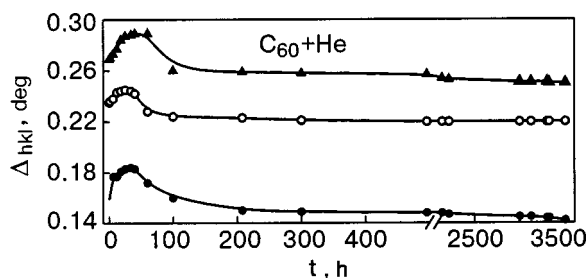
FIG. 2. Variation of the half-width of the x-ray reflections (111) (●), (220) (▲), and (311) (○) versus the helium saturation time of C_{60} fullerite at pressure 1 atm and $T = 295$ K.

FIG. 3. Temperature dependences of the lattice parameter of the cubic lattice of pure C_{60} fullerite (——)[36] and intercalated with He atoms. The data were obtained with heating (●) and cooling (▽) of the samples in a helium atmosphere.

two sections, it seems to us, make it possible to reconstruct quite reliably the process by which helium saturates C_{60} fullerite. On the basis of the energetics and geometry of the voids in an fcc lattice it can be supposed that the octahedral voids should be filled more easily than tetrahedral voids. Consequently, virtually all octahedral voids are filled at the first stage, starting, of course, with the layers near the surface. At the beginning of the first stage this should result in substantial spatial nonuniformity in the intercalant distribution and, consequently, deformation nonuniformity. Of course, voids in deep layers are filled much more slowly and this process is determined by interstitial diffusion of He atoms from layers near the surface. A new batch of atoms fills the octahedral voids which are emptied. This effect has also been observed in other experiments on the intercalation of C_{60}.[22] As the crystallite volumes are filled, the degree of nonuniformity decreases and the half-width returns essentially to its previous value. Thus, the first stage terminates with uniform and, probably, complete saturation of the octahedral subsystem. Since He atoms are small (the nominal atomic radius of He is 0.93 Å[18,22]), not only octahedral but also tetrahedral voids in the fcc fullerite lattice can be filled. The continual slow growth of the lattice parameter a of the matrix at the second (longer-lasting) stage is due to the fact that the tetrahedral subsystem starts to fill up, a process which is essentially uniform over the entire volume of the crystallite because of diffusion penetration of the intercalant. The transfer of the intercalant from the octahedral into the tetrahedral system is rapidly made up from outside the crystallite as a result of the much more rapid diffusion along octahedral voids. Comparing the duration of the two stages, the following rough estimate can be made: the diffusion coefficient in the octahedral subsystem is more than two orders of magnitude larger than in the tetrahedral system. We note that the intercalation of octahedral voids by large-diameter atoms is much more rapid at high pressures. For example, when C_{60} is held in Ne gas under 2.75 kbar pressure $a(t)$ is completely time-independent already for $t > 10$ h.[18]

The temperature dependences of the lattice parameter a on heating and cooling in the temperature range 30–300 K were investigated for C_{60} samples maximally saturated with helium. In Fig. 3 the results are compared with pure fullerite.[36] It is evident that when helium fills the octahedral (and, possibly, tetrahedral) voids in the cubic lattice of C_{60} the lattice parameters increase substantially (on the average by 0.3%) in the entire experimental temperature range, the orientational phase transition temperature increases by 10 K,
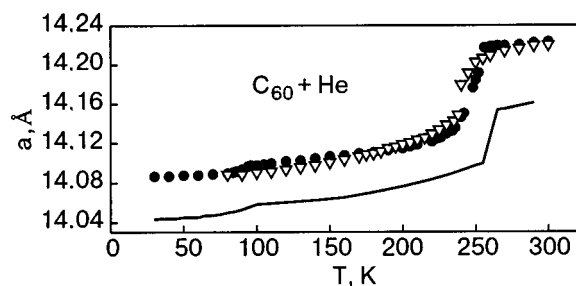
the jump in the lattice parameter (volume) at a phase transition is almost halved, and the thermal expansion coefficients near the transition temperature increase. Intercalation with helium atoms affects the vitrification process only slightly. The vitrification feature in the temperature dependence $a(t)$ is observed essentially at the same temperature as in pure fullerite, but the lattice parameter decreases somewhat.

We did not observe any appreciable effect of thermal cycling of the samples on the temperature dependences of the lattice parameter of C_{60} fullerite intercalated with He atoms. On cooling only a negligible decrease of the orientational and vitrification transition temperatures is observed (see Fig. 3).

B. Intercalation with Ar atoms

The intercalation of C_{60} with argon for 500 h performed at room temperature and 1 atm pressure had virtually no effect on the lattice parameter of the matrix to within the limits of error in determining this parameter. However, the lattice parameter tended to decrease for samples held in argon for 3500–5500 h. The half-widths of the reflections remained constant. At the same time the intensity of the reflections decreased throughout the entire intercalation time. In addition, the main drop in the intensity occurred during the first 200 h. The change in the intensity of the (111) line during intercalation is presented in Fig. 4. A qualitatively and quantitatively similar decrease in the intensity with time was also observed for certain other reflections.

The presence of argon impurity atoms in C_{60} fullerite was observed in the experiments distinctly in the temperature dependences of the lattice parameter. Although in a substantial portion of the temperature range of the low- and high-temperature phases the lattice parameters of argon-
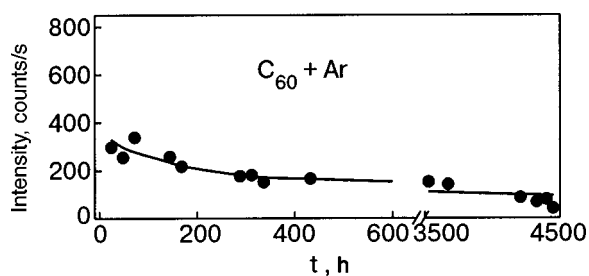

FIG. 4. Influence of the intercalation time of C_{60} fullerite intercalated with argon at 1 atm and $T = 295$ K on the intensity of the x-ray reflection from the (111) plane of the matrix.
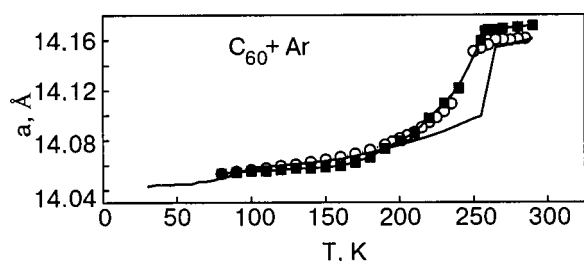
FIG. 5. Temperature dependences of the lattice parameter of Ar-intercalated fullerite C_{60}, obtained on heating (○) and cooling (■) of the samples in argon gas. Solid line —parameters of the cubic lattice of pure C_{60} fullerite.[36]

intercalated fullerite are almost identical to the values characteristic for pure C_{60}, they clearly are different in the range of the orientational phase transition (Fig. 5). The presence of an interstitial impurity has an especially strong effect on the transition temperature. This temperature decreases by more than 15 K, and the amount of Ar impurity in the samples is probably much lower than He impurity in C_{60}. The shift obtained in T_c is virtually identical to that observed previously[14,15] for C_{60} samples intercalated with argon atoms at 300 °C and pressure 1.7 kbar. The analysis performed shows that the decrease established in these works in the orientational phase transition temperature T_c corresponds to complete filling of the octahedral voids by argon.

Just as for saturation with helium, argon impurity atoms decrease the jump in the lattice parameter (volume) at a transition and substantially increase the thermal expansion coefficients near T_c (Fig. 5). The increase (almost linear) of the lattice parameter of argon-intercalated fullerite relative to pure C_{60} as T_c is approached was the same as in Ref. 15. It follows from our experiments that thermal cycling of C_{60} samples with argon impurity has virtually no effect on the character of the temperature dependences of the lattice parameter (Fig. 5). In connection with the results obtained in this part of the work, it should be noted that the effect of argon on the temperature change of the C_{60} lattice parameters is qualitatively similar to the effect of He impurity atoms, even though their change on room-temperature intercalation is much smaller than for the system C_{60}+He.

*E-mail: legchenkova@ilt.kharkov.ua

[1] P. A. Heiney, J. Phys. Chem. Solids **53**, 1333 (1992).
[2] C. H. Pennington and V. A. Stenger, Rev. Mod. Phys. **68**, 855 (1996).
[3] P. W. Stephens, L. Mihaly, P. L. Lee, R. L. Wetten, S.-M. Huagan, R. B. Kaner, F. Diederich, and K. Holczer, Nature (London) **351**, 632 (1991).
[4] R. M. Fleming, M. J. Rossiensky, A. P. Ramirez, D. W. Murphy, J. C. Tully, R. C. Haddon, T. Siegrist, R. Tucko, H. Glarum, P. Marsh, G. Dabbagh, S. M. Zahurak, A. V. Makhija, and C. Hampton, Nature (London) **352**, 701 (1991).
[5] O. Zhou, J. E. Fisher, N. Couste, S. Kycia, Q. Zhu, A. R. McGhie, W. J. Romanov, J. P. Jr. McCauley, A. B. Smith III, and D. E. Cox, Nature (London) **351**, 462 (1991).
[6] Q. Zhu, O. Zhou, N. Costel, G. B. M. Vaughan, J. P. Jr. McCauley, W. J. Romanov, J. E. Fisher, and A. B. Smith III, Science (Washington, DC, U.S.) **254**, 545 (1991).
[7] A. F. Hebard, M. J. Rosseinsky, R. C. Haddon, D. W. Murphy, S. N. Glarum, T. T. M. Plastra, A. P. Ramirez, and A. R. Kortan, Nature (London) **350**, 600 (1991).
[8] M. J. Rosseinsky, A. P. Ramirez, S. H. Glarum, D. W. Murphy, R. C. Haddon, A. F. Hebard, T. T. M. Plastra, A. R. Kortan, S. M. Zahurak, and A. V. Makhija, Phys. Rev. Lett. **66**, 2830 (1991).
[9] K. Holtczer, O. Klein, S. M. Huang, R. B. Kaner, K. J. Fu, R. L. Wetten, and F. Diederich, Science (Washington, DC, U.S.) **252**, 1154 (1991).
[10] O. Zhou and D. E. Cox, J. Phys. Chem. Solids **53**, 1373 (1992).
[11] J. E. Fisher and P. A. Heiney, J. Phys. Chem. Solids **54**, 1725 (1993).
[12] J. P. Jr. McCauley, Q. Zhu, N. Costel, O. Zhou, G. B. M. Vaughan, S. N. J. Idziak, J. E. Fisher, S. W. Tozer, D. M. Froski, N. Bykovetz, C. L. Lin, A. R. McGhie, B. Hallen, W. J. Romanov, A. M. Denenstein, and A. B. Smith III, J. Am. Chem. Soc. **113**, 8537 (1991).
[13] P. W. Stephens, L. Mihaly, J. B. Willey, S. M. Huagan, R. B. Kaner, F. Diederich, R. L. Wetten, and K. Holczer, Phys. Rev. B **45**, 543 (1992).
[14] G. E. Gadd, S. Morica, S. J. Kennedy, M. M. Elecombe, P. G. Evans, M. Blackford, D. Cassidy, C. J. Howard, P. Prasad, J. V. Hanna, A. Burchwood, and D. Levy, J. Phys. Chem. Solids **58**, 1823 (1997).
[15] G. E. Gadd, S. J. Kennedy, S. Morica, C. J. Howard, M. M. Elecombe, P. G. Evans, and M. James, Phys. Rev. B **55**, 14794 (1997).
[16] B. Morosin, J. D. Jorgensen, S. Short, G. H. Kwei, and J. E. Schirber, Phys. Rev. B **53**, 1675 (1996).
[17] J. E. Schirber, R. A. Assink, G. A. Samara, B. Morosin, and D. Loy, Phys. Rev. B **51**, 15552 (1995).
[18] J. E. Schirber, G. H. Kwei, J. D. Jorgensen, R. L. Hitterman, and B. Morosin, Phys. Rev. B **51**, 12014 (1995).
[19] S. Van Smaalen, R. Dinnebier, I. Holleman, G. von Helden, and G. Meijer, Phys. Rev. B **57**, 6321 (1998).
[20] B. Sundqvist, Adv. Phys. **48**, 1 (1998).
[21] A. N. Aleksandrovskii, V. G. Gavrilko, V. B. Esel'son, V. G. Manzhelii, B. Sundqvist, B. G. Udovidchenko, and V. P. Maletskiy, Fiz. Nizk. Temp. **27**, 333 (2001) [Low Temp. Phys. **27**, 245 (2001)].
[22] B. Morosin, Z. Hu, J. D. Jorgensen, S. Short, J. E. Schirber, and G. H. Kwei, Phys. Rev. B **59**, 6051 (1999).
[23] M. James, S. J. Kennedy, M. M. Elcombe, and G. E. Gadd, Phys. Rev. B **58**, 14780 (1998).
[24] B. Renker, H. Schober, M. T. Fernandez-Diaz, and R. Heid, Phys. Rev. B **61**, 13960 (2000).
[25] B. Renker, G. Roth, H. Schober, P. Nagel, R Lortz, C. Meingast, D. Ernst, M. T. Fernandez-Diaz, and M. Koza, Phys. Rev. B **64**, 205416 (2001).
[26] G. I. Holleman, G. von Helden, E. H. T. Olthof, P. G. M. van Bentum, R. Engeln, G. H. Nachtegaal, A. P. M. Kentgens, B. H. Meier, A. van der Avoird, and G. Meijer, Phys. Rev. Lett. **79**, 1138 (1998).
[27] G. I. Holleman, G. von Helden, A. van der Avoird, and G. Meijer, Phys. Rev. Lett. **80**, 4899 (1998).
[28] G. H. Kwei, F. Trouw, B. Morosin, and H. F. King, J. Chem. Phys. **113**, 320 (2000).
[29] I. V. Legchenkova, A. I. Prokhvatilov, Yu. E. Stetsenko, M. A. Strzhemechny, K. A. Yagotintsev, A. A. Avdeenko, V. V. Eremenko, P. V. Zinoviev, V. N. Zoryansky, N. B. Silaeva, and R. S. Ruoff, Fiz. Nizk. Temp. **28**, 1320 (2002) [Low Temp. Phys. **28**, 942 (2002)].
[30] A. N. Alexandrovskii, A. S. Bakai, A. V. Dolbin, V. B. Esel'son, G. E. Gadd, V. G. Gavrilko, V. G. Manzhelii, S. Moricca, B. Sundqvist, and B. G. Udovichenko, Fiz. Nizk. Temp. **29**, 432 (2003) [Low. Temp. Phys. **29**, 324 (2003)].
[31] S. A. Fitzgerald, T. Yildirim, L. J. Santodonato, D. A. Neuman, J. R. D. Copley, J. J. Rush, and F. Trouw, Phys. Rev. B **60**, 6439 (1999).
[32] A. I. Kolesnikov, V. E. Antonov, I. O. Bashkin, G. Grosse, A. P. Moravsky, A. Yu. Muzychka, E. G. Ponyatovsky, and F. E. Wagner, J. Phys.: Condens. Matter **9**, 2831 (1997).
[33] I. O. Bashkin, A. I. Kolesnikov, V. E. Antonov, E. G. Ponyatovsky, A. P. Kobzev, A. Yu. Muzychka, A. P. Moravsky, F. E. Wagner, and G. Grosse, Mol. Mater. **10**, 265 (1998).
[34] K. Ichimura, K. Imaeda, and H. Inokushi, Mol. Cryst. Liq. Cryst. **340**, 649 (2000).
[35] Y. Ye, C. C. Ahn, B. Fultz, J. J. Vajo, and J. J. Zinck, Appl. Phys. Lett. **77**, 2171 (2000).
[36] S. V. Lubenets, V. D. Natsik, L. S. Fomenko, A. P. Isakina, A. I. Prokhvatilov, M. A. Strzhemechnyi, N. A. Aksenova, and R. S. Ruoff, Fiz. Nizk. Temp. **23**, 338 (1997) [Low Temp. Phys. **23**, 251 (1997)].

Translated by M. E. Alferieff

Low-temperature thermal conductivity of solid carbon dioxide

V. V. Sumarokov, P. Stachowiak,* and A. Jeżowski

Institute for Low Temperatures and Structure Research of the Polish Academy of Sciences, P.O. Box 1410, 50-950 Wroclaw, Poland
(Submitted May 4, 2003)
Fiz. Nizk. Temp. **29**, 603–605 (May 2003)

Preliminary measurements of the thermal conductivity of pure carbon dioxide in the temperature range 1.5–35 K are reported. The first data below 25 K have been obtained. The thermal conductivity reaches very high values, about 700 W/(m·K), which is unusual for simple molecular crystals. A straightforward analysis of the data shows a coarse-grained sample. © *2003 American Institute of Physics.* [DOI: 10.1063/1.1542510]

Solid carbon dioxide is an example of a simple molecular crystal consisting of linear molecules (N_2, CO, CO_2, and N_2O are other examples). At equilibrium vapor pressure a CO_2 crystal possesses fcc structure, which remains in the entire range of existence of the crystal.[1,2] In the solid phase the axes of the O–C–O molecules, whose carbon atoms occupy lattice sites, are oriented along the spatial diagonals of the cubic unit cell ($Pa3$ space group).

The thermal, optical, and other properties of solid CO_2 have been studied in a wide range of temperatures and pressures; see, e.g. Refs. 1 and 2 and the references cited there. However, the thermal conductivity at equilibrium vapor pressure has been investigated only at temperatures above 27 K.[3] It is of interest to investigate the thermal conducitivity of solid CO_2 at lower temperatures. Furhtermore, comparing with previous results obtained for other simple molecular crystals would yield new information about various internal processes occurring in crystals.

This paper reports preliminary measurements of the thermal conductivity of solid carbon dioxide in the temperature range 1.5–36 K.

1. EXPERIMENTAL PROCEDURE

A CO_2 crystal was grown and heat-treated. The measurements were performed with a hand-made liquid-He experimental setup, described fully in Ref. 4.

The main part of the setup is a 36 mm long cylindrical glass ampul, which holds the sample during the experiments, with an inner diameter of 4.2 mm and a 1 mm thick wall. Thin copper rings and heat-conducting glue secure two germanium resistance thermometers to the wall of ampul. The thermometers are used to determine the the temperature and the temperature gradient. The distance between the thermometers is 12 mm and the lower thermometer is positioned ~9 mm from the bottom of the ampul.

The CO_2 crystal was grown using 99.999% chemically pure carbon dioxide gas with natural isotopic composition. A mass spectrometer was used to check the purity of the gas. The solid CO_2 sample was grown from the gas phase, starting at the bottom of the ampul. The condensation conditions were as follows: temperature~173.3 K, pressure~14 kPa, and growth rate~1.5 mm/h. A temperature gradient ~2.2 K/cm was maintained along the ampul during growth.

When the crystal completely filled the ampul, the growth process was terminated and the temperature gradient was decreased to about 1.1 K/cm. Next, the sample was cooled. The cooling rate was about 0.1 K/h in the temperature range 173–100 K, ~0.2 K/h in the range 100–70 K, and ~0.5 K/h below 70 K. At liquid helium temperatures the sample was transparent and had no visible defects or voids. When the temperature of the sample was ~4.2 K and before the measurements were started, helium gas at pressure ~1 kPa was admitted into the ampul to improve the thermal contact between the sample and the two thermometers and the gradient heater. The steady-state flow method was used to perform the CO_2 thermal conductivity measurements. The experimental error did not exceed 10%.

Other details experimental are described in Refs. 4–6.

2. RESULTS AND DISCUSSION

The measurements of the temperature dependence of the thermal conductivity of solid CO_2 at tempeartures 1.5–36 K are displayed in Fig. 1. The high-temperature carbon dioxide data of Koloskova *et al.*[3] are also shown.

The qualitative temperature dependence of the thermal conductivity $\kappa(T)$ is typical for dielectric crystals; see, e.g. Refs. 1 and 2. Initially, at the lowest temperatures the thermal conductivity increases with temperature, reaching at maximum near 5 K. At temperatures above the maximum the thermal conductivity initially decreases exponentially, after which the decrease slows down. The maximum thermal conductivity is 720 W/(m·K). This value is much higher than any value measured so far for simple molecular crystals,[5–8] except solid parahydrogen.[7] For comparison, previous data obtained for crystals of pure nitrogen,[5] nitrous oxide,[7] and parahydrogen[8] are also displayed in Fig. 1.

Even though the high maximum value of the thermal conductivity is high, which attests to the high quality of the carbon dioxide crystal used for the measurements and to the high chemical purity of the sample, the dependence $\kappa(T)$ at low temperatures is far from typical for a dielectric crystal with a low density of defects. For the typical dielectric crystal with a low density of point defects and dislocations, phonon scattering by grains or the boundaries of the sample determines the low-temperature thermal conductivity, and being independent of the phonon frequency these processes
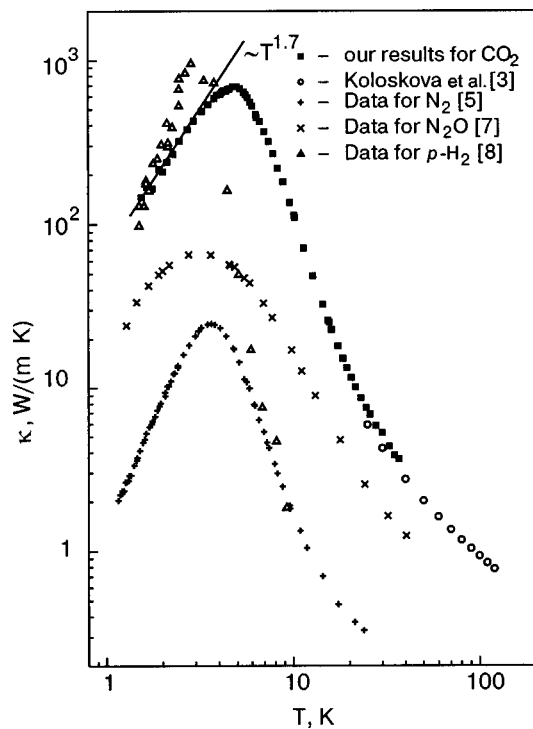
FIG. 1. Temperature dependence of the thermal conductivity of solid carbon dioxide. Previous data for nitrogen, parahydrogen, and nitrous oxide crystals are also displayed.

give $\kappa \sim T^3$. For our CO_2 sample $\kappa \sim T^{1.7}$. This dependence is close to that observed when phonon scattering by dislocation strain fields predominates.[9] Assuming in CO_2 that at low temperatures phonon scattering by dislocations predominates and using the crystal-structure data obtained from nitrogen thermal conductivity data[5] (where boudnary scattering predominated at low temperatures) the order of magnitude of the grain sizes in the experimental carbon dioxide crystal can be estimated as follows. Using the expression for the thermal conductivity of a gas $\kappa = 1/3 \, Cvl$, where C is the specific heat of the phonon gas, v is the phonon propagation velocity,

and l is the phonon mean-free path, which in our case is limited by the size of the grains in the sample, the grain size for our CO_2 sample is ~ 10 mm. This result was obtained assuming the specific heat of N_2 to be 10 times greater than for CO_2,[1] the phonon propagation velocity to be the same in nitrogen and carbon dioxide,[1] taking the experimentally determined ratio $\kappa_{CO_2}/\kappa_{N_2} \approx 100$, and taking the grain size in nitrogen to be $\sim 10^{-2}$ mm.[5] This means that the grains in our sample are large, and we could be dealing with a single crystal.

The high thermal conductivity at higher temperatures could be due to the relatively weak anharmonicity of CO_2 translational vibrations and therefore a weak phonon–phonon interaction.

A more detailed analysis of the measurements of the temperature dependence of the thermal conductivity of carbon dioxide will be published elsewhere.

*E-mail: p_stach@int.pan.wroc.pl

[1] *Physics of Cryocrystals*, edited by Yu. A. Freiman and V. G. Manzhelii, AIP, Woodbury, New York (1996).

[2] V. G. Manzhelii, A. I. Prochvatilov, V. G. Gavrilko, and A. I. Isakina, *Structure and Thermodynamic Preperties of Cryocrystals*, Begell House, New York (1998).

[3] L. A. Koloskova, I. N. Krupskii, V. G. Manzhelii, B. Ya. Gorodilov, and Yu. G. Kravchenko, Fiz. Tver. Tela **16**, 3089 (1974) [Phys. Solid State **16**, 1993 (1974)]; Fiz. Kondens. Sost., Institute for Low Temperature Physics and Engineering, Kharkov, USSR, No. 31, 69 (1974).

[4] A. Jeżowski and P. Stachowiak, Cryogenics **32**, 601 (1992).

[5] P. Stachowiak, V. V. Sumarokov, J. Mucha, and A. Jeżowski, Phys. Rev. B **50**, 543 (1994).

[6] P. Stachowiak, V. V. Sumarokov, J. Mucha, and A. Jeżowski, J. Low Temp. Phys. **111**, 379 (1998).

[7] P. Stachowiak, V. V. Sumarokov, J. Mucha, and A. Jeżowski, in *Conference on Cryocrystals and Quantum Crystals*, Freising'2002, poster presentation.

[8] O. A. Korolyuk, B. Ya. Gorodilov, A. I. Krivchikov, and V. G. Manzhelii, Fiz. Nizk. Temp. **25**, 994 (1999) [Low Temp. Phys. **25**, 708 (1999)].

[9] R. Berman, *Thermal Conduction in Solids*, Clarendon Press, Oxford (1976).